Open Access Dissertations

Theses and Dissertations

5-2018

Synergistic Effects of High Particle Fluxes and Transient Heat Loading on Material Performance in a Fusion Environment

Gregory Poppy Sinclair
Purdue University

Follow this and additional works at: https://docs.lib.purdue.edu/open_access_dissertations

SYNERGISTIC EFFECTS OF HIGH PARTICLE FLUXES AND TRANSIENT HEAT LOADING ON MATERIAL PERFORMANCE IN A FUSION ENVIRONMENT
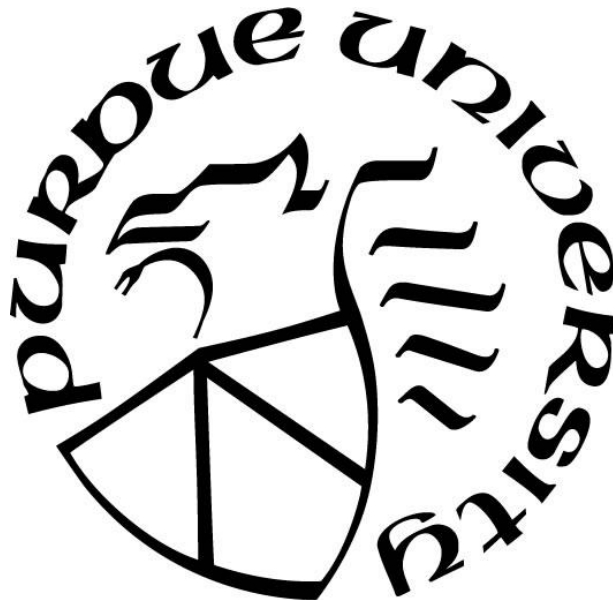
by

Gregory Poppy Sinclair

A Dissertation

Submitted to the Faculty of Purdue University

In Partial Fulfillment of the Requirements for the degree of

Doctor of Philosophy

School of Nuclear Engineering

West Lafayette, Indiana

May 2018

THE PURDUE UNIVERSITY GRADUATE SCHOOL
STATEMENT OF COMMITTEE APPROVAL

Dr. Ahmed Hassanein, Chair

>Department of Nuclear Engineering

Dr. Tatyana Sizyuk

>Department of Nuclear Engineering

Dr. Gennady Miloshevsky

>Department of Nuclear Engineering

Dr. Anter El-Azab

>Department of Materials Engineering

Dr. Zinetula Insepov

>Department of Nuclear Engineering

Approved by:

>Dr. Chan Choi

>>Head of the Graduate Program

Thank you to my loving girlfriend for supporting me through the late nights and long weekends. Thank you to my parents for encouraging me to follow my dreams and believing that I can make a difference. Thank you to my grandfather for convincing me to never give up.

ACKNOWLEDGMENTS

TABLE OF CONTENTS

LIST OF TABLES

LIST OF FIGURES

LIST OF ABBREVIATIONS

AFM atomic force microscopy

CCD Charge-coupled device

CFC carbon fiber composite

DBTT ductile-to-brittle transition temperature

ELM Edge-localized mode

FIB Focused ion beam

ICCD Intensified charge-coupled device

LPP laser-produced plasma

PFC plasma facing component

PFM plasma facing material

QCM quartz crystal microbalance

SEM scanning electron microscopy

TDS thermal desorption spectroscopy

VDE vertical displacement event

XPS x-ray photoelectron spectroscopy

UHFI ultra high flux irradiation

ABSTRACT

Author: Sinclair, Gregory, P. PhD
Institution: Purdue University
Degree Received: May 2018
Title: Synergistic Effects of High Particle Fluxes and Transient Heat Loading on Material
      Performance in a Fusion Environment
Major Professor: Ahmed Hassanein

The work presented in this thesis focuses on the thermal and structural evolution of different materials when exposed to both high-flux ion irradiation and high intensity pulsed heat loading. Nuclear fusion devices create an intense radiation environment consisting of very energetic deuterium (D^+) and helium (He^+) ions. During operation, off-normal plasma events, such as edge-localized modes (ELMs), could cause intense heating of the plasma-facing component (PFC) surface, leading to melting and possible splashing into the fusion plasma. High-Z, refractory metals, such as tungsten (W), are therefore seen as favorable, due to their high melting point, high thermal conductivity, and low sputtering yield. However, potential splashing of the molten wall could contaminate the plasma and shut down the reactor. High-flux He^+ wall loading could further exacerbate melting and splashing of the PFC surface, due to the growth of fiber form nanostructures, called fuzz, which possess a much lower mechanical and thermal strength than that of a pristine surface.

Experiments performed throughout the dissertation attempt to qualify the effect of He^+-induced surface structuring on the PFC thermal response during type-I ELMs. Elementary surface characterization revealed that He^+ loading blurs clear melting and droplet emission thresholds observed on pristine surfaces during ELM-like heat loading, inducing thermal damage gradually through localized melting and conglomeration of fuzz tendrils. The reduced thermal conductivity of fuzz nanostructures led to increased levels of erosion due to fragmentation of molten material. Decreasing the imparted heat flux, at the sacrifice of higher frequencies, through ELM mitigation techniques showed the potential for an intermediate operating window that could heal fuzz nanostructures via annealing without the onset of splashing. Tests on transversally-oriented W microstructures (which will be used in ITER) revealed that radiation hardening along grain boundaries due to high-flux He^+ loading may preferentially enhance brittle failure. Differences in penetration

depth between experimental heat loading methods (millisecond laser vs. electron beam) affected heat deposition in and plasticity of the damaged surface. Simultaneous He$^+$ particle loading and ELM-like heat loading inhibited fuzz formation due to repetitive shock-induced conglomeration. The addition of D$^+$ ion irradiation appeared to further reduce evidence of early-stage fuzz formation, due to super-saturation of D in the near-surface layer. Significant structuring due to D$^+$ particle loading may diminish the impact of ELM intensity on surface roughening and melting. Future studies need to expand upon the surface analysis presented throughout this dissertation and investigate the details of the subsurface to determine how intense thermal loading impacts gas trapping and migration. In addition, future PFC erosion research must utilize highly sensitive, *in situ* measurement techniques to obtain reliable information on material lifetime and performance.

1. INTRODUCTION

The future success of fusion devices depends on designing plasma facing components (PFCs) that can withstand the harsh radiation environment present inside the reactor. Current designs utilize either magnetic confinement or inertial confinement to drive nuclear fusion. In magnetic confinement systems, ionized fuel is controlled via the Lorentz force along magnetic field lines [1]. When confined fuel reaches a sufficient density, nuclear fusion can occur. Magnetic systems are defined as being "open" (e.g. magnetic mirror) or "closed" (e.g. tokamak), based on their field line geometry [1]. A diagram of a tokamak reactor is shown in Figure 1.1.
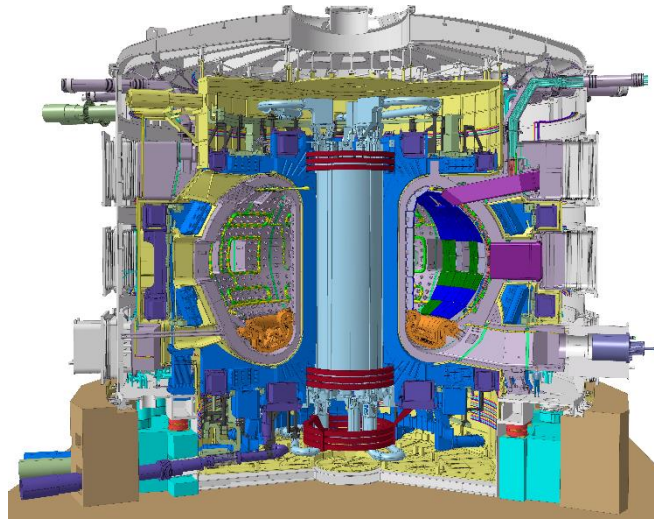
Figure 1.1: Schematic of ITER tokamak [2].

While tokamak systems do not need to worry about losing fuel along open field lines, like in the loss cone of a mirror device, buildup of reaction products in a tokamak can hinder the overall reaction rate. Consider the deuterium-tritium (DT) fusion reaction shown below:

$$^2D^+ + \ ^3T^+ \rightarrow \ ^4He^{2+}(3.54 \ MeV) + \ ^1n(14.05 \ MeV)$$
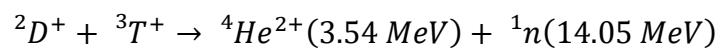
Neither of the products formed from DT can be used for future fusion reactions. Since neutrons are not charged, they travel toward the surrounding reactor wall without being affected by the induced magnetic field. However, $^4He^{2+}$ is charged and will travel along magnetic field lines, inhibiting future fusion reactions unless otherwise controlled. High levels of $^4He^{2+}$ could remove enough heat from the fusion plasma to cause instabilities

and shut down the reactor. By utilizing a divertor, tokamak systems remove $^4He^{2+}$ (also referred to as "ash") from the fusion plasma during operation along poloidal field lines [1]. A modern divertor schematic is shown in Figure 1.2.
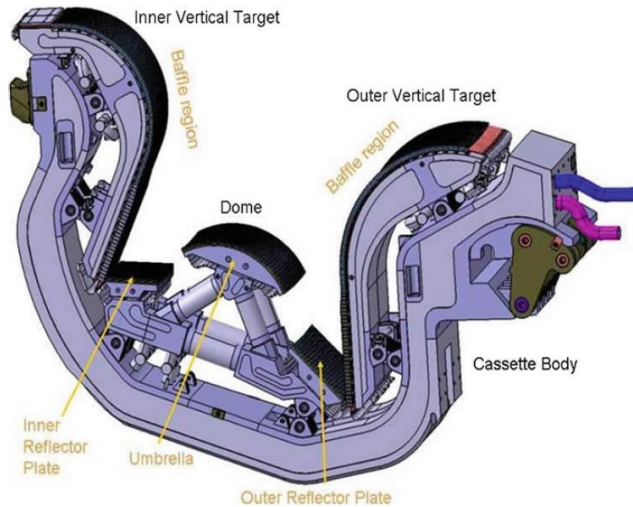
Figure 1.2: Schematic of ITER divertor cassette [1]. Reproduced with permission of Springer London in the format Thesis/Dissertation via Copyright Clearance Center.

Incident helium ions strike the divertor tiles at very high fluxes on the order of 10^{24} m^{-2} s^{-1} [3]. The divertor will also be exposed to D$^+$, T$^+$, and n loading during operation. Understanding how these various species affect material degradation of the divertor PFCs has been an important focus of many studies.

During reactor operation, off-normal plasma events can occur, resulting in intense heat loading on surrounding PFCs. Three different types of transient events may occur in a tokamak system. Major disruptions occur when the plasma current becomes unstable or the plasma density exceeds the Greenwald limit [1]. In response, magnetic confinement is lost, the plasma is cooled, and the reactor walls experience very intense heating on the order of 10-100 MJ m^{-2} for 1-10 ms [3]. Due to their catastrophic nature, major disruptions are avoided as much as possible. Changes in vertical plasma stability due to the poloidal field coils can lead to a vertical displacement event (VDE). Uncontrolled movement of the confined plasma in the vertical direction can lead to direct interaction with the first wall, imparting fluxes of ~ 60 MJ m^{-2} for 300 ms [3], [4]. Finally, edge-localized modes (ELMs) impart short, intense fluxes onto divertor plates due to periodic relaxations of the plasma to reduce high pressure gradients along the edge [5]. When the edge plasma undergoes an

ELM event, 1-10% of the core plasma energy is expelled to the scrape-off layer (SOL), where field lines intersect with the divertor surface [6]. Different types of ELMs are categorized by their intensity and frequency. Type-I ELMs are the most common and the most intense, imparting ~ 0.2-2.0 MJ m^{-2} onto divertor plates for 0.1-1 ms at a repetition rate of ~ 1 Hz [7]. Type-II ELMs possess higher frequencies and smaller heat loads than type-I ELMs, and are associated with high collisionality regimes [8]. Type-III ELMs are similar to type-I ELMs, but are lower in intensity and occur more frequently at the transition between confinement modes [4]. Additional ELM categories exist at even lower intensities, but will not be discussed here. Type-I ELMs are the most relevant when discussing material performance, because they impart the largest amount of energy in the shortest amount of time. Recent work has tried to find ways to mitigate ELM events by inducing more frequent relaxation at lower intensities. Work done at JET utilized error field correction coils to produce external magnetic perturbation fields that reduced ELM energy loss by 5% while increasing frequencies by a factor of 4 [9]. Pellet pacing has utilized both fuel and non-fuel pellet injection to trigger ELM events that possess up to 12x lower energy densities [6], [10]. Other mitigation methods include using vertical plasma oscillations and toroidal field ripples [11], [12]. Recent estimates expect that successful mitigation could keep ELM energy densities below 1 MJ m^{-2} at frequencies greater than 10 Hz [13]. Despite efforts to mitigate ELMs, mitigation will not be perfect, and small number of unmitigated ELMs will still occur [14]. Work discussed in [4] and [15] explore how different types of materials respond to ELM-like heat loading.

Tungsten (W) has been identified to be the strongest and most promising material candidate for divertor PFCs. The high-Z refractory metal has a very high melting point, a high thermal conductivity, a low sputtering yield, low tritium retention, and low activation [16]. Other candidate materials, like carbon fiber composites (CFCs), were rendered unsuitable for divertor tiles, due to unsustainable levels of erosion, severe neutron damage, and large T inventory [4], [17]. The most serious problems with using W for divertor PFCs involve its high ductile-to-brittle transition temperature (DBTT) and its high atomic number. As mentioned previously, a fusion reactor system operates more efficiently when impurity concentrations are low. Unfortunately, line radiation from impurities increases as a function of atomic number, limiting maximum tolerable atomic impurity concentrations

to $< 10^{-5}$ for W [3]. The other concern is that the temperature at which W transitions from being a ductile material to a brittle material (known as the DBTT) is high – around 673 K [18]. Therefore, divertor PFCs would need to have an operational temperature above 673 K to avoid brittle failure, but below the recrystallization temperature to prevent unsustainable thermal stress [19]. Testing of W tiles in a fusion environment have shown that high flux particle irradiation and intense ELM loading could seriously limit component lifetime.

Concerns regarding the use of W for reactor PFCs has driven research into other high-Z, refractory metals. Both molybdenum (Mo) and tantalum (Ta) have been proposed as promising alternatives, due, in part, to their high thermal strength. Select thermal properties of different high-Z candidate materials are listed in Table 1.1.

Table 1.1: Physical properties of some high-Z, refractory metals (reproduced from [16])

Material	Atomic number	Melting point (K)	Thermal conductivity (W m^{-1} K^{-1})	Specific Heat of Vaporization (kJ g^{-1})	DBTT (K)
Tungsten	74	3422	110	4.5	673 [18]
Molybdenum	42	2623	100	6.2	573 (TZM) [20]
Tantalum	73	3107	61	4.1	73 [21]

Mo exhibits a lower melting point than W, but has a lower atomic number (lower line radiation) and a higher specific heat of vaporization. Therefore, even though more melting may occur on a Mo surface, less vaporization is expected and more erosion of that surface could occur without quenching the plasma. Ta has a lower thermal conductivity than W, but appears to be more ductile at low temperatures. Therefore, Ta divertor tiles may exhibit less cracking. Work presented in [22] observed an increase in the ELM intensity threshold for surface cracking with an increase in the atomic concentration of Ta in W-Ta alloys. However, conflicting results obtained from similar experiments in [23] illustrate that the comparative thermal strength of Ta remains unclear. Some recent studies have shown that alloying W with Ta could improve material strength by inhibiting the nucleation of gas-filled blisters in the subsurface and reducing D retention [24]. Both the thermal and mechanical strength of alternative candidate materials for PFCs will be explored throughout the thesis to reveal potential benefits over W.

In addition to steady-state heat loading during operation, divertor PFCs will be exposed to pulsed heat loading via type-I ELMs that can lead to roughening and potential melting. Steady-state heat loading in the divertor region is around 10-20 MW m^{-2} [25], [26]. Transient loading during ELMs (assume ELMs refer specifically to type-I ELMs unless stated otherwise) additionally impart up to 2 MJ m^{-2} onto the PFC surface for durations of 0.1-1 ms [27]. While the presence of steady-state loads alone will not cause significant material degradation, the addition of transient pulsed heat loading can possess enough energy to lead to cracking and melting of the surface. The additional surface heating from steady-state loads reduces the thermal jump that is needed to cause melting. Work conducted in [26] showed that steady-state loading of 10 MW m^{-2} (T_{surf} = 973 K) led to significant surface damage during ELM loading that did not occur without steady-state loading. Characterizing the response of the W surface can be done using different heat loading parameters, such as the energy density, pulse duration, base temperature, or frequency. A diagram showing differences in surface response at different energy densities is shown in Figure 1.3. At very low energy densities, the surface will not be affected, because heating is below the damage threshold [28]. Once the energy density has exceeded the damage threshold, the surface will undergo roughening, as shown in [29]. Depending on the surface temperature of the component, cracking can also occur as the energy density continues to increase [28]. Recrystallization will eventually occur, imparting sufficient heating to rearrange dislocations, resulting in a new grain structure [30]. Thermal shock analysis has shown that once a surface undergoes recrystallization, the yield strength decreases, leading to more intense surface roughening and cracking [19], [31], [32]. Work done in [29] has defined clear thresholds for recrystallization on W.
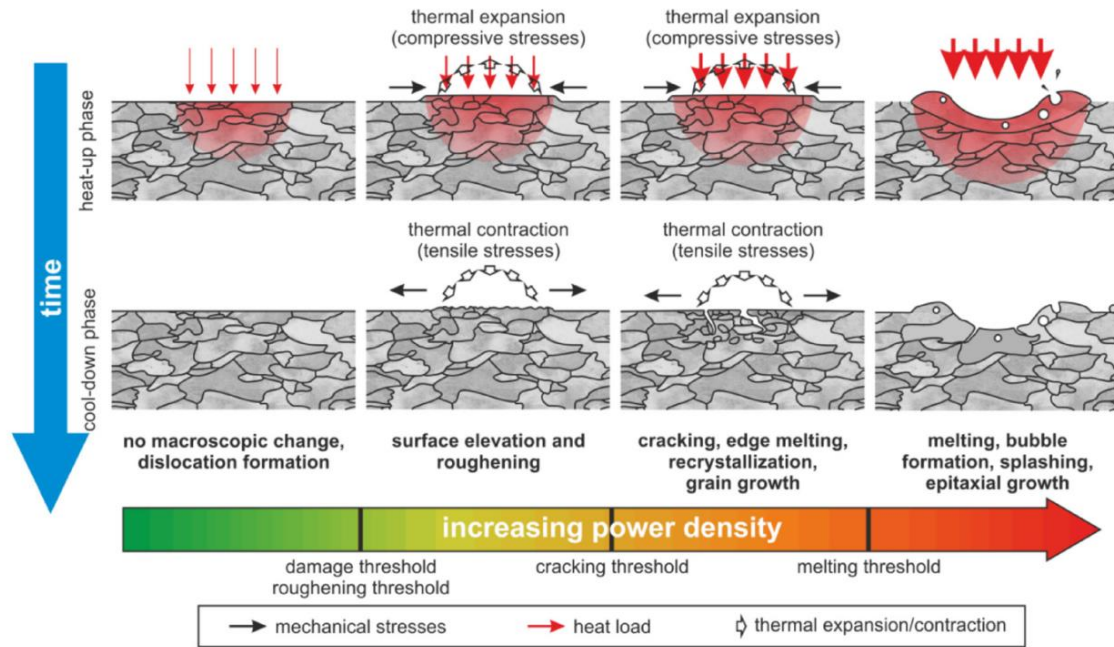
Figure 1.3: Variation in material response as ELM energy density increases. Reproduced from [13] with permission. Copyright IAEA, Vienna 2017.

Higher ELM intensities will lead to melting of the surface, imparting enough energy to briefly raise the PFC surface above the melting point [33]. As seen in Figure 1.3, melting of a specific area will drive molten material outward, forming a crater. Repetitive loading at high intensities can eventually lead to splashing of the melt layer and even vaporization [15], [25]. In a tokamak device, molten material moves according to the J x B force, causing the formation of leading edges, which become weak points along the divertor tiles [34], [35]. Exposures above the melting threshold present the most serious concerns for component viability and plasma performance. Work focused on how Mo responds to ELM-like heat loading near the melting threshold is presented in Chapter 3.

Changes in thermal strength due to the presence of high flux He loading can exacerbate melting and splashing of divertor surfaces. In 2006, research done at NAGDIS-II revealed the growth of a fiber form nanostructure, now known as fuzz, on a W-coated graphite substrate when exposed to 12 eV He$^+$ ion irradiation at a surface temperature of 1250 K and a fluence of 3.5 x 10^{27} m^{-2} [36]. The structure appeared as a dense layer of cylindrical rods along the surface. Concerns over the impact of nanostructure growth on hydrogen retention and thermal strength have inspired many studies over the past decade. Observations of fuzz nanostructure growth on the tip of a Langmuir probe in Alcator C-

Mod showed the potential for fuzz formation in a fusion environment [37]. Work done in [38] defined surface temperature, ion energy, and ion fluence windows for fuzz growth based on a collection of studies, as shown in Figure 1.4.
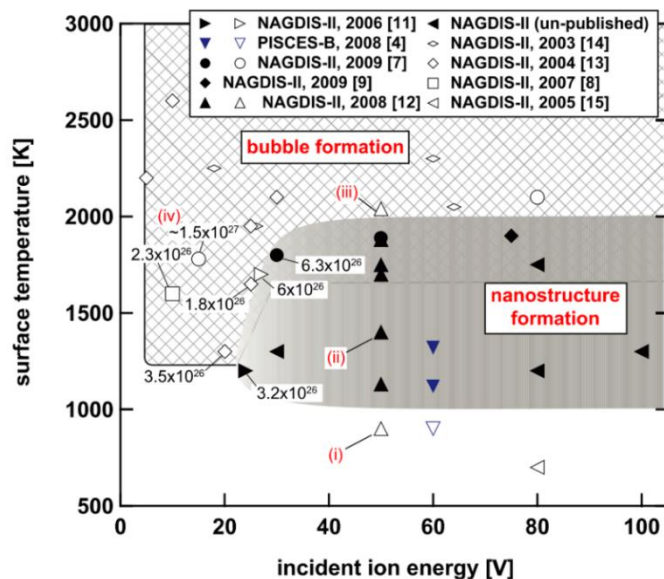
Figure 1.4: Operating windows for fuzz growth. Reproduced from [38] with permission. Copyright IAEA, Vienna 2009.

Fuzz formation is expected to occur when the surface temperature is between 1000 K and 2000 K, ion energy is above 20 eV, and ion fluence is $\sim 10^{24}$ m^{-2} [38], [39]. An SEM micrograph of a nanostructured fuzz W surface is shown in Figure 1.5. The mechanism by which the fuzz nanostructure forms remains unclear. Work outlined in [40] hypothesizes that tendrils are formed due to the rupture of implanted bubbles. Implanted He is thought to cluster together and eventually become trapped at a site in the lattice, forming a Frenkel pair. Continual growth of the helium cluster eventually forms prismatic dislocation loops from self-interstitial atoms that migrate away from the trap. Eventually, the lattice remaining between the growing He bubble and the surface reduces to a ligament and rupture occurs. Continued bubble rupture is thought to eventually produce fuzz-like nanostructures. TEM observations made in [39] led to the description of a very similar growth process, where thermally-enhanced bubbles coalesce in the subsurface, forming protrusions along the surface. Eventually, bubbles burst and create finer protrusions. Over time, repeated bursting of protrusions creates a finer and finer nanostructure, resembling the surface observed in Figure 1.5. Another theory outlined in [41] posits that nanoscale

tendrils are formed due to thermally-enhanced creep and viscoelasticity of the tungsten surface during helium bombardment. During He$^+$ irradiation, He bubbles are implanted in the near-surface region. However, stresses in the bulk drive bubbles toward the surface. At high surface temperatures, thermal creep can occur, and helium bubbles move toward the surface to reduce their potential energy. As a bubble approaches the surface, incident helium ions can form a bubble between the viscous tungsten surface layer and the bubble beneath. The driving force of the underlying bubble pushes the tungsten layer out of the surface to form a nanorod. Other theories for fuzz formation exist, but will not be discussed here. The growth of fuzz nanostructure has been observed on other materials besides W, including Mo [42]–[44], Ta [45], [46], and niobium (Nb) [47], [48], as well as other metals [49], [50]. The effect of He$^+$ ion energy on fuzz formation was investigated in Chapter 4, Section 4.1 to measure changes in fuzz layer thickness, and refine proposed growth mechanisms.
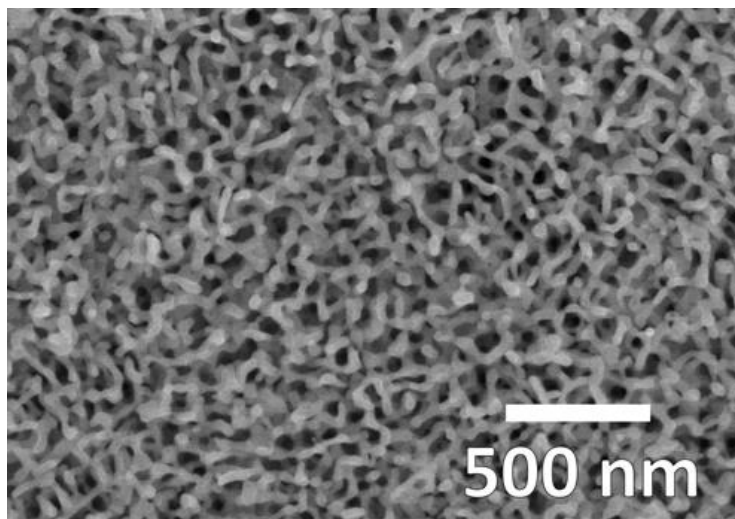
Figure 1.5: Representative SEM micrograph of fuzz nanostructure.

Large structural changes to the surface are expected to have a significant impact on the mechanical and thermal properties of the material. Work done in [51] found that fuzz formation lowers the physical sputtering yield of the surface by trapping sputtered particles in thick, heterogeneous tendrils. The existence of microprotrusions along the surface also lowers the threshold for unipolar arcing, which could lead to unsustainable levels of erosion [52], [53]. Multiple studies have tried to measure the thermal conductivity of the fuzz structure using different methods [54], [55]. Direct measurements of nanostructured W

using the 3-omega method recently measured a drop in thermal conductivity of 80% [56]. A reduction in the thermal conductivity of W PFCs during reactor operation could lead to enhanced melting and erosion during ELM loading. Investigation of the W fuzz material in response to mitigated ELM heating (< 0.5 MJ m^{-2}) showed that nanoscale tendrils appeared to reintegrate into the bulk without erosion [57]. However, scientists remain uncertain on whether erosion could occur at different ELM parameters and whether fuzz nanostructure is ultimately beneficial or detrimental to thermal shock performance. The effect of helium-induced fuzz formation on changes in surface morphology during pulsed heat loading in both unmitigated and mitigated ELM regimes are investigated further in Chapter 4 (Sections 4.2-4.4). Chapter 4, Section 4.3 presents a comprehensive analysis of W fuzz erosion during ELM loading using multiple measurement techniques. Understanding how heterogeneous fuzz nanostructure alters expected levels of degradation and erosion will help revise current performance estimates.

Additional experiments have attempted to study the effect of grain orientation on material performance. However, most research has only characterized oriented samples due to ELM-like heat loading [31], [32]. Based partly on work conducted in [32], ITER has decided to utilize W surfaces with transversally-oriented grains, which have shown to exhibit resistance to plastic deformation and parallel cracking. ITER-grade W is prepared by powder metallurgy (with sintering at 2273 – 2773 K), before being forged and rolled into rod-like geometries, producing transversal grains (oriented perpendicularly to the loaded surface) [28]. Grains end up being 100 µm long and 40 µm wide [28]. Comparisons between longitudinal, transversal, and recrystallized grain orientations under pulsed heat loading discovered that the transversal grain orientation was the most resistant to large, parallel cracks [31]. Due to poor cohesion between grains, recrystallized grains exhibit poor thermal shock performance. Despite the thermal shock resistance of transversally-oriented W, changes in material properties due to high-flux He$^+$ loading have not yet been investigated. Chapter 4, Section 4.5 explores the impact of helium bubble nucleation and migration on the thermal strength of ITER-grade W. Similar testing is also performed on the same type of W used throughout the rest of the dissertation to assess how well the work being presented reflects the true material response in a fusion environment.

Chapter 5 examines the role of base temperature and heat loading method. Due to the difficulty of testing W samples in a fusion environment (e.g. DiMES), many pulsed heat loading experiments utilize devices to replicate heat loads expected during ELM events. Heat loading methods include pulsed millisecond (ms) laser irradiation, electron beam irradiation, and plasma accelerator irradiation [15], [33], [58]. The work in Chapter 5 compares the morphology evolution resulting from both pulsed ms laser irradiation and electron beam irradiation, and discusses the benefits and drawbacks of each method. ELM-like heat loading was applied with different base temperatures to assess the impact of background, steady-state heat loading on material degradation. Results obtained present a clear understanding of how helium-induced fuzz nanostructure impacts the thermal shock performance of W divertor PFCs.

Incident D^+ ions present in a fusion environment will compete with He^+ ions for vacancies in the subsurface, affecting both the mechanical and thermal response of the W surface. When exposed to D^+ ion irradiation at fluxes above 10^{21} m^{-2} s^{-1} and temperatures below 950 K, blisters are formed in the subsurface [59]. Incident D^+ ions migrate toward intrinsic traps in the subsurface and form bubbles. Studies in [60] linked the formation of blisters to intergranular cracking below the surface. As the surface temperature increases, trapping of D diminishes due to thermally-enhanced desorption out of the surface [61]. Blistering is suppressed when W is exposed to both D^+ and He^+ ion irradiation. The presence of He^+ is thought to create a diffusion barrier to incoming D^+ ions, inhibiting implantation and blister formation [62]. In addition, the presence of D^+ has been found to prevent fuzz formation in some studies. Simultaneous dual beam ion irradiation of pure W and W-Ta alloys revealed that a 40% He^+/60% D^+ flux ratio resulted in complete prevention of fuzz formation, producing a porous surface [63]. Increasing the relative D^+ ion flux led to recrystallization [63]. Preliminary investigations on the surface response of W during combined dual beam particle loading and ELM-like heating revealed that the presence of D^+ reduced the resultant pore density on the W surface [23]. Another study that exposed W samples to sequential H/He loading and electron beam pulsed heat loading found that the presence of H did not have a significant impact on crack formation [64]. The effect of ELM intensity on surface evolution and material erosion during simultaneous dual

beam (D^+ and He^+) ion irradiation and pulsed laser irradiation is discussed further in Chapter 6.

Concluding remarks and suggestions for future work are discussed in Chapter 7. The impact of the research presented is assessed, providing the groundwork for advancement in plasma-materials interactions studies.

2. EXPERIMENTAL FACILITIES

The research presented throughout this dissertation was conducted in the Center for Materials Under Extreme Environment (CMUXE) at Purdue University. Intense heat loading and particle loading expected on reactor PFCs was replicated in a laboratory environment using a combination of heaters, ion sources, and pulsed laser systems. Certain experiments were conducted with a singular radiation source (see Chapter 3), while other experiments combined different radiation sources to study the synergistic effects on material response (see Chapters 4, 5, and 6). Both *in situ* and *ex situ* analysis techniques were utilized to assess and quantify surface degradation and erosion. Imaging of the laser-produced plasma (LPP) plume and real-time mass loss measurements provided direct evidence of surface excitation and droplet emission. Surface imaging and metrology performed afterward revealed the presence of fuzz nanostructures, melt layers, crack formation, and/or surface roughening. The facilities used for both radiation exposures and analysis are detailed below.

2.1 Experimental chambers

All pulsed heat loading studies were conducted in three different irradiation facilities: the Laser-Produced Plasma (LPP) chamber, the Ultra High Flux Irradiation (UHFI) I chamber, and the UHFI-II chamber. Each chamber utilized a 1064 nm laser for pulsed heat loading studies. More details on each chamber are listed below.

2.1.1 LPP experimental chamber

A schematic of the LPP chamber is shown below in Figure 2.1. The base pressure of the chamber was $\sim 10^{-5}$ torr. Pulsed millisecond (ms) laser irradiation studies on Mo fuzz surfaces were conducted in the chamber (refer to Chapter 4). Samples were transferred from the UHFI-I chamber (described below) and mounted on a translational stage inside the chamber to attain multiple exposures on one sample in a grid-like pattern. A quartz crystal microbalance (QCM) was also mounted on an optical stand and placed 20 mm from the sample surface at an angle of 45°. More information on the QCM mass loss

measurement technique can be found in section 2.4.1. Pulsed heat loading was applied to the Mo fuzz surface using a GSI Lumonics 1064 nm pulsed Nd:YAG ms laser. Once exiting through the shutter, the beam struck a mirror and traveled through a focusing lens with a focal length of 40 cm before striking the sample surface. All laser loading used a spot size of 1 mm, a repetition rate of 1 Hz, and a pulse duration of 1 ms. Experiments conducted examined the effect of pulse count and energy density.
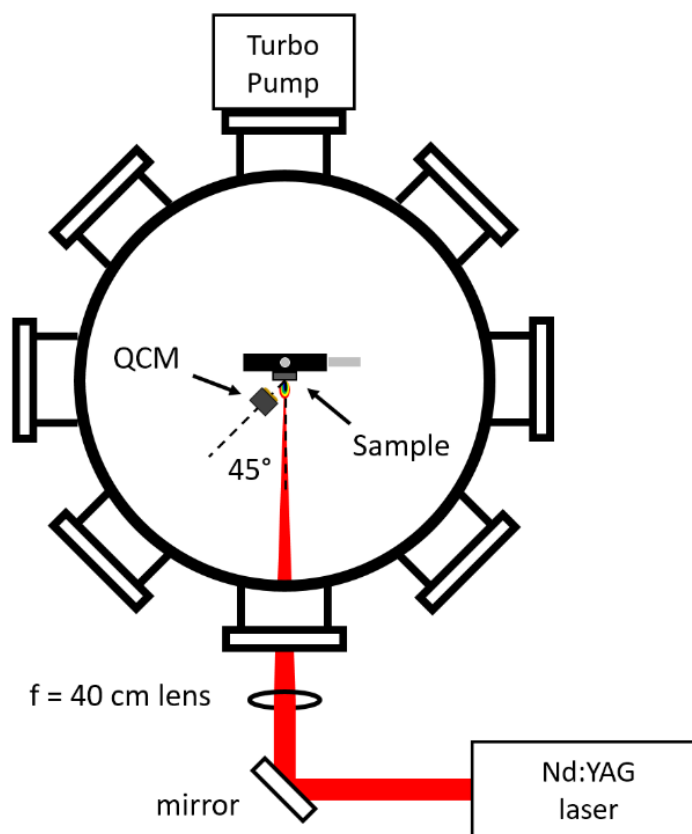
Figure 2.1: LPP experimental chamber

2.1.2 UHFI-I chamber

Some low-energy He$^+$ ion irradiations were conducted in the Ultra High Flux Irradiation (UHFI) I chamber. An experimental setup schematic for experiments done in this chamber is shown in Figure 2.2. The base pressure of the chamber is around 1×10^{-8} torr. W and Mo samples were placed on a resistive heater attached to a manipulator arm. Samples were then heated to different temperatures, using a temperature controller with PID feedback. A Kaufman & Robinson end-hall (EH) 400 broad beam ion gun was used for all He$^+$ ion irradiations. Experiments done in the UHFI-I chamber utilized a flux of 7.2

$\times\ 10^{20}$ m^{-2} s^{-1} and an ion energy of 100 eV. During ion irradiation, the working pressure in the chamber was $\sim 2 \times 10^{-4}$ torr.
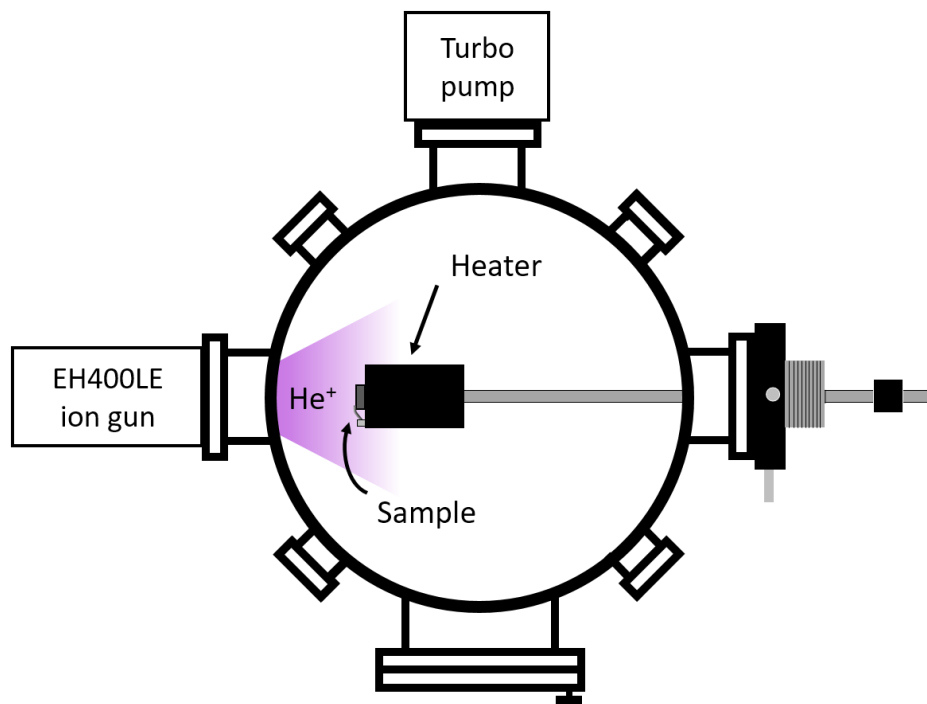
Figure 2.2: UHFI-I experimental chamber.

2.1.3   UHFI-II chamber

Most experiments presented in this dissertation were conducted in the UHFI-II chamber. Improvements over the UHFI-I chamber include more ports, a larger volume, and a more advanced stage manipulator, along with the addition of a second EH 400 broad beam ion gun and a pulsed ms laser. An experimental schematic of the UHFI-II chamber when fully utilized is depicted in Figure 2.3. The advanced capabilities of the new chamber allow for dual beam ion irradiation with additional ELM-like pulsed heat loading. Steady state heating can also be replicated using a resistive heater to raise the temperature of the sample during exposure via PID feedback. Experiments presented in Chapter 6 demonstrate the advanced capability of the new chamber.
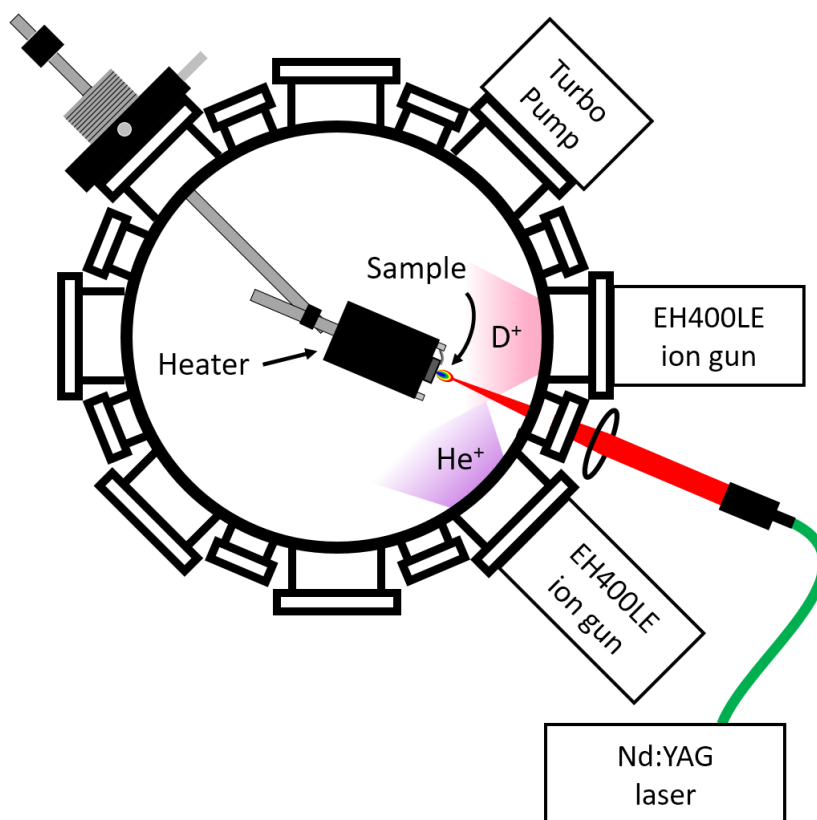
Figure 2.3: UHFI-II experimental chamber

Despite the extensive capabilities of the UHFI-II chamber, not all experiments conducted utilized every radiation source simultaneously. Experiments presented in Chapter 3 focused on the changes in surface morphology due to laser heating only. One of the EH 400 ion sources was used with pulsed laser heating in Chapters 4 and 5 to characterize the effect of helium-induced fuzz formation on the thermal and structural evolution and erosion of a W surface. As mentioned in the previous paragraph, experiments performed in Chapter 6 utilize both ion sources and the pulsed ms laser simultaneously.

The base pressure of the UHFI-II chamber is $\sim 10^{-7}$ torr. The working pressure can vary between 10^{-3} and 10^{-2} torr, depending on the number of ion sources in use at one time. Both ion sources are gridless EH broad beam sources. One gun was used for 100 eV He^+ irradiations, while the other was used for 100 eV D^+ irradiations. Fluxes, fluences, and irradiation times varied between experiments. Pulsed heat loading was supplied using a 1064 nm pulsed ms laser. All exposures utilized a spot size of 1 mm, while the repetition rate, pulse duration, energy density, and pulse count was varied. Two different lasers were utilized for experiments in this chamber, described below.

2.2 Kaufman & Robinson eH400 gridless ion/plasma source

All ion irradiations conducted throughout the dissertation utilized a high-flux, broad beam ion/plasma source to replicate particle loading in the divertor region of a tokamak. The Kaufman & Robinson end-Hall 'eH' 400 broad beam ion/plasma source produced particles fluxes up to 7.2×10^{20} m^{-2} s^{-1} at ion energies between 75 eV and 200 eV. Ion irradiations were performed with He gas and/or D gas. The broad beam of the source ensures a constant flux over the entire sample. At the low energies utilized for D$^+$ and He$^+$ ion irradiations, non-normal incidence was not a concern in certain dual beam experimental setups (see Chapters 4 and 6) that used ion incident angles of 22.5° [65]. In experiments that utilized a dual beam setup, the particle flux was significantly lower, due to geometrical attenuation of the beam.

2.3 Pulsed laser systems

2.3.1 GSI Lumonics JK702H Welding Laser

Experiments presented in Chapter 3, 4, and 5 utilized a GSI Lumonics JK702H Welding Laser. The laser system produces a pulsed 1064 nm laser beam using a Neodymium-doped Yttrium Alumnium Garnet crystal. Photons are focused and collimated before exiting the shutter. This laser system can produce a pulse of up to 6 J at a pulse duration of 1 ms. The repetition rate, pulse duration, and pulse energy can all be adjusted from the laser control panel. The system can also be externally controlled, which was done in Chapter 3, when taking intensified charge-coupled device (ICCD) camera images of the laser-produced plasma plume. Experiments were conducted with this laser system in the LPP chamber and the UHFI-II chamber, utilizing a power density between 0.38 GW m^{-2} and 2.0 GW m^{-2}, with a pulse duration of 1 ms, and a repetition rate of 1 Hz. Laser light was then aligned to the chamber using a combination of mirrors and focused using a plano-convex lens of varying focal lengths.

2.3.2 Unitek Miyachi LW25A Pulsed Millisecond Laser

Studies discussed in Chapters 4 and 6 utilized a Unitek Miyachi LW25A Pulsed Millisecond Laser. The laser system was very similar to the GSI Lumonics system. Heat

loading experiments using this laser were performed in the UHFI-II chamber. While the LW25A system also produces a 1064 nm laser pulse using a Neodymium-doped Yttrium Alumnium Garnet crystal, the light travels through an optical fiber cable after exiting the shutter. Energy calibration measurements revealed that an insignificant amount of energy is lost by traveling through the optical fiber cable. Once exiting the fiber cable, the laser pulse is collimated to produce an unfocused beam with a diameter of ~ 4 mm. The beam is then focused using a plano-convex lens of varying focal lengths before traveling into the chamber and striking the sample surface. Energy readings at the sample surface measured a total energy loss of around 30% from the shutter to the surface. Utilizing the LW25A system was much safer and easier, due to the optical fiber cable that minimized the number of mirrors needed to align the beam.

Experiments conducted with this laser system focused on the effect of different pulse energies and repetition rates on surface damage. The total power of the laser system is 25 W, which yields a maximum energy density of ~ 3 MJ m^{-2} on the sample surface. The pulse duration can be varied from 0.1 – 1 ms, and the repetition rate can be varied between 1 Hz and 30 Hz. All experiments utilized a spot size of 1 mm, while other parameters were adjusted.

2.4   In situ analysis techniques

Many different *in situ* analysis techniques were utilized to measure erosion due to ELM-induced splashing. In contrast to other erosion detection methods, such as microbalance measurements, the techniques presented below are not affected by the growth of oxide layers or collection of dust in an ambient environment [66].

2.4.1   Quartz crystal microbalance

A quartz crystal microbalance (QCM) was utilized in multiple experiments to measure levels of particle emission during pulsed laser heating. An Inficon QCM was used in conjunction with a SQC-310 Thin Film Deposition Controller to detect mass loss due to intense heat loading. A QCM consists of a quartz crystal with a gold surface resting on flexible gold contacts. Once turned on, the QCM crystal will vibrate at a specific frequency.

Changes in the vibrational frequency during pulsed heat loading can be used to estimate the amount of material that struck the crystal surface using the Sauerbrey equation:

$$\Delta f = -\frac{f_q^2 M_f}{N \rho_q S} = -\frac{f_q^2 m_f}{N \rho_q} \qquad (2\text{-}1)$$

where f_q is the fundamental resonant frequency of the quartz, N is the frequency constant of the specific crystal cut (AT or BT), and m_f is the areal density of the deposited mass (mass/surface area). During pulsed heat loading, the SQC-310 controller samples the frequency at 4 Hz and outputs thickness/time measurements ($\text{Å}/s$) using the Sauerbrey equation. Before each laser exposure, the QCM reading is zeroed. Then, $\text{Å}/s$ data is collected during laser irradiation. Rate data is then integrated over the total exposure time to obtain an estimate of the total thickness deposited onto the QCM surface. Using the surface area of the exposed gold surface (52.18 mm^2) and assuming a density of 19.3 g cm^{-3} for W, a mass value can be calculated. Data is presented as a function of pulse count and of energy density.

2.4.2   Witness plate

Two different types of witness plate collection methods were utilized throughout this thesis. In Chapter 4, a Si witness plate was mounted on an optical stand at a distance of 15 mm from the sample surface (Figure 2.4(a)). The witness plate was oriented normal to the sample surface, and was used to collect any eroded W material during pulsed heat loading. After each exposure, the witness plate was removed and analyzed via x-ray photoelectron spectroscopy (XPS). Obtained spectra reflected the surface composition of the witness plate, and were used to determine whether ELM-induced erosion occurred. See Section 2.5.4 for more information on XPS techniques.

In Chapter 6, a Mo witness plate was used to measure the existence and behavior of ELM-induced splashing under simultaneous particle and heat loading. A Si witness plate could not be used due to the intense radiation environment present during simultaneous ion irradiation and laser loading (T$_{\text{melting, Si}}$ = 1687 K) [67]. Therefore, the Mo witness plate was bent and mounted onto the sample stage, so that part of the plate hung over the W sample and collected any eroded material. The witness plate was oriented at a 45° angle

relative to the sample stage. After each exposure, the witness plate was removed from the vacuum chamber and analyzed via XPS.

Figure 2.4: Witness plate measuring techniques

2.4.3 ICCD and CCD imaging

Imaging the plasma plume during laser irradiation was done to try and observe any evidence of particle emission. Studies done in [68] and [15] successfully used a CCD camera to directly capture droplet emission from a pristine W surface during pulsed heat loading in QSPA-T. Although QCM and witness plate measurements provide clear evidence on the presence of splashing and droplet emission, they do not truly capture the delay time and velocity of emitted particles. Experiments conducted in Chapter 4 utilized a charge-coupled device (CCD) camera in an effort to capture evidence of particle emission. A CCD camera captures the intensity of different photons by using an array of capacitors that build charge proportional to the energy of photons being imaged. Capacitors are then discharged to a shift register, where charges are analyzed and transferred to memory. CCD images were captured after each laser pulse, with a delay time of about 0.9 ms (with respect to the leading edge of the laser pulse) and a gate width of 1 ms.

An intensified charge-coupled device (ICCD) camera was used for plume emission measurements presented in Chapter 3. In contrast to a CCD camera, an ICCD camera contains an image intensifier that increases the sensitivity of the device. Photons imaged by the ICCD cameras strike a photocathode, producing photoelectrons that are multiplied by a micro-channel plate. Excited electrons are then converted back to photons using a phosphor screen. Results presented in Chapter 3 demonstrate the increased sensitivity and accuracy of the ICCD camera.

2.5   Ex situ analysis techniques

Conducting extensive analysis after experimentation provides useful information on surface morphology. In addition, compositional measurements of samples and witness plates reveal the effect of different loading conditions on ELM-induced melting and splashing.

2.5.1   Scanning electron microscopy

The most extensively used characterization technique was using surface electron microscopy to describe fundamental changes in the surface structure due to different types of pulsed heat loading. A Hitachi S-4800 field-emission scanning electron microscope (FE-SEM) was used in every chapter to image the sample surface before and after exposure. In an SEM, high-voltage electrons strike the sample surface and interact with atomic structures, producing secondary electrons that reflect the topography of the surface. The intensity of detected secondary electrons decreases from areas of the sample that exhibit slopes or edges, producing a darker spot. Both low-magnification and high-magnification images are presented throughout the thesis, revealing different mechanisms of damage due to bubble formation, roughening, cracking, melting, desorption, and splashing. Although SEM imaging is incredibly useful in defining the morphology of a surface, further analysis is usually needed to fully characterize the material response.

2.5.2   Optical profilometry

Useful qualitative and quantitative information was obtained from within the laser-exposed area from some samples utilizing optical profilometry. While two-dimensional information of a surface can effectively characterize the general morphology, and identify different regimes of thermally-induced damage, SEM imaging does not provide depth information that can help quantify the degree of damage. Some samples were analyzed using a Bruker GT-K1 optical profilometer in a cleanroom environment (ISO Class 4) to obtain arithmetic roughness values and depth profiles of the damaged area. The optical profilometer uses white light interferometry to scan the surface and develop a three-dimensional map of the area of interest. The GT-K1 profilometer has a vertical measurement range of 0.1 nm – 10 mm.

One quantitative parameter of interest was the arithmetic mean roughness (R_a), which is mathematically defined by the following equation:

$$R_a = \frac{1}{l} \int_0^l |y(x)| dx \qquad (2\text{-}2)$$

where l is the measured length and $y(x)$ is the profile height function [69]. R_a values were primarily used to quantify the intensity of laser-induced surface roughening. Thermal stress imparted in the material lattice by the incident laser beam can cause deformation; the surface roughness is proportional to the magnitude of imparted thermal stress below the melting point. As the sample temperature approaches the melting point, the phase transition relieves stresses in the subsurface and yields a smooth, molten surface, as discussed in [13]. Incorporating quantitative metrics of thermal damage substantively improve surface analysis at varying laser intensities and comparative analysis between PFC candidate materials.

2.5.3   Atomic force microscopy

Depth information on microscopic and nanoscopic features within the laser-exposed spot, such as craters, droplets, and ripples, was collected using an atomic force microscope (AFM). The smaller scale of an AFM device allows for more targeted analysis of molten morphology caused by intense heat loading. During AFM measurements, a nanometer-sized tip interacts with the sample and exerts a force that is detected and measured using piezoelectric energy conversion. As the sample is scanned back and forth underneath the tip, a spatial map of forces is obtained that is then translated to a depth profile. By analyzing samples that appear molten from SEM imaging, AFM measurements can confirm the presence of a melt layer with ripple and droplet profiling. Quantitative information on the size and periodicity of molten ripples reflects the degree of melting and the characteristics of material migration.

2.5.4   X-ray photoelectron spectroscopy

Compositional information was obtained after select radiation exposures using X-ray photoelectron spectroscopy (XPS). During analysis, samples are exposed to an Mg-K_α X-ray source at 1253.6 eV. Photoelectrons produced by the photoelectric effect on the

sample surface then travel through an Argus hemispherical analyzer. The analyzer then measures the kinetic energy of photoelectrons, which can be converted to a binding energy value based on the X-ray source. The intensity of photoelectrons at different binding energies corresponds to the atomic concentration of different chemical species present on the surface. Previous He$^+$ irradiation studies on Mo have used XPS to reveal the relative increase in Mo oxide concentration with fuzz growth [44]. XPS analysis conducted in Chapters 6 and 7 measure the presence and signal intensity of WO_x on witness plates that were placed in front of the sample during pulsed heat loading. The presence of W splashing can be clearly determined by measuring the WO_x signal on a witness plate, showing the immense value of XPS.

2.5.5   Optical reflectivity

Qualitative characterization of the evolving fuzz structure due He$^+$ irradiation and pulsed heat loading was obtained by measuring the optical reflectivity of the sample. Samples were placed in a black box devoid of ambient light. A combination of halogen and deuterium light was then focused to a 1 mm beam diameter on the surface of interest. Incident photons exhibited wavelengths between 200 nm and 1100 nm. Reflected light was detected and analyzed using a Maya 2000 Pro Spectrometer [70]. The spectrometer measured reflected photons with wavelengths between 165 nm and 1100 nm (detected wavelength range diminished over time with equipment degradation). The device measured the reflected intensity and compared it with the original intensity to obtain a reflectivity value. Previous studies have showed that the reflectivity of a nanostructured fuzz surface is close to 0% [66]. The large decrease in reflectivity with nanoscale tendril growth is due to the difficulty reflected photons experience in leaving the surface. The heterogeneous tendril structure traps most photons from traveling out of the surface, contributing to a very low reflectivity. Studies conducted in Chapter 4 link the change in reflectivity during pulsed heat loading of the nanostructured surface with the decreasing fuzz density.

3. TRANSIENT HEAT LOADING ON PRISTINE SURFACES[1]

Understanding how a PFC surface in the divertor region may respond to intense heat loading during an ELM event reveals the baseline thermal strength of the material in a fusion environment. Erosion and splashing of PFCs can contaminate the plasma and shorten material lifetime. Although tungsten is currently considered the most promising candidate material for future PFCs, concerns over the thermal shock performance during type-I ELMs (transient events expected in fusion devices) necessitate the study of other comparable materials. ELM-like heat loading was applied via a pulsed Nd:YAG millisecond laser on a pristine molybdenum (Mo) surface to measure surface melting and mass loss. One potential advantage of Mo is its higher specific heat of vaporization, which could lead to reduced particle emission. Imaging of the surface after loading revealed that complete surface melting began at 1.0 MJ m^{-2} (heat load parameter of 31.62 MJ m^{-2} s$^{-1/2}$). Photon excitation also increased significantly above 1.0 MJ m^{-2}, indicating possible phase change. At 1.4 MJ m^{-2} (44.27 MJ m^{-2} s$^{-1/2}$), *in situ* mass loss measurements found an exponential increase in particle emission, indicating the presence of droplet formation and boiling. Direct comparisons of erosion during pulsed heat loading between PFC candidate materials will ensure that future fusion devices design components with optimal thermal strength.

3.1 Introduction

Instabilities within a fusion plasma compromise the structural integrity of the surrounding plasma facing components (PFCs). Magnetic fusion devices (e.g. ITER) experience periodic discharges of plasma at very high fluxes while operating in the preferred high-confinement mode (H-mode) [8]. Edge-localized modes (ELMs) are events that involve repetitive relaxation of the edge plasma during operation. Different types of ELMs are categorized by their power loss and their peak flux to the divertor region. Type-I ELMs are the most serious, imparting up to 10% of the core plasma energy onto the PFC

---

[1] A part of this chapter appeared in G. Sinclair, J. K. Tripathi, P. K. Diwakar, and A. Hassanein, *Sci. Rep.*, vol. 7, no. 1, p. 12273, 2017.

surface with a repetition rate ranging from 1 – 10 Hz [6], [71], [72]. See Chapter 1 for additional information on ELMs in ITER-type devices. As a result of intense heating, the PFC surface may crack or melt, leading to component damage and contamination of the fusion plasma [22], [33], [73]. Efforts have been made to reduce the magnitude of ELM heat loading through forced relaxation (e.g. pellet injection) [8], [74]. However, mitigated ELM technologies are still in development, and a fraction of unmitigated ELMs are still expected, with divertor heat fluxes exceeding several MJ m^{-2} [6], [14], [75], [76]. Determining safe operating windows to minimize cracking and melting, in response to these transient events, will help optimize PFC lifetime and device performance.

As mentioned in Chapter 1, tungsten (W) is the leading candidate material for PFCs in current and future fusion devices. The ITER Organization will use W as the primary divertor material [77]. Despite its favorable thermal properties, the poor response of W to low-energy He$^+$ irradiation (especially at elevated temperatures) and unmitigated ELMs could present serious problems for its viability as a future PFC. Experiments done in the laboratory and in the Alcator C-Mod tokamak have shown that nanoscale tendrils grow on the W surface in response to low energy He$^+$ irradiation at elevated temperatures [37], [38], [43], [78]. The nanostructured layer, referred to as "fuzz", has shown to exhibit reduced thermal, mechanical, and structural properties [55], [79], [80]. When coupled with the presence of ELMs described previously, potential issues such as melting and arcing put into question the strength of W as a PFC candidate material [53], [57].

Recent research shows that molybdenum (Mo) may be a promising PFC alternative [16], [38], [42]–[44]. Mo is a high-Z refractory metal with similar advantages to W, including a high melting point, low sputtering yield, and high thermal conductivity (refer to Table 1.1) [16]. A potential drawback of Mo is its high waste disposal rating under neutron exposure [16]. However, Mo does have a higher specific heat of vaporization, which will result in less evaporation during transient heat loading [16]. Fuzz formation has been shown to occur on both W and Mo, as well as other refractory metals, for certain fluence regimes and temperature windows [38], [42]–[44], [66], [81]. Recent work has estimated a temperature window for W of 1000 – 2000 K and a lower and narrower temperature window for Mo of 823 – 1073 K [38], [42]. Once ITER progresses into the nuclear phase, W surface temperatures will climb into the upper end of the fuzz formation

temperature window, making tendril growth a concern [35]. Although the nanostructure remains relatively uncharacterized, the difference in the fuzz formation window for Mo necessitates further analysis.

The presented study investigated surface damage during ELM-like heat loading, which was replicated using long-pulsed laser irradiation. Other laboratory methods for replicating type-I ELM events include the use of plasma accelerators and electron beams [22], [27]. The exposures were conducted over a wide range of energy densities to determine how the Mo surface deforms, and eventually melts with increasing intensity. Novel *in situ* mass loss techniques using a quartz crystal microbalance (QCM) were introduced and implemented to measure the trends in particle emission with increasing energy density. Studying the mechanisms of thermally-induced damage on Mo during transient plasma events will substantively affect the design of future PFCs.

3.2   Experimental setup

Heat loading experiments were conducted in the Ultra-High Flux Irradiation (UHFI) laboratory at the Center for Materials Under Extreme Environments (CMUXE) at Purdue University. The samples used in this experiment measured 10 mm $\times$ 10 mm, and were cut from a 99.95% purity, Mo foil of 0.5 mm thickness. After being cut, each sample was mechanically polished to a mirror finish. A schematic of the experimental setup used for irradiation experiments is shown in Figure 3.1. A 1064 nm pulsed Nd:YAG ms laser was used for this experiment, because of its ability to replicate the intensity and duration of type-I ELMs. The laser utilizes a flat top beam mode, which results in uniform heating over the entire beam area. The laser had a pulse duration of 1 ms and a spot size of ~ 1 mm.
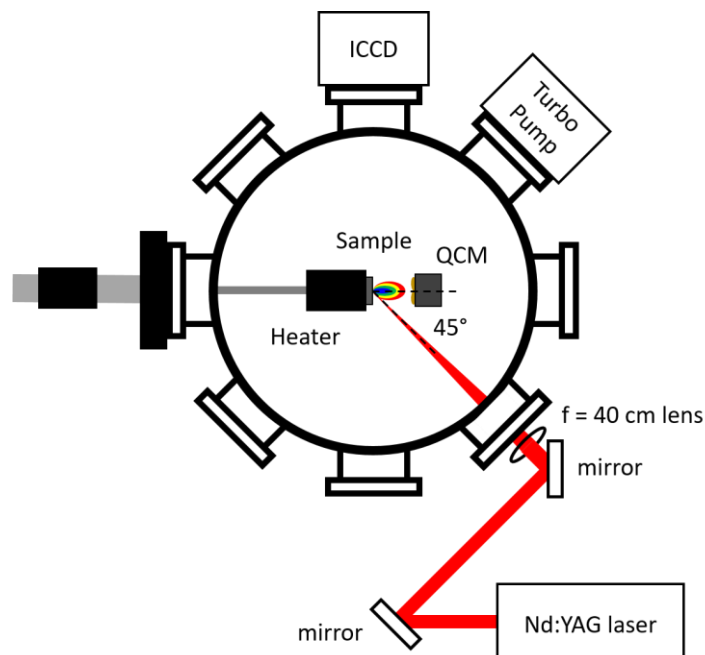
Figure 3.1: Laser irradiation chamber setup schematic.

Heat loading studies were performed by varying both the intensity and duration of laser exposure. As stated previously, unmitigated type-I ELMs possess energy densities of about $0.2 - 2.0$ MJ m^{-2}, with a duration of $0.1 - 1$ ms [82]. Energy density dependent studies consisted of 100 pulse exposures, with intensities varying between 0.6 and 1.8 MJ m^{-2}. Preliminary analysis of these exposures found that significant surface melting began at an intensity of ~ 1.2 MJ m^{-2}. The laser was then fixed at this energy density for pulse dependent studies, varying the number of pulses from 5 to 200.

During irradiation, a QCM was used *in situ* to detect particle emission from the sample surface. The QCM crystal was placed normal to the sample surface at a distance of ~ 20 mm (figure 1). Previous experiments on the angular dependence of emission show that particles leave the surface with a bias normal to the surface regardless of small variations in the incident angle [83], [84]. Before every exposure, the QCM was zeroed. A time-integrated value from that exposure was then recorded.

Plume expansion was also studied by using an intensified charge-coupled device (ICCD) camera to image particle excitation. Images were taken after the 50th laser pulse at varying energy densities. During irradiation, the camera focused on the sample surface and the area in front of the sample.

Surface characterization was conducted after exposure via *ex situ* field emission (FE) scanning electron microscopy (SEM). Imaging helped characterize the development of the molten layer on the Mo surface above a certain energy density. In addition, atomic force microscopy (AFM) was performed to measure the height profile and general topography of the molten layers for different samples that exhibited melting. By combining emission detection methods and surface morphology characterization, a comprehensive analysis of the heat loading process on Mo was developed.

3.3   Changes in surface morphology during pulsed heat loading

Exposing Mo to transient heat loading via long-pulsed laser irradiation provides invaluable information on how a PFC surface is expected to fail at higher intensities. Work done in [85] and [86] illustrate that material damage is a function of energy density, pulse shape, number of pulses, and base temperature. Therefore, energy density values mentioned below function simply to differentiate between damage regimes, and will change in magnitude under different experimental conditions. Future work will continue to expand on the synergistic relationship between different heat loading parameters.

Characterization of irradiated Mo samples using SEM revealed how the surface evolves and eventually melts with increasing energy density. Figure 3.2 shows the change in surface morphology within the exposed 1 mm spot at different energy densities. Below 1.0 MJ m^{-2}, the surface structure appeared to be slightly damaged and rough, but not melted. Previous studies have also discovered a very similar microstructure at low intensities on W [87]. At 1.0 MJ m^{-2}, the surface roughness was lower, but was not significantly molten. However, at 1.4 MJ m^{-2} and above, melting of the Mo surface could be clearly seen.

All laser-beam exposed samples that showed melting exhibited a 3-region morphology as seen in Figure 3.3. The outer most region was the pristine surface that was not heated significantly by the beam. Then, closer to the center of the beam, a roughened region existed, which was characterized by local annealing and deformation. Similar surface morphology was seen for the laser-exposed samples at energy densities below the melting threshold. However, the laser used for irradiations utilizes a flat top beam mode, which means that the energy density should have been constant over the entire exposed area. Therefore, the presence of annealing and roughening on the periphery of the molten,
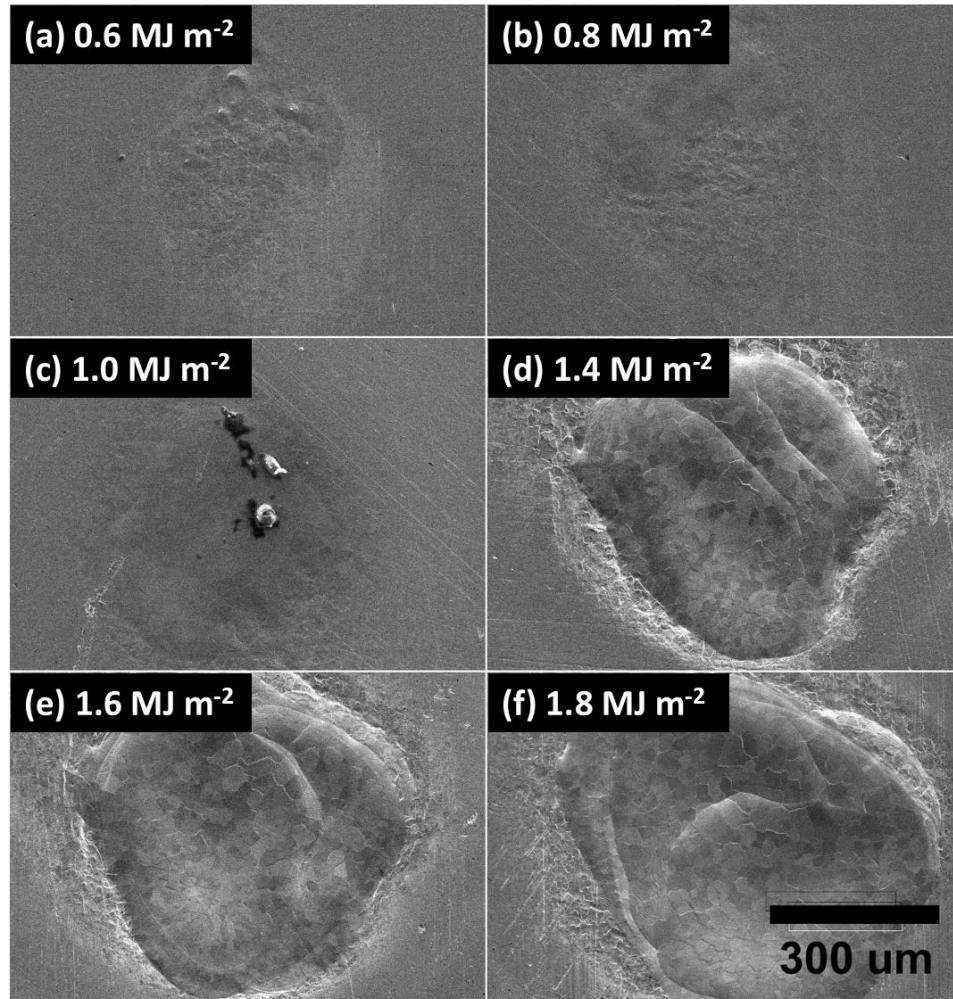
Figure 3.2: SEM micrographs of Mo surface after 100 pulse exposures at increasing energy densities. Adapted from [88] under CC BY 4.0 license.

laser-exposed spot indicates that heat was being transferred in the radial direction, outward from the center. This form of heat propagation was further observed in the third morphology region, around the center of the spot. The middle region exhibited complete surface melting and melt motion propagating radially outward from the center. Mo grains were clearly visible within the molten region – most likely a result of recrystallization after laser irradiation. A 3-region surface morphology has also been observed in other heat loading studies on W, with varying spatial profiles [89].
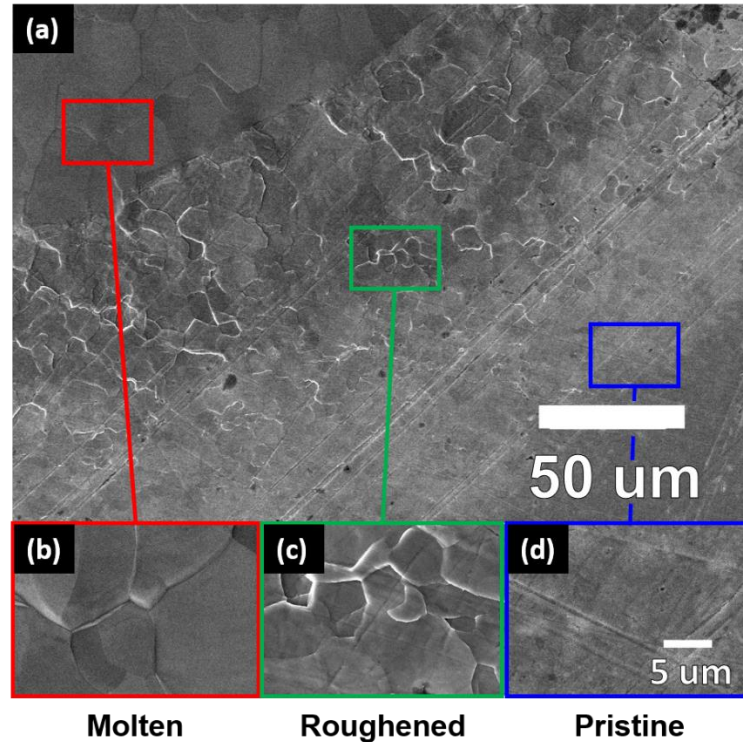
Figure 3.3: SEM micrograph of three-region morphology that is representative of heat loading above the melting threshold. High-magnification insets shown in parts (b, c, d) reveal the characteristic morphology in each region. Reproduced from [88] under CC BY 4.0 license.

Molten spots exhibit three unique characteristics: well-defined recrystallized grains, ripples that concentrate around the periphery of the spot, and a highly roughened surface surrounding the spot. The presence of ripples is a product of several molten layers, with each successive laser pulse creating a new layer. However, there does appear to be a limit to how far that molten layer propagates from the center of the spot.

SEM images were taken below, at, and above the apparent melting threshold of ~ 1 MJ m^{-2} to comprehensively define the evolving surface structure. Micrographs shown in Figure 3.4 reveal the drastic change in morphology with the formation of a molten layer. As stated previously, the surface below the melting threshold appeared to be very rough and deformed. Certain areas that appeared smooth could be due to localized melting or annealing. Above 1.0 MJ m^{-2}, the exposed Mo surface exhibited complete melting. Evidence of damage can be deduced by the presence of recrystallized grains shown in parts (b) and (c) of Figure 3.4. Surface analysis indicates that increasing the laser intensity further, above the melting threshold, does not appear to have a significant impact on grain

size. However, higher magnitude heat loading could remove various surface imperfections and impurities seen near the sample's melting threshold Figure 3.4(b). However, that relationship is difficult to quantify. Studying the motion of the molten layer is therefore an effective method of surface characterization above the melting threshold.
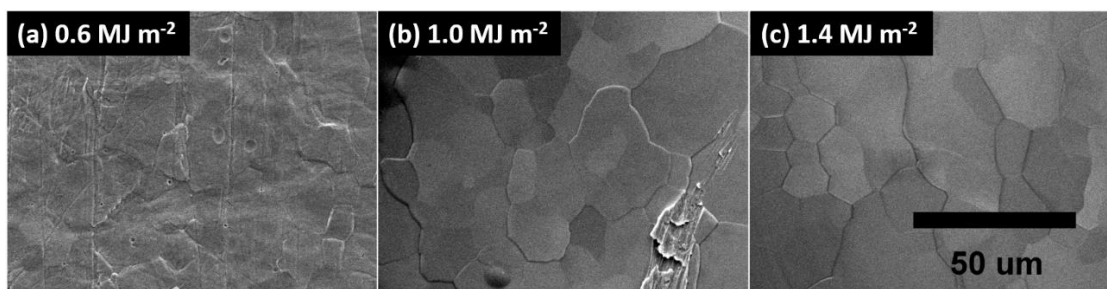
Figure 3.4: SEM micrographs of center of exposed area after 100 pulse exposures at different energy densities. Adapted from [88] under CC BY 4.0 license.

Further analysis of melt layer characteristics using AFM on a spot exposed to 100 laser pulses at 1.6 MJ m^{-2} provided additional information on the dimensions and geometry of molten layers. Figure 3.5 shows the typical topographical mode 3D AFM image from the molten region. The inset of Figure 3.5(a) shows the line profile along the dotted yellow line. The scanned area reveals a clear peak and valley structure, which is due to the stratification from different molten layers. A molten ripple structure is further observed in higher magnification images in Figure 3.5(b) (taken within dotted red circle denoted in Figure 3.5(a)). This structure has a periodicity of ~ 500 nm and an average height of ~12 nm (as shown in Figure 3.5(d)). Another example of the ripple structure is shown in Figure 3.5(c), taken from the area denoted by the dotted black circle in Figure 3.5(a). Figure 3.5(e) represents the line profile of the surface on a smaller scale than that shown in the inset of Figure 3.5(a). The line profile was measured along the dotted green line shown in Figure 3.5(a). The line profile further confirms the presence of a stratified morphology. The bump in Figure 3.5(e), at a distance of ~ 2.8 µm, clearly shows the ridge of one molten layer (marked in Figure 3.5(a) with green arrow). The FWHM of the bump is ~300 nm and height is ~60 nm. Evidence of stratified layers along the Mo surface further supports the presence of melting.
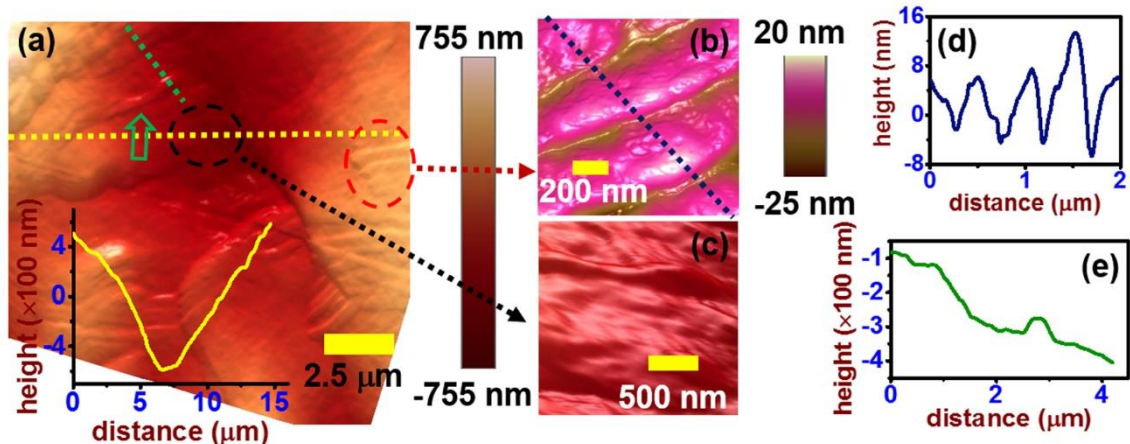
Figure 3.5: High resolution atomic force microscopy (AFM) 3D topography mode images from Mo exposed to 100 pulses at 1.6 MJ m^{-2}. Reproduced from [88] under CC BY 4.0 license.

3.4   Particle emission and surface excitation

Events of high heat loading can not only damage and possibly melt the PFC surface, but also introduce PFC material into the fusion plasma. Such contamination needs to be avoided during operation to ensure high plasma performance. High-Z materials, such as W and Mo, possess very low impurity thresholds due to their high atomic number [4]. Past studies have found that a W concentration higher than 10^{-5} could lead to quenching of the core plasma [3], [90], [91]. While contamination is not a concern during steady state operation, transient events in the plasma, such as type-I ELMs, will impart very high heat fluxes on the PFC surface that could lead to melting and splashing of the material surface. As a result, molten droplets could leave the surface and enter the plasma. The current experiment attempts to introduce some novel methods for detecting and predicting material loss. Imaging of the plasma plume emitted after irradiation was done using an ICCD camera (refer to Figure 3.1 for alignment). The device was used to correlate photon excitation by emitted species to the material response during pulsed heat loading. The intensity of emission provides a qualitative metric on the degree of heating of the Mo surface due to laser irradiation. In addition, the size and shape of the detected plume is representative of the surface evolution from heat loading.

During each exposure, ICCD images were taken at different pulse counts. Figure 3.6 shows the evolution of the plasma plume as a function of energy density after 50 pulses.

The color of each pixel corresponds to a certain intensity, and each image is scaled to itself. The intensity of each photon is directly related to the level of excitation experienced by the Mo lattice during laser irradiation. The minimum and maximum intensity levels are displayed underneath each image. Below 1.0 MJ m^{-2}, plume emission appears to be very minimal, which correlates well with imaging of the surface. At 1.2 MJ m^{-2}, a moderate increase in the maximum intensity can be attributed to the formation of a molten layer above 1.0 MJ m^{-2}, as seen in Figure 3.2 and Figure 3.4. At the melting point, particles are more energetic and have a higher mobility. Local hot spots could also lead to partial evaporation of the surface, which would increase the plume excitation. Continuing to increase the energy density leads to a drastic increase in the intensity of energetic photons. At 1.4 MJ m^{-2}, the maximum intensity climbs two orders of magnitude, indicating a significant change in the response of the Mo surface. Images of the plasma plume at 1.6 MJ m^{-2} reveal enormous intensities relative to those found below 1.4 MJ m^{-2}. SEM micrographs reveal that the large increase in photon excitation is due to the growth and propagation of the melt layer. As the melt layer is further heated with energetic photons, heat is transferred away from the center of the spot and the amount of molten Mo increases. The now-mobile material begins to move and splash, resulting in a plasma plume that consists of more energetic photons due to increased levels of ejected material. Continued heating of the melt layer will lead to evaporation, despite its high specific heat of vaporization [16]. Images of the plume clearly show that the energy density has a significant impact on the excitation of emitted species.
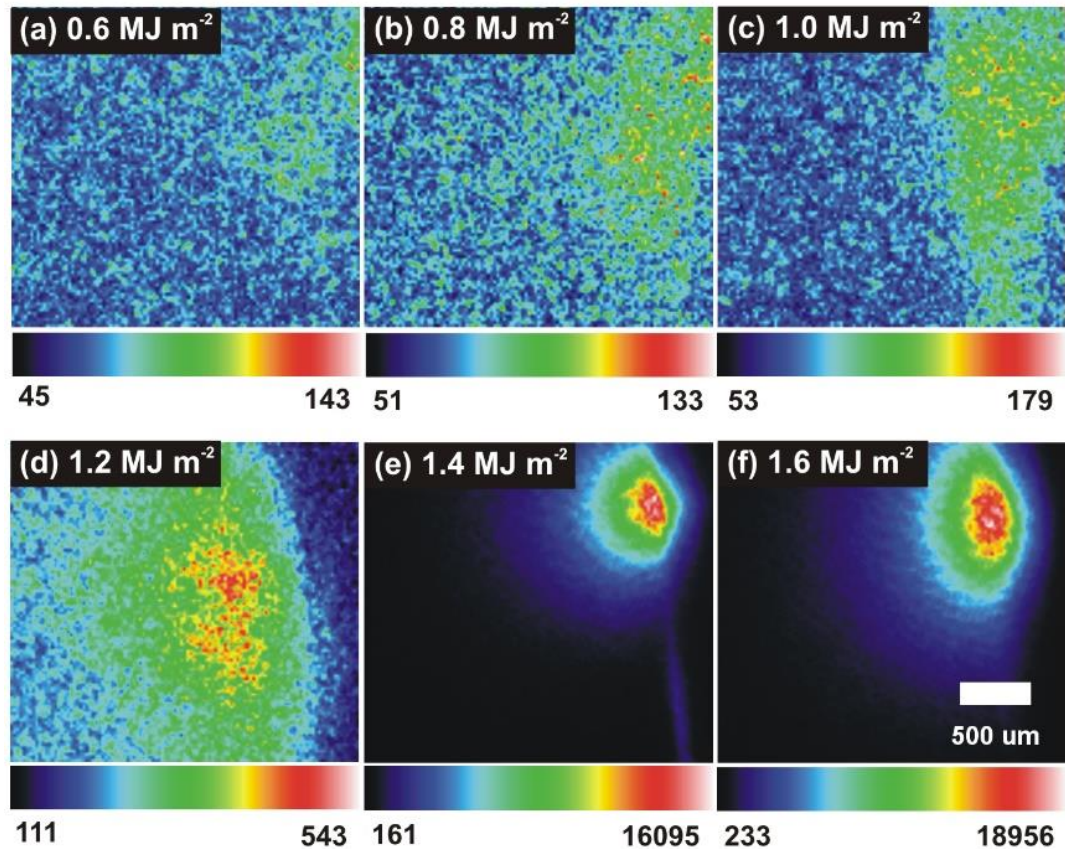
Figure 3.6: ICCD images of the plasma plume emitted from the Mo surface in response to heat loading after 50 pulses at different energy densities. The color of each pixel in an image corresponds to a certain photon intensity. Each image has its own intensity scale. Reproduced from [88] under CC BY 4.0 license.

Finding the average intensity of the emitted photons from the ICCD images helps in defining the relationship between energy density and material loss during heat loading. The average photon intensity after 50 pulses is plotted as a function of energy density in Figure 3.7 (dashed line included to show trend of data). The data further bolsters the observations made on the images in Figure 3.6; intensity remains very low until the laser energy density surpasses ~ 1.2 MJ m^{-2}. The distinct change in excitation correlates well with previous findings that surface melting occurs on W at ~ 1.4 MJ m^{-2} [55]. Although laboratory experiments cannot predict exact behavior in a reactor environment due to several constraints, clear trends in photon excitation suggest that safe operating windows can be specifically defined and controlled to avoid possible contamination of the core plasma.
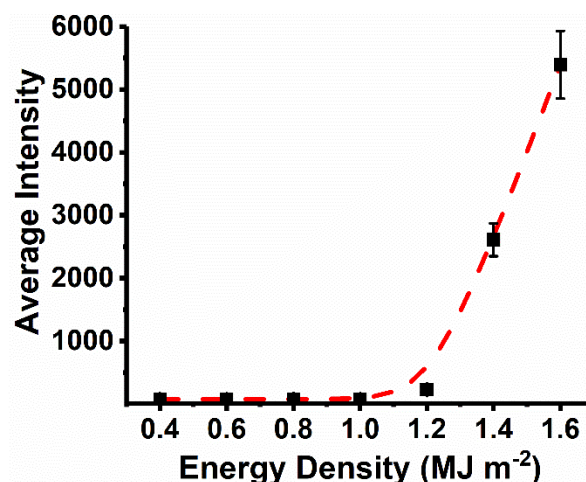
Figure 3.7: Average intensity of photon emission at increasing energy densities. Each value was calculated from the ICCD image taken after the 50th laser pulse. Adapted from [88] under CC BY 4.0 license.

Multiple studies have been conducted to help characterize the evolving material response during ELM-like heat loading at higher intensities. Work presented in [25] effectively theorizes how the PFC surface responds to transient pulses of increasing magnitude. Near the melting threshold, pulsed heat loading will create a small melt layer that will recrystallize once the pulse terminates [25]. Then, as the energy density continues to increase, the molten layer will move away from the center, creating a ripple-like structure on the periphery of the exposed spot. Finally, at high enough energy densities, the intense heat from the transient pulse begins to cause evaporation and droplet formation. The existence of a melting threshold and an emission threshold can be inferred from the results obtained in the current study via SEM, AFM, and ICCD imaging. Figure 3.7 clearly shows that at 1.2 MJ m^{-2}, the plume intensity began to increase as the surface started to melt. SEM images in Figure 3.2 also revealed evidence of melting above 1.0 MJ m^{-2}. At 1.4 MJ m^{-2}, both the surface morphology and the photon excitation changed drastically, as evidenced in both Figure 3.2 and Figure 3.7. The large increase in excitation at 1.4 MJ m^{-2} was likely due to the presence of droplet ejection and vaporization from the Mo surface [25]. Although exact threshold values will vary depending on the shape of the pulse and the number of pulses, the values provided here demonstrate the mechanisms involved in surface damage during pulsed heat loading as the ELM intensity increases.

Further refining the melting and emission behavior of Mo necessitates the direct measurement of material loss during heat loading using a QCM. Recent attempts to

experimentally measure mass removal have utilized *ex situ* methods (e.g. microbalances) [15], [57]. However, mass loss per pulse can sometimes be on the order of nanograms [15]. Possible oxidation from an ambient environment could lead to inaccurate data [42]. A QCM presents an *in situ* alternative to measure the mass loss per pulse. Work done in [92] further discuss the use of a QCM as a mass sensor.

One important factor regarding QCM measurements is that data does not represent the entire amount of mass removed from the surface. Previous work studying laser ablation of different materials show that ejected particles are not emitted isotropically [83], [84]. With the QCM placed normal to the surface plane, at a distance of 20 mm from the surface, only a small fraction of the total ejected material deposits on the surface of the QCM crystal (refer to Figure 3.1 for alignment). Nevertheless, the measurements made can provide valuable information on how emission changes with energy density.

The total amount of mass deposited onto the QCM surface after 100 laser pulses is shown as a function of absorbed laser energy density in Figure 3.8. As the energy density of the laser increases, the amount of mass detected by the QCM appears to increase exponentially. The nonlinear increase in mass loss was supported by SEM and ICCD images discussed earlier (see Figure 3.2 and Figure 3.6). Below 1.0 MJ m^{-2}, the mass deposited onto the QCM was almost negligible (< 50 ng), which was likely due to a combination of noise and potential emission of surface oxides. Between 1.0 MJ m^{-2} and 1.4 MJ m^{-2}, emission began to increase due to the onset of surface melting (as observed in Figure 3.2). The growth of the melt layer leads to higher levels of emission via splashing and possible droplet formation. Vaporization of the surface will also contribute to mass loss above a certain intensity.
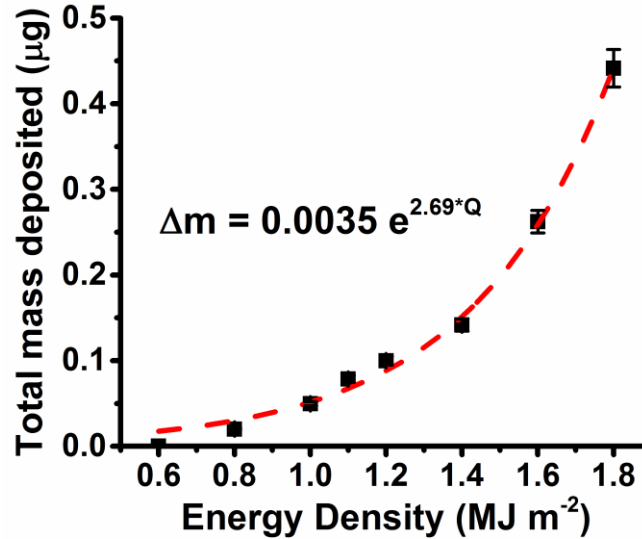
Figure 3.8: Total mass deposited onto the QCM after 100 pulse exposures at varying energy densities with an exponential fit of the form $y = ae^{bx}$. Reproduced from [88] under CC BY 4.0 license.

Exponential increases in mass loss with energy density has been observed in other work done on W. Studies presented in [15] found that particle emission increased exponentially as power density increased. Exposures were done using a plasma accelerator to replicate ELM-like heat loading. Using an *ex situ* microbalance for mass loss measurements, emission appeared to follow the equation

$$\Delta m(Q) = 0.02 \, exp(3.5Q) \tag{3-1}$$

where Δm is the specific mass loss and Q is the energy density [15]. The first term, 0.02, will be referred to as the scaling term. The second term, 3.5, will be referred to as the growth term. Although the absolute values of emission obtained in the current study are not directly comparable with those obtained in the previous study, because experimental parameters and conditions were different, the rate of mass loss is comparable. Comparing the emission behavior of W and Mo under similar irradiation conditions would provide a crude indication of which material performs better under ELM-like heat loading.

Based on the analysis done in [15], an exponential function of the same form was fit to the data in Figure 3.8. The exponential function fits the data well, with a coefficient of determination (R^2) of 0.994 (Figure 3.8). A high coefficient of determination indicates that the fit can be used to accurately predict future behavior. The exponential curve fit yields the equation

$$\Delta m(Q) = 0.0035 \, exp(2.69Q) \qquad\qquad (3\text{-}2)$$

with a growth term of 2.69. Possible reasons why the growth term for Mo is less than that for W could be due to the heterogeneity in particle emission or to the higher specific heat of vaporization of Mo. The values obtained do not provide a definitive answer on which material results in less mass loss, but instead illustrate that both materials undergo mass loss that increases exponentially with increasing ELM intensity. Future work should conduct direct comparisons between candidate PFC materials to determine which material possesses a lower growth term, and therefore causes less contamination during an ELM event. Studies discussed in Chapter 4 measured ELM-induced erosion in the presence of helium-induced "fuzz formation". Additional diagnostics will be needed to define the mechanisms of melt layer splashing and particle emission under different loading conditions. Predicting levels of contamination during type-I ELM events is of utmost importance in minimizing plasma impurities and extending component lifetimes in future devices.

3.5   Summary

Pulsed heat loading experiments performed on a Mo surface indicate that the onset of surface melting and droplet ejection at higher ELM intensities (above 1.0 MJ m^{-2}) make long-term operation unsustainable. Heat loading replicated by a pulsed Nd:YAG ms laser led to surface melting above 1.0 MJ m^{-2} (32 MJ m^{-2} s$^{-1/2}$) and enhanced particle emission above 1.4 MJ m^{-2} (44 MJ m^{-2} s$^{-1/2}$). The magnitude of these thresholds will vary, based on the number of applied pulses and the shape of the pulse, but remain an important indicator of the evolving surface morphology as a function of ELM intensity [85], [86]. Imaging done via SEM illustrates the change in surface morphology as energy density increases. Above 1.0 MJ m^{-2}, the surface begins to show signs of recrystallization. Above 1.4 MJ m^{-}

^{2}, radial propagation of molten layers away from the center of the laser-exposed area reveal the occurrence of melt motion and potential splashing. Topographical analysis done using AFM confirms the presence of a molten ripple morphology within melted spots. Motion of the molten layer in a reactor environment will also be affected by the $J \times B$ force. Future experiments that incorporate magnetic field effects would therefore provide valuable insight into how melt motion depends on ELM parameters and irregular surface morphology (e.g. fuzz formation). Material ejection was studied directly via QCM measurements and indirectly via ICCD imaging. Above 1.2 MJ m^{-2}, photon excitation of the plasma plume increased by two orders of magnitude, indicating the presence of molten or vaporized material. *In situ* mass loss measurements correlated well with ICCD data, showing an exponential increase in emission. Inspired by previous work on ELM-induced particle emission from W, the QCM measurements were fit to an exponential empirical formula [15]. The formula fits the data very well, indicating that mass loss could become a serious problem with regards to core plasma contamination without the mitigation of type-I ELMs. QCM analysis does not show an appreciable difference in the emission behavior between W and Mo. Follow-up studies will further investigate the mechanisms behind the exponential increase in mass loss from refractory metals.

Future PFC development needs to continuously examine how different materials and surface structures perform under transient heat loading to ensure acceptable material lifetimes and contamination levels for ITER and future DEMO. The effects of material composition and material working should be studied to optimize the physical and thermal properties of the component. Previous work done on alternative materials has shown that utilizing Ta and Y_2O_3 as alloying elements can improve the thermal shock performance of the PFC surface [22], [93]. Work should also be done on the synergistic effects between transient heat loading and other damage processes that take place in a fusion environment. These processes include tritium retention, helium-induced fuzz formation, and neutron irradiation. Recent work has presented conflicting results on whether fuzz formation improves or degrades the thermal response of the PFC surface during ELM-like heat loading [57], [79], [94]. Designing experiments that study the surface response of candidate materials after simultaneous particle and heat loading is critical to understanding the severity of transient, off-normal events in next step fusion devices.

4.   TRANSIENT HEAT LOADING ON SURFACES EXPOSED TO HELIUM ION IRRADIATION[2]

The work presented in this chapter explores the synergistic effects between high-flux He$^+$ ion irradiation and ELM-like heat loading on material performance. Qualifying the degree of material degradation due to He-induced fuzz nanostructure reflects the primary goal of this dissertation. Large decreases in thermal strength with fuzz formation observed in previous studies raise serious concerns over the viability of W as a divertor PFC material. Characterizing the differences in fuzz nanostructures as a function of ion energy provides insight into potential spatial variations in material strength throughout the divertor region. Changes in the surface morphology and the erosion threshold were examined on both Mo and W to examine the potential benefits of an alternative material in a complex radiation environment. Studies on nanostructured Mo in Section 4.2 provide valuable comparisons with pulsed heat loading performed on pristine Mo surfaces in Chapter 3. The effect of ELM mitigation techniques, which would decrease the imparted heat flux and increase the shock frequency, were also examined to find windows of operation where fuzz nanostructures could be removed without causing unfavorable droplet splashing. Finally, pulsed heat loading studies were performed on ITER-grade W to assess the accuracy to which experiments throughout this dissertation on differently-structured W samples predict material performance in a fusion environment. Valuable conclusions are drawn on the impact of grain orientation on the mechanisms of ion implantation and shock-induced material failure.

4.1   Effect of ion energy on helium-induced fuzz formation

Heterogeneous fuzz nanostructure growth due to high-flux, low-energy He$^+$ ion irradiation may significantly degrade the material strength of PFCs in future fusion devices. W is currently considered to be the most promising material for use in the divertor region

---

[2] A part of this chapter appeared in G. Sinclair, J. K. Tripathi, P. K. Diwakar, and A. Hassanein, *Nucl. Fusion*, vol. 56, no. 3, p. 36005, 2016 and G. Sinclair, J. K. Tripathi, and A. Hassanein, *J. Appl. Phys.*, vol. 123, no. 13, p. 133302, 2018.

due its excellent thermal and mechanical properties. However, recent studies have found large decreases in thermal conductivity and mechanical strength with fuzz formation. Potential increases in erosion and brittle failure would shorten component lifetime and enhance plasma contamination. The formation mechanism responsible for fuzz tendril growth is still being debated, as the interaction of He bubbles with the material surface remains unclear. Despite the uncertainty around the growth mechanism, experimental research has defined a parameter space for fuzz formation, based on surface temperature, ion flux, ion fluence, and ion energy. Nanostructure growth has only been observed due to low-energy He^+ ion irradiation, and the structure formation process at higher ion energies remains in development.

Therefore, the study below investigated the dependence of fuzz nanostructure growth on He^+ ion energy experimentally on W samples. SEM imaging of irradiated W samples observed that lower ion energy irradiation might exhibit a higher fluence threshold for fuzz growth. Measurements of the fuzz layer thickness did not observe any degradation at higher ion energies (at 200 eV), due to the expected onset of physical sputtering. Instead, the nanostructure layer grew nonlinearly with increasing ion energy. Imaging of the tendril-bulk interface revealed that the implantation depth profile may limit the fuzz growth rate. The optical reflectivity of irradiated samples appeared to approach a minimum value, which could be indicative of a maximum surface roughness with increasing ion energy. Additional studies near the physical sputtering threshold for He on W are needed to determine whether the fuzz nanostructure growth process is significantly altered by changes to incident ion energy.

4.1.1 Introduction

Before exploring the synergistic effects between He^+ ion irradiation and ELM-like pulsed heat loading, the growth of He-induced fuzz nanostructures on W must be characterized. Despite the benefits of W as a promising PFC material, research over the past decade has shown that high-flux, low-energy He^+ ion irradiation may strongly degrade performance. He-induced fiber-form nanostructures have been shown to reduce the mechanical strength and thermal conductivity of the W surface, which may lead to elevated levels of erosion during reactor operation [37], [56]. Clear windows for nanostructure

growth have been defined, based on surface temperature, ion flux, and ion energy [38]. Observations of fuzz formation in Alcator C-Mod confirmed that the heterogeneous nanostructure could grow in a complex fusion environment [37].

Research efforts have focused on both the effects of fuzz nanostructure on material properties and the mechanisms responsible for tendril growth. Characterization of nanostructured surfaces have revealed large decreases in mechanical strength [95], thermal conductivity [54], [56], and arcing threshold [53], [96] when compared to that of a pristine surface. Potential decreases in sputtering yield with fuzz growth have illustrated one beneficial effect of He-induced nanostructuring [51]. While the community still remains uncertain on the exact process by which fibers grow, observations of He bubbles within the fuzz tendrils illustrate the important role of migrating He bubbles at the material surface [43], [82]. Current uncertainty is based around whether He bubbles burst to deform the surface [97], or push a viscoelastic surface layer into a tendril [41]. On a macroscopic scale, studies have been performed to determine the influence of different irradiation parameters on the growth process. The appearance of fuzz formation has only been observed at elevated surface temperatures. Many He^+ ion irradiations cited in [38] reveal a clear temperature window for nanostructure growth between 1000 K and 2000 K. Below 1000 K, helium bubble mobility is insufficient to drive migration to the surface , which prevents tendril growth [38]. Above 2000 K, thermally-enhanced desorption of implanted He minimizes nanostructuring, producing significant pore formation instead [38]. The occurrence of fuzz formation has not been inhibited by changes to the microstructure. Fuzz formation has been observed on W materials with varying grain orientations [98] and grain sizes [99], [100]. Above a He^+ ion flux of $\sim 10^{22}$ m^{-2} s^{-1}, the nanostructure growth rate was observed to be constant [101]. However, fuzz formation has still been observed with fluxes below 10^{21} m^{-2} s^{-1}, as shown in Section 4.3.2. Fluence-dependent research performed in [39] used an extrapolation of fuzz thickness measurements to estimate a minimum required He^+ fluence of 4×10^{24} m^{-2}. Since a quantitative description of fuzz has not been defined, the fluence threshold should only be used as a reference point. A study performed in [101] discovered that the fuzz layer thickness increased linearly as a function of the square root of the irradiation time ($t^{1/2}$). An equilibrium model presented in [102] developed the

following equation to estimate fuzz layer thickness, based on the $t^{1/2}$ dependence observed in [101]:

$$\frac{dx_{fuzz}}{dt} = \left(\frac{D}{2t}\right)^{1/2} - Y_{net} \qquad (4\text{-}1)$$

where x_{fuzz} represents the fuzz layer thickness, t represents the irradiation time, D represents the diffusion coefficient of He in W, and Y_{net} represents the net sputtering yield due to physical sputtering of W by incident He^{+} ions. The value of D varies depending on the surface temperature. The Y_{net} was included in the equation to account for loss of fuzz nanostructure by physical sputtering by energetic He^{+} ions. A graph of the function at different ion energies, along with experimentally measured data points of fuzz thickness, at a surface temperature of 1120 K is shown in Figure 4.1. While studies in [103] and [104] disagree on the exact He^{+} ion energy threshold, physical sputtering in W is likely to begin between 100 eV and 200 eV. Cross-sectional SEM images in [102] and [105] observed a decrease in the net fuzz thickness for He^{+} ion irradiations performed at energies at 200 eV and above. Potentially conflicting results were presented in [106], where increases in the ion energy up to 300 eV enhanced the geometrical aspect ratio of fuzz nanostructures. However, the change in thickness was not measured. At sufficiently high energies, physical sputtering is expected to occur, which will impose an upper ion energy limit on fuzz formation. Low He[+] ion energies have not shown a clear threshold for fuzz formation; studies in [36] observed nanostructure growth due to 12 eV He[+] ion irradiation, albeit at a very high fluence of 3.5×10^{27} m^{-2}. Increases in the reflection coefficient, which is the defined as the probability that an incident ion does not become embedded in the lattice, with decreasing ion energy could inhibit overall implantation of He in the subsurface, which would stunt nanostructure growth [50].
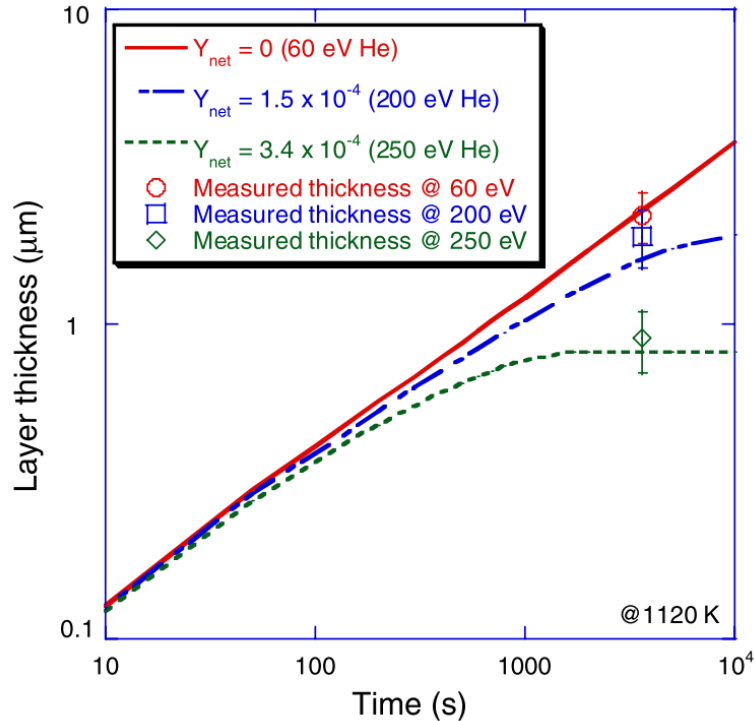
Figure 4.1: Predicted fuzz layer thickness based on equilibrium growth model for different He$^+$ ion energies. Reproduced from [102] with permission. Copyright IAEA, Vienna 2011.

High-flux, low-energy He$^+$ ion irradiations were conducted on W samples to further expand upon the work presented on ion energy dependence. Comments on the effect of ion energy on fuzz nanostructure morphology and behavior have been tangentially mentioned without thorough analysis. Surface imaging and characterization of irradiated W samples revealed how changes in ion energy impacted fuzz tendril dimensions, fuzz layer thickness, and overall surface degradation.

4.1.2 Experimental setup

He$^+$ ion irradiations were performed on W samples in the UHFI-II facility (see Section 2.1.3) in the Center for Materials Under Extreme Environment at Purdue University. Cold-rolled and annealed W foils (Alfa Aesar, 99.95% purity) were used for all experiments. Samples were cut from a single sheet with dimensions 10 mm × 10 mm × 0.5 mm and mechanically polished to a mirror finish to remove surface imperfections. During each experiment, samples were clamped to a resistive button heater that elevated

the surface temperature of the sample to 1223 K. PID feedback using thermocouples were used to maintain a constant surface temperature throughout the exposure. A gridless end-hall 'EH' ion/plasma source was utilized to impart high-flux He^+ ion irradiation on W samples for a duration of 1 h (see Figure 4.2 for experimental setup schematic). The broad beam of the ion source minimized spatial variations in particle flux.
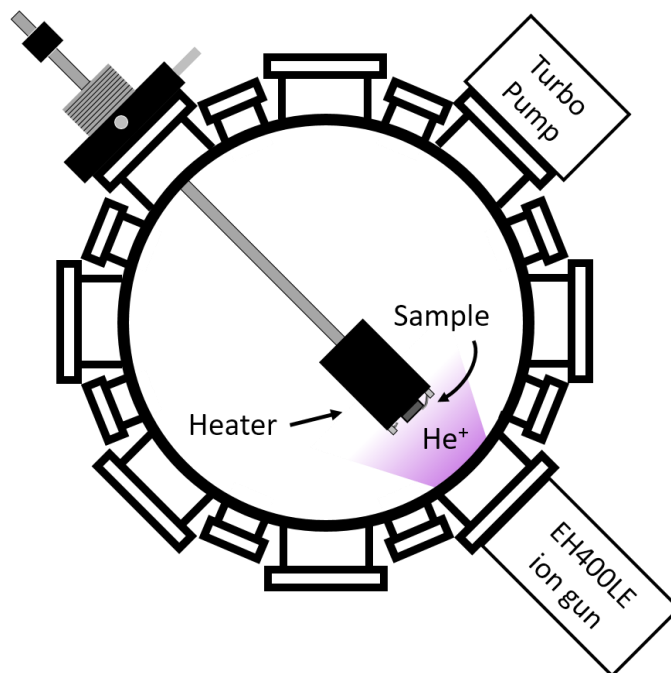
Figure 4.2: He^+ ion irradiation setup schematic in UHFI-II facility

Three different irradiations were performed at varying ion energies to assess differences in fuzz formation. While the parameters of the ion source were tuned to produce a maximum particle flux, changes in the desired ion energy created small variations in the resultant flux. Table 4.1 lists the approximate ion energies, particles fluxes, and particle fluences utilized for each experiment.

Table 4.1: Experimental parameters for performed He^+ ion irradiations

Exp.	Ion Energy (eV)	He^+ flux (m^{-2} s^{-1})	He^+ fluence (m^{-2})
1	75	1.8×10^{20}	6.5×10^{23}
2	100	5.3×10^{20}	1.9×10^{24}
3	200	6.8×10^{20}	2.4×10^{24}

Effectively characterizing the growth of fuzz nanostructures required the use of both surface analysis and cross-sectional analysis techniques. Scanning electron microscopy (SEM) of the W surface after irradiation was used to determine the size and shape of fuzz tendrils and assess the general morphology of the damaged area. Cleaving of the sample after cryogenic cooling using liquid nitrogen enabled valuable SEM imaging of the cross section. Measurements of the fuzz layer thickness from cross-sectional images added comparative value to previous studies [101], [102]. The optical reflectivity of the irradiated surfaces was also measured using a combination of halogen and deuterium light, which produced an incident photon spectrum with wavelengths between 350 nm and 850 nm. The diameter of the incident beam was 1 mm. Reflected photons were analyzed using a Maya 2000 Pro Spectrometer. Changes in reflectivity with ion energy served as a qualitative metric of areal fuzz density. Analysis of both the surface and subsurface of He^+-irradiated W samples was utilized to link changes in surface morphology with ion energy to the growth of fuzz nanostructures. Isolating the impact of certain irradiation parameters informs fuzz formation theories.

4.1.3   Results and Discussion

SEM imaging of the W surface after He^+ ion irradiation was used to assess the degree of fuzz formation at different ion energies. Figure 4.3 shows SEM micrographs of the irradiated W surfaces at different magnifications. Distinct fuzz formation only took place for 100 eV and 200 eV He^+ ion irradiations; average tendril size decreased as ion energy increased. The surface morphology shown in Figure 4.3(a, d) appeared very similar to that shown in [99] of early-stage tendril growth. While the exact parameters used in each study were not comparable due to differences in W microstructure, the observation of thinner and more developed fuzz nanostructures at higher ion fluences in [99] illustrated that fuzz formation would likely occur on the surface shown in Figure 4.3(a, d) if the fluence was increased. Higher fluence thresholds for fuzz formation at lower ion energies were also observed in [36]. Pinholes observed along the surface, as observed in Figure 4.3(d), reinforce the fuzz formation mechanism proposed in [39] and observed in [107], where large He bubbles rupture at the surface and serve as seeds for eventual tendril growth. Decreases in tendril size with increasing ion energy was also observed in [106]. Potential

increases in total He implantation at higher ion energies, as noted in [50], could lead to further refinement of fuzz nanostructures due to enhanced bubble rupturing.
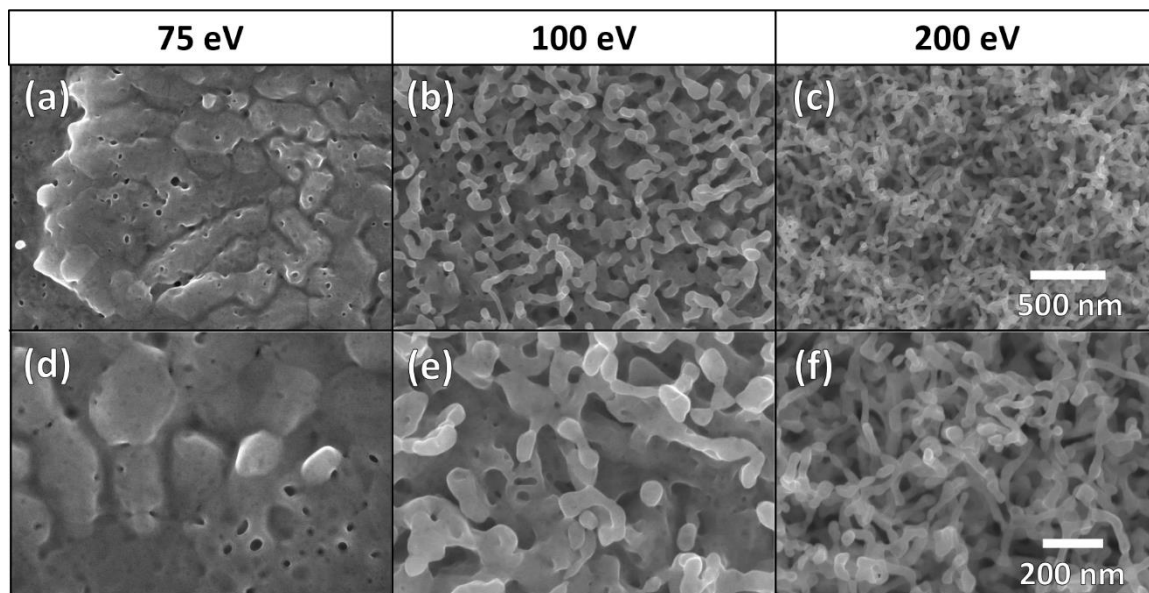
Figure 4.3: SEM micrographs of irradiated W surface at (a, d) 75 eV, (b, e) 100 eV, and (c, f) 200 eV.

Changes in the overall thickness of the W fuzz layer was measured via cross-sectional SEM imaging. Low-magnification images of the cross section after He$^+$ ion irradiation at varying ion energies are shown in Figure 4.4. As indicated by the surface imaging presented in Figure 4.3, minimal nanostructure growth took place at 75 eV. Some minor surface roughening may have been due to very early-stage tendril growth (Figure 4.4(a)). Higher ion energy exposures produced clear fuzz formation, as seen in Figure 4.4(b, c). However, the layer thickness was difficult to deduce at low magnifications. Changes in the height of the surface between images are not comparable, and was due to repositioning of the microscope between samples. Similarities in the orientation and size of the bulk microstructure below the surface illustrate that the fuzz nanostructure was not preferentially stimulated on a particular sample, as shown in [108], [109].
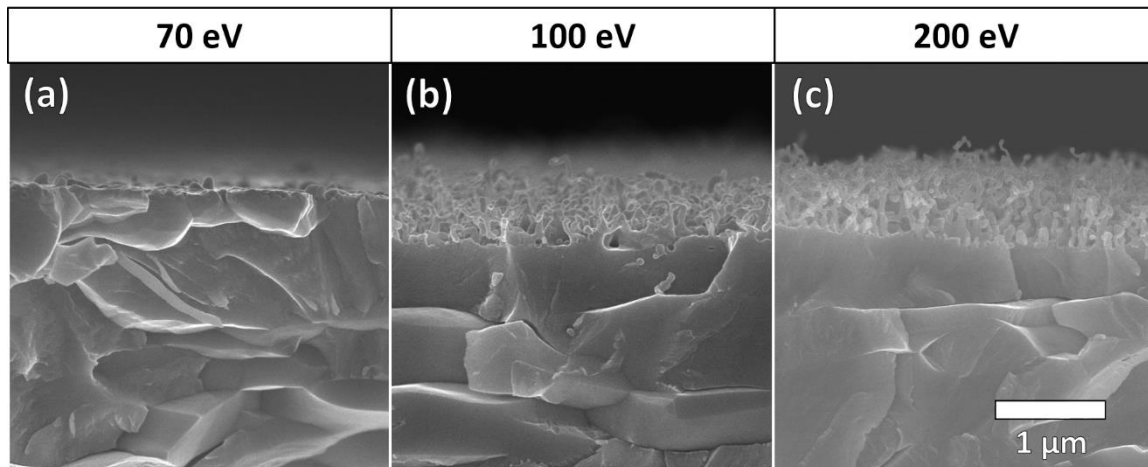
Figure 4.4: Cross-sectional SEM images of W sample at low magnification after He$^+$ ion irradiation at (a) 70 eV, (b) 100 eV, and (c) 200 eV.

Higher magnification images of the sample cross sections were used to measure the fuzz layer thickness and assess the influence of implanted He bubbles on surface structuring at different ion energies. SEM micrographs in Figure 4.5 shows the tendril-bulk interface at intermediate and high magnifications after exposure to different He$^+$ ion irradiations. As shown in the low magnification images in Figure 4.4, significant tendril growth only took place at 100 eV and 200 eV. A small protrusion present on the surface exposed to 75 eV He$^+$ ion irradiation (Figure 4.5(a)) was likely due to early-stage nanostructure formation. Other protrusions of similar dimensions were observed at other locations along the cross section. The observed protrusion does not, however, reinforce any of the proposed fuzz formation mechanisms discussed in the introduction, since its formation could be due to the formation of surrounding pinholes or due to upward viscoelastic movement. Atomic force microscopy of W samples exposed to increasing fluences of He$^+$ ion irradiation might further elucidate the formation mechanism of early-stage protrusions. The thickness of the fuzz layer on each W surface was measured using ImageJ software [110]. Due to the difficulty in obtaining cross-sectional images that were perfectly normal to the surface, unfocused surface structuring beyond the cleaving plane was observed. Therefore, the thickness measurements only considered the layer of fuzz nanostructure that was in focus to avoid overestimation. The thickness of the nanostructure was measured in three different locations on each sample, and the average thickness as a function of ion energy is shown in Figure 4.5(a, b, c). As the ion energy increased, the fuzz

layer thickness increased nonlinearly, with a maximum thickness of ~ 750 nm at 200 eV. The increase in the nanostructure thickness from 100 eV to 200 eV contrasts with the results presented in [102], where decreases in the layer height were attributed to the onset of physical sputtering. While the results are not directly comparable, due to a 3 order of magnitude difference in particle flux, the lack of any significant decrease in fuzz layer thickness at ion energies above 100 eV reveal that the rate of physical sputtering might be influenced by the properties of the surface nanostructure. High-magnification images in Figure 4.5(d, e, f) reinforce the observed decreases in tendril thickness at higher ion energies, and directly illustrate the link between implanted He bubbles and nanostructure growth. Subsurface He bubbles were observed along the tendril-bulk interface at all ion energies. However, the depth distribution of He bubbles did not appear to change between surfaces, with all bubbles being located within 200 nm of the tendril-bulk interface. Since the depth distribution of implanted He bubbles is known to be energy-dependent [111], the similar bubble density in the bulk indicates that the kinetics of bubble rupture could be impacted by He^+ ion energy. Higher ion energies caused the formation of thinner and longer fuzz layers (Figure 4.5(d, e, f)). If fuzz formation is due to the migration and subsequent rupture of He bubbles at the surface, then the depth and thickness of the nanostructure would be dependent on the rate of rupturing. As implanted bubbles migrate to the surface and rupture, the height of the bulk decreases. Deeper implantation of He at higher ion energies increases the inventory of He bubbles in the lattice as the bulk layer moves downward [111], [112]. Therefore, rupture is expected to occur to a higher degree because implanted He bubbles are present over a larger depth distribution. The bubbles then seen below the tendril nanostructure represents the He bubbles with the highest implantation depths at that energy. Gradual decreases in porosity with fuzz nanostructure growth will enable continuous bubble nucleation below the tendril-bulk interface [51], which explains the increase in nanostructure growth at higher fluences [101]. Additional experiments on the combined influence of fluence and ion energy on fuzz layer thickness are needed to determine the validity of the proposed hypothesis.
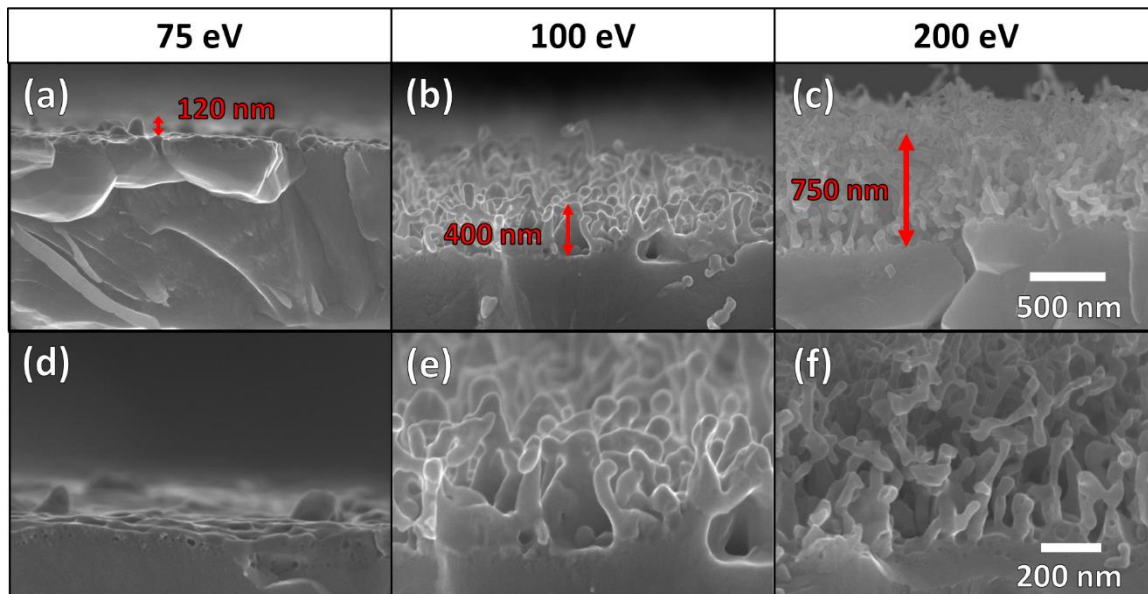
Figure 4.5: Cross-sectional SEM images of tendril-bulk interface at intermediate and high magnifications after He^{+} ion irradiation at (a, d) 70 eV, (b, e) 100 eV, and (c, f) 200 eV.

Measuring the optical reflectivity of irradiated W samples provided a qualitative metric of areal fuzz density that further help characterize the changing nanostructure. The reflectivity spectra between 350 nm and 850 nm was plotted for each sample in Figure 4.6. The reflectivity of a pristine, polished W samples was also included as a reference. The nonlinear decrease in reflectivity with increasing ion energy mirrors the changes in surface roughness shown in Figure 4.6. Work presented in [113] illustrates that increases in surface roughness can inhibit the detection of scattered light photons. The large degree of heterogeneity present on W surfaces after 100 eV and 200 eV prevents most photons from being re-emitted, and therefore yield ~ 0% reflectivity. Minor surface roughening observed due to 70 eV ion irradiation appeared to slightly decrease the optical reflectivity, due to trapping of obliquely scattered photons. Complete absorbance of incident light has also been observed due to other fuzz formation experiments on W [94], as well as experiments on alternative refractory materials, such as Ta, Mo, and Nb [42], [46], [47]. The lack of change in reflectivity between 100 eV and 200 eV He[+] irradiations indicates that the surface roughness could approach a maximum value, while the nanostructure layer depth continues to increase. Therefore, measurements of optical reflectivity on irradiated samples appears to be most useful for characterizing surfaces that have not undergone fully-formed fuzz nanostructure.
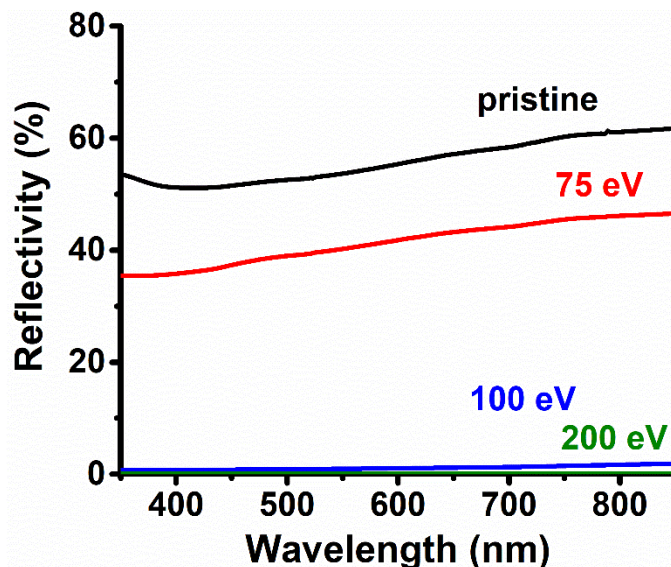
Figure 4.6: Optical reflectivity of W surface after He^{+} ion irradiation at varying ion energies. A reference spectrum of a pristine sample before irradiation was included for reference.

4.1.4   Summary

The influence of He^{+} ion energy on fuzz nanostructure growth was experimentally examined on polycrystalline W samples to predict surface evolution in a fusion environment. 1 h He^{+} ion irradiations were performed at 75 eV, 100 eV, and 200 eV at a flux on the order of $\sim 10^{20}$ m^{-2} s^{-1}. Fuzz nanostructure growth was observed for 100 eV and 200 eV irradiations, while the 75 eV irradiation produced large rod-like structures and pinhole formation. Under the bubble rupture model, surface pores could be characteristic of early-stage tendril growth. Smaller tendrils were observed due to 200 eV He[+] ion irradiation than due to 100 eV He[+] ion irradiation, which indicate that deeper penetration of He resulted in further refinement of the surface nanostructure. Measurements of the fuzz layer thickness obtained from cross-sectional SEM images found a nonlinear increase in nanostructure depth with ion energy. Future experiments should examine the presence of physical sputtering at high ion energies to determine the degree to which erosion could impact the net fuzz layer thickness. Helium bubbles that were observed at the tendril-bulk interface did not change in density or size as a function of ion energy. Therefore, the percentage of unruptured He bubbles may remain constant at different ion energies, while shifts in the implantation depth profile ultimately determine the height of fuzz

nanostructures. He$^+$ ion irradiation experiments that examine the influence of fluence and ion energy on nanostructure growth are need to further explore this hypothesis. Finally, optical reflectivity measurements revealed complete light absorption for 100 eV and 200 eV irradiations, indicating that the surface roughness may approach a maximum value during the fuzz growth process. In a fusion environment, the energy of impinging He$^+$ ions will vary significantly depending on the plasma parameters and the location of the loaded surface in the divertor region. Therefore, energy-dependent studies are needed to improve predictions on surface degradation and associated changes in thermal strength of reactor PFCs.

4.2   Studies on molybdenum

The advancement of fusion reactor engineering is currently inhibited by the lack of knowledge surrounding the stability of plasma facing components (PFCs) in a tokamak environment. During normal operation, events of high heat loading occur periodically where large amounts of energy are imparted onto the PFC surface. Concurrently, irradiation by low-energy helium ions present in the fusion plasma can result in the synthesis of a fiber form nanostructure on the PFC surface, called "fuzz". In order to understand how this heterogeneous structure evolves and deforms in response to transient heat loading, a pulsed Nd:YAG millisecond laser was used to simulate these events on a fuzz nanostructured molybdenum (Mo) surface. Performance was assessed using three metrics: nanostructure evolution, particle emission, and improvement in optical properties. Experiments performed at the upper end of the expected range for type-I edge-localized modes (ELMs) found that the helium-induced nanostructure completely disappeared after 200 pulses of the laser at 1.5 MJ m^{-2}. *In situ* mass loss measurements found that the number of particles leaving the surface increased as energy density increased and the rate of emission increased with pulse count. Finally, optical properties assisted in providing a qualitative indication of fuzz density on the Mo surface; after 400 pulses at 1.5 MJ m^{-2}, the optical reflectivity of the damaged surface is ~90% of that of a mirror polished Mo sample. These findings provided different results than previous studies done with tungsten (W), and further helps illustrate the complicated nature of how transient events of high heat

loading in a tokamak environment might impact the performance and lifetime of PFCs in ITER and future DEMO devices.

4.2.1 Introduction

The ultimate success of nuclear fusion reactors depends on the selection of plasma facing materials that can withstand the high-temperature, high-energy environment present in these devices. As mentioned in Chapter 1, W is currently the leading candidate material for plasma facing components (PFCs) due, in part, to its high melting point and low sputtering yield [16]. However, studies done over the past several years suggest that the development of a fiber form nanostructure on the W surface in response to low-energy helium ion irradiation may degrade thermo-mechanical, physical, and structural properties of the surface [55]. Therefore, understanding how this fiber nanostructure responds to transient events is of critical concern for the future development of PFCs. To investigate the effect of such fiber form surface structure on the performance of PFCs under transient heat loads, experiments have been performed using plasma accelerators, electron beams, and long pulse lasers to replicate type-I edge-localized modes (ELMs) seen in a tokamak [29]. Incidentally, these experiments have not yielded reliable conclusions on whether these nanostructures are beneficial or detrimental to the performance of the fusion reactors. Temmerman *et al.* have shown that ELM-like pulses on a nanostructured W surface did not cause material loss, and instead caused healing of the heterogeneous "fuzz" surface [57]. On the other hand, studies performed by Kajita *et al.* show that helium-induced fuzz structure reduces the threshold for unipolar arcing to occur during type-I ELMs [53]. While results from Temmerman *et al.* show that transient heat loading on W nanostructure might not cause plasma contamination, unipolar arcing events could result in very large erosion rates on the order of mg/s [80]. This level of contamination could be fatal to plasma performance in fusion reactors similar to ITER and the future DEMO.

Currently, W is considered one of the most promising options for use as a PFC material in nuclear fusion reactors [114], [115]. However, the physical mechanism responsible for low energy helium ion and/or plasma irradiation (at elevated temperatures) induced surface deterioration remains unclear. This uncertainty remains despite huge experiments and comprehensive modeling and simulation work, viz., molecular dynamic,

multiscale, and atomistic approaches [102], [116]–[122]. Therefore, studying similar properties on other refractory metal surfaces, such as Mo (as in the present case), is extremely worthwhile. Recent research does suggest that certain high-Z materials, including Mo, develop a "fuzz" nanostructure in response to low-energy helium ion irradiation [16], [38], [42], [43], [66]. Mo also exhibits interesting properties for thermonuclear fusion environments such as resistance to heat, wear, and sputtering [40]. It has very similar physical and thermal properties to W, and has proven to be a promising alternative for future PFCs [16], [42].

One important application for Mo is as diagnostic tools, such as in-vessel mirrors, which make up the first wall of ITER [40]. These single crystal Mo mirrors perform quite well in their ability to withstand erosion and possess a sufficient lifetime [123]. The robustness of Mo against deuterium plasma exposure (low physical sputtering yield, no binary compound with hydrogen reported) while maintaining a high reflectivity in the UV/VIS/NIR region, make it a worthwhile candidate for first mirrors (FMs) [124]–[126]. However, technological difficulties and relatively high costs for producing large-sized Mo crystals limit the use of such mirrors. Polycrystalline mirrors are not an alternative due to their poor performance because of roughening due to different sputtering rates for different crystal orientations, as well as their tendency to blister [127]–[129]. Therefore, Mo coatings need to be considered as a potential alternative to Mo single crystals [126].

Recently, the CMUXE surface science group reported on the effect of low-energy He$^+$ ion irradiation on a Mo surface and characterized the surface morphology, chemical stoichiometry, and optical properties as a function of target temperature in ITER-like conditions [42]. These results show a clear temperature window of 823–1073 K for the formation of Mo fiber-form nanostructures (nano-tendrils or fuzz) due to low energy He$^+$ ion irradiation [42]. Note the observed temperature window for Mo fuzz formation is significantly lower and narrower than that of the W fuzz formation (1000 – 2000 K) [53]. The difference in nanostructure growth parameters bolsters Mo as a potential alternative PFC to W. Important parameters that need to be defined to fully compare the two materials include (a) fuzz formation conditions, (b) response of fuzz to fusion environment, (c) operating windows for fuzz growth, and (d) fuzz damage thresholds, etc. [16]. In a fusion reactor, the PFC surface will be exposed to high heat and ion fluxes that can damage the

material over time. However, the operating parameters for a DEMO class reactor are still unknown, and reactor designs other than the tokamak could use parameters very different than what's expected in ITER [16]. Additionally, even though extensive research has been done on the properties of pristine surfaces of high-Z materials, it is still unknown exactly how the physical and thermal properties of the material change with a heterogeneous fuzz layer, as discussed previously. Therefore, the present study will report on the thermal response of Mo to sequential low-energy He$^+$ ion irradiation and pulsed heat loading, and compare these results to previous findings.

To help elucidate the ambiguity in quantifying fuzz damage, the present study introduces a novel method for detecting and measuring mass loss during transient heat loading events. Studies by Takamura *et al.* have comprehensively examined pulsed heat loading of nanostructured surfaces at low power densities [130]. At these low intensities, the surface is deformed via annealing instead of melting [130]. Annealing takes place below the melting point of the metal, but still causes amalgamation of fuzz fibers and surface deformation [55]. On the other hand, melting occurs when the bulk surface temperature surpasses the melting temperature of the metal. High energy density heat loading can cause melt layer growth and splashing [16]. Previously, researchers used traditional *ex situ* techniques for estimating mass loss due to erosion during high intensity heat loading events [57]. Unfortunately, these techniques involve possible contamination and oxidation of the metal surface. Therefore, in the present study, a quartz crystal microbalance (QCM) was used to measure material ejection in an *in-situ* configuration during transient heat loading, using a pulsed Nd:YAG millisecond (ms) laser. Even though the QCM could be used in conjunction with computational methods to calculate the total amount of removed mass (see Chapter 6), the current study focused instead on determining the threshold where particle emission begins. Using this tool as a method of measuring mass loss is also discussed in terms of accuracy, replicability, and standardization.

Investigating how a fuzzy surface responds to a high heat flux environment is very important in determining its viability as a PFC candidate material for future fusion applications. Studies done by Takamura *et al.* suggest that certain properties of a nanostructured surface could prove superior to that of pristine surfaces, such as a reduction in sputtering and secondary electron emission [131]. Uncertainty also exists on how to

quantify the quality of the fuzz structure. High-Z materials other than W undergo similar nano tendril growth in response to low energy He$^+$ ion irradiation, and experiments have not definitively shown that the nanostructure on one material is significantly stronger than that on another material [16]. Therefore, all options need to be considered when finding the most suitable material for ITER and/or other fusion reactors with different operating environments.

4.2.2   Experimental setup

Sequential He$^+$ ion irradiation and pulsed heat loading studies were performed in the Ultra-High Flux Irradiation (UHFI-I) facility (see Section 2.1.2) and the laser-produced plasma (LPP) experimental chamber (see Section 2.1.1) in the Center for Materials Under Extreme Environment (CMUXE) at Purdue University [42], [44]. The samples used were cut from a cold-rolled Mo sheet with a purity of 99.95% and a thickness of 0.5 mm. Each sample measured 10 mm × 10 mm and every sample of a certain material was cut from the same sheet. Prior to exposure, the samples were mechanically polished to a mirror finish. For helium ion (He$^+$) irradiation experiments, a Kaufman & Robinson, Inc., EH (End Hall) 400 ion-source gun was used. This gun is a grid-less end-Hall "eH" Ion / Plasma source. The ion gun includes broad beam End-Hall ion sources and automated power supply controllers. The broad divergent beam improves throughput by uniformly covering a wide deposition zone. The base pressure of the ultra-high vacuum (UHV) chamber was 1.0×10^{-8} torr, while the working pressure during irradiation was around 2.0×10^{-4} torr. The sample temperature during irradiation was 873K. The selection of ion flux, ion energy, and sample temperature was based on previous studies done internally [42], [44]. Thermocouples were used for a precise temperature measurement. He$^+$ ion irradiations were performed at a flux of 7.2×10^{20} ions m^{-2} s^{-1} and a total fluence of 2.6×10^{24} ions m^{-2}. The ion energy was kept at 100 eV.

After ion irradiation, samples were exposed to transient heat loading using long-pulsed laser irradiation. A GSI Lumonics 1064 nm pulsed Nd:YAG millisecond (ms) laser was used for these studies, which replicates the heat load and time duration of type-I ELMs. Note that the heat load during these transient events is expected in the range of 0.2 - 2.0 MJ m^{-2} in normal ITER tokamak conditions, with a duration of 0.1-1 ms [82]. The pulse

width (FWHM) and spot size used in the study was 1 ms (with a repetition rate of 1 Hz) and 1 mm, respectively. A schematic diagram of the system is shown in Figure 4.7. This heat loading process was performed as a function of laser pulse count and energy density. Fixing the laser pulse count at 200, the energy density was varied from 1.2 to 2.3 MJ m^{-2}. For the laser pulse dependent study, the number of laser pulses was varied from 1 - 200. During the pulse dependent studies, the energy density was kept constant at 1.5 MJ m^{-2}. This value was chosen after analyzing damage thresholds from the energy density dependent studies. Work performed in [55] also found similar melting thresholds in W.
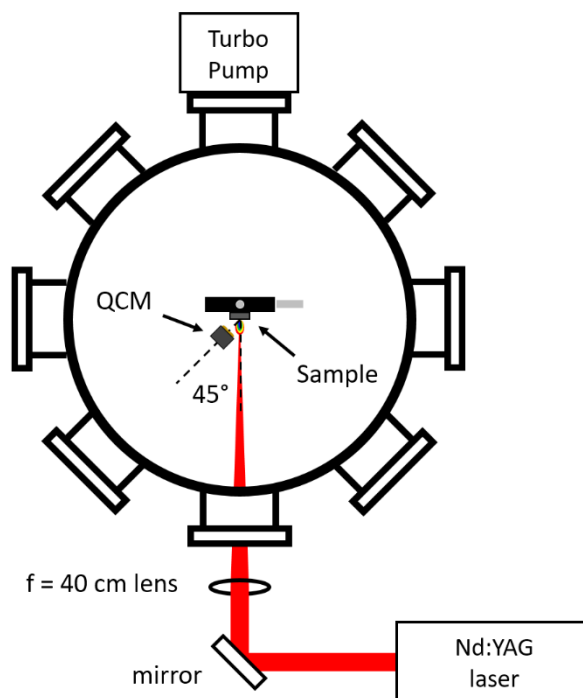
Figure 4.7: Long-pulsed laser irradiation setup schematic

When calculating the energy density, certain assumptions had to be made in simplifying the experimental process. The energy density values reported in this report were calculated based on the assumption that the nanostructured surface maintains a constant absorption rate throughout each irradiation. However, due to changes in optical reflectivity as pulse count increases, the power absorbed slowly decreases. However, this effect is minimal due to the long pulse width used with ms laser irradiation (instead of femto or nanosecond laser irradiation). Further analysis on why the amount of power absorbed depends on the surface reflectivity can be found in work done in [132].

The mass loss due to transient heat loading from the fuzz surface was measured *in situ* using a QCM. As evidenced in Figure 4.7, the QCM is placed 20 mm away from the sample surface at an angle of 45° relative to the sample plane. For each exposure, the QCM is zeroed, and a time-integrated value representing the mass deposited onto the vibrating crystal during that exposure is recorded.

After exposure, samples were taken out of the UHV chamber and *ex situ* field emission (FE) scanning electron microscopy (SEM) using the "Hitachi S-4800 Field Emission SEM" was performed for characterizing ion-induced surface evolution. Atomic force microscopy (AFM) studies using the Bruker Innova atomic force microscope was conducted to understand the ion-induced, nanoscale changes on selective samples. Also, X-ray photoelectron spectroscopy (XPS) was performed on certain samples to obtain compositional information on the helium-irradiated surface. During XPS measurements, photoelectrons were excited using a Mg-Kα (energy = 1253.6 eV) X-ray source (SPECS XRC-1000) and the emitted photoelectrons were analyzed using an omicron argus hemispherical electron analyzer, with a round aperture of 6.3mm. No sample charging was observed during XPS measurements. Finally, optical reflectivity measurements were taken over a spectrum of incident light (using a combination of halogen and deuterium light, with a beam diameter of ~1 mm) ranging from 200 to 1120 nm wavelengths.

4.2.3   Changes in surface morphology

4.2.3.1   Mo fuzz formation

Figure 4.8 shows FE-SEM images of a pristine and a 100 eV He$^+$ ion irradiated Mo sample. The damaged sample was irradiated with a fluence of 2.6×10^{24} ions m^{-2} (flux of 7.28×10^{20} ions m^{-2} s^{-1}) at a temperature of 873 K. SEM imaging of a polished, pristine sample shows a reasonably clean and flat surface down to a micrometer scale, with few mechanically-polished induced scratches (Figure 4.8(a)). After He$^+$ ion irradiation at 873 K, the entire Mo surface became covered with dense nano-tendril fiber form structures (fuzz), as evidenced in Figure 4.8(b) and Figure 4.8(c). The CMUXE surface science group has recently conducted experiments that show such nanostructure evolution [42], [44]. He is a chemically inert gas with almost zero solubility in most metals. However, it can diffuse rapidly through the metal surface due to its small atomic weight, leading to He bubble

formation underneath the surface at crystallographic defects. He irradiation-induced damages can be so significant that they can damage the surface even in the absence of displacement damage and native defects [103], [132]. Recent studies now suggest that this process of helium bubble formation is responsible for Mo fuzz growth [42]–[44]. *Ex situ* XPS (not shown) of the nanostructured surface shows a strong MoO_3 signal without any other impurity. Optical reflectivity measurements on these fine nanostructures show ~0% reflectivity (~100% absorption) [42], [44]. The size of these nanostructures and thickness of the nanostructured (fuzz) layer are dependent on surface temperature and ion irradiation flux and/or fluence [42], [44].
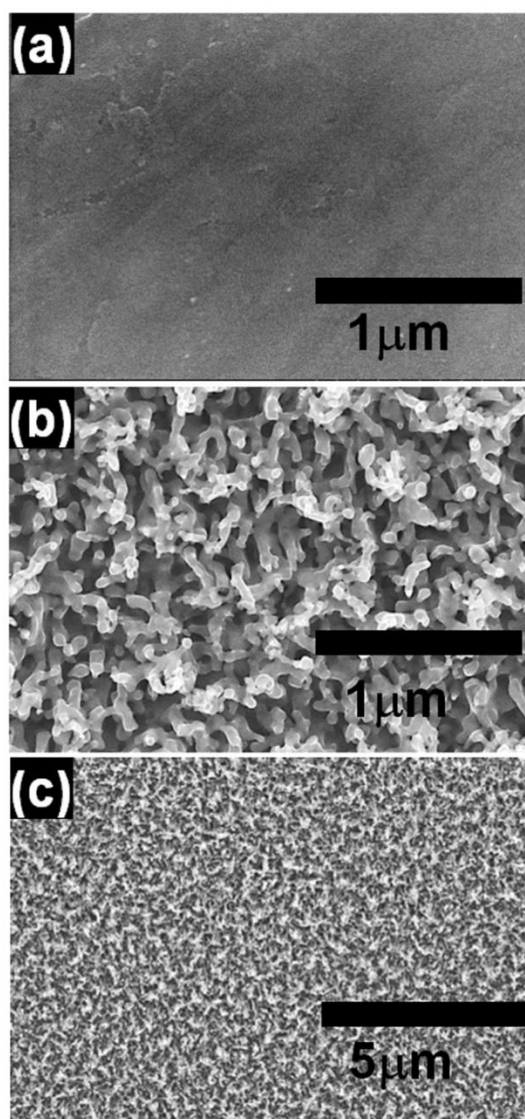
Figure 4.8: SEM micrographs of Mo surface: (a) pristine and (b & c) ion-irradiated. Reproduced from [133] with permission. Copyright IAEA, Vienna 2016.

4.2.3.2   Thermal degradation of fuzz tendrils due to pulsed heat loading

The formation of nanoscale tendrils on PFC materials (Mo in the present case) could lead to unexpected increases in erosion. Very small amounts of material loss during operation could lead to immediate plasma cooling (quenching) [4], [134]. Recent findings suggest that fuzz formation could lower the thermal conductivity of the component surface, which would increase the degree of melting during transient events [82]. Imaging of the surface after pulsed heat loading will help characterize the thermal response of the fuzz nanostructure.

Studies done internally show that transient heat loading replicated with a pulsed ms laser may destroy and remove fuzz structures. Both energy density and laser pulse dependent studies were performed on these surfaces. For pulse dependent studies, the energy density was fixed at a constant value of 1.5 MJ m^{-2}. Note that the selected energy density matches well with the findings in [82], where the melting threshold for W fuzz was between 0.58 MJ m^{-2} and 2.1 MJ m^{-2}. SEM micrographs in Figure 4.9 show the Mo fuzz surface after transient heat loading as a function of pulse count, ranging from 5-200 laser pulses. Figure 4.9 clearly shows the development of molten craters within the damaged area. As the pulse count increased, the width of the craters increased significantly. Molten craters and splashed liquid droplets could result from overheating of near surface defects and other imperfections. Overall, the craters have an average size of around 6 μm. Micron-size craters start appearing after only 5 pulses of the laser. One of these craters has been highlighted in Figure 4.9(a). An inset from the same figure shows a high-resolution SEM image of one specific molten crater. Inside the molten area, no fuzz is found as expected. The loss of volume as evidenced by the crater topography and the absence of nano-tendrils (fuzz) within the molten area of the crater (inner area) clearly indicates that melting was induced by pulsed heat loading.
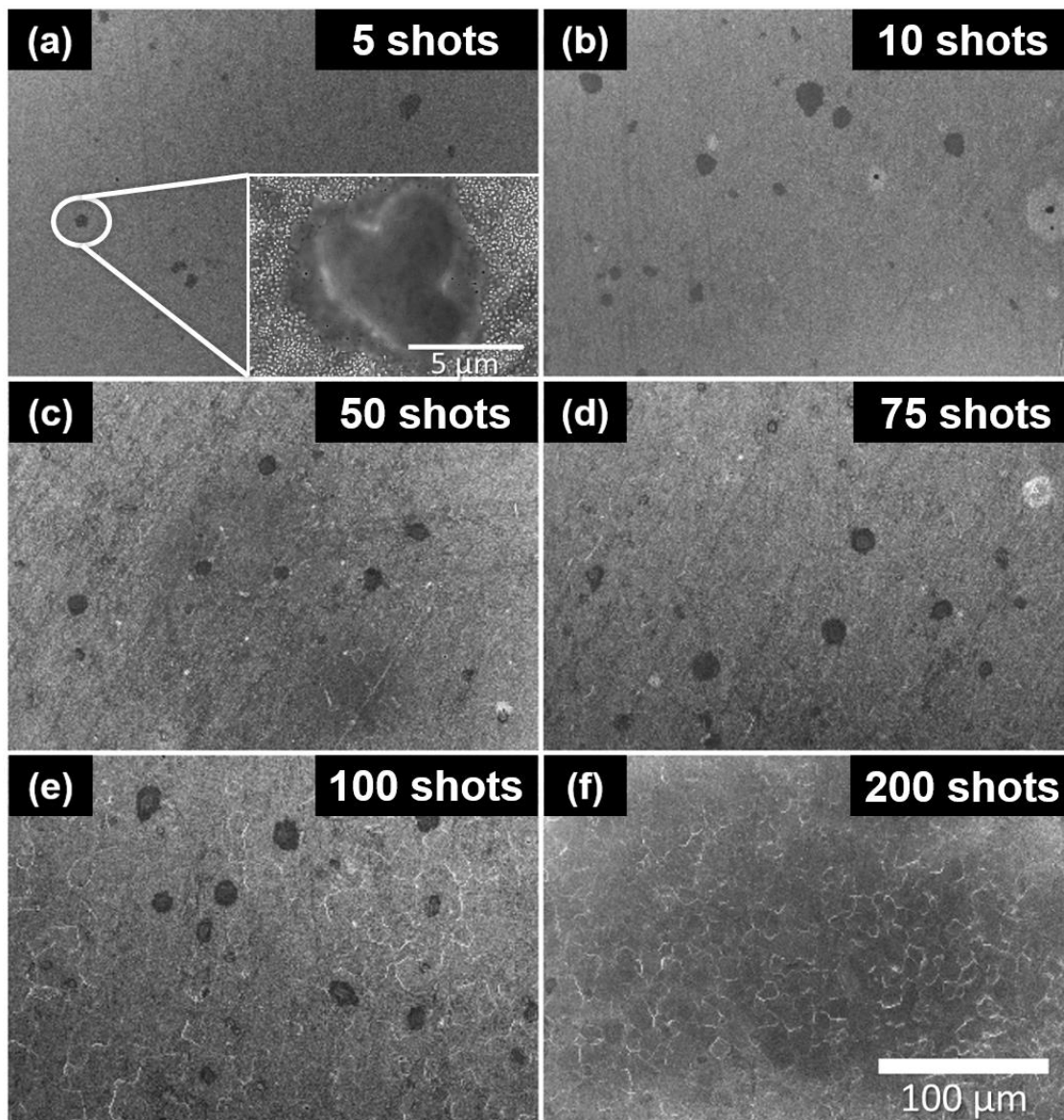
Figure 4.9: SEM micrographs of Mo fuzz surface after pulsed heat loading at 1.5 MJ m^{-2} for different pulse counts. Inset in (a) shows morphology of marked molten crater. Reproduced from [133] with permission. Copyright IAEA, Vienna 2016.

Even though the features shown in Figure 4.9 are referred to as craters, their formation was due to melt motion and splashing, not physical sputtering. Previous studies have found that a melt layer can develop in response to transient loading [135]. With repeated instabilities, the melt layer undergoes splashing and mass loss. Figure 4.9(f) shows that the Mo surface developed a melt layer over the entire damaged area after being exposed to 200 pulses at 1.5 MJ m^{-2}, as evidenced by the lack of fuzz nano-tendrils on the

surface. During irradiations at lower pulse counts, molten craters begin to form in certain "hot spots" along the surface with lower melting thresholds. The reason for the localized nature of surface melting can be attributed to the high heterogeneity in fuzz nanostructure. Melt motion causes the material to move outwards from the initial point of melting and form a crater topography. These surface structures are precursors to the development of a full melt layer. During localized crater formation, many different small, separate molten layers form along the surface. Further studies could be done using FIB to determine the exact height of these structures. However, referring to them as molten craters most accurately describes the melting process during pulsed heat loading.

In addition to damage within the molten craters, significant degradation and additional melting occurred in the area surrounding the craters (near the circumference of the molten area) as pulse count increased. The Mo fuzz density of the area surrounding the molten area depleted significantly beginning at just 5 laser pulses and continued to decrease up to 200 pulses (Figure 4.9 and Figure 4.10). Figure 4.10 shows low and high-resolution SEM images of the Mo surface after laser pulse dependent studies, with exposures varying in laser pulse count from 5 to 200. As evidenced in Figure 4.10(c), there was a significant change in the surface morphology after the 5 pulse exposure, when compared to the undamaged Mo fuzz surface (Figure 4.8). After 100 laser pulses, only a few nanostructures (Mo fuzz), along with some nanoscale pores, were left on the surface. Surface degradation after 200 pulses was more extreme, exhibiting complete surface melting, limited nanopore growth, and most importantly, a complete absence of Mo nanoscale tendril structures (fuzz).
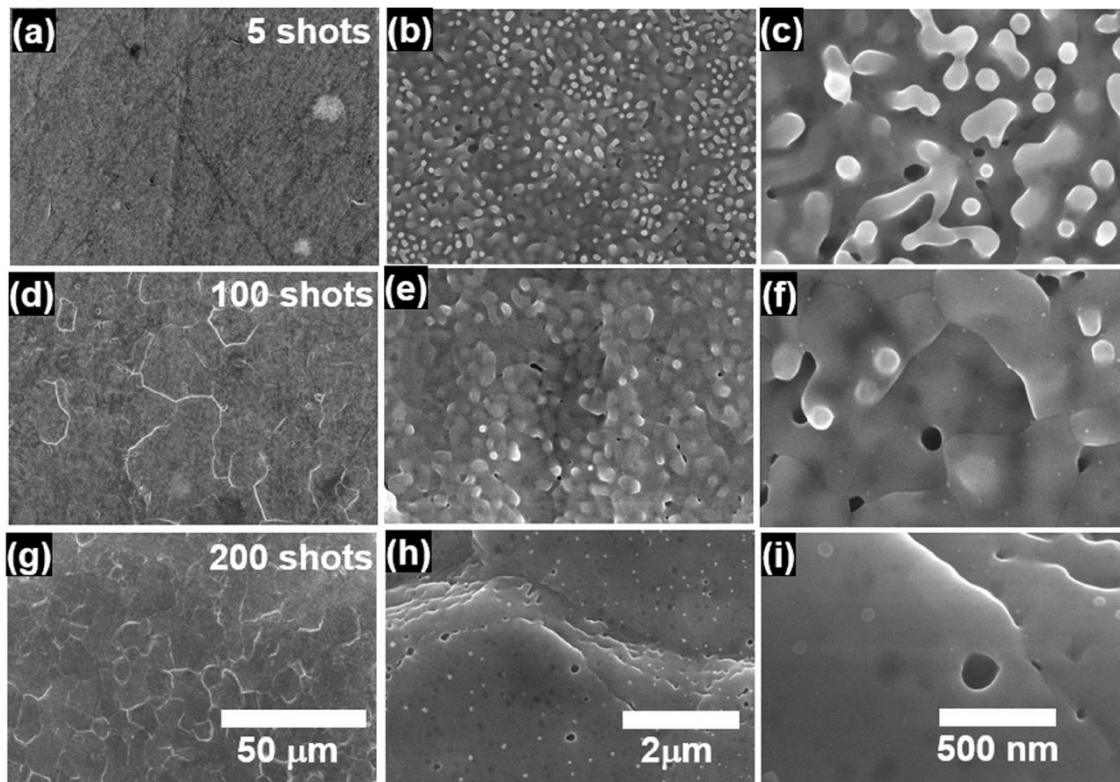
Figure 4.10: SEM micrographs of Mo fuzz surface at different magnifications after pulsed heat loading at 1.5 MJ m^{-2} for increasing pulse counts. Reproduced from [133] with permission. Copyright IAEA, Vienna 2016.

The increase in both the number density and the average size of the craters, mentioned above, indicate a link between surface melting and crater growth. To quantify the growth of the craters, a histogram showing the size distribution of craters as a function of laser pulse count is shown in Figure 4.11. The figure clearly showed the enhancement in the average size of the craters with the pulse count, *viz.,* 4.9 μm (1 pulse) to 6.2 μm (50 pulses) to 7.2 μm (100 pulses). Noticeably, at 100 laser pulses, a few craters are very large in size, with some stretching up to 12 μm in width (Figure 4.9 and Figure 4.11). At 200 laser pulses, localized molten crater formation eventually led to complete melting across the surface.
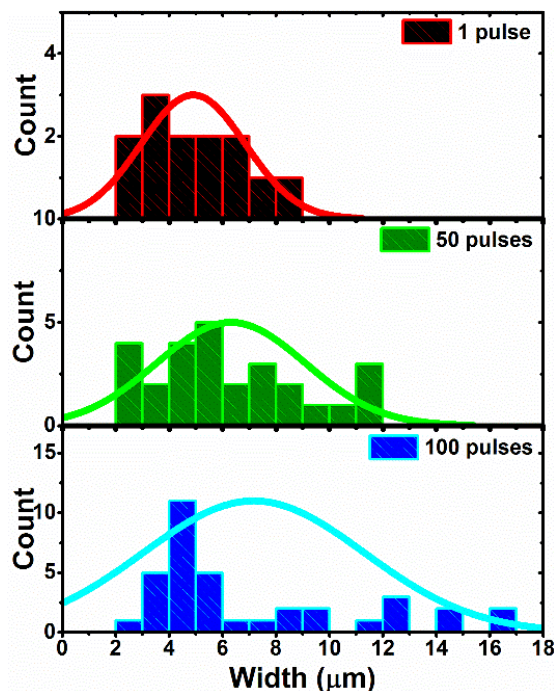
Figure 4.11: Molten crater width distribution histogram for heat loading at different pulse counts; normal distribution curve is shown for each exposure. Reproduced from [133] with permission. Copyright IAEA, Vienna 2016.

Surface atomic force microscopy (AFM) was performed on the part of the Mo fuzz surface exposed to 200 pulses at 1.5 MJ m^{-2} to characterize the molten layer. Figure 4.12 shows high-resolution AFM images from these surfaces. Figure 4.12(a) depicts the amplitude mode two-dimensional (2D) AFM images in a 3×3 μm^2 scan area. These images show the melted and recrystallized micro grains on the entire surface, reinforcing the findings from the SEM images. Figure 4.12(b) and Figure 4.12(c) show amplitude and topography mode AFM images (500×500 nm) in 2D and 3D modes, respectively, from different regions. Figure 4.12(d) shows the line profile of the marked region in Figure 4.12(b). Figure 4.12(d) clearly shows the melted layers (profiling the region marked by the arrows on Figure 4.12(b) and Figure 4.12(c)). As evidenced in both SEM and AFM studies, there is no evidence of either Mo nano tendril fiber form structure (fuzz) or crater formation (as observed for lower laser pulse counts) on the Mo surface. The absence of any separated craters after 200 pulses was most likely to due to complete melting across the surface. Because the craters have already expanded, and led to complete surface melting, laser irradiations at higher pulse counts are assumed to lead to complete surface melting as well. The continued damage done at higher laser pulse counts may lead to significant particle

emission and plasma contamination. The thermal properties of the Mo surface after the fuzz structure has melted are unclear. The surface melting seen in these studies was expected, because of the high energy densities (upper end of type-I ELM region) used during the pulsed heat loading process.
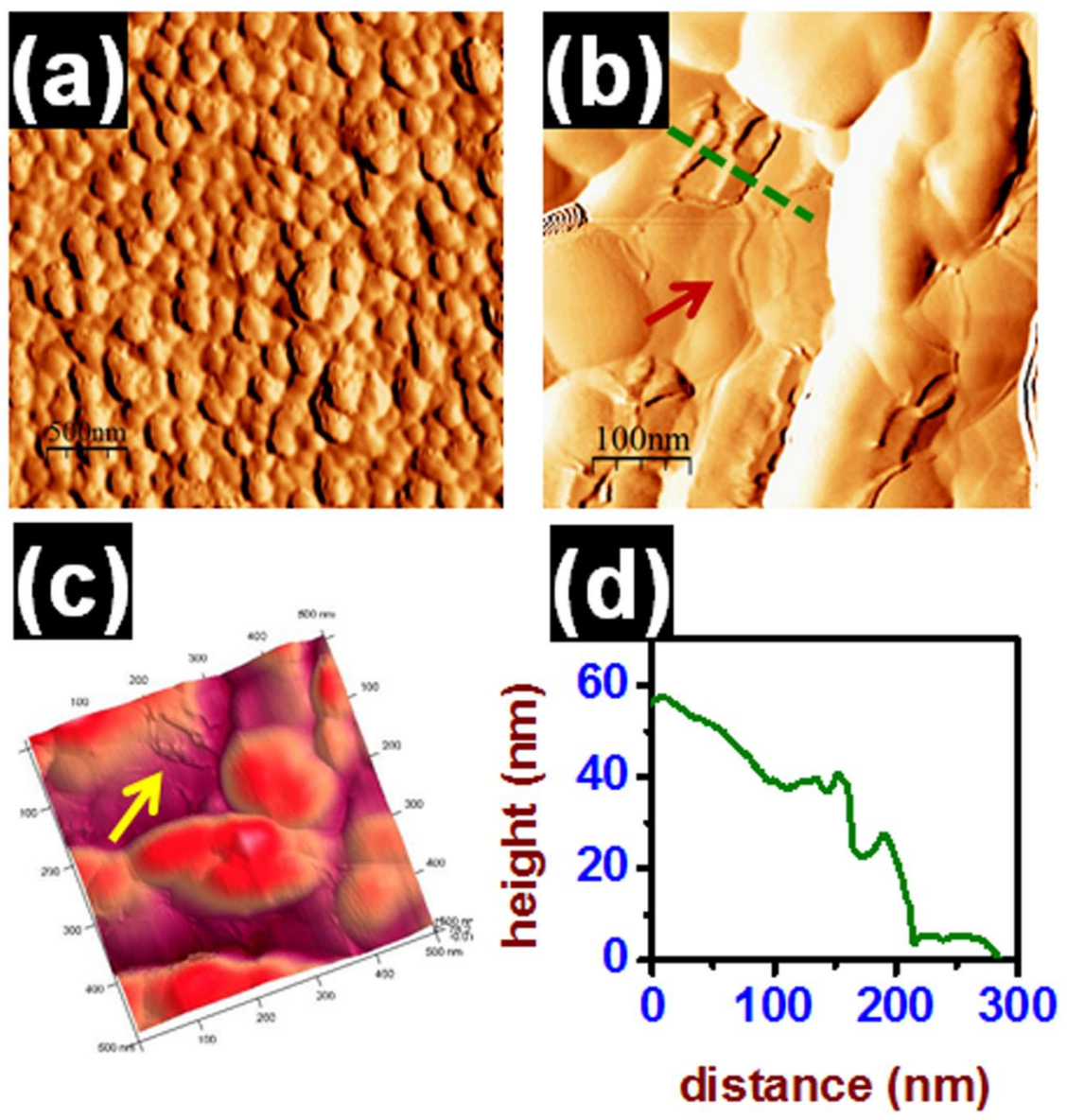
Figure 4.12: High-resolution AFM 2D and 3D topography images of the Mo fuzz surface exposed to 200 pulses at 1.5 MJ m^{-2}. Reproduced from [133] with permission. Copyright IAEA, Vienna 2016.

Previous studies have found that He$^+$-induced, nano-fiber fuzz formation could also result in lower melting thresholds and similar microscale molten crater formation under pulsed heat loading. One observation worth noting is the absence of cracks along the surface after pulsed heat loading took place. Work done in [136] found that fuzz formation improved the crack resistance of the surface structure under transient loading, when compared to similar experiments done on pristine surfaces. The absence of cracks in the current study was most likely the result of the high energy density used in the experiment, raising the temperature of the sample above the DBTT. Work presented in [137] further investigated the thermal properties of the nanostructured surface by experimentally measuring the thermal conductivity of an ion-damaged W layer using the 3-omega method. They found a 60% reduction in the thermal conductivity as compared to the pristine sample [137]. This finding correlates with a lower melting threshold for the fiber form Mo surface. The dependence of this melting process on crater formation was also found in [138]. In this study, they found the development of micrometer-sized "balls" or "liquid droplets" on the surface of a nanostructured W sample in response to pulsed heat loading [138]. These "balls" were thought to be the precursor to surface melting of the fiber form surface. Further characterizing the structure and formation of these "balls" could help draw similarities to the experiment discussed in this paper and further understand the fuzz melting process. They discussed the possibility that the "balls" could be thought of as dust particles, and could therefore be attributed to higher levels of contamination during transient heat loading. If these balls are actually molten droplets as a result of the melting and degradation of the fiber form nanostructures, then the melting process in each experiment seemed to follow the same process. Based on the data shown in Figure 4.9 and Figure 4.10, droplet formation and surface melting could lead to the enhanced particle emission and contamination put forward in [138]. The formation of this structure was also reported in [79], with references to multiple studies that have found similar molten droplet formation and localized melting during ELM-like pulsed heat loading. In the report, they also theorized that particle emission could be directly based on this melting mechanism. This theory is examined in more detail in the following section by studying the occurrence and behavior of fuzz removal in response to pulsed heat loading.

4.2.4   Analysis of Mo erosion

One of the most serious problems that fuzz nanostructure growth poses is that of plasma contamination for future fusion reactors. The acceptable plasma impurity concentrations for high-Z candidate materials are much lower than those for low-Z materials, even though high-Z materials tend to have a lower sputtering yield to begin with [3]. Quenching of the core plasma is possible if the atomic concentration of W exceeds 10^{-5} [3]. Recently, internal studies have shown that, under normal divertor conditions, pristine Mo and W are expected to erode at a net rate of 1 mm/burn-yr [16]. Studies done internally have also shown that core plasma contamination is not expected to change significantly between different high-Z candidate materials [16]. Although these results are very promising, in-depth analysis of particle emission from nanostructured, high-Z metals under transient heat loading, specifically, has not been conducted. If the growth of fiber form nano-tendrils weakens the thermal strength of the surface, as localized molten crater formation has indicated above, then enhanced particle emission might lead to unsustainable levels of contamination during normal operation. Important research done by Yu *et al.* reported that above a surface temperature of 2000 K, the thickness of the fuzz layer began to decrease [139]. Their experiments involved simultaneous D and He plasma exposure and laser irradiation on W samples [139]. At low intensities, it was shown that pulsed heating actually stimulated the growth of the fuzz nano-tendrils [139]. Due to the high energy density used in the current study, the surface temperature should exceed 2000 K, and lead to fuzz layer reduction via splashing and erosion [55]. In the limited number of experiments done analyzing melting and splashing of nanostructured high-Z materials under ELM-like heat loads, the most common method of measuring particle emission involves *ex situ* mass removal measurements [57], [94]. Many times, balances are used that have a resolution of around 10 μg [94]. When performing experiments on the development of a Mo fuzz layer, the CMUXE surface science group observed higher levels of oxidation on the nanostructured Mo surface when compared to the pristine surface [42]. Finding increased oxidation was attributed to the increased surface area with fuzz growth; when the sample was removed from high vacuum, oxidation commenced along that heterogeneous surface [42]. Contamination from oxidation and possible dust collection therefore render

ex situ measurements inaccurate, especially when attempting to measure mass differences on the order of nanograms (ng) or μg [75].

Utilizing a QCM promises to be an improved, *in situ* method for measuring the presence and trends in particle emission during transient heat loading. The differences in the vibration of the QCM crystal, as material is deposited onto the surface, correspond to a calculated value for the amount of mass removed [92]. The time-integrated values for mass deposited during exposure are calculated by the control unit using equation (2-1). In a high vacuum system, the concentration of oxides and dust is approximately zero, which will prevent any contamination or confounding of the results.

Due to the nonhomogeneous particle emission spectrum during ms laser irradiation, the QCM cannot be used to accurately measure the total mass loss rate during pulsed heat loading. Previous studies done internally to investigate the angular dependence of particle emission using a QCM found a ~ 70% reduction in particle collection at 10° when compared to collection at 45° [83]. Further research found that as the pulse duration increased, the particle emission distribution became wider and the standard deviation increased [84]. Because the QCM is being placed at a 45° angle relative to the sample plane (optimized condition for this experiment) in the present study, most of the mass leaving the surface of the sample will not be picked up by the QCM. Therefore, the results discussed should not be representative of the total mass loss during ELM-like heat loading. Nevertheless, the values obtained can help to identify the evidence of Mo fuzz removal and the rate with which such particle emission changes over time (as a function of laser pulse count).

The energy density dependent studies were conducted first to determine the melting threshold of Mo fuzz. In the study, the number of laser pulses was kept constant at 200 per exposure, while the energy density was varied from 1.2 - 2.3 MJ m^{-2}. For each exposure, the QCM time-integrated value for mass deposited was recorded. The relationship between the mass deposited (removed Mo fuzz) onto the QCM per exposure and the energy density of the laser is shown in Figure 4.13(a). The results clearly show that splashing is occurring, and that the amount of material emitted increases with energy density. Localized melting, as shown in Figure 4.10, is likely driving emission. Higher energy densities create larger thermal jumps, which results in a larger melt layer and more splashing. Different curves

were fit to the data to quantify the positive correlation between the mass deposited and the energy density. An exponential fit, of the same form shown in Chapter 3, yielded the highest coefficient of determination, with $R^2 = 0.967$. The equation is shown below:

$$\Delta m = 0.05 * exp(1.38Q) \qquad \qquad (4\text{-}2)$$

where Δm is the total mass deposited and Q is the laser energy density. The nonlinear increase in emission was also measured from pulsed heat loading of pristine W and Mo [15]. While the mass emitted from a pristine Mo surface during pulsed heat loading increased exponentially, the emission exhibited some linearity in a transition region.
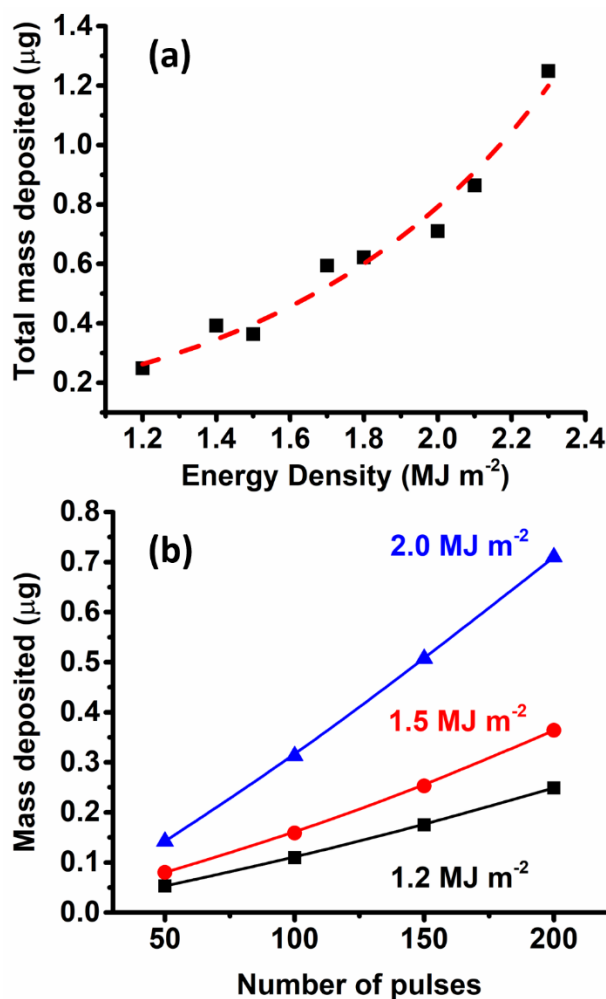
Figure 4.13: Total mass deposited onto QCM for (a) 200 pulse exposures at different energy densities and (b) exposures at different energy densities as a function of pulse count. Reproduced from [133] with permission. Copyright IAEA, Vienna 2016.

The lack of any noticeable transition region in the data shown in Figure 4.13(a) mirrors the gradual degradation of fuzz tendrils shown in Figure 4.10. Defining distinct energy density thresholds for different damage mechanisms appears to be more difficult on a fuzz surface. Future work should attempt to define a maximum energy density at which fuzz tendrils conglomerate and melt without causing splashing.

The evidence of mass deposition on the QCM during transient heat loading proves that Mo fuzz could have an adverse effect on the performance of the fusion plasma under normal operating conditions, if the mass removed is significant (leading to high levels of plasma contamination). Nevertheless, further research is important for gaining a deeper understanding of the fuzz removal mechanism, and performing more experiments in a laboratory setting is necessary to ensure the safe and sustainable operation of current and future tokamaks (DEMO). Additionally, the enhancement in the Mo fuzz mass loss with laser energy density reveals a melted surface layer growth on the Mo sample, as has also been seen in high-resolution SEM and AFM micrographs (Figure 4.9 and Figure 4.12). Examining mass loss over time (based on the number of laser pulses) is a very useful metric for understanding material lifetime and plasma sustainability. Measuring the amount of the eroded mass during transient heat loading provided critical information for designing future DEMO devices. As evidenced in Figure 4.13(b), mass removal had a strong dependence on laser energy density and laser pulse count, with twice as much mass being removed at 2.0 MJ m^{-2} than at 1.5 MJ m^{-2}.

One potentially dangerous side effect of transient heat loading on high-Z materials (that was not tested in the present study but should be discussed) is the occurrence of unipolar arcing. Previous research has shown that simulating ELM-like heat loads using long-pulse laser irradiation on fiber form W can induce arcing along the surface [53]. At an energy density of 5 MJ m^{-2}, a pulse width of 0.6 ms, and a floating potential of -60 V, arcing was initiated and lasted for ~ 2.8 ms, destroying the fuzz structure along its path [53]. A follow up experiment to determine the erosion rate during arcing found that in one arcing event, W fuzz eroded at a rate of 10 μg ms^{-1} (approximately corresponds to one type-I ELM event) [80]. Erosion at that level is a factor of 10^6 higher than the most pessimistic estimates of fuzz erosion without arcing [75]. Experiments done with the Divertor Materials Evaluation System (DiMES) in DIII-D found that in a tokamak environment,

arcing can occur on the W fuzz surface during vertical displacement event (VDE)-like exposures [140]. However, no particle emission was detected in these studies. More experiments should examine the potential erosion from arcing on nanostructured PFCs to determine and quantify the incremental particle emission and contamination that is taking place. The impact of the fuzz nanostructure on the reduction of the arcing threshold should also be analyzed further. Studies done in [141] revealed that scratches on a nanostructured W surface could affect the path of the arc track. Other mechanisms of particle emission and PFC erosion also need to be investigated and understood. If the erosion rates are indeed on the scale of tens of $\mu g\ ms^{-1}$, then both splashing seen in the current study and unipolar arcing might lead to unsustainable levels of plasma contamination in future fusion reactors.

4.2.5   Qualifying changes in fuzz density using optical reflectivity

Tracking the optical properties of the Mo fuzz surface during the transient heat loading process provides an additional metric for characterizing how the surface nanostructure evolves over time. Recent studies done internally showed that Mo fuzz growth reduced the optical reflectivity of the Mo surface from 30% - 50% to almost 0% [42], [44]. Therefore, the strong dependence of optical reflectivity on the surface microstructure was used to qualitatively characterize the evolving fuzz degradation process during pulsed heat loading.

Figure 4.14(a) shows the optical reflectivity spectra for pristine and Mo fuzz nanostructured samples. These spectra show the minimum (corresponding to fuzz structure) and maximum (corresponding to pristine structure) optical reflectivity values as a reference. The fuzz surface exhibited a much lower reflectivity than that of the pristine surface. To understand how the reflectivity evolves during pulsed heat loading, reflectivity spectra was measured for different pulse count exposures. These spectra are shown, along with the reference values, in Figure 4.14(b). The spectra clearly show that the reflectivity increased with increasing laser pulse count. A summary of measurements shown in Figure 4.14(b) was presented in Figure 4.14(c) by using reflectivity values at $\lambda = 670$ nm. As the number of pulses increased, the reflectivity increased to ~ 90% of the pristine reflectivity. A critical inspection of Figure 4.14(c) revealed a relatively slow rate of recovery for optical reflectivity up to 200 laser pulses, which reflected SEM micrographs in Figure 4.9 that

showed complete disappearance of nanostructure at 200 pulses. At 200 laser pulses and above, the reflectivity values increased significantly (~ 20% for 200 pulses), which was due to further refinement of the surface structure after melting. SEM and AFM micrographs, shown in Figure 4.9, Figure 4.10, and Figure 4.12 illustrate this melting process. At 400 laser pulses, the optical reflectivity reached almost 90% of its original (pristine) value. This optical reflectivity recovery process has also been observed in other studies done on W nanostructure [142]. In these experiments, W fuzz was synthesized by He plasma irradiation with a similar ion energy and fluence. Afterwards, the W samples were exposed to pulsed heat loading by a ruby laser, with a similar pulse width and energy density to the studies done here. By measuring the optical reflectivity of the sample, they found that above 1.2 MJ m^{-2}, optical reflectivity recovered by almost 100%. These findings can be qualitatively correlated with the evolving density of fuzz structures during transient heat loading. The findings presented here also correlate well with the studies done in [57], where they reported a reduction in fuzz density with increasing laser energy density during transient heat loading. The noticeable difference between these studies is that their experiment was performed using lower laser energy densities (0.1 - 0.5 MJ m^{-2}). Therefore, molten crater formation was not seen in their study, and they concluded that melting is not expected at the lower end of the type-I ELM spectrum. However, similarities in the evolution and degradation of this fuzz nanostructure in response to pulsed heat loading stresses the importance of further research to understand whether this damage mechanism is ultimately devastating or not to the overall performance of the plasma and the lifetime of the components.
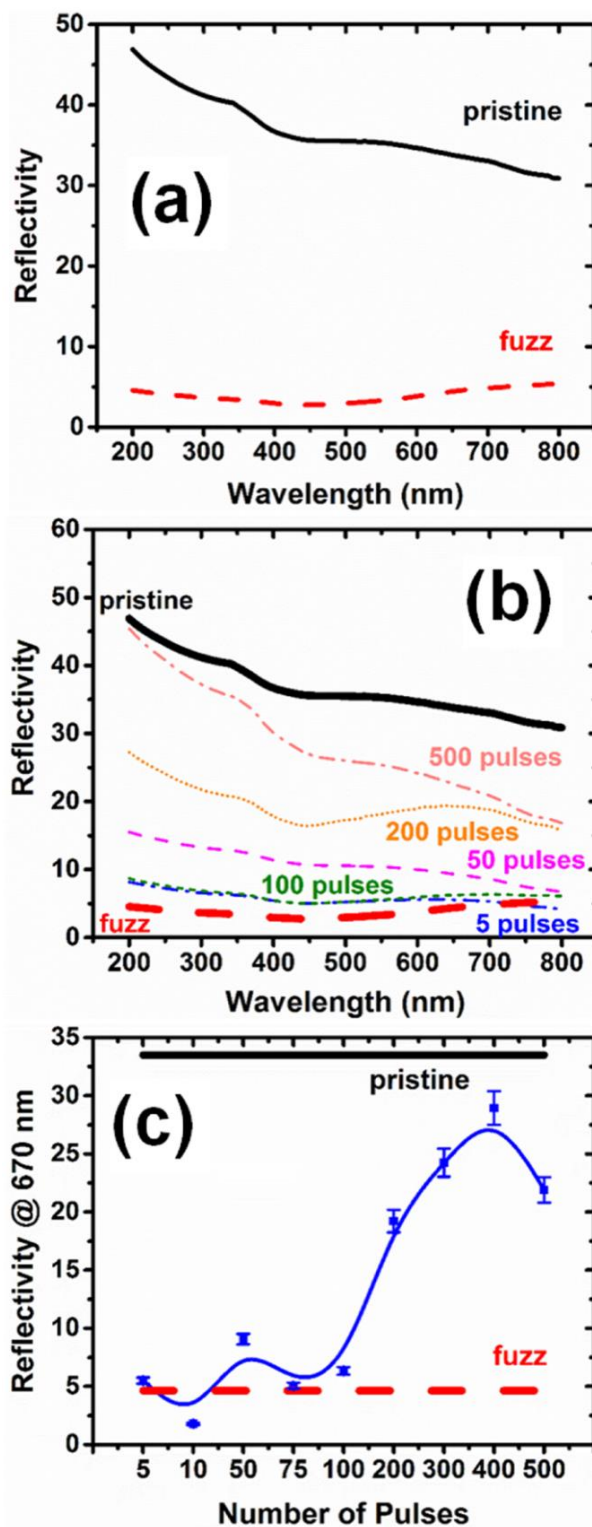
Figure 4.14: Optical reflectivity measurements for (a) pristine and fuzzy Mo surfaces, (b) Mo fuzz surface after loading at 1.5 MJ m^{-2} for increasing pulse counts, and (c) exposures done at 1.5 MJ m^{-2} displayed as a function of pulse count using reflectivity values at $\lambda = 670$ nm. Reproduced from [133] with permission. Copyright IAEA, Vienna 2016.

4.2.6 Summary

Cold-rolled Mo sheets of 99.95% purity and 0.5 mm thickness were used for the present study. 10×10 mm samples were cut from the same sheet and mechanically polished to a mirror-finish. The samples were irradiated at a normal incidence by 100 eV He^+ ion irradiation with an ion fluence of 2.6×10^{24} ions m^{-2} (ion flux of 7.2×10^{20} ions $m^{-2} s^{-1}$) at a temperature of 873K. Ion irradiation-induced Mo surface deterioration was observed and characterized using field emission (FE) and scanning electron microscopy (SEM). Microscopy studies on a pristine Mo sample reveal a clean and flat surface, down to several micrometers, along with a few polishing-induced scratches. The ion-irradiated sample shows the formation of a nano tendril fiber form structure (fuzz) on the molybdenum surface. Transient heat loading was applied using a high power, pulsed Nd:YAG ms laser on the Mo fuzz surface. Transient heat load induced Mo fuzz mass removal was monitored using a highly sensitive quartz crystal microbalance (QCM) in an *in situ* configuration. Experiments were performed at the upper end of the expected type-I ELM range, at energy densities between 1.2 - 2.3 MJ m^{-2}, for observing and characterizing the melting process of the molybdenum fuzz.

QCM analysis found that high intensity, pulsed heat loading results in mass loss, where the amount of particle emission increases with energy density. Even though the purpose of the current study was to examine the threshold for possible splashing and particle emission, more research should be done on characterizing the emission distribution in order to estimate the total amount of mass loss. The presence of material splashing and erosion with pulsed heat loading normal to the material surface raises serious concerns about particle emission and plasma contamination inside a fusion device. In a tokamak environment, the incident ion particle flux during an ELM or a disruption from the scrape-off layer (SOL) will be at a very steep incident angle [135]. Due to the low inclination, more splashing and particle emission could occur than seen in the current study. Further research should be done to investigate the dependence of particle emission on incident heat flux angle.

SEM micrographs illustrate that the molybdenum fuzz on the surface is being melted by a localized molten crater formation mechanism. For laser exposures at or above 200 pulses, almost complete molybdenum fuzz removal is observed, along with total surface melting. Using SEM and high-resolution atomic force microscopy (AFM) also reveals

complete surface melting for 200 laser pulse exposures (having 1.5 MJ m^{-2} laser energy density). Optical reflectivity measurements were performed on all samples to characterize the degradation of the fuzz structure during pulsed heat loading. These results indicate that the reflectivity increases with laser pulse count, yielding, at best, a ~ 90% recovery of the original reflectivity value (pristine sample). The recovery rate was relatively slow for lower laser pulse count exposures (up to 200 pulses), but increased above 200 laser pulses.

The evidence of mass deposition on the QCM during transient heat loading could represent a serious setback for the utilization of Mo and other high Z materials as PFCs under the conditions used in this study. Fusion devices demand PFCs with high thermal stability and low erosion rates to ensure high plasma performance. Future research is necessary to understand potential fuzz removal mechanisms, and conclude whether or not this helium-induced nanostructure will present a serious problem for the design and operation of future fusion reactors, such as ITER and DEMO.

4.3 Studies on tungsten

Transient heat loading and high-flux particle loading on plasma facing components (PFCs) in fusion reactors can lead to surface melting and possible erosion. Helium-induced fuzz formation is expected to exacerbate thermal excursions, due to a significant drop in thermal conductivity. The effect of heating during edge-localized modes (ELMs) on the degradation and erosion of a tungsten (W) fuzz surface was examined experimentally in the UHFI-II facility at CMUXE. W foils were first exposed to low-energy He$^+$ ion irradiation at a fluence of 2.6×10^{24} ions m^{-2} and a steady-state temperature of 1223 K. Then, samples were exposed to 1000 pulses of ELM-like heat loading, at energy densities between 0.38 and 1.51 GW m^{-2} and at a steady-state temperature of 1223 K. Comprehensive erosion analysis measured clear material loss of fuzz nanostructure above 0.76 GW m^{-2} due to melting and splashing of the exposed surface. Imaging of the surface via scanning electron microscopy (SEM) revealed that sufficient heating at 0.76 MJ m^{-2} and above caused fiber form tendrils to conglomerate and form droplets. Repetitive thermal loading on molten surfaces then led to eventual splashing. *In situ* erosion measurements taken using a witness plate and a quartz crystal microbalance found an exponential increase in mass loss with energy density. Compositional analysis of the witness plates revealed an

increase in the W 4f signal with increasing energy density above 0.76 MJ m^{-2}. The reduced thermal stability of fuzz nanostructure puts current erosion predictions into question and strengthens the importance of mitigation techniques.

4.3.1 Introduction

Low impurity radiation and high component lifetime are critical design parameters in future fusion devices. Plasma facing components (PFCs) need to be engineered to withstand the high particle and heat fluxes expected during reactor operation. In addition to steady-state heat loading of 10-20 MW m^{-2}, PFCs in the divertor will also be exposed to transients of several GW m^{-2} [13]. Near-term devices, like ITER, expect edge-localized modes (ELMs) to occur regularly. Unmitigated type-I ELMs could possess energy densities up to 10 MJ m^{-2}, with durations of $0.1 - 1$ ms and repetition rates around 1 Hz [13], [28], [143]. Several studies have shown that this type of heat loading is likely to cause intense melting and cracking [25], [33], [85]. Therefore, various ELM mitigation techniques, such as ELM pacing, are being developed to limit thermal damage by keeping the maximum energy density below 0.5 MJ m^{-2}, at the sacrifice of higher frequencies [8], [9], [14], [28]. Recent work on lithium granule injection in DIII-D concluded that a small fraction of ELMs will still, however, remain unmitigated [14]. Therefore, the effect of unmitigated ELMs on material degradation still needs to be characterized.

Current material testing for future PFCs is largely performed on W, due its superior thermal and mechanical strength [16], [79], [144]. The presence of both steady state and transient heat loading, however, may lead to cracking and melting of the W surface. Recent studies have shown that the added impact of He^{+} ion loading could drastically reduce the thermal strength of the W surface, due to the formation of fuzz [36], [38], [43]. Tendril conglomeration during intense heat loading has shown to lower the threshold for surface melting [94]. Direct measurements of the nanostructured layer revealed that the thermal conductivity of the tungsten surface could drop by up to two orders of magnitude [54], [56]. One study observed the presence of surface cracking on W samples exposed to simultaneous He^{+} plasma irradiation and pulsed heat loading above the ductile-to-brittle transition temperature, illustrating the potentially negative impact of implanted He on material strength [145]. While the synergistic effects between low energy He^{+} ion loading

and ELM transient heat loading are not fully understood, the apparent reduction in thermal strength raises serious questions about changes in component erosion under these conditions.

Multiple diagnostic techniques have been used to characterize how W material might be lost during reactor operation due to splashing and vaporization. ELM-like heat loading of pristine W using the quasistationary plasma accelerator (QSPA-T) found distinct thresholds for surface melting and droplet ejection, and an exponential increase in erosion with energy density [15], [68]. In addition, 80% of droplets were emitted within a 45° angle of the surface normal. Transient heat loading studies performed within CMUXE with a pulsed Nd:YAG laser measured small levels of erosion from a pristine W surface with a silicon (Si) witness plate [33]. Work done on a nanostructured W fuzz surface found that melting and erosion might not exhibit specific thresholds, due to uneven melting of the heterogeneous surface [82]. Temperature measurements using an IR camera discovered that melting traces were formed on a nanostructured surface below the melting point of W [55]. While mitigated ELMs with energy densities below 0.5 MJ m^{-2} appear to cause some level of melting, the lack of any measured erosion could indicate potential reintegration and "healing" effects to the surface [57]. The effect of higher intensity, unmitigated ELMs on the structural integrity of nanostructured W remains unclear.

A comprehensive erosion analysis was therefore performed on He$^+$-irradiated W samples using a pulsed millisecond (ms) laser to replicate type-I ELM loading. Surface characterization was complemented by imaging of the plasma plume and direct measurement of eroded material. By utilizing several erosion detection methods, a clear understanding of how He$^+$ irradiation impacts plasma contamination and component viability can be developed.

4.3.2 Experimental setup

Sequential He$^+$ ion irradiation and ELM-like pulsed heat loading was performed in the UHFI-II (Ultra High Flux Irradiation - II) facility at the Center for Materials Under Extreme Environment (CMUXE) at Purdue University. Cold-rolled W samples (99.95% purity, Alfa Aesar) with dimensions 10 mm × 10 mm × 0.5 mm were cut from a single sheet and mechanically polished to a mirror finish. The samples were then exposed to 100

eV He$^+$ ion irradiation, using the experimental setup depicted in Figure 4.15(a). The ion gun was a grid-less end-hall 'EH' ion/plasma source, producing a flux of 7.2×10^{20} m^{-2} s^{-1} (2.6×10^{24} ions m^{-2} fluence). The W sample was clamped to a button heater to provide steady-state heating at a base temperature of 1223 K. After ion irradiation, the sample was exposed to pulsed ms laser irradiation at different energy densities within the expected unmitigated type-I ELM range, as depicted in Figure 4.15(b). The 1064 nm Nd:YAG pulsed ms laser utilized a pulse duration of 1 ms and a repetition rate of 1 Hz, with a flat top spatial profile. Each laser irradiation experiment consisted of 1000 pulses at the following energy densities: 0.38, 0.76, 1.14, and 1.51 MJ m^{-2}. Reported energy densities represent the energy absorbed by the sample surface. Approximately 33% of the pulse energy was lost due to the use of optics for focusing and transmission. An additional amount of energy will be reflected, depending on the optical reflectivity of the surface. The pulse energy was therefore adjusted, so that the energy absorbed divided by the irradiated area (1 mm spot size) yielded the desired energy density. During the experiment, the reflectivity is expected to fluctuate between 0% and 40% as fuzz formation and melting takes place [94]. Therefore, an average optical reflectivity of 20% was used for all exposures, to maintain consistency. Steady-state heating was also applied during laser exposures, maintaining the sample at a base temperature of 1223 K. In a reactor environment, both particle and heat loading are applied to the surface at grazing incidence (~ 4.5°) [146]. However, previous studies show that at lower ion energies (< 218 eV), incidence angle has very little effect on nanostructure formation [65]. While physical sputtering changes significantly based on the angle of incidence [4], droplet splashing of a molten layer is not expected to vary based on the incident angle.
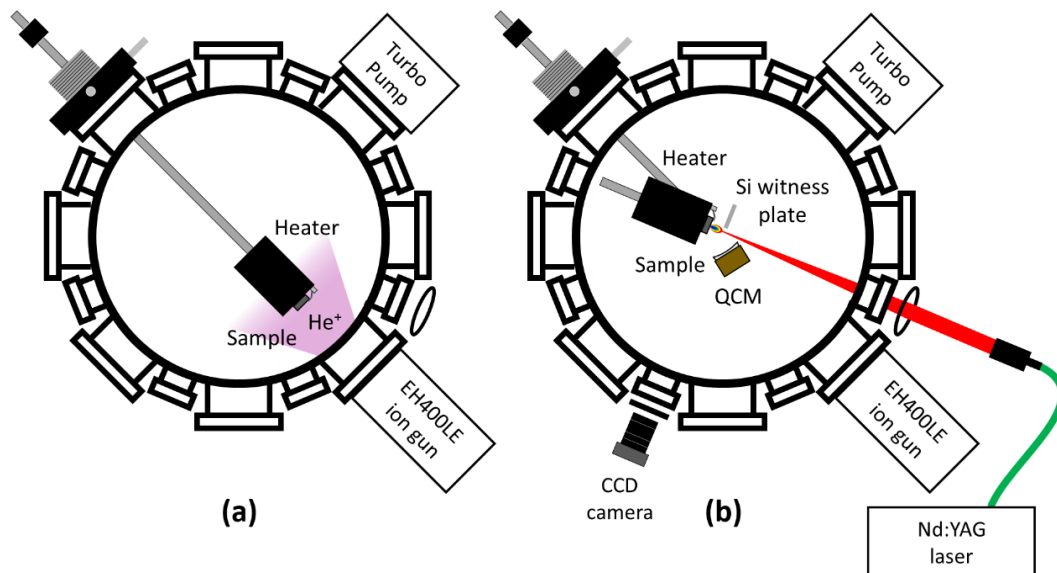
Figure 4.15: UHFI-II chamber; (a) ion irradiation setup schematic & (b) long-pulsed laser irradiation setup schematic.

Many different *in situ* methods were used to characterize and measure W erosion during pulsed heat loading. A quartz crystal microbalance (QCM) was placed 30 mm from the sample surface at an angle of 45 degrees relative to the sample surface. The collection area of the QCM crystal is 52.18 mm^2, the sampling rate was 4 Hz, and the resolution is ± 0.001 nm. During each laser exposure, changes in the QCM vibrational frequency were used to estimate the amount of mass deposited on the QCM crystal using the Sauerbrey equation, as discussed in section 2.4.1 [92]. A Si witness plate (30 mm x 10 mm) was also placed in front of the W sample during each 1000 pulse irradiation to collect any eroded material. The plate was positioned normal to the sample, at a distance of 15 mm from the surface (as depicted in Figure 4.16). Based on the droplet imaging performed in [68], eroded material was assumed to exhibit a straight line trajectory. After each irradiation, the Si witness plate was removed and analyzed via X-ray photoelectron spectroscopy (XPS) with a Mg-K$_\alpha$ source (1253.6 eV). Comparing the relative intensity of the W4f$_{7/2}$ (WO$_3$) peak for different exposures provides a reliable, qualitative metric of W splashing and mass loss at different ELM intensities. All XPS data was analyzed using CasaXPS software [147]. Finally, a charge-coupled device (CCD) camera was placed 42 cm from the sample surface to image side profiles of the plasma plume that developed during laser exposures at different energy densities. The camera recorded photons over the entire visible range,

using a gate width of 1 ms and a delay time of ~ 0.9 ms with respect to the leading edge of the laser pulse.
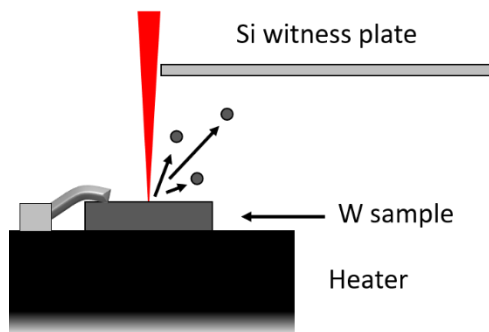
Figure 4.16: Si witness plate setup

After ion and laser exposures, each W samples was analyzed via *ex situ* via field-emission scanning electron microscopy (FE-SEM). Imaging the deformation of the W fuzz surface after laser exposure at different intensities provided insight into possible material erosion mechanisms.

4.3.3 Deformation of fuzz nanostructure due to pulsed heat loading

The presence of nanoscale tendrils has been shown to alter the thermal evolution of the W surface during pulsed heat loading. The significant reduction in thermal conductivity due to fuzz formation could lead to overheating and increased levels of melting, which would compromise reactor performance [56]. The exact process by which the nanostructure would deform and lead to melting during an ELM is currently unclear. Recent studies show that at low energy densities, the fuzz tendrils might undergo an annealing process, returning the surface to a pseudo-pristine state [57]. The sequential ion and laser irradiations conducted attempt to characterize how tendrils respond to higher intensity loading.

SEM micrographs of the nanostructured W surface after 1000 laser pulses at increasing energy densities are shown in Figure 4.17. All exposures conducted at ≥ 0.76 MJ m^{-2} resulted in the complete disappearance of fuzz tendrils. Heat loading performed at 0.38 MJ m^{-2} did not cause any appreciable surface damage. Other work on the thermal loading of pristine W at elevated temperatures yielded similar damage thresholds (accounting for changes in surface properties) [28], [148]. The roughened surface observed at 0.76 MJ m^{-2} consisted of molten droplets that have recrystallized, forming a grain

boundary network. Increasing the energy density to 1.51 MJ m^{-2} did not have a significant impact on the resultant surface morphology. Similar experiments conducted in Chapter 5 with fewer pulses still observed the presence of fuzz tendrils after heat loading at 0.6 MJ m^{-2}, showing the combined effect of both pulse count and energy density on the melting threshold. The significant impact of steady-state heating on surface morphology and bubble formation has also been previously characterized [149]. In this study, W samples were exposed to sequential He$^+$ and laser irradiation at an energy density, pulse count, and pulse duration similar to that in the current study. The resultant surface exhibited cracking and surface roughening, but fuzz tendrils and subsurface bubbles remained present [149]. Since the laser irradiation was done at room temperature (RT), W behaved as a brittle material and the surface temperature remained too low to facilitate significant desorption of trapped He. The disappearance of the fuzz nanostructure appears to be inherently linked to the desorption of He from the sub-surface. Heat loading performed at a low number of pulses resulted in the presence of pores along the surface (see Chapter 5). Repetitive heating of the W surface above the melting point led to thermally-enhanced desorption of trapped He; as the number of pulses increased, the areal pore density decreased. Since the amount of trapped He diminished with increasing pulse count, the intermediate pores that facilitated desorption began to disappear from repetitive melting of the surface. The resultant microstructure was therefore likely due to fragmentation and recrystallization of the melt layer during cooling. Utilizing a pyrometer (to measure surface temperatures) would help characterize the expected phase transition during heat loading. Laser exposures done on a W fuzz surface at RT yield a vastly different morphology, due to the ~ 900 K difference in base temperature [149]. Lower temperatures during pulsed heat loading appear to inhibit thermal migration of He vacancies to the surface, and therefore exhibit a more fuzz-like nanostructure. Since surface temperatures on divertor tiles are expected to exceed 1223 K in ITER, any unmitigated type-I ELMs will likely lead to complete fuzz degradation and eventual surface melting and erosion [150].
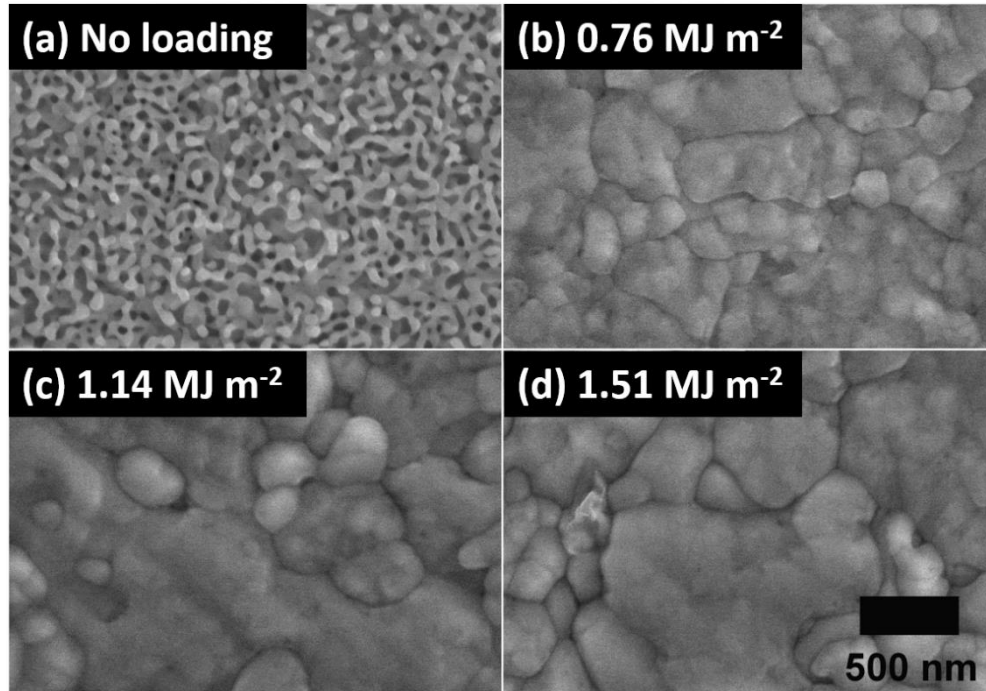
Figure 4.17: Surface microstructure of W fuzz surface after 1000 pulses of laser irradiation at the following intensities: (a) no loading, (b) 0.76 MJ m^{-2}, (c) 1.14 MJ m^{-2}, and (d) 1.51 MJ m^{-2}. Reprinted from [151], with the permission of AIP Publishing.

4.3.4   Analysis of W erosion

Once a melt layer forms on the W surface, splashing and droplet formation can occur. Repetitive heat loading of the molten surface imparts large pressures that shift molten material outward from the center of the exposed area, even in the absence of a magnetic field [152]. As illustrated in previous studies, heat loading of sufficient intensity can move the melt layer so quickly that part of the melt fragments into droplets and leaves the surface [25], [152]. Previous work on pristine W has found distinct energy density thresholds for surface melting and droplet ejection (when other parameters are held constant) and estimated expected erosion due to ELM-like heat loads [15]. In general, pristine W is expected to melt if the heat flux factor (expressed as the product of the power density and the square root of the pulse duration) exceeds 50 MJ m^{-2} s$^{-1/2}$ (at room temperature) [35]. However, the melting threshold will vary with pulse count, base temperature, and surface structuring. Work presented in Chapter 5 discovered that distinct thresholds for melting and erosion do not exist for W surfaces that have undergone helium-induced fuzz formation. Instead, transient heat loading causes the conglomeration of fuzz tendrils under different

energy densities, repetition rates, and pulse counts [94], [95]. The onset of localized melting could lead to unexpected increases in overall erosion. While the normal incidence in the current study does not accurately replicate the grazing incidence expected in ITER [146], the laser-produced plasma during a millisecond time scale was observed to propagate outward, normal to the sample, regardless of the incident angle. Other laboratory experiments that utilize different heat loading methods, e.g., energetic electron beams, result in significant differences in erosion at varying incident angles due to the large differences in penetrations depths and the resulting surface heating. Therefore, the measured splashing of molten material can be assumed to be more relevant to that expected in a fusion device. The current study utilized three different experimental analysis techniques to directly measure the amount of W material lost due to transient heat loading.

Imaging the plasma plume produced by laser irradiation with a CCD camera provided a qualitative metric of surface excitation and splashing. As mentioned previously, the presence of a melt layer does not guarantee that erosion took place. Measuring levels of photon excitation in response to pulsed heat loading helped separate melting and splashing processes as distinct, because melting alone will not cause a large spike in emitted photon intensity. Figure 4.18 shows the resultant plasma plume after the 200th laser pulse at different energy densities (minimum and maximum photon intensities are displayed below each image). No plasma plume was detected for exposures done at 0.38 MJ m^{-2} or 0.76 MJ m^{-2}. The lack of a plasma plume at 0.38 MJ m^{-2} is expected, due to the lack of surface damage, as noted in section 4.3.3. In addition, previous studies have measured the damage threshold for pristine W to be between 0.19 MJ m^{-2} and 0.38 MJ m^{-2} [13], [32]. Despite the addition of a fuzz nanostructure, the comparison is still apt at low intensity (reported intensities reflect energy absorbed). The presence of a plasma plume at 1.14 MJ m^{-2} indicated that melt motion was of sufficient intensity to cause splashing and droplet emission. While both exposures at 0.76 MJ m^{-2} and 1.14 MJ m^{-2} resulted in surface melting, as seen in Figure 4.17, the melt layer formed at 0.76 MJ m^{-2} did not exhibit melt motion of sufficient intensity to cause splashing that could be detected by the camera. The CCD images of the plume do not directly provide information on particle emission, but instead reflect the level of surface excitation due to transient heat loading.
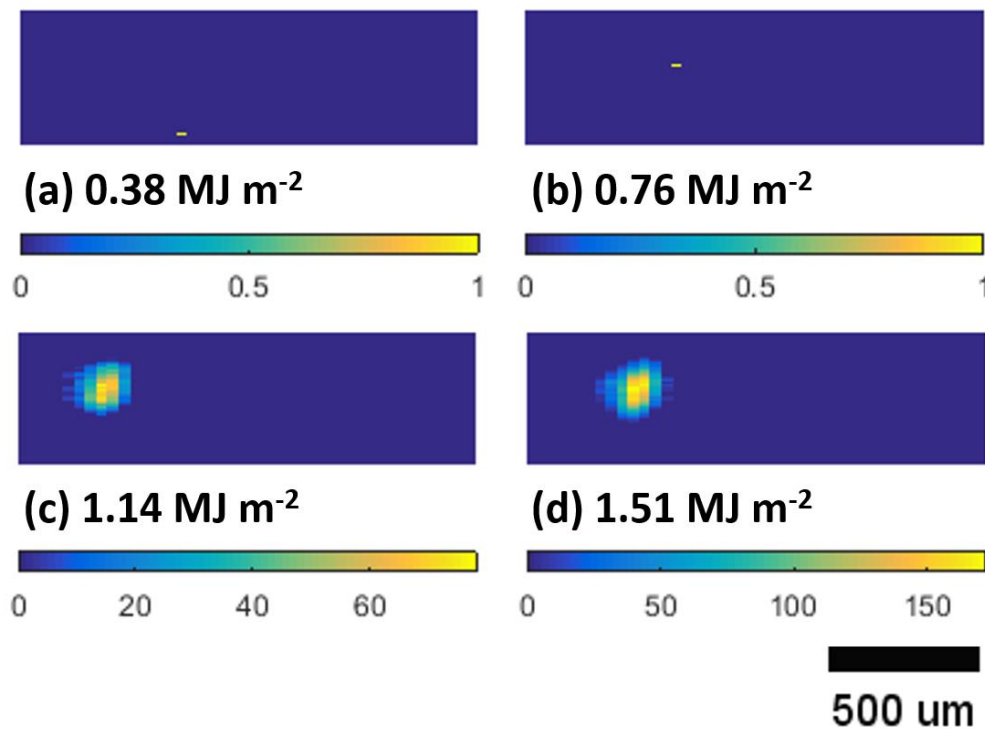
Figure 4.18: Images of plasma plume captured using a CCD camera after 200th laser pulse at (a) 0.38 MJ m^{-2}, (b) 0.76 MJ m^{-2}, (c) 1.14 MJ m^{-2}, and (d) 1.51 MJ m^{-2}. Reprinted from [151], with the permission of AIP Publishing.

The maximum photon intensity increased by a factor of 2 from 1.14 MJ m^{-2} to 1.51 MJ m^{-2}, as seen in Figure 4.19(a), which shows the effect of impact energy on surface excitation and possible droplet formation. The trend observed via CCD imaging reflects previous plasma-surface modeling, where an incident plasma moving with sufficient intensity can fragment the melt layer and cause splashing [152]. The change in maximum intensity as a function of pulse count reveals the role that the changing surface morphology had on emitted photons. Figure 4.19(b) shows that the photon intensity reached a maximum during the first 200 pulses. Decreased thermal strength due to the presence of fuzz tendrils leaded to more intense heating. Once the fuzz structure had been destroyed via surface melting, the thermal strength improved and the emitted photon intensity diminished. Another pulsed heat loading study conducted on nanostructured W measured a significant drop in radiation intensity when the surface reached its melting point [55]. Changes in photon emission as a function of pulse count suggests that future work should investigate how to mitigate ELM parameters to restore the W surface to a pristine state without causing unsustainable levels of erosion.
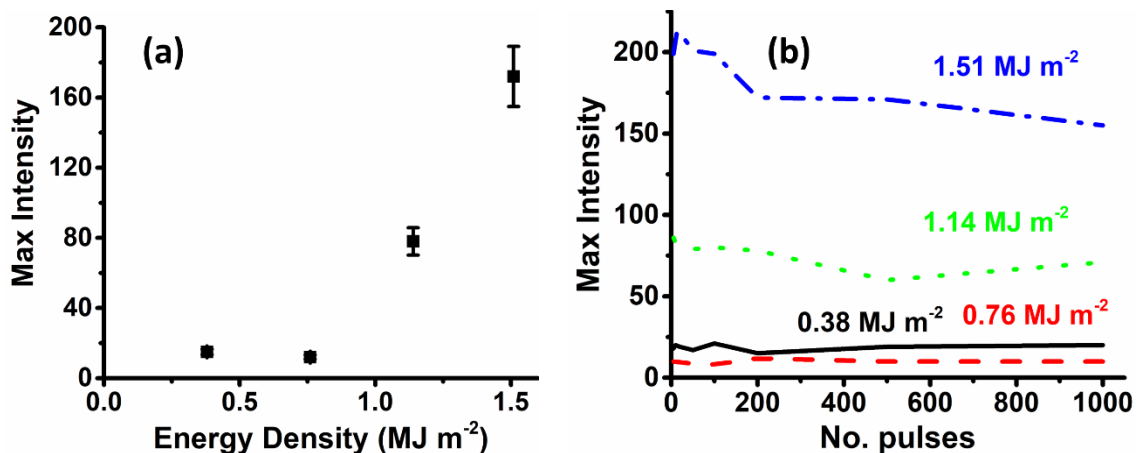
Figure 4.19: Maximum photon intensity of plasma plume as a function of (a) energy density and (b) pulse count for different energy densities. Reprinted from [151], with the permission of AIP Publishing.

Direct measurements of ejected W material using *in situ* methods quantify the healing/destructive response of fuzz nanostructure on overall PFC performance. Low intensity, ELM-like heat loading on W fuzz (< 0.5 MJ m^{-2}) concluded that tendrils reintegrate back into the bulk without causing any material removal [57]. However, experiments performed in Chapter 5 at higher energy densities revealed that deformation of the fuzz nanostructure could be accompanied by significant levels of erosion. The current study utilized a Si witness plate to collect W material that was ejected during transient heat loading. After each exposure, witness plates were removed from the chamber and analyzed via XPS. Survey scans of 0.76 MJ m^{-2} and 1.14 MJ m^{-2} exposures (not pictured) both detected a small W 4f signal on the Si surface. The presence of a W 4f signal in both survey spectra revealed that the fuzz nanostructure might not completely reintegrate into the bulk due to loading in the unmitigated type-I ELM range. Region spectra of the W 4f signal shown in Figure 4.20 reveals an increase in W signal with increasing energy density. Most of the W 4f signal was seen in a WO$_3$ chemical state, due to oxidation of deposited W droplets during system transfer, as discussed in [42]. The presence of a doublet peak was due to a signal from each spin-orbit component, and has been observed in other pulsed heat studies on pristine W [33]. The peaks were identified using Gaussian-Lorentzian curve fitting with commercial CasaXPS software [147]. Increases in the relative magnitude of the W4f $_{7/2}$ (WO$_3$) and W4f$_{5/2}$ (WO$_3$) peaks with an increase in laser energy density revealed an effect of incident photon energy on the intensity of splashing, despite

the similarities in resultant surface morphologies. Further studies are needed to compare the energy density dependence on splashing during and after the destruction of the fuzz nanostructure (at lower pulse counts). Differences in overall erosion seem to only be affected by heat loading while fuzz tendrils are still present along the surface.
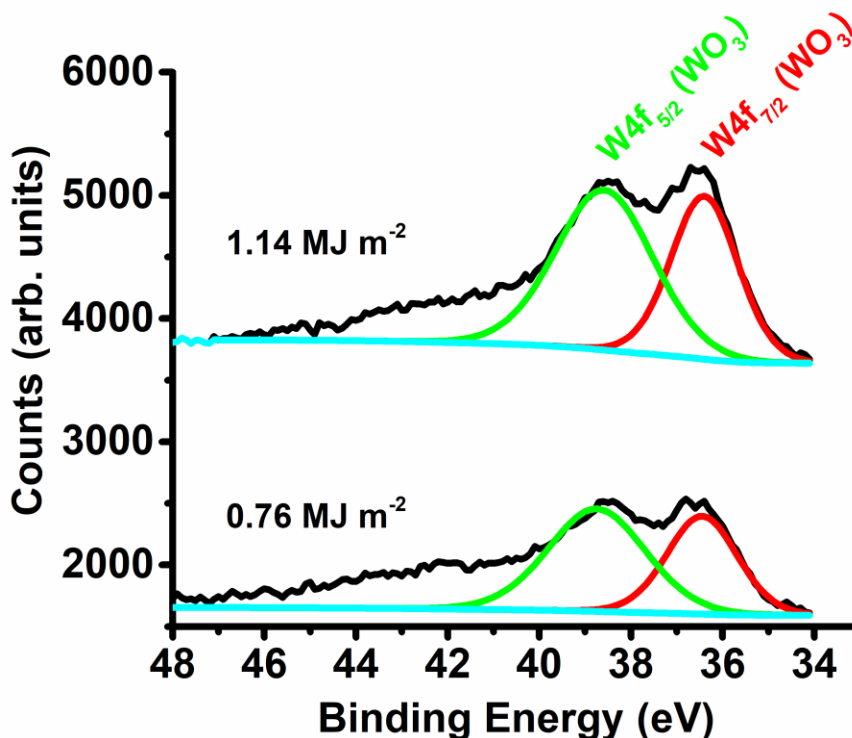
Figure 4.20: XPS region spectra of W 4f doublet peak on Si witness plate after laser exposures at 0.76 MJ m^{-2} and 1.14 MJ m^{-2}. Reprinted from [151], with the permission of AIP Publishing.

QCM mass analysis was also performed to reinforce and validate the Si witness plate XPS analysis. Measuring emitted mass *in situ* eliminates the effect of oxidation on the amount of material detected, as discussed in [42]. The amount of mass deposited onto the QCM crystal during each laser exposure at different energy densities is shown in Figure 4.21. Note that data was not taken for the 0.38 MJ m^{-2} exposure, due to the lack of surface damage. The data was fit to an exponential curve of the form $\Delta m = a * e^{bQ}$, where Δm is the amount of mass deposited, Q is the energy density, and a and b are fitting parameters. The curve fit the data very well, with $R^2 = 0.95$. The exponential increase in deposited mass with increasing energy density reflects other erosion measurements done on both pristine and nanostructured W surfaces (see Chapter 5 for more information) [15].
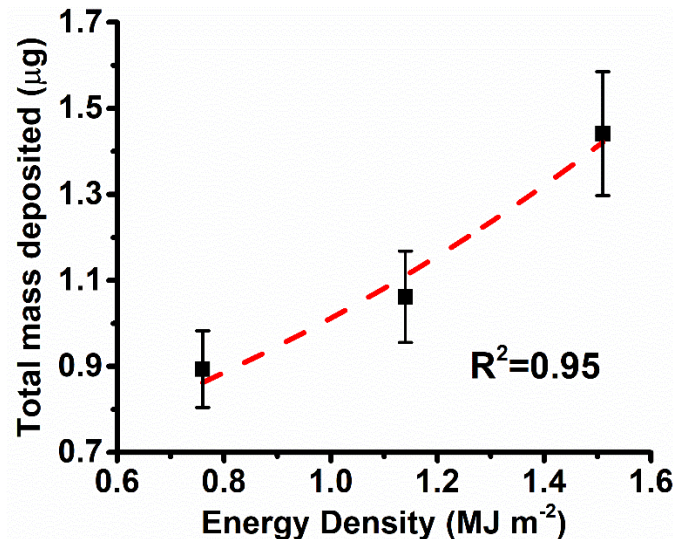
Figure 4.21: Total mass deposited onto QCM after 1000 pulses at different energy densities; dashed line shows exponential curve fit of data. Reprinted from [151], with the permission of AIP Publishing.

In a reactor environment, only a small area of the divertor region will likely be exposed to the intense steady-state and transient heat loading being replicated in the current experiment. When other factors such as spatial changes in ELM intensity and He$^+$ particle flux along the divertor surface are considered, the effective erosion rate will be significantly lower [35], [153]. Local redeposition of eroded material was not considered [75], [154]. Higher plasma pressures in the divertor region ($\sim 10^4$ Pa) will suppress droplet emission, while the presence of a magnetic field will cause gap bridging and leading edges via the J $\times$ B force [73], [155]. Despite the myriad assumptions made in the mass loss estimates, W fuzz clearly undergoes some degree of erosion when exposed to unmitigated ELMs above 0.76 MJ m^{-2}. Performing qualitative comparisons of material splashing and erosion help reveal the effect of fuzz tendril growth on material performance. Performing comprehensive erosion experiments during simultaneous particle and heat loading would be more difficult, but would yield more insight into potential concerns over component lifetime and plasma performance.

4.3.5   Summary

Multiple erosion analysis techniques were used to characterize how helium-induced fuzz nanostructure affects the thermal response of W during ELM-like heat loading. Pulsed laser exposures were conducted at different energy densities in the unmitigated type-I ELM

range to assess surface melting and droplet emission when mitigation fails. Even at 0.76 MJ m^{-2}, 1000 pulses of laser loading destroyed fuzz tendrils and caused significant surface melting. Higher intensity exposures resulted in similar surface morphology. CCD imaging of the plasma plume, resulting from laser irradiation, revealed that the energy of emitted photons after exposure at 0.76 MJ m^{-2} was not high enough to be detected by the camera, despite the observed molten surface morphology in Figure 2. Decreases in the maximum photon intensity after 200 pulses indicated that droplet ejection and surface excitation diminished once the fuzz nanostructure was removed. Future work should examine the pulse count dependence on the deformation and destruction of fuzz tendrils. ELM mitigation techniques, such as pellet injection, could therefore find pacing parameters that would quickly reintegrate the heterogeneous nanostructure without causing intense splashing.

Mass loss measurements made *in situ* were utilized to estimate total erosion at different ELM intensities. The XPS analysis conducted on a Si witness plate confirmed that splashing did occur during pulsed heat loading, even at 0.76 MJ m^{-2}. The relative intensity of the $W4f_{7/2}$ (WO_3) peak increased as the laser energy density was raised above 0.76 MJ m^{-2}. The direct observation of W on the Si witness plate used during transient heat loading at 0.76 MJ m^{-2} suggested that the CCD plume images did not accurately reflect erosion processes. Direct measurements of mass deposition using a QCM confirmed and strengthened the XPS witness plate analysis, indicating that the splashing could increase nonlinearly as the laser intensity increased. Differences in the W signal between 0.76 MJ m^{-2} and 1.14 MJ m^{-2} exposures was likely due to splashing dynamics of the molten W fuzz surface. However, performing experiments at lower pulse counts will be critical in comparing the splashing-induced erosion between a nanostructured and a pristine surface. While more studies are needed to confirm whether the thermal strength of the W surface can be restored due to pulsed heating, the clear presence of splashing imposes additional limitations on acceptable ELM parameters if fuzz formation cannot be avoided. Mitigation techniques need to consider the synergistic effects between particle irradiation and heat loading to ensure optimal performance for ITER and beyond.

4.4   Effect of ELM mitigation on thermal degradation

Mitigation of transient plasma events in a future fusion device is necessary to minimize thermal damage on surrounding plasma facing components (PFCs). Intense heat loading caused by an edge-localized mode (ELM) can lead to melting and splashing of the PFC surface. ELM mitigation involves triggering these events at higher frequencies, which lowers the effective heat flux imparted on the material. Unfortunately, concurrent, high-flux He^+ ion irradiation on tungsten (W), which is the leading candidate material for future PFCs, has been shown to drive the development of an arborescent nanostructure, known as fuzz. Large drops in thermal conductivity and mechanical strength with fuzz formation necessitate a reconsideration of the impact of ELM mitigation on material damage and erosion. Three different types of experiments were designed to characterize the synergistic effect between He^+ ion irradiation and pulsed heat loading (replicated with a pulsed millisecond laser) that is expected in the divertor region.

W samples exposed to pulsed heat loading underwent roughening in the form of a shale-like surface morphology, regardless of frequency. The addition of simultaneous He^+ ion irradiation with pulsed heat loading promoted splashing of molten material and caused significant pore formation. Increasing the frequency to 10 Hz produced a smoother W surface. However, when the total laser power was held constant, increasing the frequency decreased the laser energy density, which significantly decreased surface melting and enhanced early stage fuzz formation. Results obtained raise an important question of whether ELM mitigation parameters can be tuned to anneal out any He-induced surface structuring without causing unsustainable splashing of molten material.

4.4.1   Introduction

Harsh radiation environments impact materials' thermal strength via multiple damage mechanisms that occur simultaneously. PFCs in nuclear fusion reactors, like ITER, must withstand both intense particle and heat fluxes over long periods of time. The divertor region, where non-fuel species are removed from the plasma, contains PFCs that experience particle fluxes $\sim 10^{24}$ m^{-2} s^{-1}, leading to surface deformation and gas implantation [3]. In addition, off-normal plasma events impart intense heat fluxes > 100 MJ m^{-2} that can cause cracking, melting, splashing, and vaporization [13], [20]. Material

loss via splashing and vaporization could potentially cool and terminate the fusion plasma, while also reducing component lifetime [91], [135]. Tungsten (W) has come to the forefront as a leading PFC candidate material due to its high melting point (3695 K), high thermal conductivity, and low sputtering yield (among other desirable properties), which should minimize plasma contamination during reactor operation [16], [114], [156].

One potential problem with utilizing W as a PFC is the observed decrease in thermal and mechanical strength with the growth of helium-induced, fiber-form nanostructures. Recent research performed in various studies have found that a fragile, arborescent nanostructure, commonly known as "fuzz", develops on W surfaces when exposed to low-energy He$^+$ ion irradiation at surface temperatures between 1000 and 2000 K and at ion fluences above 10^{24} m^{-2} [36], [38], [157]. Fuzz formation has also been observed on other refractory metals, with each metal exhibiting a different temperature window for structure formation [42], [43], [45], [47], [158]. While the fuzz formation mechanism is still debated, work done in [41] hypothesizes that growth could be driven by the movement of He bubbles in the near surface layer [41]. Pressurized He bubbles that form at intrinsic traps in the subsurface could be pushing thin W layers away from the surface (material flow enhanced by creep at elevated temperatures), forming fibers. Additional information on other proposed fuzz formation mechanisms can be found in Chapter 1. Fuzz tendrils grown from different He$^+$ ion irradiation experiments [82], [159], [160] have been shown to exhibit poor mechanical strength, and can easily be scraped off the surface [37]. In addition, fuzz tendrils exhibit poor thermal diffusivity, which substantially decreases the thermal conductivity of the W surface [56]. Erosion of the fuzz nanostructure into the fusion plasma, via sputtering and/or splashing (as described below), could lead to significant radiation losses, and shut down the reactor [91], [161]. The high atomic number of W (Z = 74) limits the maximum acceptable atomic concentration in plasma to $\sim 10^{-5}$ [3].

Reductions in thermal strength with fuzz formation only further exacerbate potential melting and splashing of the W surface during transient plasma events. While major disruptions and vertical displacement events (VDEs) impart large heat fluxes onto the surrounding walls, edge-localized modes (ELMs) will occur at a much higher frequency (~ 1 Hz) and are therefore a larger concern when it comes to component degradation [7],

[25], [162]. Type-I ELMs possess the highest heat fluxes (several MJ m^{-2}) over the shortest time scales (0.1 – 1 ms), and have become a focus of recent research on potential melting and splashing in future fusion devices [7], [71]. Pulsed heat loading with millisecond (ms) lasers, electron beams, and plasma accelerators have shown that above a certain energy density, the W surface undergoes sufficient heating to cause surface melting [15], [33], [85]. Repetitive loading of the molten W surface then causes fragmentation of the melt layer, leading to droplet emission [18], [73], [163]. Surface cracking dominates when steady-state heating does not heat the surface above the ductile-to-brittle transition temperature (DBTT) of ~ 600 K [58], [156]; at high temperatures, thermal shocks deform the W material plastically, leading to surface roughening [31], [164]. In ITER-like reactors, W divertor PFCs are expected to exhibit average steady-state temperatures of ~ 1373 K [150]. The addition of He-induced fuzz formation causes larger changes in surface temperature during a thermal shock, due to the decrease in thermal conductivity [55]. The reduced thermal diffusivity of the fuzz nanostructures retard heat transfer to the bulk, and lead to localized tendril conglomeration driven by overheating (as presented in Sections 4.2 and 4.3) [55], [94]. As a result, W fuzz surfaces exhibit melting at lower energy densities and lower pulse counts. Since fuzz formation has been observed in current fusion reactors [37], new methods need to be developed to reduce the intensity of type-I ELMs and protect W PFCs.

Efforts to mitigate type-I ELMs revolve around triggering the transient event at an elevated frequency to reduce pressure buildup along the plasma edge. Mitigation techniques that are currently being developed include pellet injection [10] and external magnetic perturbation [11]. Work performed in [10] achieved a 12× reduction in energy density to the divertor. The ELM frequency, f_{ELM}, is inversely proportional to the ELM energy loss, ΔW_{ELM}:

$$f_{ELM} \times \Delta W_{ELM} = (0.2 - 0.4) \times P_{SOL} \qquad (4\text{-}3)$$

where P_{SOL} is the power ejected into the scrape-off layer (SOL) [165]. Recent reports on ITER have specified that 0.5 MJ m^{-2} will be the maximum allowable energy density during operation, which could increase frequencies above 10 Hz [13], [143]. However, acceptable ELM parameters have not considered the synergistic effects of intense particle loading and

transient heat loading. Reductions in thermal strength due to concurrent fuzz formation are expected to enhance surface melting and droplet splashing.

The study below investigates the effect of the ELM frequency, f_{ELM}, and the growth of helium-induced fuzz nanostructure, on surface morphology and material erosion. ELM-like heat loading exposures are conducted at both *constant energy* and *constant power*, while varying the frequency. Changes in surface morphology at varying f_{ELM} provide an indication of the optimal parameters for mitigated ELMs to avoid surface melting. In addition, simultaneous He$^+$ ion irradiation and pulsed heat loading exposures reveal how reduced f_{ELM} values could help "heal" the fuzz nanostructure without causing splashing. Developing windows of acceptable mitigated ELM operation will minimize thermal fatigue on reactor PFCs.

4.4.2 Experimental setup

Simultaneous He$^+$ ion irradiation and ELM-like heat loading experiments were performed in the UHFI-II facility at the Center for Materials Under Extreme Environment (CMUXE) at Purdue University. All samples were cut from a 2 mm thick W foil of 99.95% purity (Alfa Aesar). The W foil was cold-rolled and annealed, yielding an average grain size of ~ 3 - 4 µm (measured via EBSD) [23]. All samples used in the study measured 10 mm × 10 mm (from the same W foil). The polycrystalline grain structure observed in these samples has been observed in many other W samples used for fusion material testing, and thus serves as an apt reference material. Each sample was then mechanically polished to a mirror finish to ensure a smooth, pristine surface free of impurities.

All experiments conducted in the UHFI-II facility used a combination of steady-state heating, particle loading, and transient heating (refer to the schematic in Figure 4.22). W samples were clamped to a resistive heater that used a feedback loop to maintain a constant temperature of 1223 K to mimic steady-state heating in the divertor region. ELM-like, transient heat loading was replicated using a 1064 nm Nd:YAG pulsed ms laser, due to its ability to impart heating of similar intensities and durations. The flat top spatial profile of the beam ensured even heating over the 1 mm spot size. All exposures utilized a pulse duration of 1 ms, while the frequency, pulse count, and energy density were varied based on the experiment. Due to energy losses caused by using optics for focusing and

transmission (~ 33%), as well as beam reflection at the sample surface (~ 50% on average), reported energy densities reflect the amount of energy absorbed by the sample. 100 eV He$^+$ ion irradiations utilized a grid-less end-hall 'EH' ion/plasma source, producing a flux of 3.0×10^{20} m^{-2} s^{-1}. Utilizing a broad beam ion source minimizes any angular effects due to non-normal incidence; work done in [65] reinforces the minimal impact that grazing incidence in a reactor environment has on fuzz formation at low ion energies.
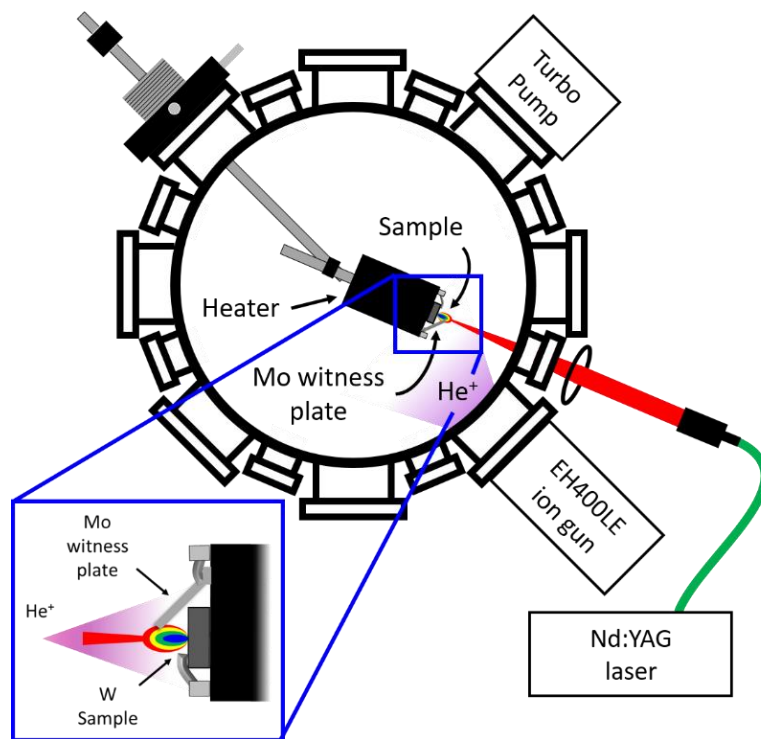
Figure 4.22: UHFI-II experimental setup schematic; inset shows witness plate schematic.

Three different types of experiments were performed to examine the effects of fuzz formation and ELM frequency on material response (summarized in Table 4.2). The first experiment (denoted as "laser only") exposed W samples to 3600 pulses of laser heating at an energy density of 0.76 MJ m^{-2} and repetition rates (or frequencies) of 1 Hz, 2 Hz, and 10 Hz. The total exposure time decreased as the frequency increased. The second experiment (denoted as "laser + He (const. energy))" exposed W samples to simultaneous 100 eV He$^+$ ion irradiation and pulsed ms laser heating for 3600 pulses at a constant energy density of 0.76 MJ m^{-2}, while varying the frequency. Since each irradiation contained 3600 pulses, the total ion fluence was lower at higher repetition rates. The third experiment (denoted as "laser + He (const. power))" exposed W samples to simultaneous 100 eV He$^+$

ion irradiation and pulsed ms laser heating at varying frequencies, keeping the total laser power ($f_{ELM} \times \Delta W_{ELM}$) constant at 0.76 MW m^{-2}. The three different exposures provide insight into how surface structuring due to He bubble migration affects thermal response, and how increasing the ELM frequency under constant power conditions could help mitigate these negative effects.

Table 4.2: Exposure conditions for particle and heat loading experiments

Exp.	Energy Density [MJ m^{-2}]	Frequency [Hz]	No. pulses	He flux [m^{-2} s^{-1}]	He fluence [m^{-2}]
Laser only					
1	0.76	1	3600	0	0
2	0.76	2	3600	0	0
3	0.76	10	3600	0	0
Laser + He$^+$ (const. energy)					
4	0.76	1	3600	3.0×10^{20} m^{-2} s^{-1}	1.1×10^{24} m^{-2}
5	0.76	2	3600	3.0×10^{20} m^{-2} s^{-1}	5.4×10^{23} m^{-2}
6	0.76	10	3600	3.0×10^{20} m^{-2} s^{-1}	1.1×10^{23} m^{-2}
Laser + He$^+$ (const. power)					
7	0.76	1	3600	3.0×10^{20} m^{-2} s^{-1}	1.1×10^{24} m^{-2}
8	0.38	2	7200	3.0×10^{20} m^{-2} s^{-1}	1.1×10^{24} m^{-2}
9	0.076	10	360000	3.0×10^{20} m^{-2} s^{-1}	1.1×10^{24} m^{-2}

Analysis focused on characterizing changes in surface morphology and looking for evidence of droplet splashing due to transient heat loading. A molybdenum (Mo) witness plate was placed inside the vacuum chamber during every exposure to collect any W material that was ejected from the sample surface. Mo was chosen, due to its superior thermal properties in a high temperature environment [16]. The witness plate was placed at 45° relative to the sample plane, as depicted in the inset of Figure 4.22. After each exposure, the Mo witness plate was removed and was characterized via *ex situ* X-ray photoelectron spectroscopy (XPS) with a Mg-Kα source (1253.6 eV) to look for the presence of a W signal. Since molybdenum and tungsten are both refractory metals, and possess similar properties, their XPS peaks overlap. Therefore, analysis remained qualitative, and focused on drawing conclusions on possible material erosion from changes in the shape and skew of the peak in the W4f region. XPS analysis was conducted using commercial CasaXPS software [147]. All W samples were also characterized after

transient heat loading via field-emission scanning electron microscopy (FE-SEM). Evidence of surface structuring and melt layer formation due to different combinations of ion irradiation and pulsed laser irradiation identify windows of mitigated ELM operation that would minimize PFC surface damage and ensure plasma stability.

4.4.3 Changes in surface morphology due to pulsed heat loading at varying ELM frequencies

4.4.3.1 Laser only exposures

Performing baseline experiments with a pulsed ms laser isolated damage mechanisms solely caused by transient heat loading. Figure 4.23 shows SEM micrographs of W surfaces after being exposed to 3600 laser pulses at 0.76 MJ m^{-2}, using varying frequencies. During each irradiation, samples were heated to a base temperature of 1223 K. All samples exhibit significant surface roughening and possess a molten, shale-like
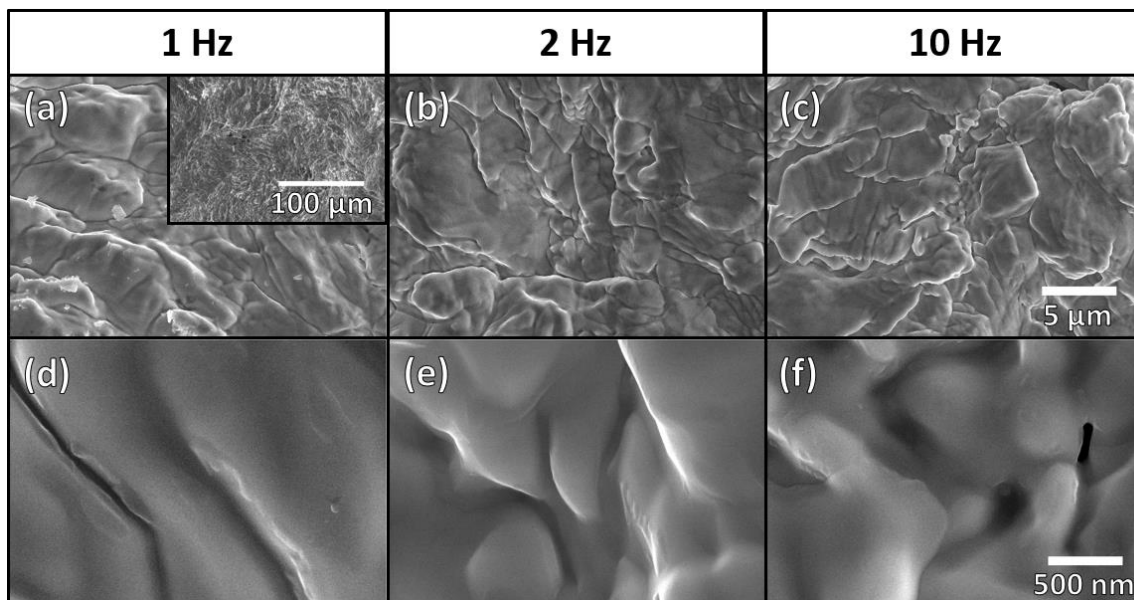
Figure 4.23: SEM micrographs of tungsten surface after laser only exposures at 0.76 MJ m^{-2} for 3600 pulses, at varying repetition rates (frequencies).

microstructure. The similarities between the morphology shown in the inset of Figure 4.23(a) and the elevated temperature exposures (at 673 K) in [28] demonstrate the plastic deformation of the W surface above the DBTT. While higher magnification images of the W surface after irradiation (Figure 4.23(d-f)) revealed that increasing the frequency did not

drastically affect surface deformation, small polishing artifacts seen in Figure 4.23(a) indicated that the lower frequency exposures exhibited lower levels of recrystallization.

The onset of melting on all samples was due to a combination of the high base temperature and the high frequency used in the exposure. IR camera scans performed in [58] found that 2-3 s were required for the W sample to return to its base temperature. Since the inter-pulse time was a maximum of 0.999 s in the current experiment, heating from the previous pulse contributed to the peak temperature for the subsequent pulse, eventually raising the sample temperature above its melting point. Similar shale-like morphologies obtained in [28] reinforce the occurrence of surface melting on pristine W surfaces due to pulsed laser irradiation and steady-state heating.

4.4.3.2 Laser + He$^+$ exposures (constant energy)

Extensive work on low-energy He$^+$ ion irradiation of W and other refractory metals has shown that He-induced nanostructure formation appears to weaken both the thermal and mechanical strength of the near surface layer [55], [56]. Sequentially exposing samples to He$^+$ ion irradiation, followed by pulsed heat loading, provides useful information on the properties of the fully-featured, heterogeneous fuzz structure, but does not accurately replicate conditions in a fusion environment [57]. A single ITER-like plasma discharge could produce up to 10^4 ELMs in addition to steady-state, high-flux He$^+$ ion/plasma loading [68]. Therefore, conducting simultaneous ion irradiation and pulsed heat loading exposures more closely mirrors potential PFC damage mechanisms expected at the strike point during reactor operation.

Figure 4.24 shows SEM micrographs of W surfaces after being exposed to simultaneous He$^+$ ion irradiation and pulsed heat loading at 0.76 MJ m^{-2} for 3600 pulses, while varying the frequency (repetition rate). Utilizing 3600 pulses for each exposure effectively decreased the time of irradiation (and ion fluence) as the repetition rate increased. None of the exposed samples revealed any evidence of fuzz formation, indicating that the periodic thermal shocks were of sufficient intensity to interrupt growth and migration of He bubbles. At low magnification (Figure 4.24(a, b, c)), each surface exhibits a shale-like microstructure, as previously observed in Figure 4.23(a, b, c) and other heat loading studies using similar parameters [23], [145]. However, the addition of

simultaneous He$^+$ ion irradiation to the 1 Hz exposure (Figure 4.23(d) vs. Figure 4.24(d)) appeared to promote the formation of small ripples and surface pores. The formation mechanism behind the surface pores remains unclear, but the observation of surface pores in other simultaneous He$^+$ ion irradiation and pulsed laser heating exposures indicates that the pores could be created during the shock-induced release of trapped gases [23]. Ripples present in Figure 4.24(d) were likely caused by thermal creep driven by the movement of He bubbles near the surface; higher frequency exposures led to enhanced gas desorption, preventing structure growth. Utilizing a higher He$^+$ flux might have caused the formation of the scales seen in [149].
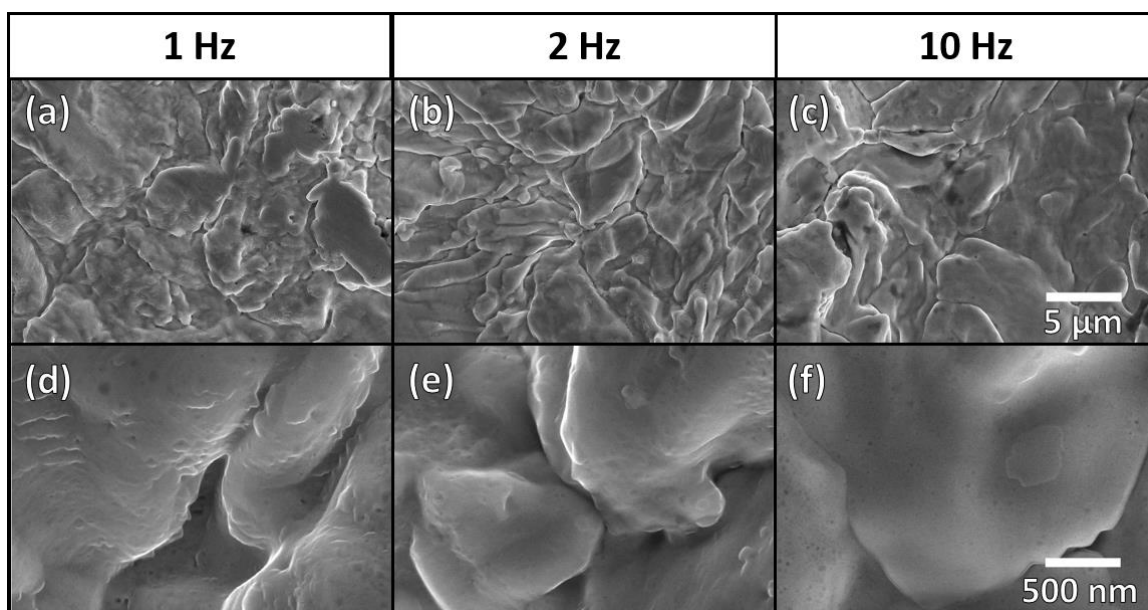
Figure 4.24: SEM micrographs of W surface after simultaneous He$^+$ ion irradiation and pulsed laser loading at 0.76 MJ m^{-2} for 3600 pulses (const. energy), using varying repetition rates (frequencies).

As the repetition rate increased, the W surface became smoother due to enhanced melting. While the shale-like structure apparent at lower magnifications remained consistent at different frequencies, the microstructure at higher magnifications evolved significantly. The ripples observed along the surface from the 2 Hz exposure (Figure 4.24(e)) were not as numerous as the ripples on the surface from the 1 Hz exposure (Figure 4.24(d)). As the frequency increased to 10 Hz, the ripples disappeared completely, because the total ion fluence during laser irradiation decreased and the He that was implanted in the subsurface was immediately desorbed via pulsed heat loading at a rate too high to have

influenced the morphology of the W surface. Therefore, the W surface exposed to 3600 pulses of laser heating at 0.76 MJ m^{-2} and 10 Hz (Figure 4.24(f)) appears smooth and molten. The SEM images of the W surface, however, are insufficient to assess the degree of melt splashing and droplet emission that occurred at different repetition rates.

4.4.3.3   Laser + He$^+$ exposures (constant power)

While changing the repetition rate of the pulsed ms laser during simultaneous exposure provides important information on how higher cycle loading affects PFC response at different frequencies, ELM mitigation techniques will also affect the energy density imparted on the material surface. As stated in Equation (4-3), under constant power, the ELM energy loss decreases as the ELM frequency increases, due to a smaller buildup of pressure within the plasma edge [8], [165]. Currently, the synergistic effects between particle irradiation and transient heat loading on material response are poorly understood at high frequencies and low energy densities.

Keeping the total laser power constant, W samples were exposed to simultaneous He$^+$ ion irradiation and pulsed heat loading at different repetition rates. As the repetition rate increased, the laser energy density decreased accordingly. Unlike the exposures in section 4.4.3.2, every W sample was subjected to the same total He$^+$ ion fluence. SEM micrographs of the W surfaces after irradiation are shown in Figure 4.25. The W surface shown in Figure 4.25(a, d) is the same as the surface shown in Figure 4.24(a, d), since the 1 Hz repetition rate was used as the baseline. Doubling the frequency to 2 Hz reduced the laser energy density to 0.38 MJ m^{-2}, which significantly increased pore formation and promoted early-stage fuzz formation. Similar early-stage fuzz formation has been observed on other refractory metals exposed to He$^+$ ion irradiation only [66], indicating that the laser energy density was too low to cause significant thermal roughening of the surface. The lack of laser-induced damage agrees with other research that has measured the damage threshold on pure W exposed to 100 thermal shocks to be between 0.19 and 0.38 MJ m^{-2} [148]. Work performed in [57] proposed that ELMs of a certain intensity could heal a fuzzy W surface without causing any erosion. Pulsed heat loading at 0.38 MJ m^{-2} and 2 Hz appeared to inhibit fuzz formation (Figure 4.25(e)), but SEM images cannot deduce whether significant particle emission took place (erosion analysis is presented in section

4.4.4). Further increasing the frequency to 10 Hz removed any sign of thermal damage on the W surface (Figure 4.25(c, f)). At 10 Hz, the adjusted energy density was 0.076 MJ m^{-2}, which is significantly below the damage threshold quoted by other characterization studies [26], [28], [148]. Mechanical scratches on the surface from sample polishing were not affected (Figure 4.25(c)), and fuzz formation was not interrupted (Figure 4.25(f)). Evidence of early-stage fuzz formation can be observed, and higher fluence irradiations would likely form fully-developed fuzz nanostructures. Increasing the frequency by a factor of 10, while leaving the total power constant, drastically reduced the degree of thermally-induced material damage. However, reducing the intensity of thermal shocks lets He-induced fuzz formation occur uninhibited, which could lead to enhanced erosion if mitigation were to fail. Finding ELM mitigation parameters that prevent both ion-induced structure formation and surface melting and splashing would help ensure device stability during operation.
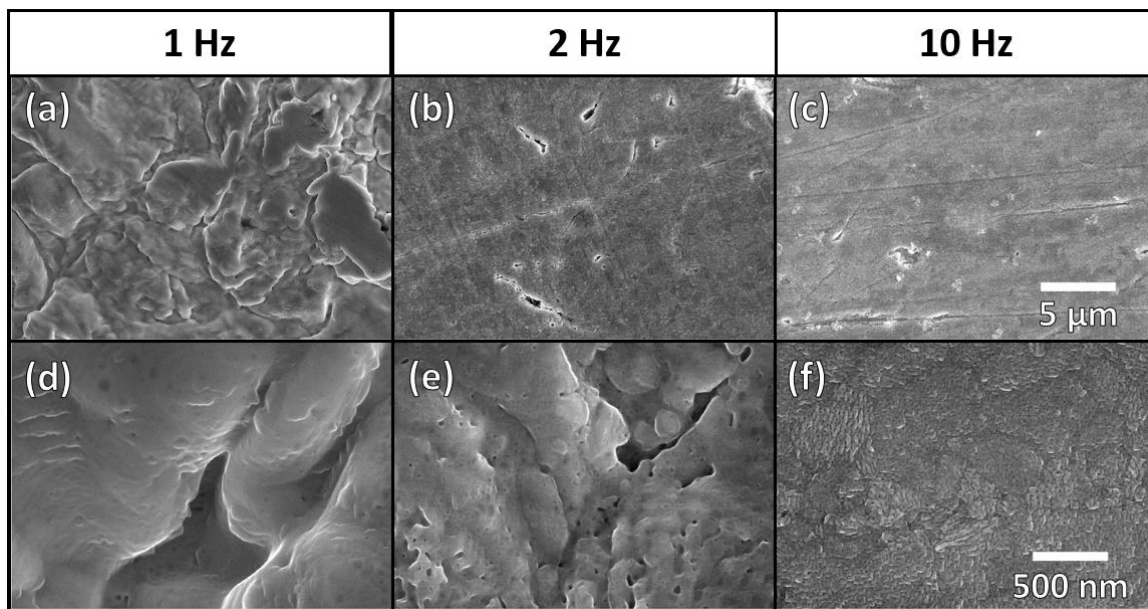
Figure 4.25: SEM micrographs of W surface after simultaneous He$^+$ ion irradiation and pulsed laser loading at 0.76 MJ m^{-2} (const. power), using varying repetition rates (frequencies).

4.4.4 Measuring material erosion at varying ELM frequencies

Predicting the lifetime of PFCs made from W or other proposed refractory metals is ultimately dependent on the rate of material erosion. During reactor operation, mass loss could be due to physical sputtering or to fragmentation of molten surface layers from

splashing [17], [152]. Intense loading during transient plasma events will cause erosion via droplet ejection if significant melting has occurred [68]. A qualitative assessment of the presence of and trends in W mass loss was performed by placing Mo witness plates in front of the W samples during transient heat loading exposures. Mo witness plates were then scanned via XPS after irradiation to measure the surface composition. Survey scans of all the witness plates (figure not shown) contained Mo, C, and O peaks, which were to be expected, since the XPS data was taken using *ex situ* methods. However, the survey scans did not clearly show the presence of W, due to the overlap of the W 4f signal and the Mo 4p signal. Figure 4.26 shows high-resolution scans of the W 4f signal and the Mo 4p signal for a pristine Mo witness plate, a pristine W surface, and the two 1 Hz exposures ("laser only" and "laser + He (const. energy)"). The locations for the pristine form of the Mo $4p_{3/2}$ peak and the MoO_2 form of the Mo $4p_{3/2}$ peak are indicated by red, dashed lines. The locations for the pristine forms of the W $4f_{7/2}$ and the W $4f_{5/2}$ peaks are also denoted by blue, dashed lines; the oxide peaks were not denoted due to their overlap with the Mo 4p peaks. The spectrum for the laser only exposure at 0.76 MJ m^{-2} and 1 Hz was very similar to the pristine Mo spectrum, showing that the surface melting seen in Figure 4.23(a, d) was not significant enough to cause any splashing. However, the simultaneous laser irradiation and He$^+$ ion irradiation exposure did yield distinct pristine W 4f signals (indicated by dashed lines), despite a similar shale-like surface morphology. While peaks representing the oxide forms of the W 4f signals would accompany the pristine W 4f peaks, they were difficult to resolve due to their overlap with the Mo $4p_{3/2}$ peaks. Nevertheless, the presence of the W $4f_{7/2}$ and W $4f_{5/2}$ peaks from the combined particle and heat loading exposure indicated that concurrent He$^+$ ion irradiation significantly reduced the thermal properties of the W surface, which increased the melt layer and caused splashing and droplet emission.
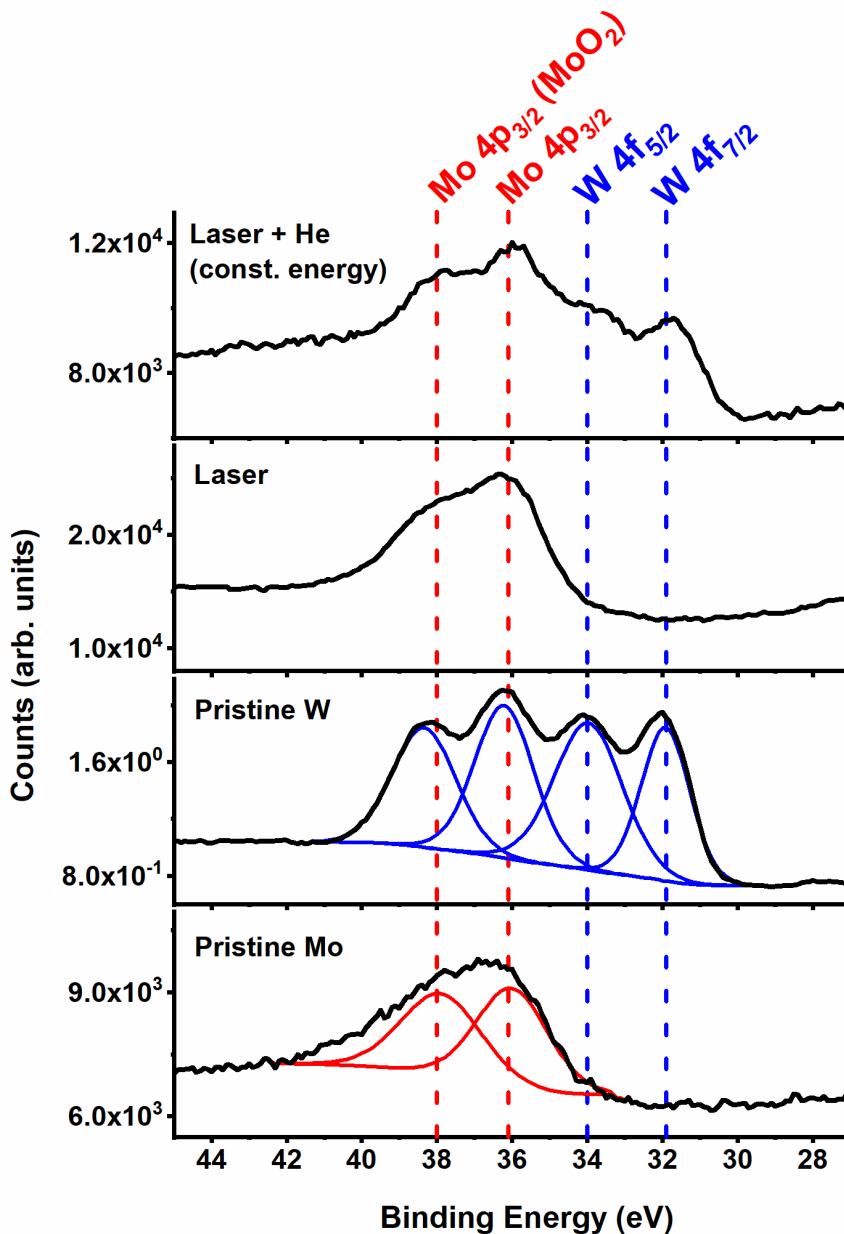
Figure 4.26: XPS region spectra of W 4f and Mo 4p signals on Mo witness plates from 1 Hz, 0.76 MJ m^{-2} exposures.

Examining changes in mass loss at different repetition rates (ELM frequencies) while keeping the total power constant provides valuable insight into how to minimize component damage during ELM mitigation in a fusion environment. Figure 4.27 shows XPS region scans of the W 4f signal and the Mo 4p signal from Mo witness plates after simultaneous He$^+$ ion irradiation and pulsed laser irradiation at a constant laser power and varying repetition rates (pristine Mo and pristine W spectra are also shown as a reference).
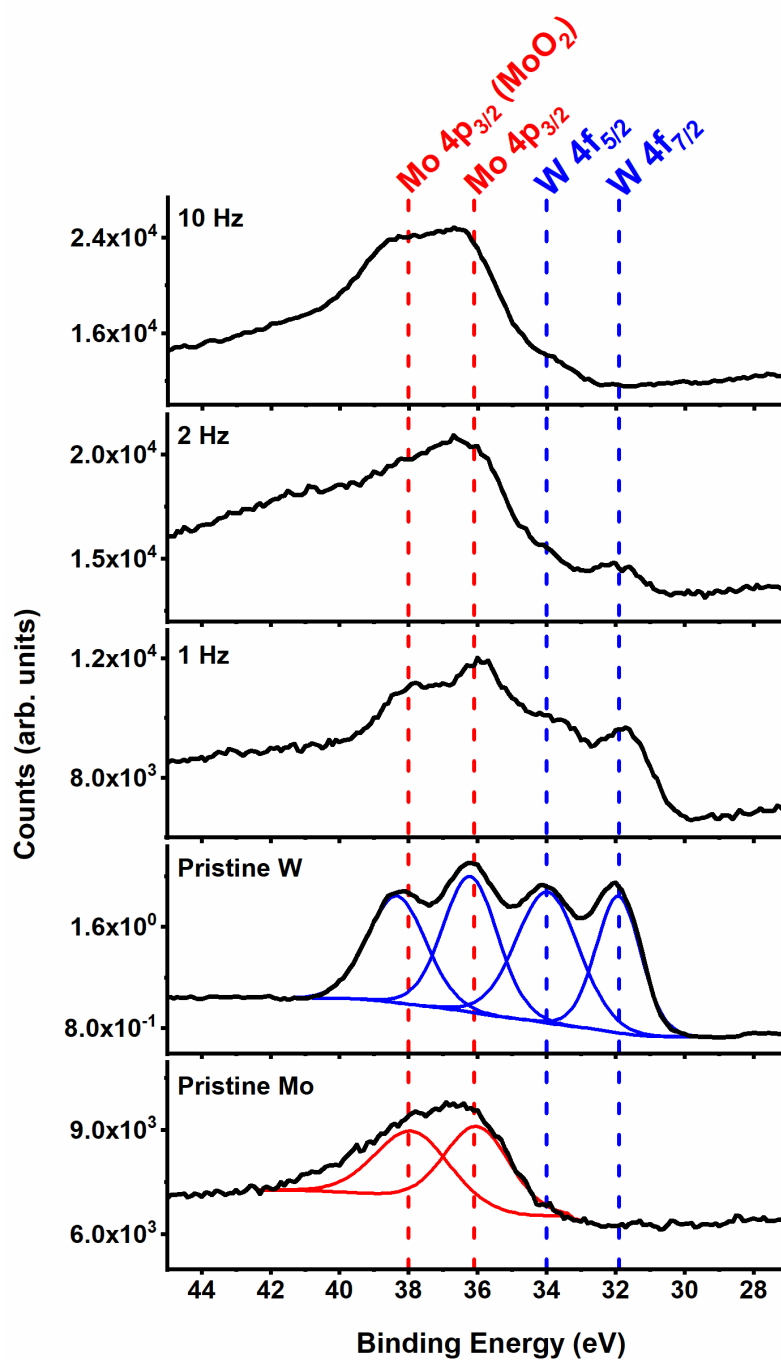
Figure 4.27: XPS region spectra of W 4f and Mo 4p signals on Mo witness plates from simultaneous He$^+$ ion and laser irradiations at a constant laser power.

As the repetition rate of the laser increased, the energy density of the laser decreased accordingly. At 2 Hz and 0.38 MJ m^{-2}, a small but distinct W 4f signal was present, which showed that some degree of splashing did occur, despite the early-stage fuzz morphology

seen in Figure 4.25(e). Sequential He$^+$ ion irradiation and transient heat loading applied in Pilot-PSI at 0.5 MJ m^{-2} did not yield any measurable erosion, proposing that the W fuzz structure had been reintegrated, or healed [57]. The lack of a W 4f signal at 10 Hz and 0.076 MJ m^{-2} is expected, due to the incredibly low laser intensity being used and the lack of any thermal damage, as seen in Figure 4.25(f). Similar exposures performed in [85] on pristine W surfaces found no signs of damage at 0.07 MJ m^{-2}. Looking forward, comprehensive studies need to examine if preventing ELM-induced damage at the cost of preserving ion-induced damage (e.g. fuzz formation) by mitigating ELMs to high frequencies and low intensities will optimize component lifetime. Current concerns over the potential failure of ELM mitigation could cause enhanced erosion of an ion-damaged surface [14]. Developing mitigation parameters that "heal" the undesirable fuzz nanostructure from the W surface would protect against large impurity radiation during an unmitigated ELM event and maximize plasma performance in future fusion devices.

4.4.5   Summary

Simultaneous He$^+$ ion irradiation and pulsed laser loading on W surfaces at different laser frequencies revealed that He-induced nanostructuring strongly influences changes in surface morphology and erosion. Transient heat loading at an energy density of 0.76 MJ m^{-2} caused surface roughening in the form of a shale-like microstructure. SEM images taken at high magnification revealed that the addition of concurrent He$^+$ ion irradiation led to pore formation and the ripple growth. Further cross-sectional analysis is needed to fully characterize the ripples that developed along the surface, but pore formation was likely an artifact of thermal shock-induced He desorption. XPS analysis of Mo witness plates discovered that the addition of He$^+$ ion irradiation also caused a measurable amount of W erosion. While fully-grown W fuzz has been found to lower the thermal conductivity and enhance surface melting, more research is needed to fully understand the effect of He particle loading on thermal strength. Increasing the laser frequency (or repetition rate), while keeping the energy density constant, produced a smoother surface, while maintaining a shale-like morphology. Additional experiments kept the total laser power constant, increased the repetition rate, and decreased the energy density to replicate the impact of ELM mitigation on material response more accurately. As the frequency of laser irradiation

increased, He-induced fuzz formation became more dominant, due to the decrease in thermal annealing. However, exposing W samples to simultaneous He$^+$ and laser irradiation at 2 Hz and 0.38 MJ m^{-2} still led to a small amount of W erosion. While the primary goal of ELM mitigation is to minimize thermal damage on the material surface, future research should also investigate whether ELM mitigation could both prevent splashing of molten material and anneal out He-induced fuzz nanostructure. Mechanisms behind the growth and migration of He bubbles in the subsurface need to be further refined to understand how to inhibit tendril growth. Preventing large changes in the thermal and mechanical strength of W as a plasma-facing material would extend component lifetime and ensure plasma stability during operation.

4.5   Effect of grain orientation on material plasticity and gas trapping dynamics

Qualifying the expected performance of W divertor surfaces in an ITER-type device is only valid for materials that underwent similar forging and processing. While W has is currently the leading candidate material for PFCs, the thermal and mechanical strength of W components will vary significantly depending on the microstructure. Thermal shock tests found that orienting the grain perpendicularly to the loaded surface prevents the formation of parallel cracks due to ELM-like heat loading, which inhibit heat transfer to the bulk. Transversally-oriented W also exhibits very minimal surface roughening when exposed to high heat fluxes. However, testing of oriented W microstructures have not yet considered the effect of high-flux particle loading on material properties. Changes in the growth and rigidity of He-induced nanostructures with grain orientation were therefore explored.

In this experiment, ELM-like heat loading was applied to two different types of W materials with and without pre-exposure to high-flux, low-energy He$^+$ ion irradiation. Cold-rolled and annealed W with longitudinally-oriented grains that is used throughout this dissertation was tested, as well as ITER-grade W with transversally-oriented grains. Longitudinally-oriented W samples possess grains that are parallel to the loaded surface, and were tested in this study to indicate the accuracy to which testing performed throughout this dissertation informs potential performance in a fusion environment. Pulsed heat loading was done in the mitigated ELM regime, at an intensity of 0.5 MJ m^{-2}. In the absence

of He$^+$ ion irradiation, surface damage was only observed on ITER-grade W, revealing minimal degrees of recrystallization and grain growth. The addition of He$^+$ ion irradiation significantly enhanced stress in the material lattice, resulting in widespread crack formation on ITER-grade W samples. Both types of W materials exhibited similar fuzz nanostructures due to He$^+$ ion irradiation, and comparable levels of fuzz conglomeration due to pulsed heat loading. The longitudinally-oriented W samples did not undergo cracking, and instead experienced plastic deformation within the heat-loaded area. Drastic increases in brittle failure on ITER-grade W with the addition of He$^+$ ion irradiation were likely due to radiation hardening caused by preferential nucleation of He bubbles at grain boundaries. W surfaces with transversally-oriented grains are therefore likely to undergo higher degrees of cracking than what is predicted throughout this dissertation and in previous, external research. Careful analysis on the influence of grain orientation on irradiation-enhanced brittleness need to be conducted to further inform PFC design.

4.5.1 Introduction

Selecting the right material for reactor PFCs depends on not only which material is used, but how a material is processed. As discussed in section 1, high-Z materials have recently come to the forefront for use in the divertor region. The combination of intense particle fluxes ($\sim 10^{24}$ m^{-2} s^{-1}) and steady-state heat fluxes ($\sim$ 10-20 MW m^{-2}) demand the use of a material with both high thermal and mechanical strength [3], [25]. The additional impact of ELMs will impart heat fluxes exceeding 10 MJ m^{-2} on divertor surfaces [72]. Low-Z materials (e.g. carbon) were previously considered for divertor PFCs, due to their low radiation losses and favorable thermal properties [4], [166]. However, unsustainable levels of physical and chemical erosion, large T co-deposition, and significant neutron activation have raised serious concerns over the use of carbon-based materials in an ITER-type device [156]. In contrast, high-Z materials, such as W, Mo, and Ta, exhibit low levels of sputtering, low chemical erosion, and low T retention [16]. While many high-Z, refractory metals possess similar properties, W is currently the leading candidate due, in part, to its comparatively higher melting point and thermal conductivity [16]. In 2013, the ITER Organization changed the planned divertor material to W [167], [168]. Various

studies discussed in [35] and [13] effectively summarize the research that has been conducted on the use of W as a divertor PFC material.

While W might exhibit superior thermal shock performance to other candidate materials, the methods by which W divertor plates are manufactured and processed will have a significant impact on the ultimate surface response. During an ELM event, intense heat loading of the surface will impart significant stress on the lattice; shock-induced fracture is expected to occur first at the grain boundaries within the material [169]. Significant research has been conducted on randomly oriented microstructures, and how the average grain size influences the material response [29], [170]–[172]. The use of nanocrystalline materials (with grain size < 100 nm) has been shown to increase ductility and enhance radiation resistance (to He^+ plasma loading) [173], [174]. However, lower heat flux thresholds for recrystallization with smaller grain sizes are thought to enhance material degradation and overheating during transient ELM loading [29]. W divertor surfaces therefore need to be manufactured to minimize damage due to both particle and heat loading. Recent research has focused primarily on the impact of grain orientation on high heat flux performance. Three different types of grain orientations were investigated in [32]: longitudinal (L), transversal (T), and recrystallized (R). The orientations were classified based on the plane of the loaded surface (L = parallel to the loaded surface, T = perpendicular to the loaded surface). Mechanical testing discovered that the L orientation exhibited the highest strength, while the R orientation underwent the highest degree of plastic deformation [32]. Although the T-oriented sample was very brittle, ELM-like heat loading with a pulsed electron beam revealed that the transversal grain orientation performed the most favorably [32]. Other studies performed in [31], [164], and [175] also observed that the T orientation maximizes long-term thermal strength by suppressing the formation of cracks parallel to the loaded surface and plastic deformation along the surface. Parallel cracks observed on L and R oriented samples in response to high heat flux loading create a thermal barrier that would retard diffusion of incident heat to the bulk and promote overheating and eventual melting [31]. In addition, poor cohesion between grains in the R oriented sample was observed during cross-sectional analysis, which raises the concern for complete grain exfoliation during reactor operation [31]. Based on the results of thermal

shock exposures on differently oriented materials, the ITER Organization officially decided to use transversally-oriented W for the divertor tiles [31].

While the transversal grain orientation shows preferential behavior due to intense heat loading expected during ELM events, the combined effect of particle loading on material performance has not been comprehensively investigated. Simultaneous ELM-like pulsed laser heating and deuterium plasma loading at a laser power density of 0.38 GW m^{-2} revealed that deuterium blisters were much larger on the L-oriented sample than those formed on the T-oriented sample [176]. While cracks appears on both samples, the L-oriented sample also underwent significant thermal roughening [176]. Similar experiments performed in [177] concluded that the cracking threshold was selectively reduced on T-oriented samples due to hydrogen embrittlement at trapping sites. The current lack of research into the influence of grain orientation on the synergistic effects between high-flux particle loading and ELM-like heat loading raises concerns over whether transversally-oriented W would still be the highest performing in an ITER-type device.

The experiment below compared the material response of differently oriented W microstructures when exposed to sequential He$^+$ ion irradiation and ELM-like pulsed laser heating. Exploring the role of grain orientation on the growth and subsequent degradation of He-induced fuzz formation provided insight into how the microstructure could be altered to curtail unfavorable structure formation and minimize surface melting. Radiation exposures were conducted on longitudinally-oriented, annealed W and transversally-oriented, ITER-grade W. Pre-characterization of the microstructures revealed distinct differences in material strength. He$^+$ ion irradiation was conducted to induce fuzz formation. Then, ELM-like heat loading was applied at the maximum type-I ELM intensity expected in ITER for differing pulse counts. Some W samples were only exposed to pulsed laser loading, so that surface damage could be properly attributed to either particle loading or heat loading. Post-mortem analysis focused on characterizing the degradation of fuzz nanostructures and the mechanisms of material failure due to intense thermal shocks. Changes in surface evolution with increasing pulse count were also investigated to examine the time dependence of material performance in a reactor environment. Further research on the influence of grain orientation on material performance in a fusion environment is needed to ensure success for ITER and beyond.

4.5.2   Experimental setup

Sequential low-energy He$^+$ ion irradiation and pulsed ms laser irradiation experiments were conducted on W materials in the UHFI-II facility at the Center for Materials Under Extreme Environment (CMUXE) at Purdue University. To examine the effect of grain orientation on thermal and mechanical strength, two different types of W materials were investigated. Cold-rolled and annealed W foils (Alfa Aesar, 99.95% purity) of 2 mm thickness were used as a control material. These samples exhibited longitudinally-oriented grains. Previous EBSD measurements (data not shown) measured an average grain size of 3-4 µm [23]. Since all other experiments performed throughout this dissertation (excluding Mo studies) utilize the same grade of W, the material was used for the current experiment to function as a baseline for comparison. These W samples will hereafter be denoted as "L-W" due to their grain orientation. W samples of 2 mm thickness with a transversal grain orientation were also tested (Plansee AG, 99.5% purity, donated by Forschungszentrum Jülich). These W samples were produced by a combination of powder metallurgy and subsequent sintering at 2273-2773 K [28]. W samples were then be rolled into rod-like geometries, with grains oriented perpendicularly to the loaded surface (transversal) [28]. Grains were approximately 100 µm long and 40 µm wide [28]. The manufacturing process met the ITER material specifications, and serve as a close approximation of the final material that will be used in the ITER divertor region [178]. Therefore, the transversally-oriented samples will hereafter be denoted as "T-W." 10 mm × 10 mm samples were cut and mechanically polished to a mirror finish to remove surface imperfections. Rockwell Hardness (RWH) testing was performed on both types of materials to obtain comparative information on mechanical strength.

Two different types of experiments were performed to isolate surface damage due to pulsed heat loading and surface damage due to high-flux particle loading. The experimental parameters used for each exposure are listed in Table 4.3. A schematic of the experimental setup for each type of exposure is shown in Figure 4.28. Half of the W samples were exposed to 100 eV He$^+$ ion irradiation using a gridless end-hall 'EH' ion/plasma source at a flux of 5.3×10^{20} m^{-2} s^{-1} and a fluence of 1.91×10^{24} m^{-2}. Utilizing a broad beam ion source minimized spatial variations in flux across the sample surface. During ion irradiation, W samples were clamped to a resistive button heater that elevated

the surface temperature to 1223 K to induce fuzz formation. A PID controller was used to maintain a constant temperature during the irradiation. All W samples were then exposed to ELM-like heat loading using a pulsed 1064 nm Nd:YAG ms laser. The intensity and duration of laser heating closely replicated the heat fluxes expected during an ELM event in an ITER-type device. The accuracy with which a pulsed ms laser replicates heat loading during an ELM event is further explored in Chapter 5. The beam exhibited a flat top spatial profile, which resulted in even heating across the exposed area. All pulses were 1 ms in duration and were imparted on the W surface at a repetition rate of 1 Hz. The energy density (H_{THL}, units of MJ m^{-2}) absorbed by the surface was used as the primary metric of laser intensity. Beam optics used to focus the laser spot to 1 mm in diameter resulted in a $\sim$ 17% loss in pulse energy. Additional energy losses occurred at the sample surface, where incident photons were reflected based on the surface reflectivity. Optical reflectivity measurements of He$^+$ ion irradiated and pristine surfaces (as described in Section 2.5.5) yielded reflectivities of $\sim$ 50% and 0%, respectively. Due to the gradual increase in reflectivity of a fuzzy surface due to subsequent pulsed ms laser irradiation observed in Section 4.2.5, maintaining a constant absorbed energy density would be very difficult. Therefore, an average reflectivity of 20% was utilized for laser irradiation of fuzzy surfaces. Reported values of H_{THL} reflect the remaining photon energy that was absorbed. A constant H_{THL} value of 0.5 MJ m^{-2} was used to replicate the maximum expected ELM intensity in ITER if mitigation techniques are successful [143]. By purposely triggering ELMs at an elevated frequency, the plasma energy lost per event would decrease, resulting in lower intensity thermal shocks on divertor surfaces [143], [179]. Further research on the effect of ELM mitigation on thermal damage and erosion can be found in Section 4.4. Conducting experiments in the mitigated ELM regime will continue to improve predictions on expected divertor performance.

Table 4.3: Experimental parameters for particle loading and heat loading exposures.

Exp.	Material	H_{THL} (MJ m^{-2})	No. pulses	He$^+$ flux (m^{-2} s^{-1})	He$^+$ fluence (m^{-2})
1	L-W	0.50	100	0	0
2	L-W	0.50	1000	0	0
3	T-W	0.50	100	0	0
4	T-W	0.50	1000	0	0
5	L-W	0.50	100	5.3×10^{20}	1.91×10^{24}
6	L-W	0.50	1000	5.3×10^{20}	1.91×10^{24}
7	T-W	0.50	100	5.3×10^{20}	1.91×10^{24}
8	T-W	0.50	1000	5.3×10^{20}	1.91×10^{24}

A multitude of surface analysis techniques were utilized to both qualitatively and quantitatively evaluate the effect of grain orientation on thermal strength. Scanning electron microscopy (SEM) effectively characterized the general morphology of irradiated surfaces and revealed the brittle versus ductile behavior of the material under different conditions. Optical profilometry via white light interferometry provided useful quantitative information on the degree of plastic deformation caused by ELM-like heat loading on various surfaces with and without the added presence of He-induced fuzz nanostructures. Depth profiling of the exposed spot obtained using optical profilometry also effectively illustrated the qualitative differences in irradiated surfaces between material types. Characterizing the differences in surface response between longitudinally-oriented W used throughout the dissertation and ITER-grade W show the effect of oriented structures on thermal strength and indicate the accuracy to which the experiments presented throughout this document will predict material performance in a fusion environment.
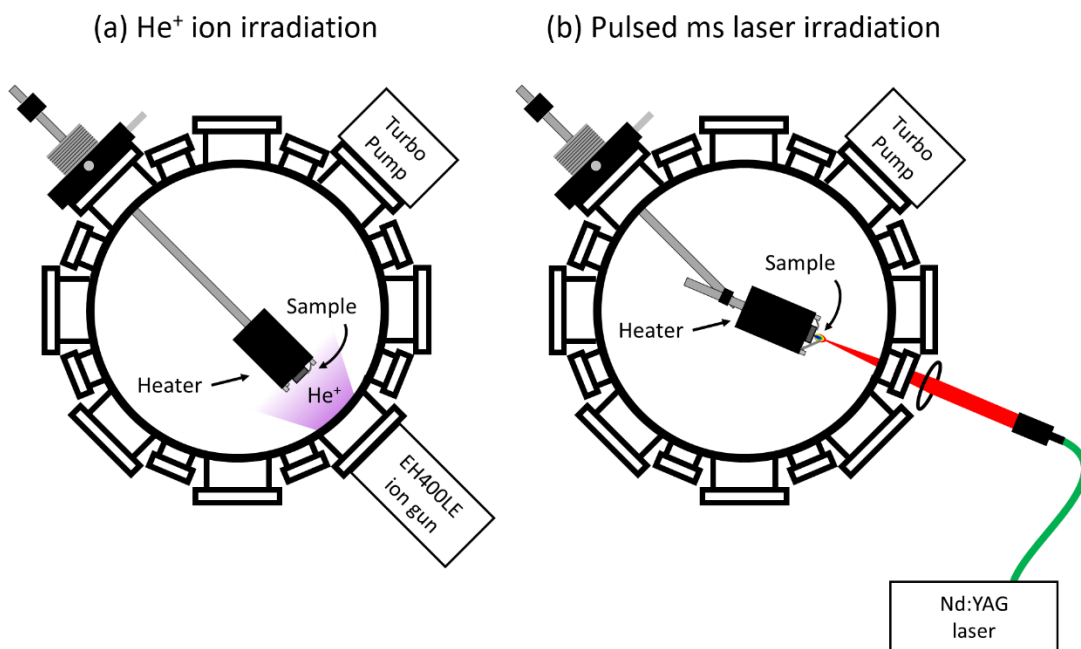
Figure 4.28: UHFI-II facility; (a) He$^+$ ion irradiation setup schematic and (b) pulsed ms laser irradiation setup schematic.

4.5.3 Results and discussion

Prior to radiation exposures, the mechanical strength of L-W and T-W samples was investigated via Rockwell Hardness (RWH) testing. Five tests were performed on each material with a 1/16" ball penetrator and a 100 kg major load (B scale). Indented diameters were measured using a light microscope and averaged for each material. As shown in Table 4.4, the average RWH value was slightly larger for the L-W than the T-W, which was likely due to the presence of grain boundary weak points that are parallel to the applied stress vector. Higher levels of brittle deformation on T-W samples contributed to a larger indented diameter. The Brinell hardness was also calculated for each material, based on the applied force (981 N) and the indented area. Both materials possessed Brinell hardness values that were similar to what has been reported elsewhere for W, confirming the accuracy of the RWH tests [180]. Finally, the ultimate tensile strength (UTS) was found for each material based on RWH value, using a Hardness Conversion Chart in [181]. A higher UTS value for the L-W samples indicated that the presence of longitudinally-oriented grains increased the material's resistance to deformation. Tensile tests performed

in [32] revealed that a sample with longitudinally-oriented grains exhibited a larger ultimate tensile strength than that of a sample with transversely-oriented grains. The observation of small cracks along the periphery of indented spots on the T-W sample further reinforced the material's relative weakness to brittle fracture.

Table 4.4: RWH Test Results

Material	RWH (B)	Indented diameter (mm)	Brinell Hardness (MPa)	Ultimate Tensile Strength (MPa)
L-W	113.5	0.7596041	2164.734	1365.162
T-W	110.5	0.7989335	1956.851	1206.583

SEM micrographs of the polished microstructure and cross section for both L-W and T-W are shown in Figure 4.29. Images of the surface (Figure 4.29(a & b)) revealed a similar grain size between materials, but cross-sectional images (Figure 4.29(c & d)) illustrated the clear difference in grain orientation and the extended length of grains on T-W samples. Additional characterization of the cross-sectional plane via electron backscatter diffraction (EBSD) would effectively quantify the differences in microstructure between the two W materials.
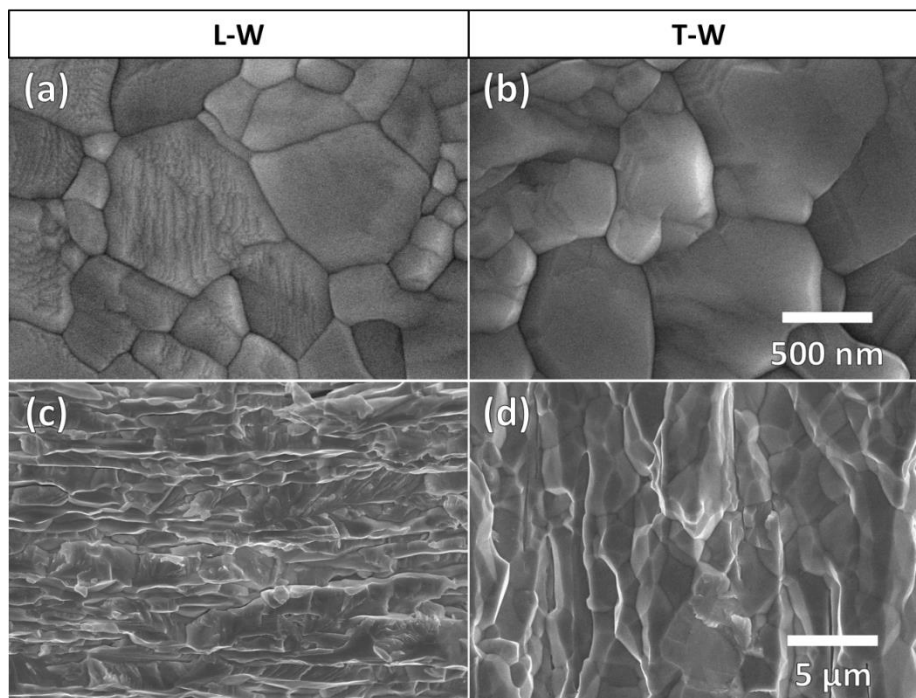
Figure 4.29: SEM micrographs of pristine surface and cross section for both W materials

Pulsed laser heat loading was applied to both types of materials without additional He$^+$ ion irradiation to isolate mechanisms of surface damage caused by thermal shocks. Both L-W and T-W samples were exposed to 100 and 1000 laser pulses at 0.5 MJ m^{-2}, while being heated to a base temperature of 1223 K to replicate steady-state heating expected in the divertor region [19]. Post-irradiation surface analysis revealed that the L-W samples did not undergo any observable surface damage. While previous studies have observed a lower threshold for thermal damage (~ 0.38 MJ m^{-2}), the tests were performed on a different type of W material [148]. Small changes in the forging and working of different W samples could have been responsible for the apparent 0.12 MJ m^{-2} discrepancy in the damage threshold. Variations in other heat loading parameters (pulse duration, repetition rate, pulse shape, etc.) between studies could have also led to the lack of surface damage on L-W samples. Small laser-exposed spots were identified on T-W samples, and the change in surface morphology due to pulsed laser irradiation at varying pulse counts is shown in Figure 4.30. SEM images of the surface were taken away from the laser spots (Figure 4.30(a, d)) to provide a point of comparison. After 100 laser pulses, the W surface appeared to exhibit noticeable grain growth (Figure 4.30(b, d)). The increase in grain size continued to occur at 1000 laser pulses, as seen in Figure 4.30(c, f). Studies in [29] also observed significant grain growth on cold-rolled, ultrafine-grained W samples with pulsed ms laser irradiation; the average grain size near the spot center increased from 500 nm to 35 µm after 1000 laser pulses. Pulsed laser irradiation at 0.5 MJ m^{-2} was of significant intensity to induce recrystallization on T-W samples. Neither the 100 nor the 1000 pulse exposure resulted in melting or cracking. Further increasing the number of applied pulses might have eventually caused cracking, as shown for longitudinally-oriented W in [31]. One study noted that shock-induced surface roughening could be a precursor for surface cracking due to gradual increases in defect concentration during cool-down [26]. Future studies need to examine whether decreases in grain boundary density with recrystallization and grain growth could impact gas retention and particle-induced surface structuring.
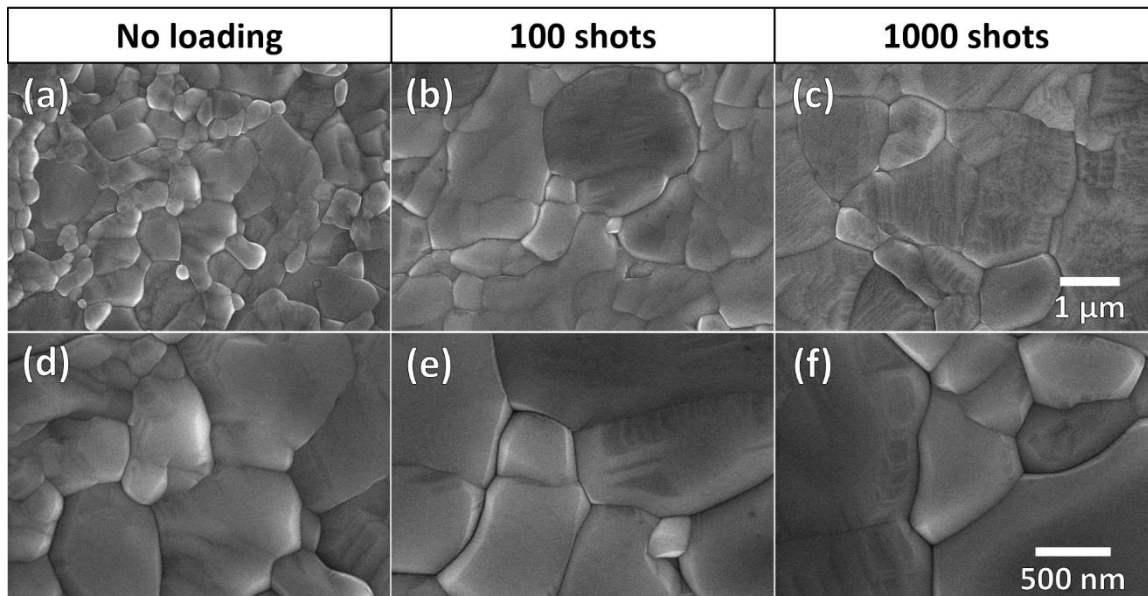
Figure 4.30: SEM micrographs of T-W surface after pulsed laser loading at increasing pulse counts

Studying the interaction between particle loading and heat loading on material strength has recently become a point of concern for future fusion devices due to observed decreases in thermal conductivity with He-induced fuzz formation. Findings of a heterogeneous, arborescent nanostructure due to low-energy, high-flux He$^+$ ion irradiation has motivated a multitude of studies on the properties of this "fuzz" structure and how it will ultimately affect divertor performance [36]. Measurements of reduced mechanical strength [37], reduced thermal conductivity [56], and reduced arcing threshold [96] have raised serious concerns over elevated levels of erosion in a reactor environment, which would harm plasma performance and limit component lifetimes. The current study exposed select L-W and T-W samples to low-energy He$^+$ ion irradiation before pulsed ms laser irradiation to examine how grain orientation impacted nanostructure growth and subsequent removal. SEM micrographs in Figure 4.31 show both L-W and T-W surfaces after 100 pulses and 1000 pulses of pulsed heat loading at 0.5 MJ m^{-2}. Images of the surface taken away from the laser spot were also taken for comparison. Both W materials exhibited significant fuzz growth due to He$^+$ ion irradiation, as seen in Figure 4.31(a, d). Smaller fuzz tendrils grown on T-W might have been a result of elevated structure growth due to enhancements in He bubble mobility along transversal grain boundaries, but was likely due to small variations in ion flux between irradiations. As the number of pulses applied to the

surface increased, the areal fuzz density gradually decreased, as characterized on Mo in Section 4.2. However, recovery of the surface back to a pristine state was not observed after 1000 pulses, which is primarily due to the relatively low energy density being used. During pulsed ms laser irradiation, incident photons transferred heat to the lattice. Due to the geometrically-driven reduction in thermal diffusivity of the fuzz region, incident energy was not diffused effectively to the bulk, resulting in overheating and localized tendril conglomeration. More information on the shock-induced degradation of fuzz tendrils can be found in Chapter 5. The fuzz degradation process did not depend on the orientation of the material, as evidenced by the similar areal fuzz densities in Figure 4.31(b, e) and Figure 4.31(c, f). The lack of research on the effect of ELM-like heat loading on the behavior of fuzz nanostructure external to the work presented throughout this dissertation limits the conclusions that can be made about material behavior in a fusion environment. Experiments performed in Pilot-PSI observed the complete disappearance of fuzz nanostructure due to sequential He^+ plasma irradiation and 1 ELM-like heat pulse with a maximum intensity of 0.5 MJ m^{-2} [57]. Unfortunately, the study described in [57] did not specify the microstructure of the W samples that were used beyond stating that they were polycrystalline. Research performed in [55] observed tendril conglomeration that is somewhat similar to that shown in Figure 4.31 due to sequential He^+ plasma irradiation
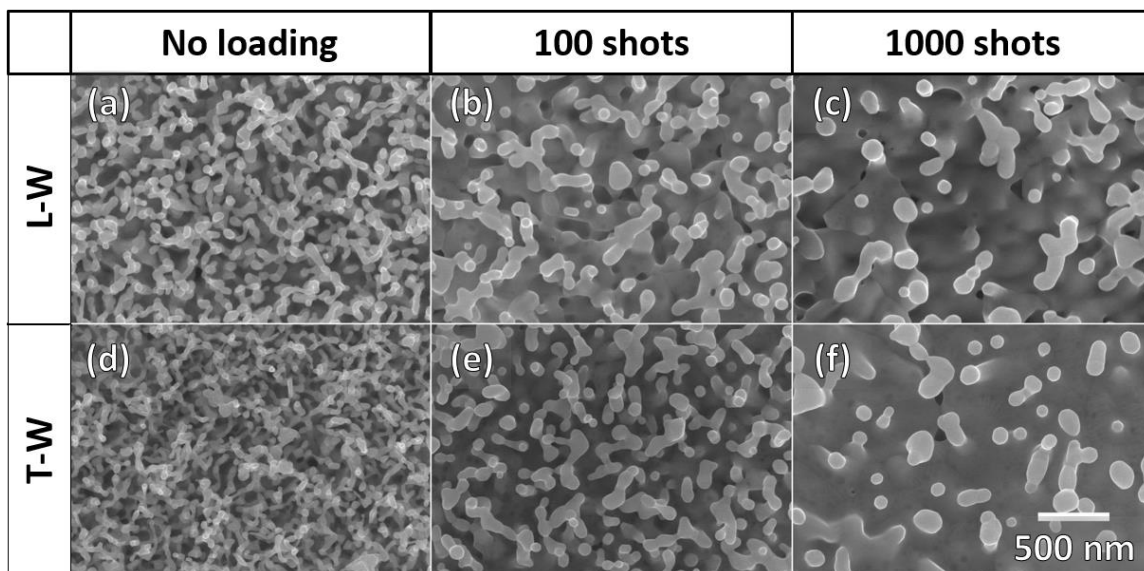
Figure 4.31: SEM micrographs of L-W and T-W surfaces exposed to sequential He^+ ion irradiation and pulsed laser loading at increasing pulse counts.

and pulsed ms laser irradiation on W samples with an unspecified microstructure. Future experiments need to more comprehensively characterize the grain character of the materials being used for radiation exposures. While the nanoscale response of the material did not depend on the grain orientation, decreases in fracture strength due to perpendicularly-oriented grains in T-W strongly affected mechanisms of macroscopic failure.

High-magnification SEM images of the W surface after sequential He$^+$ ion irradiation and pulsed laser heat loading did not provide information on the brittle vs. ductile behavior of each material. Optical profilometry was therefore conducted on the spots exposed to 1000 laser pulses to measure the height profile of the irradiated area and assess the degree of surface deformation. The arithmetic surface roughness (R_a) was also calculated for each spot. SEM micrographs of each spot, along with the height profile taken across the center of the spot, are shown in Figure 4.32. Both laser-irradiated spots have a diameter of ~ 0.6 mm. Pulsed laser irradiation on L-W produced a much more roughened surface, with R_a = 0.629 µm. Peaks and valleys that were observed within the laser-irradiated area on L-W were due to significant levels of plastic deformation, resulting in surface roughening. Grain boundaries oriented parallel to the loaded surface may have inhibited heat transfer to the bulk, and enhanced thermal stress in the near-surface region. In contrast, the T-W underwent minimal plastic deformation, and instead exhibited significant surface cracking. The appearance of cracking without plastic deformation in Figure 4.32(b) refutes the theory proposed in [26]. One potential explanation for the lack of plastic deformation on T-W is that the added presence of He-induced fuzz nanostructure lowered lattice stress by inhibiting heat transfer to the bulk, which caused fuzz tendril conglomeration and partial surface recovery. The presence of longitudinally-oriented grains in L-W raised the UTS of the material, enhancing plasticity [32]. Therefore, under the same degree of pulsed heat loading, the L-W samples experienced more plastic deformation without undergoing brittle failure. Either increasing the laser energy density or the pulse count would have eventually induced enough stress to exceed the UTS and cause surface cracking.
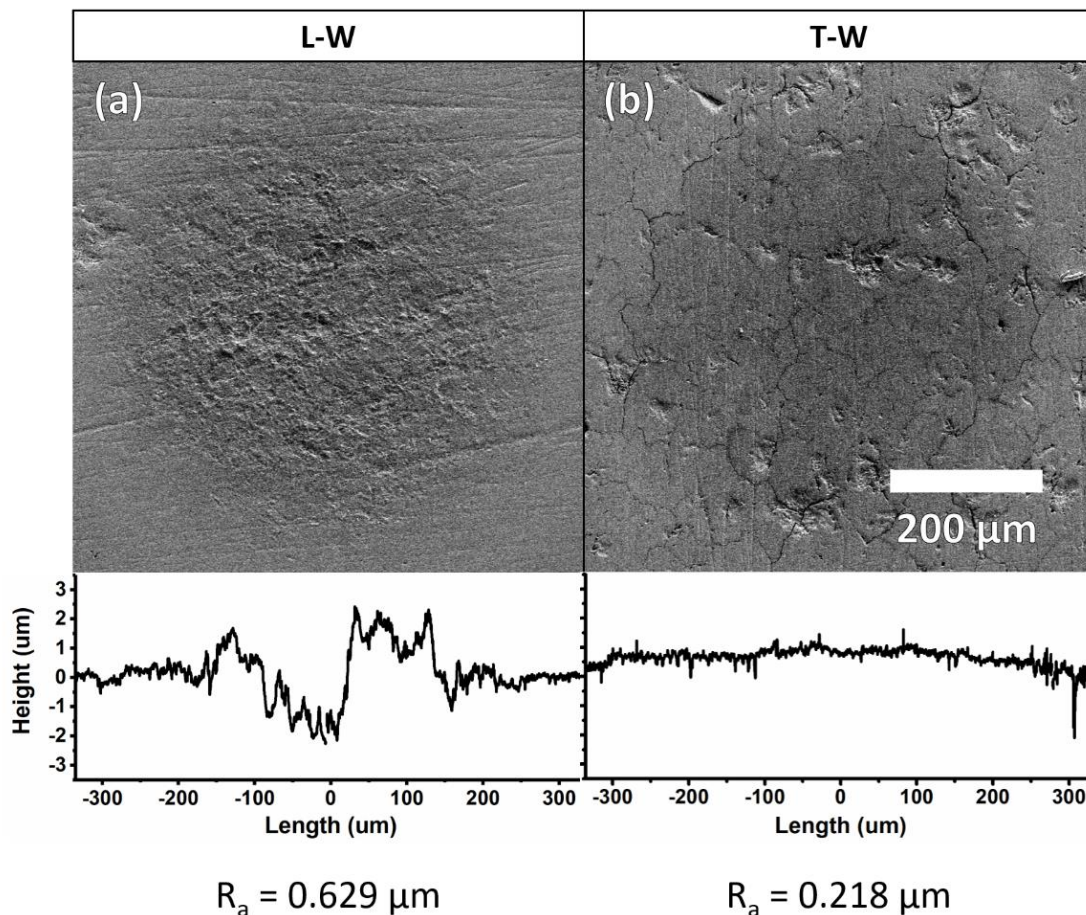
Figure 4.32: SEM micrograph and height profile of spots exposed to sequential He$^+$ ion irradiation and 1000 of pulsed laser irradiation. Arithmetic mean roughness values are also displayed.

Higher levels of fuzz degradation near cracks on T-W further illustrate the influence of grain boundaries on He bubble trapping and migration. While the growth mechanism for fuzz formation remains unclear, many theories propose that tendrils grow due to movement of He bubbles at the surface. Atomistic modeling of implanted He atoms in W revealed that He clusters formed at intrinsic traps in the subsurface migrate toward the surface due to the presence of a thermodynamic driving force in the lattice [182]. Previous He$^+$ ion irradiation experiments on W revealed that grain boundaries in the material could serve as nucleation sites for implanted He; bubbles would then migrate through the lattice [173], [183]. MD simulations presented in [184] and [185] found that the cohesive energy of a grain boundary increased as concentration of trapped He increased. Since the cohesive energy is directly proportional to the brittleness, higher levels of He trapping at grain

boundaries would enhance intergranular cracking. One reason for the absence of cracking on T-W samples that were not pre-exposed to low-energy He$^+$ ion irradiation (Figure 4.30) could be due to grain boundary weakening caused by He bubble nucleation. Select SEM micrographs have been displayed in Figure 4.33 to highlight changes in surface morphology and thermal behavior near the crack edge. A low-magnification image in Figure 4.33(a) clearly showed that the areal fuzz density decreased near surface cracks. During pulsed laser heat loading, thermal stress collected at grain boundaries, which formed localized "hot spots" and eventually led to brittle failure in the form of cracks. Higher surface temperatures near the crack edge enhanced fuzz conglomeration and caused minor surface melting, which could have led to the crack bridging seen in Figure 4.33(b). The appearance of fuzz tendrils right along the crack edge (Figure 4.33(c)) and inside of the crack (Figure 4.33(d)) reinforce the lack of plastic deformation at grain boundaries during pulsed heat loading on T-W samples. While minimizing intense surface roughening observed in Figure 4.32(a) on L-W is thought to be desirable, the enhancement in cracking
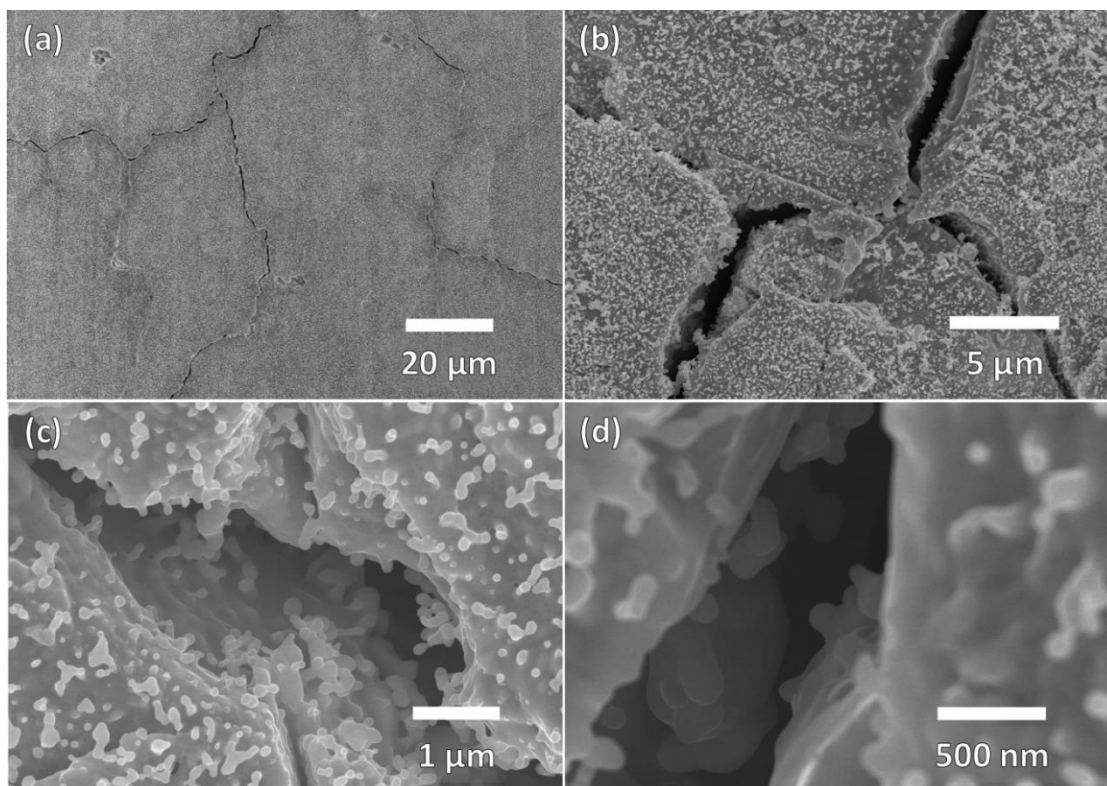
Figure 4.33: SEM micrographs of crack formation within the laser-exposed area after sequential He$^+$ ion irradiation and 1000 pulses of pulsed laser irradiation.

due to the preferential nucleation of implanted He at oriented grain boundaries presents serious concerns regarding component reliability in future fusion devices. Methods to minimize radiation hardening in W materials due to high-flux particle loading need to be explored to ensure constant material strength.

4.5.4 Summary

Materials testing of W samples with transversally-oriented grains found that the added presence of low-energy, high-flux He^+ ion irradiation substantially enhanced crack formation beyond what was previously expected. The ITER Organization selected W with transversally-oriented grains for use in the divertor to avoid cracking parallel to the loaded surface and to maximize thermal strength. However, adequate research has not been conducted on how concurrent He^+ ion irradiation will impact the brittleness and morphology of the material. ITER-grade W samples (T-W) with transversally-oriented grains were tested alongside cold-rolled and annealed W samples (L-W) with longitudinally-oriented grains (same W material used throughout this dissertation) for comparison. All samples were exposed to 100 pulses or 1000 pulses of pulsed ms laser irradiation at 0.5 MJ m^{-2} to replicate the maximum heat loading expected during a mitigated ELM event. Half of the samples were pre-exposed to He^+ ion irradiation to induce fuzz formation.

Pre-characterization of both W materials revealed that T-W exhibited a lower UTS. While L-W samples did not experience any noticeable surface damage due to pulsed ms laser irradiation without pre-exposure to He^+ ion irradiation, minor grain growth was observed on T-W samples, revealing the presence of recrystallization. Both L-W and T-W samples possessed very fuzz nanostructures when exposed to He^+ ion irradiation. In addition, the shock-induced fuzz tendril conglomeration kinetics did not appear to have a dependence on crystallographic orientation. However, macroscopic plastic deformation was observed only on L-W samples, due to higher material plasticity, and widespread surface cracking was observed only on T-W samples. Measurements of R_a found a 3 × higher surface roughness on L-W samples. Results obtained did not clearly indicate why pulsed heat loading of T-W samples yielded a smoother surface. Additional cross-sectional analysis would reveal the role of grain character in material response. Surface cracks on T-

W samples pre-exposed to He$^+$ ion irradiation could have been caused by a preferential increase in the cohesive energy of grain boundaries by He bubble nucleation. Potential degradation of mechanical strength due to radiation hardening on ITER-grade W could promote the use of differently-oriented materials that exhibit better resistance to particle loading.

While studying the interaction between He$^+$ ion loading and ELM-like transient heat loading provides further insight into device performance, many other sources of radiation also need to be considered. The influence of D$^+$ ion loading (and other hydrogen isotope loading) on thermal strength needs to be examined further to determine if implantation and nucleation will significantly impact grain boundary strength and surface morphology. Work presented in Chapter 6 begins to explore the synergistic effects between D$^+$ ion irradiation and He$^+$ ion irradiation on material strength. While pulsed heat loading utilized a constant energy density of 0.5 MJ m^{-2} to replicate mitigated ELM conditions, large increases in intensity during unmitigated ELM events could lead to complete surface melting and splashing of molten material. Since unmitigated ELMs are still expected in an ITER-type device, the onset of ELM-induced erosion on ITER-grade W needs to be characterized. Utilizing transversally-oriented grains for divertor surfaces have been shown to limit cracking and surface roughening when tested within a narrow operating window. However, more comprehensive testing over a wider set of radiation environments is needed before confirming the superiority of a particular grain orientation for use in the divertor region.

5. COMPARING TRANSIENT HEAT LOADING METHODS ON SURFACE EVOLUTION AND PARTICLE EMISSION[3]

In Chapter 4, several experiments were presented that revealed the complex synergistic effects between high-flux He^+ particle loading and ELM-like heat loading on material strength. However, replicating high heat fluxes with a pulsed ms laser does not perfectly replicate the ELM event in a reactor environment. Therefore, other laboratory-based methods of imparting pulsed heat loading on PFC candidate materials need to be examined. In addition, the research in Chapter 4 did not fully consider the effect of background, steady-state heat loading on the mechanisms of surface degradation. Steady-state heat loading in a fusion environment could raise surface temperatures in the divertor region above 1000 K, exceeding the DBTT for W.

In the current study, mirror-finished W foils were exposed to 100 eV He^+ ion irradiation at a fluence of 2.6 x 10^{24} ions m^{-2} and a temperature of 1200 K. Then, samples were exposed to two different types of pulsed heat loading meant to replicate type-I edge-localized mode (ELM) heating at varying energy densities and base temperatures. Millisecond (ms) laser exposure done at 1200 K revealed a reduction in fuzz density with increasing energy density due to the conglomeration and local melting of W fibers. At higher energy densities ($\sim$ 1.5 MJ m^{-2}), RT exposures resulted in surface cracking, while 1200 K exposures resulted in surface roughening, demonstrating the role of base temperature on the crack formation in W. Electron beam heating presented similar trends in surface morphology evolution; a higher penetration depth led to reduced melt motion and plasticity. *In situ* mass loss measurements obtained via a quartz crystal microbalance (QCM) found an exponential increase in particle emission for RT exposures, while the prevalence of melting from 1200 K exposures yielded no observable trend.

5.1   Introduction

Advancement in fusion reactor design toward a successful power-producing device critically depends on details of plasma-material interactions under high particle and heat loads. Component failure during operation can seriously degrade plasma performance and material lifetime. W has therefore come to the forefront as a promising material for future PFCs, due its favorable thermal and mechanical properties, as detailed in Chapter 1.

However, studies done over the previous decade have shown that tungsten's capacity as a PFC material might be seriously compromised due to radiation damage from low-energy helium (He^+) ions. Many studies have observed the growth of nanoscale, fiber-form tendrils on the W surface in response to high-flux, low-energy He^+ ion irradiation within a specific temperature window [36], [38], [43], [103].

Since the discovery of fuzz formation, many different experiments have been conducted to try and characterize this heterogeneous surface structure. Work done in [51] found a reduction in the physical sputtering yield with fuzz growth. Other studies have shown a reduction in the unipolar arcing threshold on nanostructured W surfaces, which could lead to significant levels of erosion during device operation [53], [186]. Research has also been performed to characterize the surface response during transient heat loading events. An edge-localized mode (ELM) is a destructive type of transient event that can occur during tokamak operation [25]. During an ELM, the edge plasma relaxes and imparts large heat fluxes onto the PFC surface. Type-I ELMs possess the highest flux and power loss when compared to other types of ELMs, making these events a critical point of concern for reliable operation (see Chapter 1 for additional information) [25]. This type of high cycle heat loading may lead to surface cracking, melting, and erosion of the material surface [25], [162]. In addition, recent studies have discovered that fuzz formation could drastically decrease the thermal conductivity of the W surface, which would degrade tungsten's thermal shock performance and exacerbate other material problems during transient heat loading [55], [137].

Until recently, pulsed heat loading research has focused on low magnitude ELMs to determine damage and cracking thresholds. Higher magnitude ELMs have not been as widely studied because of techniques in development to "mitigate" ELMs to ≤ 0.5 MJ m^{-2} [55], [143]. However, these mitigation techniques are not fully developed, so research on

the melting and potential splashing of the He^+ ion-induced fuzz nanostructure during unmitigated ELMs (energy densities up to several MJ m^{-2}) remains important for the development of advanced PFCs [28], [146].

The proposed study aims to investigate the structural and thermal response of nanostructured W to ELM-like heat loading using two different methods. Currently, pulsed heat loading experiments utilize long-pulsed lasers, electron beams, or plasma accelerators to replicate the flux and timescale of type-I ELMs [33]. After being exposed to low-energy He^+ ion irradiation to initiate fuzz formation, tungsten samples were exposed to pulsed heat loading via either laser or electron beam irradiations at varying energy densities. Field-emission scanning electron microscopy (FE-SEM) was used to observe the degradation of nanoscale tendrils on the W surface during heat loading. In addition, an *in situ* quartz crystal microbalance (QCM) was used to measure particle emission from the sample surface. Instead of focusing on the absolute amount of material ejected from the surface, analysis focused on the relative trends in mass loss at different energy densities and surface conditions (i.e., pristine vs. fuzz). Conducting a multi-faceted examination on the deformation and melting of nanostructured W due to various forms of pulsed heat loading is of great interest to understand the behavior of PFCs in a fusion environment.

5.2   Experimental setup

Research efforts were split between the JUDITH 1 (Juelich Divertor Test Facility in Hot Cells) facility [58] at Forschungszentrum Jülich and the UHFI-II (Ultra High Flux Irradiation - II) facility at the Center for Materials Under Extreme Environment (CMUXE) at Purdue University. Cold-rolled W samples (99.95% purity) with dimensions 10 mm $\times$ 10 mm $\times$ 0.5 mm were cut from the same sheet and mechanically polished to a mirror finish devoid of major imperfections. First, samples were exposed to 100 eV He^+ ion irradiation, with an ion flux of 7.2 x 10^{20} ions m^{-2} s^{-1} (2.6 x 10^{24} ions m^{-2} fluence) at a temperature of 1200 K, using the UHFI-II facility illustrated in Figure 5.1(a). The ion gun is a grid-less end-hall 'EH' ion/plasma source. The ion gun includes a broad beam End-Hall ion source and an automated power supply controller. The broad divergent beam improves throughput by uniformly covering a wide deposition zone.

After ion irradiation, some of the W samples were exposed to pulsed heat loading via long-pulsed laser irradiation. A schematic of the laser loading system is shown in Figure 5.1(b). A 1064 nm pulsed Nd:YAG millisecond (ms) laser was focused onto the W fuzz surfaces, with a 1 mm spot size. The laser utilized a flat top beam mode to ensure even heating over the entire spot. W fuzz samples were mounted on a translational stage inside the chamber in order to attain multiple exposures, in an *in situ* condition, on one sample in a grid-like pattern. In order to replicate both the intensity and duration expected for type-I ELMs in fusion devices, the pulse width was set to 1 ms, the repetition rate was set to 1 Hz, and the energy density varied between the following values: 0.6 - 1.6 MJ m^{-2} (19 - 57 MJ m^{-2} s$^{-1/2}$) [7]. The heat load parameter (expressed in MJ m^{-2} s$^{-1/2}$) is approximately equal to the product of the power load (MW m^{-2}) and the square root of the pulse duration (s$^{1/2}$). Each exposure consisted of 200 pulses. In addition, W fuzz samples were set at different temperatures during exposures – RT and 1200 K – to determine the effect of base temperature on the surface response.
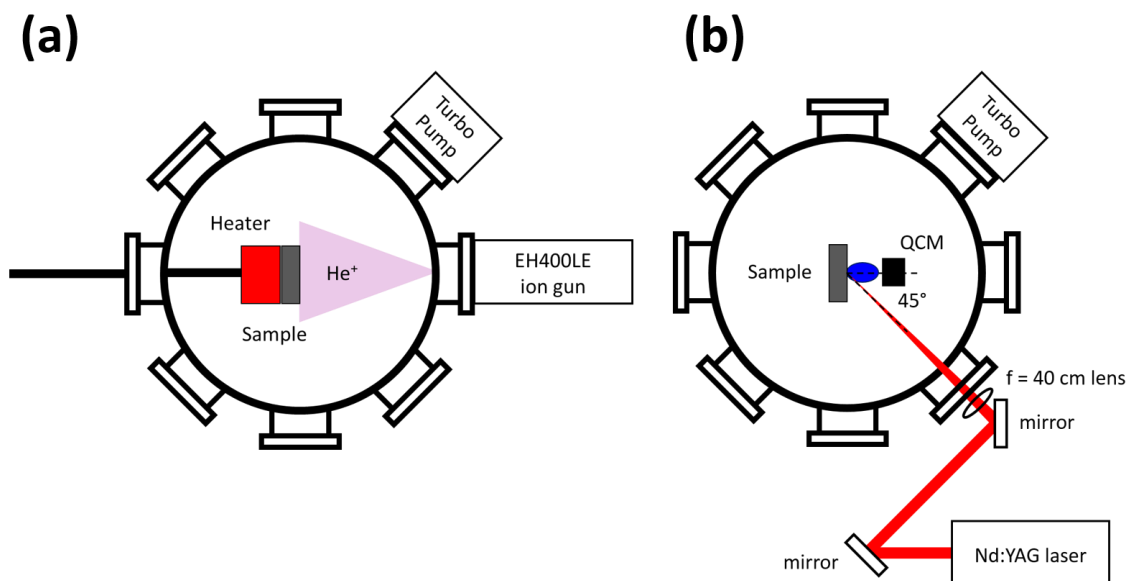
Figure 5.1: UHFI-II chamber; (a) ion irradiation setup schematic & (b) long-pulsed laser irradiation setup schematic.

During laser irradiation, a quartz crystal microbalance (QCM) was situated in front of the sample surface to detect any emitted particles. The QCM was oriented normal to the sample surface, with the crystal toward the laser exposed spot at a distance of 20 mm. The resolution of the QCM is ± 0.01 angstroms. The collection size of the detector surface is

52.18 mm^2. During each exposure, the thickness of material deposited on the crystal was measured by an Inficon SQC-310 Thin Film Deposition Controller. The mass deposited was then calculated using the Sauerbrey equation [92]. Utilizing an *in situ* method to measure mass loss possesses inherent advantages over other *ex situ* techniques used in previous experiments. Significant amounts of oxide formation found in previous fuzz formation experiments on molybdenum after removing a sample from vacuum indicate that the added mass from oxides could confound *ex situ* mass loss measurements [42].

The remaining nanostructured tungsten samples were sent to Forschungszentrum Jülich and were exposed to pulsed electron beam irradiation in the JUDITH 1 facility (short for Juelich Divertor Test Facility in Hot Cells). The schematic of the facility is shown in Figure 5.2. The pulse width of the electron beam was set to 1 ms, and each exposure consisted of 200 pulses at an energy of 120 keV. By scanning a 4 x 4 mm^2 area at very high frequencies (~ 50 kHz), the electron beam provided homogeneous heat loading during each exposure. To understand the surface response over a wide range of ELM intensities, exposures were done at 0.38 and 1.51 MJ m^{-2} (12 and 48 MJ m^{-2} s$^{-1/2}$). Similar to the laser heat loading experiments, some of the samples were heated to 1200 K, while others were kept at RT.
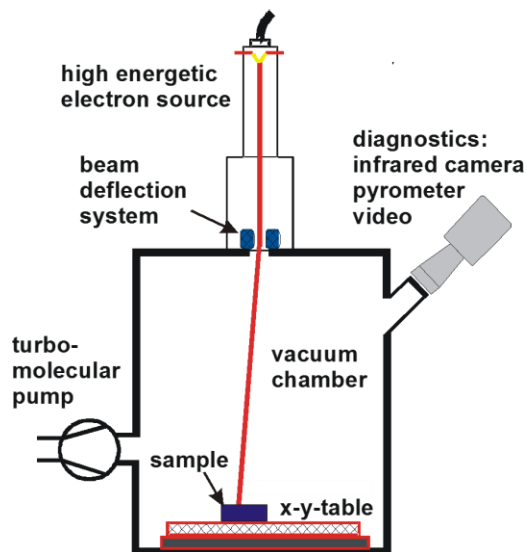
Figure 5.2: Schematic of JUDITH 1 electron beam irradiation setup

Surface characterization was conducted after laser and electron beam exposures via *ex situ* field-emission (FE) scanning electron microscopy (SEM). Imaging of the W samples after pulsed heat loading helped to compare the changes in surface morphology

between methods and draw some conclusions about how accurately these methods reproduce tokamak-like conditions. Data obtained on the presence of and trends in particle emission via QCM measurements helped further provide important information on how large magnitude transient events can affect component lifetime and plasma performance in future fusion devices.

5.3   Surface evolution during pulsed heat loading

Imaging of the sample after pulsed heat loading was very useful in characterizing the effect of melting on changes in surface morphology. Once W fiber form tendrils on the sample surface melt, droplet ejection via splashing can take place. The SEM analysis shown serves as a first step in defining windows for safe operation in ITER-like devices.

During laser heat loading, samples were exposed to 200 pulses at energy densities between 0.6 MJ m^{-2} and 1.6 MJ m^{-2}, at two different base temperatures – RT and 1200 K. SEM micrographs in Figure 5.3 illustrate the surface response for irradiations at 1200 K. Performing pulsed heat loading experiments at elevated temperatures was done to more accurately replicate conditions expected in ITER-like devices [37], [177]. The unexposed fuzz structure is shown in Figure 5.3(a) to provide a baseline for morphology changes. At an intensity of 0.6 MJ m^{-2}, nanoscale tendrils begin to degrade and decrease in density (Figure 5.3(b)). The surface also appears roughened due to tendril conglomeration. Similar surface evolution was also found in similar experiments after 300 laser pulses at about 0.8 MJ m^{-2} [55]. Future work on the thermal properties of fuzz tendrils is required to determine the driving mechanism for this decrease in fuzz density at low magnitudes. At 1.0 MJ m^{-2}, the W surface appears to experience significant surface melting as evidenced by the significant reduction in roughness and complete absence of any prominent nanoscale tendrils (fuzz). Finally, heat loading at 1.4 MJ m^{-2} results in complete surface melting, with an apparent reduction in the presence of footprints from any fuzz tendrils. The presence of ripples (as seen in Figure 5.3(d)) along the molten surface might be indicative of melt motion [73]. Atomic force microscopy analysis conducted in Chapter 4 shows that heat loading of sufficient intensity could generate ripples within the exposed area. W heat loading studies presented in [15] found that molten samples exhibit large increases in mass loss and droplet ejection above a certain energy density threshold. Potential contamination

of the plasma due to mass loss from the PFC surface necessitates further research to find how surface melting is related to mass ejection to optimize reactor performance.
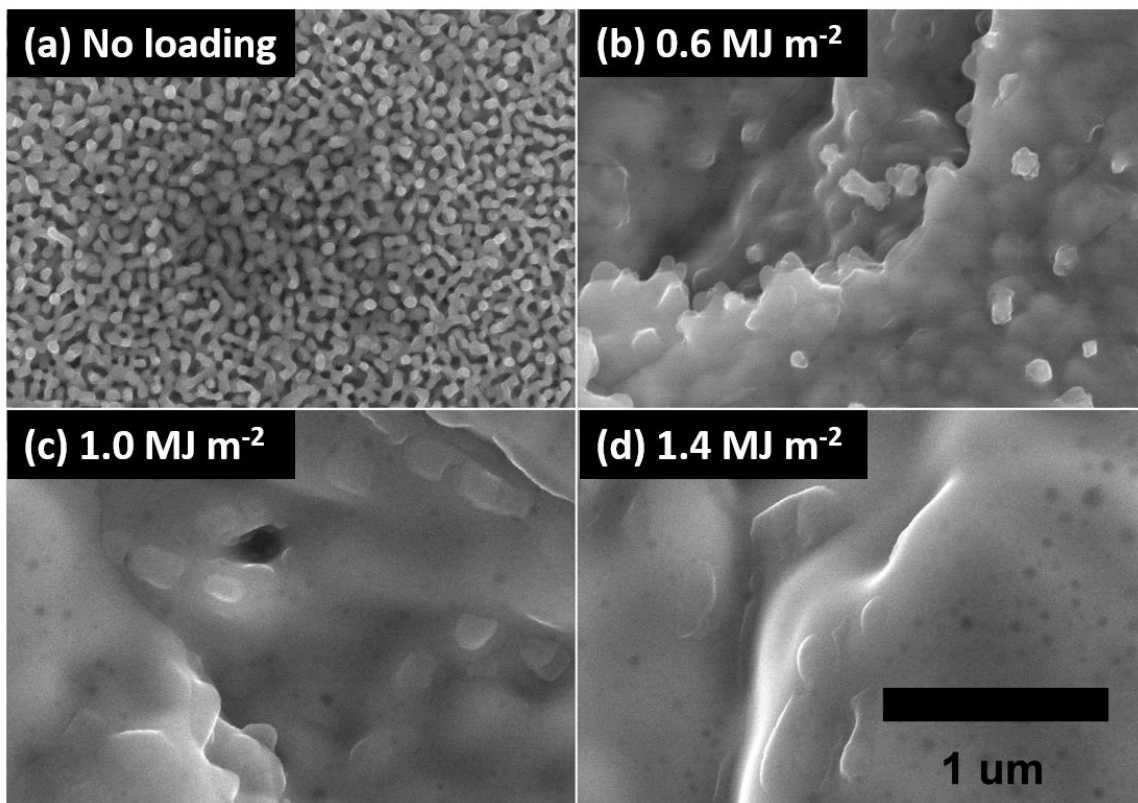
Figure 5.3: SEM micrographs of W fuzz surface after 200 pulses of laser heating at a base temperature of 1200 using the following energy densities (a) no loading, (b) 0.6 MJ m^{-2}, (c) 1.0 MJ m^{-2}, and (d) 1.4 MJ m^{-2}. Reproduced from [187] under CC BY-NC-ND 4.0 license.

Therefore, additional heat loading experiments were done on similar nanostructured W samples using electron beam irradiation. JUDITH 1 was used for the electron beam loading experiments. As mentioned previously, the duration and intensity of an electron beam closely correlates with that of a type-I ELM in an ITER-like device [58]. SEM micrographs shown in Figure 5.4 serve as a summary of the surface response to each type of heat loading (at low and high ELM intensities) for unheated and heated (1200 K) exposures on W fuzz samples. Due to the high heterogeneity in fuzz formation, the starting W surface structures are not quantitatively comparable. Therefore, analysis will remain qualitative, based around the surface features that develop during pulsed heat loading.
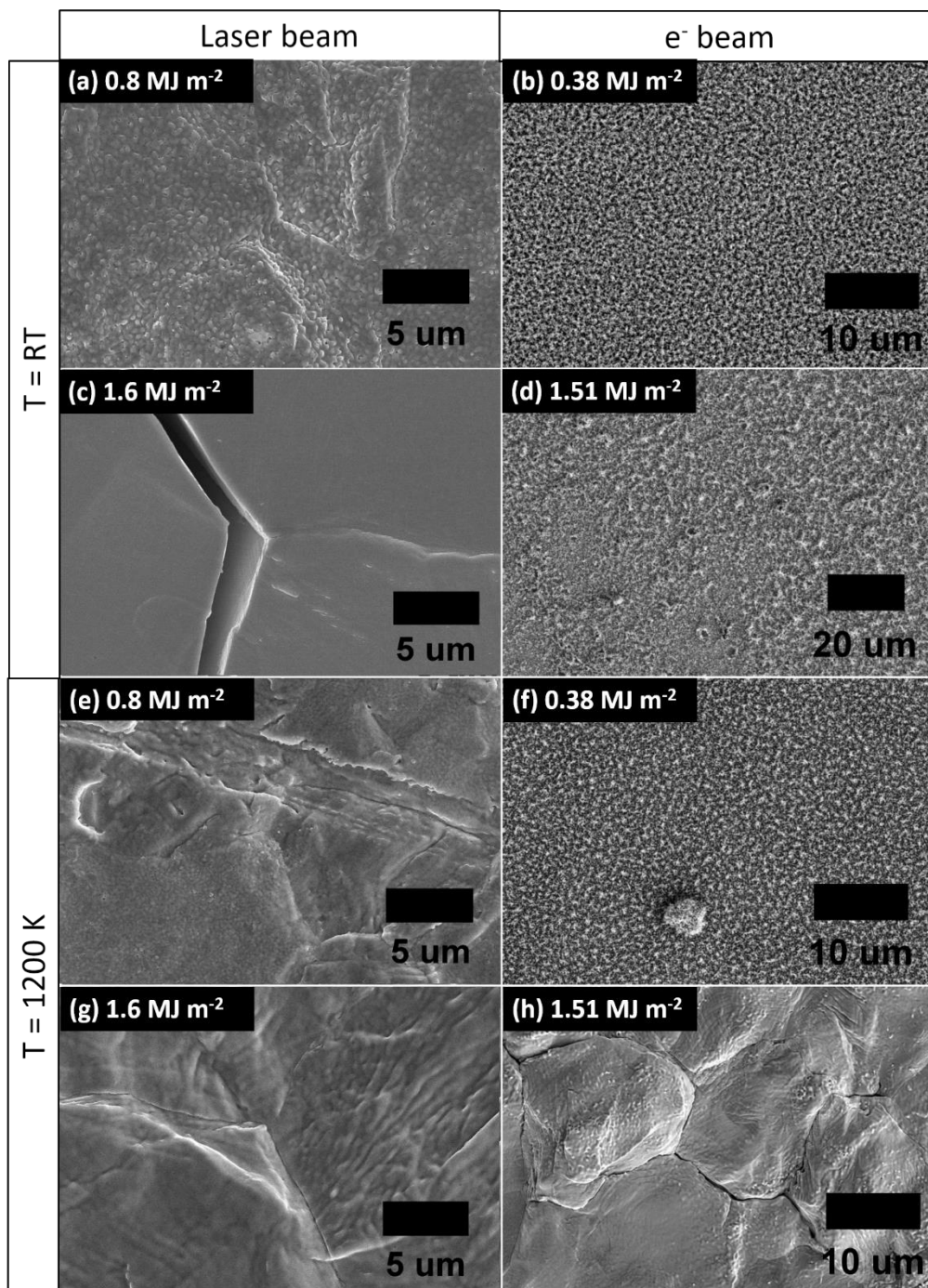
Figure 5.4: Comparative SEM micrographs of W nanostructured samples exposed to laser and electron beam loading at varying base temperatures and energy densities. Reproduced from [187] under CC BY-NC-ND 4.0 license.

Room temperature exposures led to large differences in surface response between loading methods. At low intensities, both the laser beam and the electron beam caused slight damage to the fiber form nanostructure, but did not cause significant surface melting

or brittle failure. The roughening seen on the laser exposed sample can be attributed to its higher energy density. Higher intensity exposures done at 1.5 MJ m^{-2} and 1.6 MJ m^{-2} revealed a large discrepancy in surface response between loading methods. While the laser exposed sample appeared completely molten and possessed a large crack within the irradiated area (Figure 5.4(c)), the electron beam exposed sample appeared only slightly damaged, with no evidence of crack formation (Figure 5.4(d)). Previous RT studies on pristine W found that both electron beam irradiation (done in JUDITH 1) and laser beam irradiation at similar intensities led to extensive crack formation [58]. Therefore, the surface response seen in Figure 5.4(d) was unexpected. Conducting additional experiments at a wider range of energy densities will help characterize the brittle behavior of nanostructured W during pulsed heat loading at RT.

Experiments done at 1200 K yielded more comparable results between laser heat loading and electron beam heat loading methods, which further strengthen the impact of base temperature on surface evolution. Raising the temperature to 1200 K appeared to enhance the degree of fuzz reduction at low intensities. The laser irradiated sample did not undergo complete surface melting (Figure 5.4(e)), but did possess a lower fuzz density than the sample exposed at RT in Figure 5.4(a). Similarly, the electron beam irradiated surface in Figure 5.4(f) (@ 1200 K) exhibited a lower fuzz density than the corresponding surface in Figure 5.4(b) (@ RT). The reduction in the density of nanoscale tendrils along the surface was most likely due to the conglomeration of tendrils during the heating process due to the tendrils' reduced thermal strength, as seen in Chapter 4. A higher base temperature results in a higher surface temperature before laser heating, which decreases the thermal jump necessary to cause melting and conglomeration of the W fiber-form tendrils, as discussed in [188]. The link between He desorption from the W nanoscale fibers and the structural degradation of the tendrils is currently unknown. However, higher levels of He diffusion out of the material is expected at higher surface temperatures during pulsed heat loading. At high intensities, the W surface responded similarly to both methods of pulsed heat loading. Both surfaces underwent complete surface melting and appeared roughened. The reason that crack formation occurred on the electron beam irradiated sample was most likely due to the higher penetration depth of the electron beam. Even though each type of beam utilizes approximately the same intensity, the pulse energy from

the electron beam becomes distributed throughout the first couple of μm into the surface, while the pulse energy from the laser beam is all deposited at the surface. Therefore, the laser irradiated spot will have a more developed melt layer, leading to higher levels of plasticity, effectively reducing the material's ability to crack. The difference in surface morphology directly contradicts results found in [58], where no significant change in surface structure was observed between electron beam and laser beam loading after 100 pulses at varying energy densities. However, a lower repetition rate and pulse count make comparisons between studies difficult. More work needs to be conducted using SEM and FIB analysis techniques to fully characterize the differences between heat loading methods.

Clear differences in ductility and crack formation at different base temperatures reveal the potential misrepresentation of the W surface response from unheated pulsed loading. Figure 5.4(c) & Figure 5.4(g) show the surface morphology on the W fuzz samples after RT and 1200 K laser heat loading at 1.6 MJ m^{-2} (200 pulses). While a large micrometer size crack was formed on the unheated W fuzz sample, no crack was found on the heated W fuzz sample. Neither sample appeared to contain any fiber-form nanoscale tendrils due to complete surface melting, but the W fuzz sample exposed at 1200 K appeared to have higher levels of surface roughening. The increased roughness was most likely due to melt motion. The suppression of crack formation in preheated samples has also been observed in [28], where a base temperature as low as 673 K prevented the growth of any cracks on pristine W. Recent work in [189] also reported the suppression of crack formation with increasing base temperature on W samples exposed to hydrogen plasma and laser heat loading. Differences in the surface response can be explained by the ductile to brittle transition of W. At RT, W behaves as a brittle material. Thermal shocks therefore cause brittle failure, resulting in the formation of a crack. In contrast, heating W above its ductile to brittle transition temperature (~ 500-700 K) increases the plasticity of the material, and prevents brittle failure [136]. Future work should explore the thermal response of nanostructured W at more temperatures, in order to create a map of the surface response as a function of base temperature and power density (similar to [189]). Then, in-depth analysis can be done on how low-energy He$^+$ ion irradiation affects the ductile to brittle transition temperature of W.

Despite the differences between the electron beam and the laser beam, neither device perfectly simulates the particle loading expected in tokamak devices during off-normal events. Therefore, research going forward should invest more effort into discussing how different experimental pulsed heat loading methods replicate type-I ELM events using facilities such as DiMES [140]. Significant changes in surface response with higher base temperatures help reinforce the incorporation of sample heating during pulsed heat loading experiments. Studies at elevated temperatures will better represent the expected material response during transient heat loading inside fusion devices.

5.4   Effect of fuzz formation on particle emission

Recent work has shown that helium-induced nanostructuring might reduce the threshold for surface melting [94]. As a result, a larger melt layer could lead to higher levels of melt motion and droplet ejection, as discussed briefly in [155], which would complicate tungsten's viability as a PFC candidate material. Recent studies, both numerical and experimental, suggests that the thermal conductivity of the fiber form nanoscale tendril structure (fuzz) could be significantly lower than that of bulk tungsten (up to 80% lower) [56], [78], [82], [94], [137]. Such a large decrease in thermal conductivity strengthens the observation of surface melting from SEM images. As the energy density increases above the melting threshold, further pulsed heat loading will cause ejection of molten material, sending droplets into the fusion plasma [25]. Using a QCM during laser heat loading in an *in situ* configuration provided important information on the presence of and trends in particle emission. Although the small collection angle of the microbalance limited the results to be largely qualitative, data presented below demonstrated the potential viability of the device as an improved means of mass loss detection over traditional microbalances.

Measurements of the mass deposited onto the QCM after laser heat loading at increasing energy densities on unheated and heated (1200 K) W fuzz samples are presented in Figure 5.5(a). Based on previous QCM studies done in CMUXE, an error of $\pm$ 10% was applied. Data collected for unheated exposures reveals an exponential increase in mass deposited as the energy density increased. These results mirror those found with pulsed heat loading on pristine Mo, shown in Chapter 3. SEM imaging of the sample (figure not shown) showed small amounts of surface melting between 1.0 MJ m^{-2} and 1.2 MJ m^{-2},

which might explain the small amount of mass being detected. XPS measurements made on exposed QCM crystals confirmed that the signal detected will be due to emission of W or W-oxide (not due to impurity erosion). However, the degree of melting increased significantly for energy densities above 1.2 MJ m^{-2}, which correlates well with QCM data. An exponential curve was fit to the data (the 0.4 MJ m^{-2} data point was not included because no mass was deposited), as can be seen in Figure 5.5(b), to define the relationship between the mass deposited onto the QCM and the laser energy density. The exponential fit has the following equation:

$$\Delta m = e^{-7.01+2.46*Q+0.28*Q^2} \tag{5-1}$$

where m is the mass deposited and Q is the energy density. The curve fits well, with an R^2 value of 0.77. A high coefficient of determination (R^2) indicates that the curve should accurately predict future behavior. Studies presented in [15] also observed an exponential increase in mass loss with increasing energy density on pristine W. In addition, the study in [15] observed increased droplet ejection with the growth of the melt layer. While the trends in particle emission might be similar between pristine and nanostructured W, the magnitudes of emission might vary drastically. More data needs to be collected within the regime where melting and possible droplet ejection are expected (1.0 – 1.5 MJ m^{-2}) to better understand the onset of particle emission.
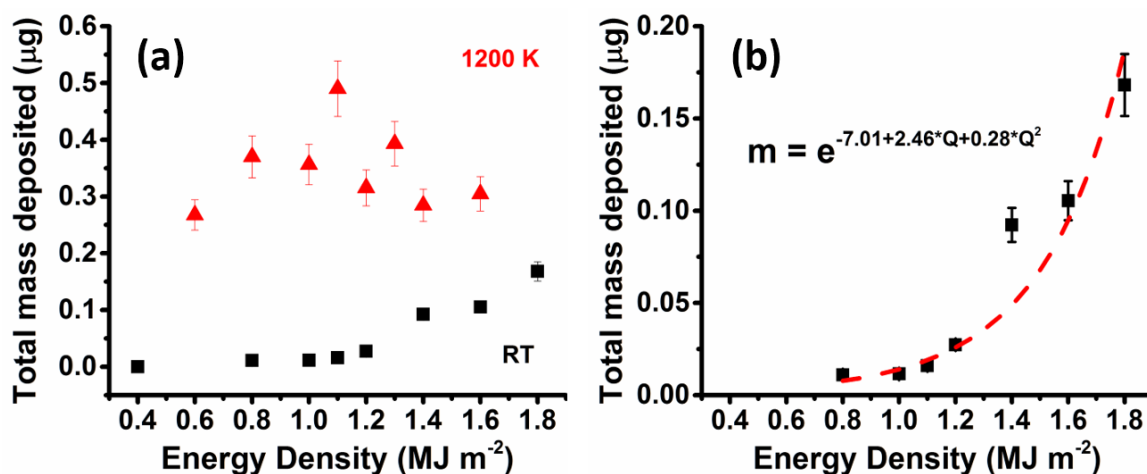
Figure 5.5: Total mass deposited onto QCM after 200 pulses of laser heat loading at increasing energy densities on (a) W fuzz samples at different base temperatures and (b) W fuzz at T = RT with an exponential regression line. Reproduced from [187] under CC BY-NC-ND 4.0 license.

W fuzz samples exposed at a base temperature of 1200 K did not exhibit any observable trend in the mass lost as a function of energy density (Figure 5.5(a)). Most data points obtained did not differ significantly, based on their associated error. The similar amounts of mass deposited onto the QCM is primarily due to the consistent presence of melting across all intensities. At a base temperature of 1200 K, the thermal jump required to produce melting is significantly reduced when compared to RT exposures [188]. Therefore, even low energy density irradiations resulted in significant melting and particle emission. The variation between data points was most likely due to the heterogeneity in the angular distribution of emitted particles. Future studies should not only investigate the threshold at which enhanced emission begins and the trend in emission with energy density, but also compare behavior at different base temperatures. The results presented in Figure 5.5 demonstrated that the reduction in thermal conductivity with He$^+$ irradiation could exacerbate plasma contamination and component lifetime concerns in reactor operation.

5.5   Summary

Measuring the effect of low-energy He$^+$ ion irradiation on surface melting and particle emission during ELM-like heat loading was conducted by using pulsed laser irradiation and electron beam irradiation. Studies were performed at two different base temperatures – RT and 1200 K – to understand the effect of base temperature on surface response. Laser irradiated samples revealed the presence of 3 different morphology regimes. At low intensities, the fuzz density decreased and led to some surface roughening. As the energy density increased, fuzz density approached zero and the entire surface became molten. Higher intensity exposures at elevated temperatures led to surface roughening due to melt motion, while room temperature exposures did not exhibit roughening. Neither sample appeared to exhibit a clear surface melting threshold, because the fiber form nanostructure began to undergo local conglomeration and melting at relatively low intensities. As the energy density increased, the melting of the fibers only intensified to the point at which the surface became devoid of any nanostructures. The onset of melting through a weakened surface structure could lead to higher levels of plasma contamination at low ELM intensities during reactor operation.

Comparisons to similar heat loading studies done using electron beam irradiation effectively illustrated the effects of the difference in penetration depths between both techniques. Common behavior of the nanostructured W samples included the reduction in fuzz density with low magnitude heating and complete surface melting for high magnitude heating on preheated samples. Unexpected results obtained at RT necessitate further experimentation. Crack formation in the electron beam irradiated sample at elevated temperatures highlight the important difference in penetration depth between laser heating and electron beam heating. ELM heating of PFCs in tokamaks will exhibit characteristics of both laser and electron beam pulsed heating. Future work needs to focus on the physical differences between heat loading methods and how to best simulate type-I ELM events in a laboratory setting.

In situ measurements of mass loss during laser heat loading highlight the role of base temperature in the growth and emission of the melt layer. Heat loading done at RT yielded an exponential increase in mass deposited on the QCM with increasing energy density. The increase in emission correlates well with the increase in the size of the molten layer (Figure 5.3). An exponential curve was fit to the data and yielded a moderately high R^2 value. In contrast, exposures done at 1200 K yielded no discernable trend in emission. The presence of a significant melt layer, even at low intensities (Figure 5.4(e)), points to the existence of droplet ejection below 1.0 MJ m^{-2}, which could cause significant plasma contamination and reliability problems in a reactor environment.

Results obtained in the current study and in previous work help lay the groundwork for comprehensive transient heat loading experiments utilizing different pulsed heat loading methods. Presented experimental results on the thermal shock performance of PFC candidate materials should be discussed in terms of its replicability to ELMs in future fusion devices. Material challenges regarding lifetime and performance can then be discussed with more certainty.

6. TRANSIENT HEAT LOADING ON SURFACES EXPOSED TO DUAL BEAM (HELIUM AND DEUTERIUM) ION IRRADIATION

The work in this chapter builds on the work presented in Chapters 3 and 4 to determine how the addition of concurrent D^+ ion irradiation impacts surface melting and erosion due to intense, ELM-like heat loading. The addition of He^+ ion irradiation appeared to degrade the thermal strength of the exposed surface, which enhanced melting via localized tendril conglomeration. In addition, erosion measurements found that the He-induced fuzz nanostructure growth process did not inhibit melt-layer splashing. Healing the fuzz tendrils without erosion may only be possible at very low intensities that will be exceeded in the mitigated ELM regime in ITER. While the changes in material response due to He^+ ion irradiation were important in assessing the thermal strength of fuzz nanostructures, the additional presence of D^+ ion irradiation must be tested to more accurately reflect the complex radiation environment present in a fusion device.

In this study, W samples were exposed to simultaneous ELM-like heat loading and high-flux He^+ and D^+ ion irradiation at different ELM intensities to further elucidate the complex synergistic effects inherent in a fusion environment. ELM-like heat loading was replicated using a 1064 nm Nd:YAG pulsed millisecond laser at different energy densities. Exposures produced a shale-like microstructure with or without concurrent He^+ and D^+ ion irradiation. However, adding D^+ to a simultaneous laser + He^+ irradiation reduced pore formation and inhibited early-stage nanostructure formation. Changes in surface morphology with the addition of D^+ could be attributed to super-saturation in the near-surface layer. While the addition of He^+ and D^+ clearly increased W erosion, the laser energy density did not have as clear of an effect. Increasing the ELM intensity reduced the number of pores, but increased the pore size. Future studies need to explore whether near-surface D impacts pore formation and total He desorption. Continued research on the combined effect of high-flux particle irradiation and transient heat loading will help refine predictions of material performance for ITER and beyond.

6.1 Introduction

Predicting the performance of plasma-facing components (PFCs) in a fusion environment requires multi-species exposure facilities that can reveal the synergy between different forms of incident radiation. PFCs in the divertor region of an ITER-like device, where non-fuel components are removed from the plasma, must withstand intense particle bombardment and heat loading. Tungsten (W) is currently the leading candidate material for the ITER divertor, because of its superior material properties such as a high melting temperature, high thermal conductivity, low tritium retention, and low sputtering yield due to high surface energy [190], [191]. Steady-state heat loading during nuclear operation in ITER could exceed 10 MW m^{-2}, which would raise surface temperatures above 1373 K [19], [79]. In addition, buildup of pressure along the plasma edge induces edge-localized modes (ELMs), which can impart up to 10 MJ m^{-2} of additional heating onto the divertor surface at the strike point [28]. Thermal spikes caused by transient events, such as ELMs, can cause significant material damage in the form of cracking, melting, and vaporization [13]. Splashing of a molten surface layer adds impurities to the plasma; a W atomic concentration above 10^{-5} could shut down the reaction (via plasma quench) [3]. Electron beams [85] and plasma accelerators [15], in addition to pulsed ms lasers, have been used in a laboratory setting to investigate the impact that ELM events have on PFC damage and erosion. Results obtained have revealed the presence of clear thermal damage regimes that depend on the intensity, duration, frequency, and quantity of ELM events.

The addition of high-flux He^+ ion irradiation blurs damage thresholds due to the growth of a fiber-form nanostructure, known commonly as "fuzz". First observed in work performed in [36], fuzz tendrils grow from the W surface due to the formation and movement of He bubbles in the subsurface. The exact formation mechanism remains unclear [38], [50], [97], [192], but many different experiments have revealed how nanostructure growth impacts material strength. A fuzzy W surface exhibits a lower sputtering yield, lower hydrogen retention, and higher resistance to cracking under transient heat loading [190], [193]. Experimental findings also have revealed a significant drop in thermal conductivity with fuzz formation [56]. As a result, fuzz tendrils appear to undergo melting via localized tendril conglomeration when exposed to ELM-like heat loading at lower intensities (as presented in Chapters 4 and 5). Gradual surface melting on

a nanostructured surface makes it difficult to define the exact change in melting threshold. Work performed in [194] found that ELM intensities exceeding 0.5 MJ m^{-2} led to the complete disappearance of the fuzz nanostructure and did not result in any splashing. However, some areas of the W divertor will be exposed to simultaneous He$^+$ ion irradiation and ELM-like heat loading [193], which could produce significant fuzz nanostructure if ELM heat fluxes are insufficient to "heal" the surface. Characterizing the growth and deterioration of He-induced fuzz nanostructure during concurrent transient heat loading is therefore instrumental in predicting component lifetime and erosion.

Additional particle loading by deuterium ions (D$^+$) could interrupt the fuzz formation process and significantly impact the W surface response during an ELM event. D$^+$ ion irradiation has been shown to cause blister formation in W at low surface temperatures (320 – 815 K) [195]–[198]. Higher temperatures raise the thermal mobility of trapped D, producing a relatively smooth surface [199], [200]. Recent experiments have shown that the addition of D$^+$ to a He$^+$ ion irradiation (in either a mixture gas or a separate beam configuration) has inhibited both fuzz formation and blister formation [62], [63], [201]–[203], even though mixed gas exposures performed in PISCES-B still obtained minimal fuzz nanostructure growth [101]. The lack of blister formation has been attributed to the presence of near-surface He bubbles acting as a diffusion barrier, which prevents coalescence and growth of implanted D [62], [203]. The suppression of fuzz nanostructure was attributed to surface destabilization caused by rapid D desorption at high surface temperatures [202]. When ELM-like heat loading has been simultaneously applied to D$^+$ particle loading, D retention increased by ~ 40%, which conflicts with the theory of rapid desorption at elevated temperatures [204]. Increases in D retention were attributed to the formation of cracks from transient heat loading, which enhanced D mobility deeper into the material [204]. Investigations on the combined effect of simultaneous He$^+$ irradiation, D$^+$ irradiation, and ELM-like transient heat loading on gas retention and surface morphology remain largely unexplored due, in part, to the complex experimental setup required. Preliminary studies discussed in [23] reveal that adding D$^+$ to a simultaneous He$^+$ + ELM exposure reduces pore density and increases material erosion via splashing.

The study below expanded upon the work performed in [23] to examine how the ELM intensity impacts surface damage, erosion, and gas retention. Different radiation

environments expected in a fusion environment were carefully replicated using the UHFI-II irradiation facility to explore the synergistic effects between He^+ irradiation, D^+ irradiation, and ELM-like heat loading applied using a pulsed laser. Cross-sectional imaging provided insight into trapping and desorption of different gas species during a thermal shock. Analyzing changes in surface morphology with both loading environment and ELM intensity revealed the effect of concurrent ion irradiation on surface melting. Expectations of ELM-induced melting and splashing were revisited using spectroscopy-based erosion analysis. Conducting more multi-species irradiation experiments going forward is key to optimizing PFC design and anticipating long-term material concerns.

6.2   Experimental setup

Radiation exposures were conducted in the UHFI-II (Ultra-High Flux Irradiation) chamber within the Center for Materials Under Extreme Environment (CMUXE) at Purdue University. The UHFI-II irradiation chamber is specifically designed to study the complex synergistic effects between particle loading and heat loading expected in a fusion environment; previous manuscripts reveal some of the valuable results obtained with the facility [23], [63], [202]. All experiments were performed on 10 mm $\times$ 10 mm $\times$ 2 mm W samples (99.95% purity, Alfa Aesar) that were cut from a single sheet (cold-rolled and annealed). Prior to exposure, all samples were mechanically polished to a mirror finish.

Each experiment involved a combination of He^+ ion irradiation, D^+ ion irradiation, steady-state heat loading, and/or transient heat loading. Figure 6.1 shows a schematic of the UHFI-II facility, with each radiation source labeled. W samples were clamped to a resistive button heater that provided steady-state heating to yield a surface temperature of 1223 K. A PID controller was used to minimize temperature fluctuations. Two gridless End-Hall ion sources (Kaufman & Robinson, Inc.) were used to provide high-flux He^+ and D^+ irradiation at an ion energy of 100 eV. The ion fluxes and fluences varied depending on the experiment being performed. Using broad beam ion sources ensured homogeneous irradiation across the entire sample, and using low ion energies minimized differences in implantation and structuring at non-normal incidence (22.5°) [65]. Finally, ELM-like transient heat loading was replicated using a pulsed 1064 nm Nd:YAG millisecond (ms) laser. All pulses were 1 ms in duration and struck the sample at a repetition rate of 1 Hz.

Heating was even across the entire 1 mm spot due to a flat top spatial profile. The beam was focused onto the sample using a combination of different optics that removed ~ 33% of the original pulse energy; an additional 40% of the beam energy was lost due to surface reflection. Absorbed beam intensities were reported as energy densities (H_{THL}, units of MJ m^{-2}) or as heat flux factors (F_{HF}, units of MJ m^{-2} s$^{-1/2}$). F_{HF} values were calculated by dividing the energy density by the pulse duration $\left(F_{HF} = H_{THL}/\sqrt{t_p}\right)$. Metrics of intensity cannot solely predict material performance, but function to compare the surface response of differently sized ELMs.
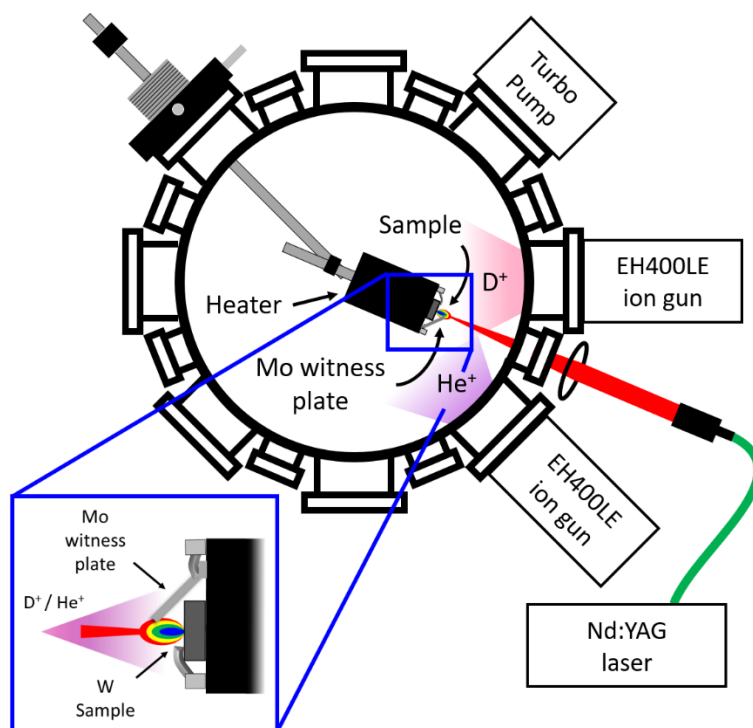
Figure 6.1: UHFI-II experimental setup schematic; inset shows witness plate schematic.

W samples were subjected to different radiation environments that investigated both the impact of He$^+$ and D$^+$ irradiation and the effect of differently sized ELMs on surface degradation and erosion. The experimental parameters for each exposure can be found in Table 6.1. "Laser" experiments imparted 3600 laser pulses onto the W surface at different energy densities. "Laser + He$^+$" experiments simultaneously imparted 3600 laser pulses and 100 eV He$^+$ irradiation at a flux of 6.0×10^{20} m^{-2} s^{-1} onto the W surface at different energy densities. Finally, "Laser + He$^+$ + D$^+$" experiments simultaneously imparted 3600 laser pulses, 100 eV He$^+$ irradiation at a flux of 3.0×10^{20} m^{-2} s^{-1}, and 100 eV D$^+$ irradiation

at a flux of 3.5×10^{20} m^{-2} s^{-1} onto the W surface at different energy densities. The ion fluxes used in the current study were similar to those in a previous study to maintain consistency and to enable crude comparative analysis [23]. Performing radiation exposures at different ELM intensities effectively builds off of the work conducted in [23] and reveals how thermal spikes caused by transient heat loading impact the migration of trapped gases and the onset of surface melting.

Table 6.1: Experimental parameters for radiation exposures performed with different loading conditions and different laser energies

Exp.	H_{THL} (MJ m^{-2})	F_{HF} (MJ m^{-2} s$^{-1/2}$)	He$^+$ flux (m^{-2} s^{-1})	He$^+$ fluence (m^{-2})	D$^+$ flux (m^{-2} s^{-1})	D$^+$ fluence (m^{-2})
Laser						
1	0.38	12	0	0	0	0
2	0.76	24	0	0	0	0
3	1.14	36	0	0	0	0
4	1.51	48	0	0	0	0
Laser + He$^+$						
5	0.38	12	3.0×10^{20}	1.08×10^{24}	0	0
6	0.76	24	3.0×10^{20}	1.08×10^{24}	0	0
7	1.14	36	3.0×10^{20}	1.08×10^{24}	0	0
8	1.51	48	3.0×10^{20}	1.08×10^{23}	0	0
Laser + He$^+$ + D$^+$						
9	0.38	12	3.0×10^{20}	1.08×10^{24}	3.5×10^{20}	1.26×10^{24}
10	0.76	24	3.0×10^{20}	1.08×10^{24}	3.5×10^{20}	1.26×10^{24}
11	1.14	36	3.0×10^{20}	1.08×10^{24}	3.5×10^{20}	1.26×10^{24}
12	1.51	48	3.0×10^{20}	1.08×10^{24}	3.5×10^{20}	1.26×10^{24}

A combination of imaging and spectroscopy was utilized to characterize the trapping and movement of gases below the surface and the degradation, melting, and splashing present on the surface. During every exposure, a molybdenum (Mo) witness plate was clamped to the sample holder and oriented at a 45° angle relative to the sample plane to collect any W material that could have been emitted due to ELM-induced splashing (depicted in the inset of Figure 1). After each irradiation, the Mo witness plate was removed and analyzed via ex situ X-ray photoelectron spectroscopy (XPS) with an Mg-Kα source (1253.6 eV). The surface composition was measured to look for the presence of W. Despite the overlap between the Mo 4p$_{3/2}$ signal (35.50 eV) and the WO$_3$ 4f$_{7/2}$ signal (36.1 eV),

qualitative changes in peak shape and location provide insight into the differences in W melting and splashing at different ELM intensities under varying ion irradiation environments [147], [205]. Peak analysis was conducted using commercial CasaXPS software [147]. Differences in W erosion were attributed to changes in surface morphology by imaging W samples after irradiation via field-emission scanning electron microscopy (FE-SEM). Additional imaging of the subsurface was conducted using a focused ion beam (FIB) to mill out a selected area within the exposed laser spot. FIB profiling provided valuable information on the trapping and movement of He bubbles with and without the added presence of concurrent D^+ irradiation. Investigating the synergistic effects between different forms of radiation expected in the divertor region helps refine predictions on material performance in an ITER-type device.

6.3   Effect of experimental loading condition on surface morphology and erosion

The thermal response of W to intense heat loads during an ELM event can be altered by the addition of particle loading. In this experiment, three different loading conditions that are expected in the divertor region of an ITER-type device were replicated using a combination of broad beam ion sources and a pulsed ms laser. As discussed in [191], trapping and migration of implanted He can cause fuzz formation, which lowers the thermal conductivity of the surface [56]. The addition of D^+ has inhibited fuzz growth, which has been attributed to rapid D desorption at the surface [23], [63]. Laser, Laser + He^+, and Laser + He^+ + D^+ exposures were conducted to further explore the interactions between implanted He and D on surface morphology evolution.

Initial characterization of the resultant surface morphology in the absence of pulsed laser heating effectively distinguishes surface damage caused by incident ions and incident laser photons. SEM micrographs in Figure 6.2 show the W surface away from the laser spot after exposures with no ion irradiation, He^+ ion irradiation, and simultaneous He^+ + D^+ ion irradiation. Grain boundaries were more difficult to observe on surfaces exposed to ion irradiation than the surface without any ion irradiation, due to small degrees of nanostructuring. Fuzz tendrils were clearly observed on the surface exposed to He^+ ion irradiation (Figure 6.2(b)). Pore formation was also present, which reflects the potential bursting of He bubbles at the surface. When W surfaces were exposed to simultaneous He^+

+ D$^+$ ion irradiation, fuzz nanostructure growth was inhibited, yielding a surface with rod-like structures that may reflect early-stage tendril growth (Figure 6.2(c)). The reduction in fuzz formation with the addition of D$^+$ ion irradiation was also observed in [202], and may be due to thermal stresses in the near-surface region caused by D super-saturation that result in minor annealing of the surface [111].
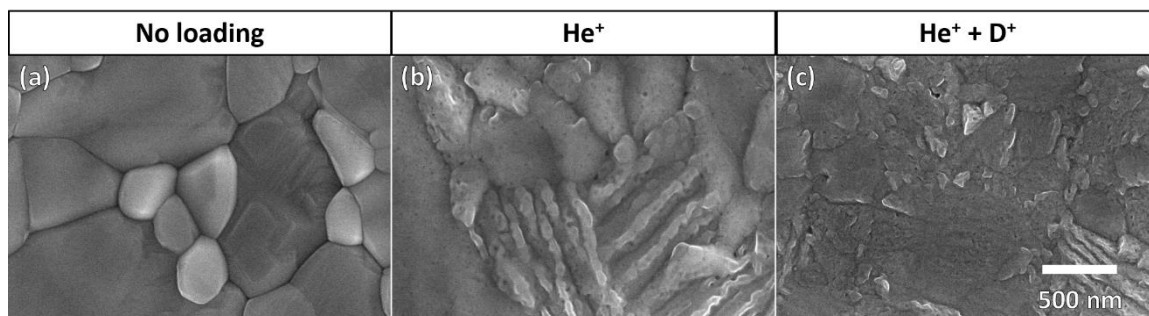
Figure 6.2: SEM micrographs of W surface after the following particle loading: (a) no loading, (b) He$^+$ loading, and (c) He$^+$ + D$^+$ loading without pulsed heat loading.

Within the laser-exposed area, the W surface exhibited significant thermal roughening, regardless of the loading condition. The SEM micrographs in Figure 6.3 illustrate the surface response due to 1 h exposures with different loading conditions at a laser energy density of 1.51 MJ m^{-2} (48 MJ m^{-2} s$^{-1/2}$). Low-magnification and intermediate-magnification images reveal the formation of a shale-like morphology on all samples. A similar shale-like morphology was observed in [23] and [145], albeit at a lower laser energy density. Studies performed in [28] also obtained a similar shale-like morphology to that observed in Figure 6.3(a). The addition of D$^+$ ions marginally reduced the degree of roughening and produced a more molten surface (Figure 6.3(c, f)). The roughening caused by the incident laser photons can be attributed to thermal stress in the near-surface region, which deformed the material plastically.
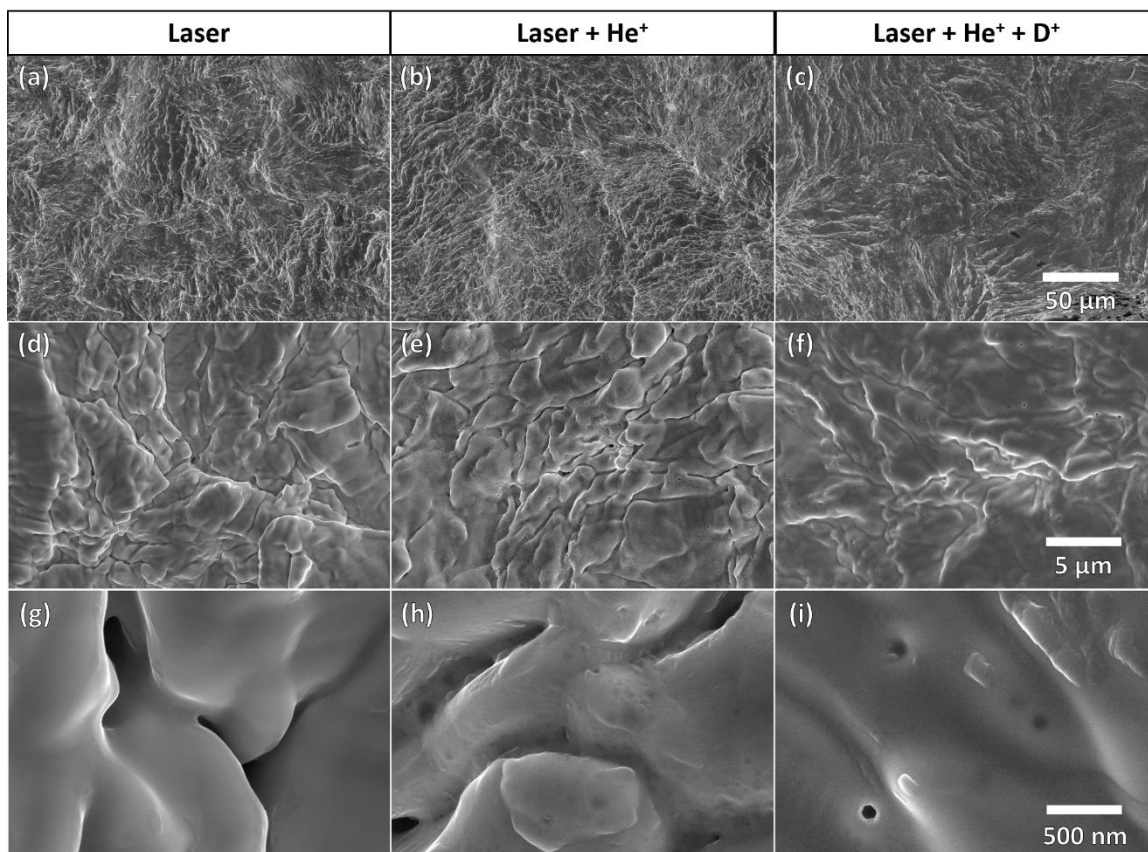
Figure 6.3: SEM micrographs of W surface after (a, d, g) laser only loading, (b, e, h) laser + He$^+$ loading, and (c, f, i) laser + He$^+$ + D$^+$ loading at a laser energy density of 1.51 MJ m^{-2}.

Crack formation was inhibited within the laser-exposed area, due to the steady-state heating being applied to the sample during each exposure. Surface cracking along the periphery of the spot on the laser only exposed sample, shown in Figure 6.4, was likely due to large thermal gradients around the spot edge. Bubble nucleation in the near-surface region due to concurrent ion irradiation appeared to reduce thermally-induced stress, effectively increasing the cracking resistance, as observed in [136]. The characteristic size of the microstructure did not change with the introduction of concurrent ion irradiation, illustrating that the structure formation was solely due to laser heating.
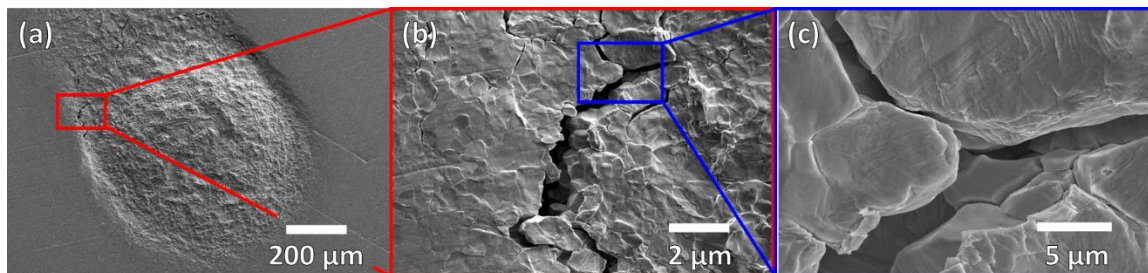
Figure 6.4: SEM micrographs of periphery of W spot exposed to 3600 pulses of laser only loading at 1.51 MJ m^{-2}.

At higher magnifications, subtle differences in surface morphology due to different loading conditions illustrate how D$^+$ irradiation might prevent fuzz growth. The smooth folds and ridges seen on the surface in Figure 6.3(g) were caused by annealing and subsequent roughening of the surface. Significant enhancements in areal pore density with the addition of He$^+$ ion irradiation indicate the competition between He$^+$-induced fuzz growth and ELM-induced tendril conglomeration (Figure 6.3(h)). As seen in Chapters 4 and 5, ELM-like heating of a fuzz nanostructure promotes tendril melting and reintegration. However, since ELM-like heating and He$^+$ ion irradiation were applied simultaneously to the W surface, growth and destruction mechanisms competed to produce the resultant surface. At 1.51 MJ m^{-2}, the laser pulses were of sufficient intensity to stunt fuzz growth. Pores along the surface were formed by helium implantation, bubble growth, and subsequent migration toward the surface, as seen in [23]. Small ripples along the surface were likely artifacts of early-stage fuzz tendril destruction driven by a high laser intensity. The appearance of small fuzz tendrils on W surfaces exposed to simultaneous He$^+$ irradiation and pulsed laser loading in [206] was likely due to higher ion flux and the decreased base temperature, which would have enhanced bubble growth and reduced thermal annealing and melting of the surface. The current lack of other simultaneous He$^+$ + ELM loading exposures limits the conclusions that be drawn about the effect of concurrent pulsed heat loading on the behavior of helium-induced fuzz nanostructure. Adding D$^+$ ions to the radiation exposure appeared to suppress near-surface pores and early-stage tendril growth, producing a relatively smooth surface (Figure 6.3(i)). Some pores were still observed within the exposed area, but their formation is unclear. Since the W sample was heated to a base temperature of 1223 K, a significant amount of D would have desorbed shortly after being implanted, since the highest deuterium traps in W (at low

ion energy) occur at around 2 eV (maximum desorption temperature ~ 1100 K) [207]. Imaging of the surface cannot solely determine whether the smooth surface was produced via continuous D implantation and desorption, or if thermal shocks caused deeper D and He trapping and inhibited surface structuring. Incident He$^+$ would have implanted deeper into the surface than incident D$^+$, suppressing He bubble migration (fuzz formation) and reducing pore formation, as seen in Figure 6.2(c) [203]. The intense laser heating further reduced any evidence of fuzz tendril growth. Further D$^+$ ion irradiation studies at high temperatures (> 1200 K) are needed to isolate the effect of D$^+$ ions on the suppression of fuzz nanostructure without the additional heating of the incident laser pulse.

Comparing the cross sections of irradiated samples begin to reveal the complex interactions between implanted He and D on the resultant surface morphology. FIB milling was performed on W samples that were exposed to laser + He$^+$ and laser + He$^+$ + D$^+$ irradiation at a laser energy density of 0.76 MJ m^{-2} (24 MJ m^{-2} s$^{-1/2}$) to produce the cross-sectional SEM images shown in Figure 6.5. Cross-sectional SEM images were taken from 0.76 MJ m^{-2} samples, since subsurface bubbles and traps would be more apparent at lower ELM intensities. The presence of numerous tendril-like structures close to the surface in Figure 6.5(a) could be due to early-stage, He-induced fuzz formation. High heterogeneity along the surface in the form of ripples and folds (as seen in Figure 6.3(h)) can be attributed to intense thermal roughening. Randomly distributed, nanoscopic voids near the surface were due to He bubble growth, as seen in [191] for early-stage fuzz formation. In the absence of periodic thermal shocks, helium bubbles would have driven the growth of a fully developed fuzz nanostructure, as seen in [23]. Adding D$^+$ to the exposure yielded a much smoother surface and reduced the areal density of early-stage fuzz tendrils (Figure 6.5(b)). The lack of surface roughening in Figure 6.5(b) remains poorly understood, but could be partially due to rapid desorption of D near the surface and/or deeper gas trapping, creating a smooth surface devoid of He bubbles.
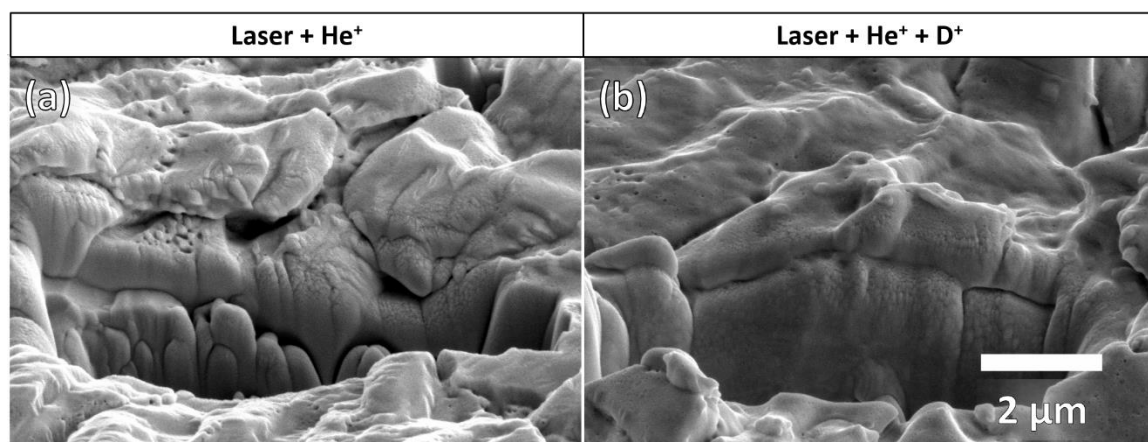
| Laser + He$^+$ | Laser + He$^+$ + D$^+$ |

Figure 6.5: FIB micrographs of W cross section after (a) laser + He$^+$ loading and (b) laser + He$^+$ + D$^+$ loading at a laser energy density of 0.76 MJ m^{-2}.

Measurements of material erosion were made using a Mo witness plate to determine whether the presence of D$^+$ ions enhanced surface melting and droplet splashing. Repetitive transient heat loading of a molten surface has been shown to cause splashing via shock-induced fragmentation [152]. Some studies have attributed splashing to the occurrence of a Kelvin-Helmholtz instability along the molten surface [68], [163]. Measuring changes in erosion with the addition of concurrent ion irradiation reveals the role of gas implantation and migration on thermal strength. After each exposure, XPS scans of Mo witness plates were conducted to detect the presence of W. Survey scans revealed the presence of Mo, W, oxygen, and carbon (figure not shown). Region scans of the W 4f signal from witness plates that were used in the three 1.51 MJ m^{-2} (48 MJ m^{-2} s$^{-1/2}$) exposures are shown in Figure 6.6 (along with a reference scan of a pristine Mo surface). Signal intensities obtained are not comparable between scans, due to differences in witness plate geometries and variations in vacuum pressure in the XPS analysis chamber. Figure 6.6(a) shows the Mo 4p peak (composed of Mo 4p$_{3/2}$, MoO$_2$ 4p$_{3/2}$, and MoO$_3$ 4p$_{3/2}$ signals) present on the witness plate. The laser only exposure (Figure 6.6(b)) caused some measurable degree of W erosion, due to the appearance of two bumps within the combined peak at 36.1 eV and 38.3 eV, representing the WO$_3$ 4f$_{7/2}$ and WO$_3$ 4f$_{5/2}$ signals [205]. Unoxidized peaks were not observed, which indicates that the W eroded onto the witness plate experienced oxidation during sample transfer between vacuum chambers. No significant oxidation was expected inside the irradiation chamber, since the base pressure was ~ 10^{-7} torr. The addition of He$^+$ ions to the radiation exposure also yielded distinct WO$_3$ peaks, but produced an additional

peak around 32 eV. The W $4f_{7/2}$ signal is found around 32 eV, so some of the eroded W remained unoxidized during sample transfer. The difference in W oxidation could be due to differences in the surface roughness of the Mo witness plate, the length of time that the Mo sample was exposed to an ambient environment, or an increase in the size of eroded W droplets (higher surface to volume ratio = decrease in W oxidation). An increase in the relative magnitude (compared to the combined Mo 4p/WO$_3$ 4f peak) of the W $4f_{7/2}$ peak with the addition of D$^+$ could be attributed to an increase in molten droplet size, but further experiments are needed to rule out the other two factors dealing with witness plate preparation and handling.
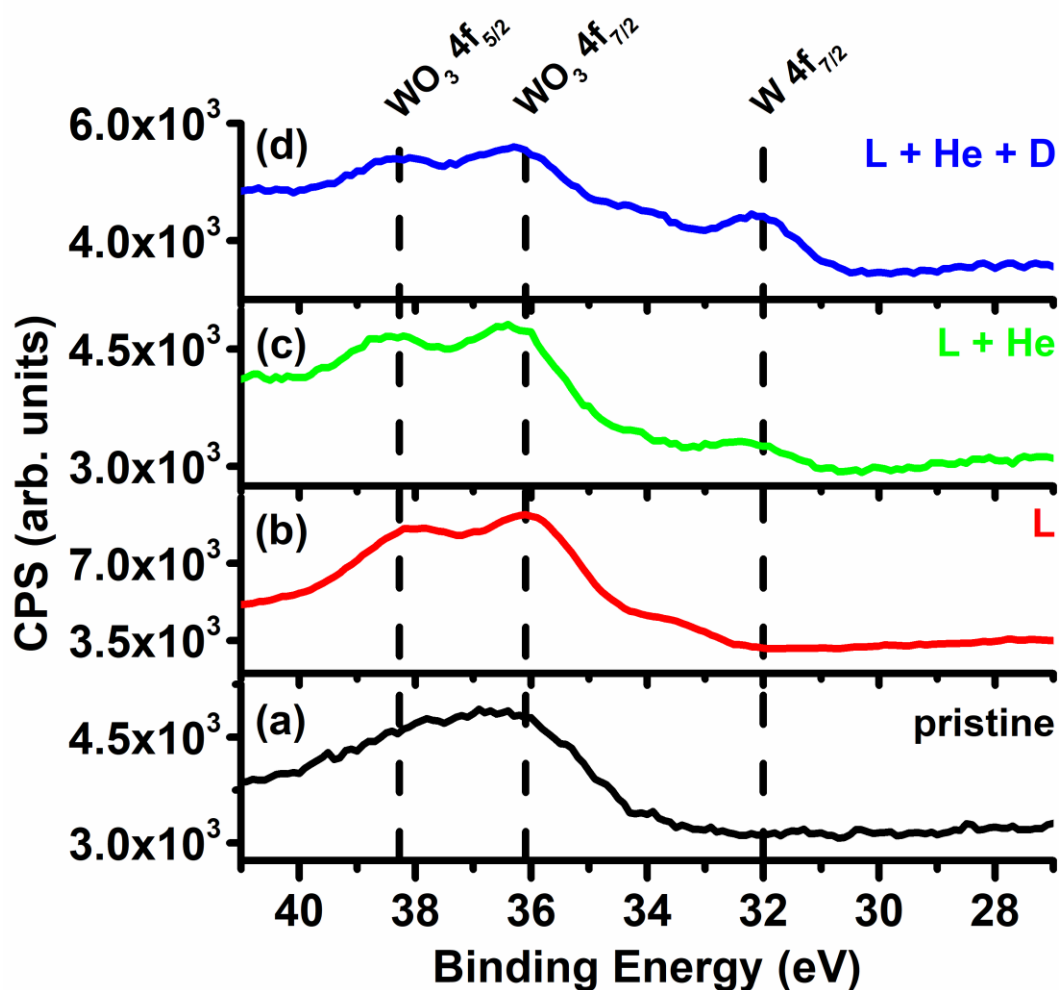
Figure 6.6: XPS region spectra of W 4f signal on Mo witness plates exposed to different irradiations at a laser energy density of 1.51 MJ m^{-2}; (a) pristine Mo sample, (b) laser loading, (c) laser + He$^+$ loading, and (d) laser + He$^+$ + D$^+$ loading (all at 1.5 MJ m^{-2}).

Additional heating caused by lattice stress from D super-saturation could explain an increase in W erosion. Studies in [201] hypothesize that simultaneous He$^+$ and D$^+$ ion irradiation causes super-saturation of D in the near-surface region (implanted He acts as a diffusion barrier), which induces additional stresses on the lattice. The buildup of thermal stress in the material caused by large-scale D trapping lowers the threshold for melting, subsequently relieving internal stresses and producing the smooth surface seen in Figure 6.3(i). Additional analysis of surface evolution (via real-time surface temperature measurements) and desorption (via thermal desorption spectroscopy) during pulsed heat loading in the presence of D$^+$ ion irradiation is needed to confirm erosion measurements.

6.4 Effect of laser energy density on thermal response

The ultimate performance of a divertor PFC will not only depend on stresses induced by gas implantation, but also on the intensity of ELMs that strike the surface. Varying the amount of energy deposited on the W surface significantly impacts the level of surface roughening, melting, and splashing. The heat flux has been used in many different studies as the primary metric to assess material damage expected during an ELM event [15], [33], [148]. While other parameters, such as the duration [208], frequency [28], pulse shape [86], base temperature [209], and quantity [210] will also affect surface response, the ELM intensity remains the most direct and widely used criterion. Both the energy density (H$_{THL}$) and the heat flux factor (F$_{HF}$) are commonly used to quantify the ELM intensity. Work presented in Chapters 4 and 5, as well as external studies in [149] and [211], have investigated the thermal strength of W when exposed to sequential or simultaneous He$^+$ or D$^+$ ion irradiation, but laboratory research has not yet examined the combined effect of simultaneous He$^+$ and D$^+$ ion irradiation on material degradation and splashing at different ELM intensities. Comparing how implanted He and D gases affect morphology evolution and thermal strength at varying laser energy densities closely replicates divertor conditions near the strike point, which helps inform acceptable ELM operating windows.

Increasing the heat flux factor to the surface appeared to reduce surface structuring and inhibit gas migration to the surface. SEM micrographs of the W surface after 1 h laser + He$^+$ + D$^+$ exposures at increasing laser energy densities are shown in Figure 6.7. At 0.38 MJ m^{-2} (12 MJ m^{-2} s$^{-1/2}$) (Figure 6.7(a, e)), the W surface did not appear to experience any

degree of surface melting, and yielded a surface very familiar to that shown in Figure 6.2(c) without pulsed laser heating. Previous studies have measured the damage threshold on W to occur between 0.19 and 0.38 MJ m^{-2} (at a base temperature of 1273 K), so the lack of surface degradation is to be expected [164]. Radiation exposures conducted at a laser energy density of 0.76 MJ m^{-2} and above yielded a shale-like microstructure, as seen in Figure 6.3(f) and in [23]. The appearance of a shale-like morphology on W samples exposed to laser and laser + He$^+$ loading indicate that micron-scale surface roughening was primarily due to pulsed laser heating. Images taken at an intermediate magnification revealed that surface melting became more dominant as the ELM intensity increased (Figure 6.7(b-d)). Phase transitions began to occur within the exposed area as the heat flux factor increased; the onset of melting relieved thermal stresses and yielded a smoother surface. High-magnification micrographs (Figure 6.7(f-h)) reveal that enhancements in surface melting at higher laser energy densities was accompanied by a decrease in the areal density of surface pores. In addition, the pore size significantly increased at higher heat fluxes. Based on the lack of pores seen from D$^+$ ion irradiations in other work [195], [204], [212], the appearance of pores can be solely attributed to movement of He in the near surface region. Surface imaging is insufficient to determine whether the overall amount of D desorption substantially changed as the heat flux factor increased. The decrease in pore density accompanied by the increase in pore size could be due to thermal shock-induced clustering of He bubbles. Increases in fuzz tendril size with increasing surface temperatures during He$^+$ ion irradiation illustrated that higher temperatures might produce larger He bubbles [43]. While fuzz nanostructure was not observed due to potential super-saturation of D in the near-surface, He bubble migration was still expected, producing the pores seen in Figure 6.7. Further research, utilizing depth profiling (via nuclear reaction analysis) and desorption measurements (via thermal desorption spectroscopy), are needed to elucidate the changes in trapping and desorption of He and D when exposed to ELM-like heat loading.
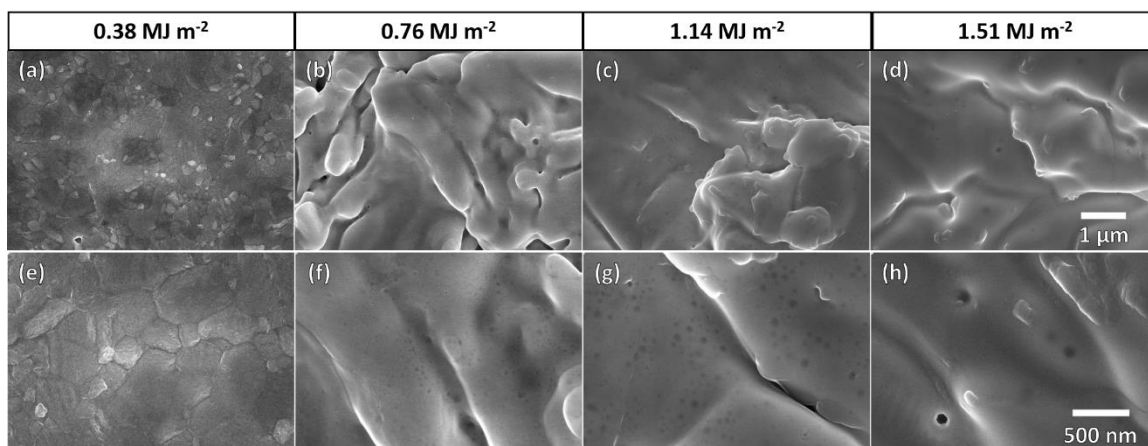
Figure 6.7: SEM micrographs of W surface after laser + He$^+$ + D$^+$ loading at a laser energy density of (a) 0.38 MJ m^{-2}, (b) 0.76 MJ m^{-2}, (c) 1.14 MJ m^{-2}, and (d) 1.51 MJ m^{-2}.

Measurements of material erosion were made at different laser heat flux factors to determine whether significant changes in surface morphology with the addition of D$^+$ ion irradiation impacted splashing intensity. Similar to the erosion analysis presented in section 6.3, Mo witness plates were analyzed after radiation exposures using XPS. Survey scans showed the presence of Mo, W, oxygen, and carbon (figure not shown). Region scans of the W 4f signal were taken to investigate the effect of the laser energy density on the shapes and locations of different peaks. Figure 6.8 shows the W 4f region scans performed on Mo witness plates after laser + He$^+$ + D$^+$ exposures at different energy densities (a scan from a pristine Mo sample is also included). Surprisingly, the shape of the combined W 4f and Mo 4p peak did not change significantly at different energy densities. Even exposures conducted at a laser energy density of 0.38 MJ m^{-2} resulted in measurable W erosion, as evidenced by small peaks at 36.1 and 38.2 eV (locations of the WO$_3$ 4f$_{7/2}$ and WO$_3$ 4f$_{5/2}$ peaks, respectively). Since melting was not observed at 0.38 MJ m^{-2} (Figure 6.7(e)), any degree of W erosion was not due to droplet splashing. Surface degradation caused by ELM-like heat loading might have reduced the energy threshold for physical sputtering by incident D$^+$ and He$^+$ ions to below 100 eV [102], [114]. However, further experiments would be needed to examine the possibility of physical sputtering. WO$_3$ peaks were also observed on Mo witness plates exposed to laser + He$^+$ + D$^+$ radiation exposures at 0.76 MJ m^{-2}, 1.14 MJ m^{-2}, and 1.51 MJ m^{-2} (Figure 6.8(c, d, e)). Distinct trends in erosion with heat flux factor observed from ELM-like heat loading studies done with and without He$^+$ ion irradiation (presented in Chapters 3 and 4) demonstrate the clear impact of D$^+$ on material
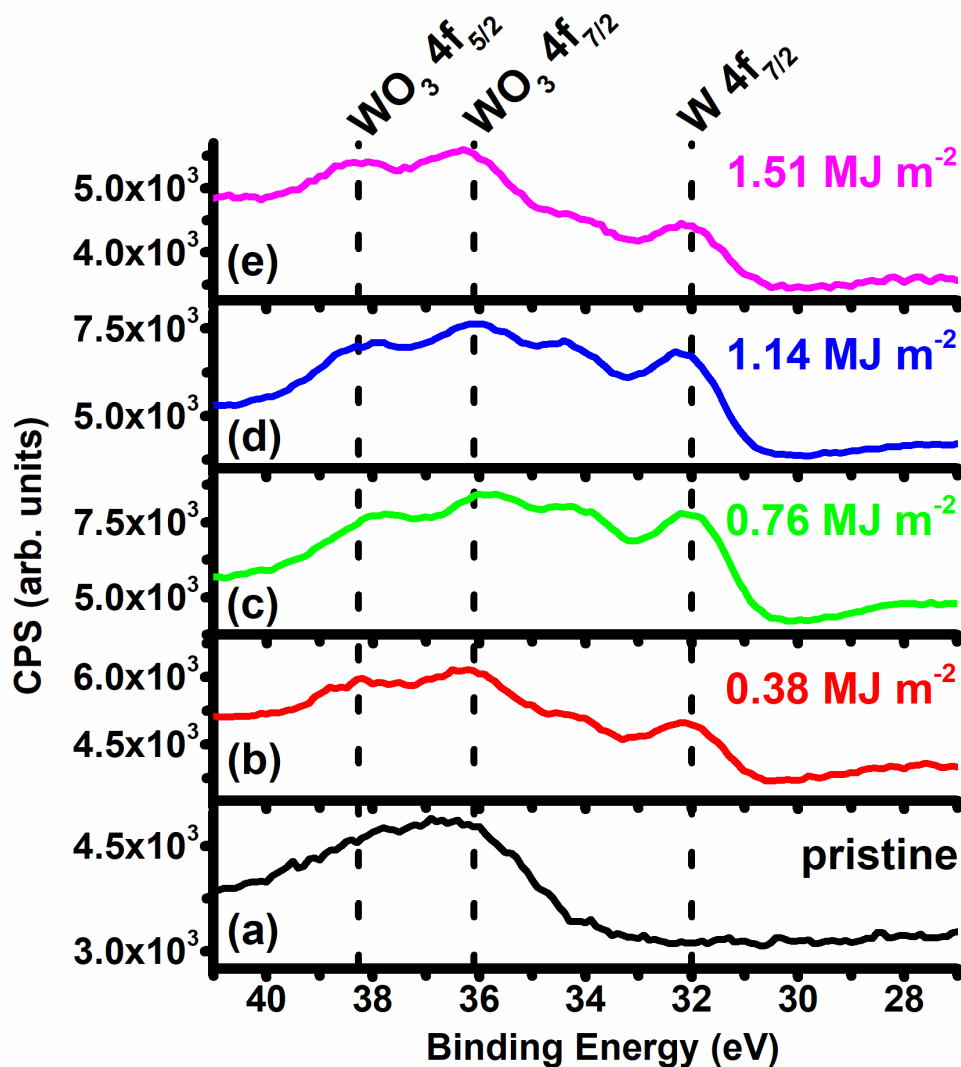
Figure 6.8: XPS region spectra of W 4f signal on Mo witness plates exposed to laser + $He^+ + D^+$ loading at the following energy densities: (a) pristine Mo sample, (b) 0.38 MJ m^{-2}, (c) 0.76 MJ m^{-2}, (d) 1.14 MJ m^{-2}, and (e) 1.51 MJ m^{-2}.

strength. The lack of a distinct increase in erosion with laser energy density, as observed in Figure 6.8, indicates that potential super-saturation of D in the near-surface region might have controlled the resultant thermal strength, limiting the effect of energy density on erosion. However, the magnitude of the W $4f_{7/2}$ peak did fluctuate at different laser intensities, which potentially reflects the level of W oxidation that occurred during sample transfer. Changes in the intensity of the peak at 32 eV could have been due to increases in droplet/particle size, lowering the relative amount of oxidized W. SEM images in Figure 6.7 indicated that increasing the energy density enhanced surface melting, but did not

provide information on the mechanism of droplet splashing. Real-time imaging of eroded W droplets (or particles) during radiation exposure, as shown in [68], would explain the differences in W oxidation observed at different laser heat flux factors.

6.5   Summary

ELM-like heat loading, accompanied by simultaneous dual beam He^+ and D^+ ion irradiation on W samples, was explored for the first time at different energy densities to characterize the synergistic effects between implanted gases on surface morphology and erosion. A pulsed ms laser was used to replicate transient heat loading caused by ELM events. Three different experiments were performed to examine the effect of laser only loading, laser + He^+ loading, and laser + He^+ + D^+ loading. All exposures caused the formation of a shale-like microstructure that did not vary with the addition of ion irradiation. W samples exposed to laser + He^+ + D^+ loading exhibited a slightly smoother surface (evident at high magnifications) than those exposed to laser + He^+ loading, which was likely due to a suppression of He-induced structure formation caused by the super-saturation of D. Cross-sectional SEM images revealed a distinct decrease in the presence of early-stage, fuzz-like tendrils with the addition of D^+ ion irradiation, yielding a more homogeneous subsurface, potentially caused by irradiation-enhanced recrystallization. While all three loading conditions yielded W erosion at a heat flux factor of 1.51 MJ m^{-2}, relative changes in the amount of oxidized W measured indicate that the addition of He^+ and D^+ could have increased the size of droplets that were emitted from melt layer splashing.

Changing the laser intensity did not have a significant impact on W erosion, but did affect the migration of implanted He bubbles. Thermal damage, in the form of surface roughening or melting, was not observed at 0.38 MJ m^{-2} (12 MJ m^{-2} $s^{-1/2}$), because the intensity was close to the damage threshold for W. Higher energy density exposures yielded significant pore formation accompanied by a shale-like microstructure. The formation of pores were attributed to the migration of He bubbles toward the surface, due to the lack of pore formation observed due to D^+ ion irradiations of W. As the heat flux factor of the laser increased, the pores became less numerous and more massive. Increases in fuzz tendril size observed in previous studies as the surface temperature increased

indicated that the change in pore size was solely due to transient heat loading. The implanted D therefore functioned to minimize early-state nanostructure formation in a potentially super-saturated, near-surface layer. Measurements of thermal desorption within a spot exposed to ELM-like heat loading could reveal whether He desorption is related to the areal density and size of surface pores. Erosion analysis revealed that the addition of D^+ irradiation resulted in mass loss at 0.38 MJ m^{-2}, which conflicted with the lack of observable damage on the surface. Future studies will have to investigate whether ELM-like heat loading might reduce the energy threshold for physical sputtering. Erosion at higher laser intensities was attributed to melt layer splashing. However, a clear dependence on energy density was not observed. Since XPS witness plate analysis only effectively reveals the presence of W erosion, other *in situ* erosion measurement techniques need to be considered to comprehensively define ELM parameters that will avoid unsustainable levels of splashing and erosion. Developing a database of erosion measurements from different laboratories will ultimately reveal the true response of a W divertor surface in an ITER-type device.

7. SUMMARY

Investigating the response of different plasma facing component (PFC) candidate materials to events of high intensity, pulsed heat loading was conducted to examine how thermal shock performance might be diminished in a fusion environment when exposed to high-flux particle loading. Experimental campaigns involved exposures to different types of pulsed heat loading with and without additional He^+ and D^+ irradiation under different sequencing (sequential and simultaneous). Material testing was performed on W, which is currently the leading PFC candidate material, and Mo, which has been considered as a promising alternative material. Results obtained throughout the dissertation show that previous predictions on divertor PFC performance due to ELM heat loading may need to be revised to consider additional surface evolution caused by impinging He^+ and D^+ ions. Changes in the mechanical and thermal strength of the loaded surface were studied by using a combination of *in situ* and *ex situ* analysis techniques. The effects of different radiation environments on performance were assessed by examining the irradiated surface for the presence of melting and measuring any eroded material. Conclusions on the consequences of ion-induced surface structuring will help inform future PFC design to optimize component lifetimes and plasma performance.

The impact of ELM heat loading on surface degradation and melting was investigated in Chapter 3 to provide a baseline for comparison with experiments that incorporated additional particle loading. Mechanisms of thermal damage, such as roughening, melting, and splashing, occurred at clearly defined ELM intensity thresholds. The onset of surface melting between 1.0 and 1.4 MJ m^{-2} was accompanied by the presence of ripples that reflected the radial movement of the melt layer. The periodicity of the ripples were measured to assess the intensity of melting induced by laser heating. Grain growth was not observed as a function of ELM intensity above the melting threshold. Analysis of ELM-induced erosion revealed a distinct transition region around 1.2 MJ m^{-2}, where the intensity of emitted photons and the magnitude of erosion increased nonlinearly. Large increases in particle emission above a specific ELM intensity reinforce the importance of ELM mitigation to minimize plasma contamination.

Incident He$^+$ ion irradiation has been shown to reduce the thermal conductivity of the loaded surface by driving nanoscale tendril growth due to the thermally-enhanced migration of He vacancies, as seen in Chapters 4 and 5. Higher ion energies were shown to increase the thickness of the fuzz nanostructure layer, due to deeper implantation of He$^+$ ions. He clusters trapped over a larger depth at higher ion energies enhanced nanostructure growth. Pulsed heat loading of fully-formed fuzz tendrils resulted in localized melting driven by nanostructure conglomeration. The poor heat diffusion in the nanowires caused overheating, and the nanostructure began to melt and conglomerate. After 1000 laser pulses on fuzzy W surfaces, fuzz nanostructures had completely disappeared, even at an energy density of 0.76 MJ m^{-2}. Pulsed heat loading at 0.38 MJ m^{-2} and 1 Hz did not result in any noticeable thermal damage on the loaded surface, keeping the fuzz tendrils unaltered. Erosion of W fuzz nanostructures was directly measured due to pulsed heat loading at 0.76 MJ m^{-2} and above, revealing that nanostructure conglomeration may result in some splashing. Results did not show any clear evidence that the thermal strength of the material returned to that of an unirradiated surface after tendril structures disappear. Comprehensive erosion analysis conducted in sequential He$^+$ irradiation and laser loading studies (Section 4.3) revealed that the laser-produced plasma plume yielded lower photon intensities after 200 laser pulses. The decrease in photon intensity could be linked to the gradual disappearance of the fuzz nanostructure. ELM mitigation has been proposed as one solution to minimize thermally-induced damage. Therefore, pulsed heat loading studies were performed on W fuzz surfaces at varying repetition rates to reflect the increase in ELM frequency during mitigation. One experiment kept the energy density constant, while varying the laser repetition rate, and another experiment kept the total power constant, while varying both the laser repetition rate and the energy density. Constant energy density exposures found that at higher repetition rates, the loaded surface became smoother, inhibiting He-induced structure formation. Constant power exposures found that increasing the repetition rate significantly reduced the degree of thermally-enhanced degradation and decreased ELM-induced erosion. Pulsed heat loading at 10 Hz did not interrupt fuzz formation and inhibited particle emission. However, if mitigation failed in a reactor environment, the unaffected fuzz nanostructure could then yield much higher erosion rates than that of a pristine surface. Therefore, ELM mitigation needs to determine safe windows

of operation that will minimize both He-induced fuzz formation and ELM-induced melting. Finally, the surface response of cold-rolled, annealed W samples with a longitudinal grain orientation studied throughout this dissertation was benchmarked against transversally-oriented W samples that will be used in ITER. The prominence of grains oriented perpendicularly to the loaded surface in ITER-grade W resulted in lower cracking thresholds and reduced plastic deformation. Radiation hardening due to He^+ ion irradiation appeared to weaken ITER-grade W preferentially, increasing the cohesive energy of grain boundaries and enhancing brittle failure. Therefore, radiation exposures on the W materials presented throughout this dissertation may have underestimated the degree of brittle failure in a reactor environment.

The impact of D^+ irradiation on surface morphology during simultaneous laser + He^+ + D^+ loading was explored as a function of loading condition and ELM intensity. While none of the surfaces exhibited significant structure formation, small degrees of surface roughness due to laser + He^+ loading disappeared with the addition of D^+ loading. The mechanism by which incident D^+ ions contributed to a smooth surface remains unknown and requires cross-sectional analysis. However, potential super-saturation of D near the surface due to the presence of a diffusion barrier by implanted He^+ ions could have induced thermal stress in the lattice, which led to enhanced recrystallization. Thermal desorption measurements of D with and without simultaneous He^+ loading would provide more insight into the significant change in surface morphology with D^+ loading. Particle erosion was enhanced with the addition of He^+ ions and D^+ ions. However, witness plate measurements were unable to determine whether physical sputtering was present, in addition to ELM-induced splashing. Changing the intensity of ELMs did not have a clear influence on net erosion in the presence of D^+ ion irradiation, which could be due to the dominant impact of D super-saturation on the thermal response of the surface. Future research needs to examine whether changes in gas implantation and migration due to simultaneous He^+ + D^+ ion irradiation may substantively impact the thermal strength of the loaded surface.

While the experiments conducted in the thesis reveal evidence on how incident plasma species might impact the thermal and mechanical response of divertor PFCs, many mechanisms remain uncertain and experimentation in a true fusion environment needs to be expanded. Using real reactor systems such as those in JET and DIII-D (DiMES) for

careful plasma-material interactions research will qualify the usefulness of laboratory findings. No linear plasma device or heat loading system will be able to truly replicate the exact conditions present in a reactor. Therefore, regularly isolating key damage mechanisms in the lab and comparing them to reactor findings maximizes the productivity and rate of progress in the plasma-facing materials community.

7.1   Suggestions for future work

Observed reductions in thermal strength due to high-flux particle loading expected in a fusion environment necessitate further research to quantify changes in material response. Most of the work presented throughout this dissertation focuses on qualitative comparisons between surfaces exposed to different radiation environments. While the experiments provide insight into the mechanisms governing fuzz formation and ELM-induced erosion, advanced PFC design requires additional quantification to ensure high material performance in future fusion reactors.

Developing a database on erosion rates due to ELMs of different parameters is critical to predicting impurity concentrations in fusion plasmas. ELM-induced splashing may occur in an ITER-type device, and lead to quenching of the plasma due to intense line radiation. Previous laboratory experiments have utilized microbalances to measure erosion caused by intense heat loading. However, ambient exposure will contaminate samples due to oxidation and dust collection. Detecting microgram or nanogram levels of erosion require precise, *in situ* measurement techniques. Work in Chapters 3, 4, and 5 illustrated how quartz crystal microbalances (QCM) may be incorporated into pulsed heat loading experiments to measure the presence and rate of erosion. However, the use of a QCM in this capacity remains underdeveloped and requires further benchmarking to ensure results that are accurate on an absolute basis. Using witness plates, as shown in Chapters 4 and 6, produced very stable results, but may present setup challenges, due to the need for mounting hardware that can withstand the harsh radiation environment present during an exposure. In addition, witness plates function well to determine whether erosion occurred via XPS analysis, but do not provide information on erosion rates and are difficult to compare to one another. Developing a system where samples could be weighed to a fine degree (< 10 µg) without exposure to an ambient environment would be optimal, but

difficult to implement. Quantitative erosion metrology development is one of the keys to producing reliable predictions on material performance.

Radiation experiments could derive more insightful conclusions if the mechanisms behind fuzz formation were refined. Many different theories have been proposed for the growth of fiber-form nanostructures in response to low-energy, high-flux He^+ ion irradiation. However, scientists in the field remain divided on which theory most closely approximates true behavior. While experimental discovery has quantified the changes in mechanical and thermal properties of the W surface due to fuzz formation, theoretical and computational efforts are needed to explain why these changes occur. Additional modeling of He clustering and subsequent cluster migration through the W lattice will refine how bubbles interact with the surface (rupture vs. viscoelastic tendril growth). He^+ ion irradiation experiments performed at high fluxes and increasing fluences would reflect early-stage tendril growth; cross-sectional analysis at each fluence step may reveal the development of He bubbles and the role that the He bubbles play in nanostructure formation.

The synergistic effects between incident He^+ and D^+ ions on surface evolution at high temperatures remain underdeveloped. While results in Chapter 6 attributed the reduction in surface roughness with D^+ irradiation to super-saturation in the near-surface region, the mechanism behind this process is not understood. Previous studies have hypothesized that at equal ion energies, impinging He^+ ions will cluster at larger depths than impinging D^+ ions. As a result, He clusters will act as a diffusion barrier, and limit D implantation to a maximum depth, causing super-saturation. However, at high surface temperatures, implanted D would become desorbed. Performing irradiation experiments with post-mortem thermal desorption spectroscopy (TDS) would reveal whether D would remain trapped or become desorbed. The degree of D desorption could then be compared between experiments with and without simultaneous He^+ ion irradiation to further elucidate the effect of He implantation on D trapping. Analogous experiments could be performed, where the desorption of He was measured, but would require more advanced TDS equipment than what CMUXE currently possesses.

Conducting additional experiments under combined radiation environments will help refine predictions on material response in an ITER-type device. More

experimentation should be done on the effect of ELM mitigation on thermally-induced damage to determine if an operating window exists where fuzz nanostructures could be healed without splashing. Changing the relative ion energies of He^+ and D^+ ions in combined ion irradiation experiments will help reveal whether He forms a diffusion barrier and why the addition of D has enhanced melting. Finally, conducting additional He^+ + ELM experiments with comprehensive erosion analysis will further illustrate the exact effect of He-induced fuzz formation on surface melting and droplet splashing.

REFERENCES

[1]   T. J. Dolan, *Magnetic Fusion Technology*, 1st ed., vol. Winter / S. New York: Springer, 2013.

[2]   ITER Organization, "Photos - Technical," *iter.org*, 2013. [Online]. Available: https://www.iter.org/album/Media/7 - Technical.

[3]   H. Bolt *et al.*, "Plasma facing and high heat flux materials - Needs for ITER and beyond," *J. Nucl. Mater.*, vol. 307–311, pp. 43–52, 2002.

[4]   G. Federici *et al.*, "Plasma-material interactions in current tokamaks and their implications for next step fusion reactors," *Nucl. Fusion*, vol. 41, no. 12R, p. 1967, 2001.

[5]   ITER Physics Basis Editors, ITER Physics Expert Group Chairs and Co-Chairs, and ITER Joint Central Team and Physics Unit, "Chapter 1: Overview and summary," *Nucl. Fusion*, vol. 39, no. 12, pp. 2137–2174, Dec. 1999.

[6]   A. Hassanein, T. Sizyuk, and I. Konkashbaev, "Integrated simulation of plasma surface interaction during edge localized modes and disruptions: Self-consistent approach," *J. Nucl. Mater.*, vol. 390–391, pp. 777–780, Jun. 2009.

[7]   G. Federici, A. Loarte, and G. Strohmayer, "Assessment of erosion of the ITER divertor targets during type I ELMs," *Plasma Phys. Control. Fusion*, vol. 45, no. 9, pp. 1523–1547, Sep. 2003.

[8]   A. W. Leonard, "Edge-localized-modes in tokamaks," *Phys. Plasmas*, vol. 21, no. 9, p. 90501, Sep. 2014.

[9]   Y. Liang *et al.*, "Active Control of Type-I Edge-Localized Modes with n = 1 Perturbation Fields in the JET Tokamak," *Phys. Rev. Lett.*, vol. 98, no. 26, p. 265004, Jun. 2007.

[10]   L. R. Baylor *et al.*, "Reduction of Edge-Localized Mode Intensity Using High-Repetition-Rate Pellet Injection in Tokamak H -Mode Plasmas," *Phys. Rev. Lett.*, vol. 110, no. 24, p. 245001, Jun. 2013.

[11]   A. W. Degeling *et al.*, "Magnetic triggering of ELMs in TCV," *Plasma Phys. Control. Fusion*, vol. 45, no. 9, pp. 1637–1655, Sep. 2003.

[12]   Y. Liang *et al.*, "Active control of type-I edge localized modes on JET," *Plasma Phys. Control. Fusion*, vol. 49, no. 12B, pp. B581–B589, Dec. 2007.

[13]   Y. Ueda *et al.*, "Baseline high heat flux and plasma facing materials for fusion," *Nucl. Fusion*, vol. 57, no. 9, p. 92006, 2017.

[14]   A. Bortolon *et al.*, "Mitigation of divertor heat flux by high-frequency ELM pacing with non-fuel pellet injection in DIII-D," *Nucl. Mater. Energy*, vol. 12, pp. 1030–1036, Aug. 2017.

[15]   N. Klimov *et al.*, "Experimental study of PFCs erosion under ITER-like transient loads at plasma gun facility QSPA," *J. Nucl. Mater.*, vol. 390–391, pp. 721–726, Jun. 2009.

[16]   J. N. Brooks *et al.*, "Plasma-facing material alternatives to tungsten," *Nucl. Fusion*, vol. 55, no. 4, p. 43002, 2015.

[17]   R. Neu *et al.*, "Tungsten: an option for divertor and main chamber plasma facing components in future fusion devices," *Nucl. Fusion*, vol. 45, no. 3, pp. 209–218, Mar. 2005.

[18]   J. Linke, "Plasma facing materials and components for future fusion devices—development, characterization and performance under fusion specific loading conditions," *Phys. Scr.*, vol. T123, no. T123, pp. 45–53, Apr. 2006.

[19]   T. Loewenhoff *et al.*, "Impact of combined transient plasma/heat loads on tungsten performance below and above recrystallization temperature," *Nucl. Fusion*, vol. 55, no. 12, p. 123004, Nov. 2015.

[20]   A. R. Raffray *et al.*, "High heat flux components—Readiness to proceed from near term fusion systems to power plants," *Fusion Eng. Des.*, vol. 85, no. 1, pp. 93–108, Jan. 2010.

[21]   Plansee, "Tantalum Material Properties and Applications," 2016. [Online]. Available: https://www.plansee.com/en/materials/tantalum.html.

[22]   M. Wirtz *et al.*, "Comparison of the thermal shock performance of different tungsten grades and the influence of microstructure on the damage behaviour," *Phys. Scr.*, vol. T145, no. T145, p. 14058, Dec. 2011.

[23] S. Gonderman *et al.*, "Effects of in-situ dual ion beam (He + and D +) irradiation with simultaneous pulsed heat loading on surface morphology evolution of tungsten-tantalum alloys," *Nucl. Fusion*, vol. 58, no. 2, p. 26016, Feb. 2018.

[24] Y. Zayachuk *et al.*, "Deuterium retention in tungsten and tungsten–tantalum alloys exposed to high-flux deuterium plasmas," *Nucl. Fusion*, vol. 52, no. 10, p. 103021, 2012.

[25] J. M. Linke *et al.*, "Performance of plasma-facing materials under intense thermal loads in tokamaks and stellarators," *Fusion Sci. Technol.*, vol. 46, no. July, pp. 142–151, 2004.

[26] T. Loewenhoff *et al.*, "Evolution of tungsten degradation under combined high cycle edge-localized mode and steady-state heat loads," *Phys. Scr.*, vol. T145, no. T145, p. 14057, Dec. 2011.

[27] I. E. Garkusha *et al.*, "Tungsten erosion under plasma heat loads typical for ITER type I ELMs and disruptions," *J. Nucl. Mater.*, vol. 337–339, pp. 707–711, Mar. 2005.

[28] A. Huber *et al.*, "Investigation of the impact of transient heat loads applied by laser irradiation on ITER-grade tungsten," *Phys. Scr.*, vol. T159, no. T159, p. 14005, Apr. 2014.

[29] A. Suslova *et al.*, "Recrystallization and grain growth induced by ELMs-like transient heat loads in deformed tungsten samples.," *Sci. Rep.*, vol. 4, p. 6845, 2014.

[30] M. A. Meyers *et al.*, "Shear localization in dynamic deformation of materials: microstructural evolution and self-organization," *Mater. Sci. Eng. A*, vol. 317, no. 1–2, pp. 204–225, Oct. 2001.

[31] M. Wirtz *et al.*, "Transient heat load challenges for plasma-facing materials during long-term operation," *Nucl. Mater. Energy*, vol. 12, pp. 148–155, Dec. 2016.

[32] M. Wirtz *et al.*, "Thermal shock response of deformed and recrystallised tungsten," *Fusion Eng. Des.*, vol. 88, no. 9–10, pp. 1768–1772, Oct. 2013.

[33] A. Suslova *et al.*, "Material ejection and surface morphology changes during transient heat loading of tungsten as plasma-facing component in fusion devices," *Nucl. Fusion*, vol. 55, no. 3, p. 33007, Mar. 2015.

[34] J. W. Coenen *et al.*, "Evolution of surface melt damage, its influence on plasma performance and prospects of recovery," *J. Nucl. Mater.*, vol. 438, pp. S27–S33, Jul. 2013.

[35] R. A. Pitts *et al.*, "A full tungsten divertor for ITER: Physics issues and design status," *J. Nucl. Mater.*, vol. 438, pp. S48–S56, Jul. 2013.

[36] S. Takamura *et al.*, "Formation of Nanostructured Tungsten with Arborescent Shape due to Helium Plasma Irradiation," *Plasma Fusion Res.*, vol. 1, p. 51, 2006.

[37] G. M. Wright *et al.*, "Tungsten nano-tendril growth in the Alcator C-Mod divertor," *Nucl. Fusion*, vol. 52, no. 4, p. 42003, Apr. 2012.

[38] S. Kajita *et al.*, "Formation process of tungsten nanostructure by the exposure to helium plasma under fusion relevant plasma conditions," *Nucl. Fusion*, vol. 49, no. 9, p. 95005, Sep. 2009.

[39] S. Kajita *et al.*, "TEM observation of the growth process of helium nanobubbles on tungsten: Nanostructure formation mechanism," *J. Nucl. Mater.*, vol. 418, no. 1, pp. 152–158, 2011.

[40] F. Sefta, "Surface response of tungsten to helium and hydrogen plasma flux as a function of temperature and incident kinetic energy," University of California, Berkeley, 2013.

[41] S. I. Krasheninnikov, "Viscoelastic model of tungsten 'fuzz' growth," *Phys. Scr.*, vol. T145, p. 14040, Dec. 2011.

[42] J. K. Tripathi *et al.*, "Temperature dependent surface modification of molybdenum due to low energy He+ ion irradiation," *J. Nucl. Mater.*, vol. 464, pp. 97–106, 2015.

[43] G. De Temmerman *et al.*, "Nanostructuring of molybdenum and tungsten surfaces by low-energy helium ions," *J. Vac. Sci. Technol. A Vacuum, Surfaces, Film.*, vol. 30, no. 2012, p. 41306, 2012.

[44] J. K. Tripathi, T. J. Novakowski, and a. Hassanein, "Tailoring molybdenum nanostructure evolution by low-energy He+ ion irradiation," *Appl. Surf. Sci.*, vol. 353, pp. 1070–1081, 2015.

[45] S. Kajita *et al.*, "Fuzzy nanostructure growth on Ta/Fe by He plasma irradiation," *Sci. Rep.*, vol. 6, no. 1, p. 30380, Sep. 2016.

[46] T. J. Novakowski *et al.*, "Deuterium desorption from ion-irradiated tantalum and effects on surface morphology," *J. Nucl. Mater.*, vol. 504, pp. 1–7, Jun. 2018.

[47] T. J. Novakowski, J. K. Tripathi, and A. Hassanein, "Nb $_2$ O $_5$ Nanostructure Evolution on Nb Surfaces via Low-Energy He $^+$ Ion Irradiation," *ACS Appl. Mater. Interfaces*, vol. 8, no. 50, pp. 34896–34903, Dec. 2016.

[48] T. J. Novakowski *et al.*, "Temperature-dependent surface porosity of Nb2O5 under high-flux, low-energy He+ ion irradiation," *Appl. Surf. Sci.*, vol. 362, pp. 35–41, Jan. 2016.

[49] S. Kajita *et al.*, "Fuzzy nanostructure growth on precious metals by He plasma irradiation," *Surf. Coatings Technol.*, vol. 340, pp. 86–92, Apr. 2018.

[50] K. D. Hammond, "Helium, hydrogen, and fuzz in plasma-facing materials," *Mater. Res. Express*, vol. 4, no. 10, p. 104002, Oct. 2017.

[51] D. Nishijima *et al.*, "Sputtering properties of tungsten 'fuzzy' surfaces," *J. Nucl. Mater.*, vol. 415, no. 1 SUPPL, pp. 96–99, 2011.

[52] S. A. Barengolts, G. A. Mesyats, and M. M. Tsventoukh, "Initiation of ecton processes by interaction of a plasma with a microprotrusion on a metal surface," *J. Exp. Theor. Phys.*, vol. 107, no. 6, pp. 1039–1048, Dec. 2008.

[53] S. Kajita, S. Takamura, and N. Ohno, "Prompt ignition of a unipolar arc on helium irradiated tungsten," *Nucl. Fusion*, vol. 49, no. 3, p. 32002, 2009.

[54] S. Kajita *et al.*, "Measurement of thermophysical property of plasma forming tungsten nanofiber layer," *Jpn. J. Appl. Phys.*, vol. 55, no. 5, p. 56203, May 2016.

[55] S. Kajita *et al.*, "Thermal response of nanostructured tungsten," *Nucl. Fusion*, vol. 54, no. 3, p. 33005, 2014.

[56] S. Cui *et al.*, "Thermal conductivity reduction of tungsten plasma facing material due to helium plasma irradiation in PISCES using the improved 3-omega method," *J. Nucl. Mater.*, vol. 486, pp. 267–273, Apr. 2017.

[57] G. De Temmerman *et al.*, "Helium effects on tungsten under fusion-relevant plasma loading conditions," *J. Nucl. Mater.*, vol. 438, pp. S78–S83, 2013.

[58] M. Wirtz *et al.*, "Comparison of thermal shock damages induced by different simulation methods on tungsten," *J. Nucl. Mater.*, vol. 438, pp. S833–S836, Jul. 2013.

[59] K. Tokunaga *et al.*, "Blister formation and deuterium retention on tungsten exposed to low energy and high flux deuterium plasma," *J. Nucl. Mater.*, vol. 337–339, pp. 887–891, Mar. 2005.

[60] M. Oya *et al.*, "Surface morphology changes and deuterium retention in Toughened, Fine-grained Recrystallized Tungsten under high-flux irradiation conditions," *J. Nucl. Mater.*, vol. 463, pp. 1037–1040, Aug. 2015.

[61] W. M. Shu *et al.*, "Deuterium retention, blistering and local melting at tungsten exposed to high-fluence deuterium plasma," *J. Nucl. Mater.*, vol. 390–391, pp. 1017–1021, Jun. 2009.

[62] M. Miyamoto *et al.*, "Observations of suppressed retention and blistering for tungsten exposed to deuterium–helium mixture plasmas," *Nucl. Fusion*, vol. 49, no. 6, p. 65035, Jun. 2009.

[63] S. Gonderman *et al.*, "Effect of dual ion beam irradiation (helium and deuterium) on tungsten–tantalum alloys under fusion relevant conditions," *Nucl. Mater. Energy*, vol. 12, pp. 346–352, 2017.

[64] N. Lemahieu *et al.*, "Synergistic effects of ELMs and steady state H and H/He irradiation on tungsten," *Fusion Eng. Des.*, vol. 98–99, pp. 2020–2024, Oct. 2015.

[65] F. W. Meyer *et al.*, "Energy dependence of He-ion-induced tungsten nanofuzz formation at non-normal incidence angles," *Nucl. Mater. Energy*, vol. 12, pp. 366–371, Mar. 2017.

[66] T. J. Novakowski, J. K. Tripathi, and A. Hassanein, "Temperature-dependent surface modification of Ta due to high-flux, low-energy He+ ion irradiation," *J. Nucl. Mater.*, vol. 467, pp. 244–250, Dec. 2015.

[67] "Silicon," *Sigma-Aldrich*, 2017. [Online]. Available: https://www.sigmaaldrich.com/MSDS/MSDS/DisplayMSDSPage.do?country=US &language=en&productNumber=647101&brand=ALDRICH&PageToGoToURL =https%3A%2F%2Fwww.sigmaaldrich.com%2Fcatalog%2Fproduct%2Faldrich% 2F647101%3Flang%3Den.

[68] B. Bazylev *et al.*, "Experimental and theoretical investigation of droplet emission from tungsten melt layer," *Fusion Eng. Des.*, vol. 84, no. 2–6, pp. 441–445, Jun. 2009.

[69] E. S. Gadelmawla *et al.*, "Roughness parameters," *J. Mater. Process. Technol.*, vol. 123, no. 1, pp. 133–145, 2002.

[70] Ocean Optics, "Maya2000Pro Series Spectrometers Installation and Operation Manual," 2009.

[71] A. V. Bogomolov *et al.*, "Study of the ELM fluctuation characteristics during the mitigation of type-I ELMs," *Nucl. Fusion*, vol. 55, no. 8, p. 83018, Aug. 2015.

[72] A. Loarte *et al.*, "Transient heat loads in current fusion experiments, extrapolation to ITER and consequences for its operation," *Phys. Scr.*, vol. T128, no. T128, pp. 222–228, Mar. 2007.

[73] G. Miloshevsky and A. Hassanein, "Effects of plasma flow velocity on melt-layer splashing and erosion during plasma instabilities," *Nucl. Fusion*, vol. 54, no. 3, p. 33008, Mar. 2014.

[74] A. Shabbir *et al.*, "Correlation analysis for energy losses, waiting times and durations of type I edge-localized modes in the Joint European Torus," *Nucl. Fusion*, vol. 57, no. 3, p. 36026, Mar. 2017.

[75] J. N. Brooks *et al.*, "Plasma–surface interaction issues of an all-metal ITER," *Nucl. Fusion*, vol. 49, no. 3, p. 35007, 2009.

[76] B. Sieglin *et al.*, "Power load studies in JET and ASDEX-Upgrade with full-W divertors," *Plasma Phys. Control. Fusion*, vol. 55, no. 12, p. 124039, Dec. 2013.

[77] M. Merola *et al.*, "Overview and status of ITER internal components," *Fusion Eng. Des.*, vol. 89, no. 7–8, pp. 890–895, Oct. 2014.

[78] G. M. Wright *et al.*, "Comparison of tungsten nano-tendrils grown in Alcator C-Mod and linear plasma devices," *J. Nucl. Mater.*, vol. 438, pp. S84–S89, Jul. 2013.

[79] Y. Ueda *et al.*, "Research status and issues of tungsten plasma facing materials for ITER and beyond," *Fusion Eng. Des.*, vol. 89, no. 7–8, pp. 901–906, 2014.

[80] S. Kajita *et al.*, "Arcing on tungsten subjected to helium and transients: ignition conditions and erosion rates," *Plasma Phys. Control. Fusion*, vol. 54, no. 3, p. 35009, 2012.

[81] J. K. Tripathi, T. J. Novakowski, and A. Hassanein, "Tuning surface porosity on vanadium surface by low energy He+ ion irradiation," *Appl. Surf. Sci.*, vol. 378, pp. 63–72, Aug. 2016.

[82] S. Kajita *et al.*, "Sub-ms laser pulse irradiation on tungsten target damaged by exposure to helium plasma," *Nucl. Fusion*, vol. 47, no. 9, pp. 1358–1366, 2007.

[83] J. R. Freeman *et al.*, "Laser wavelength dependence on angular emission dynamics of Nd : YAG laser-produced Sn plasmas," *Plasma Sources Sci. Technol.*, vol. 21, no. 5, p. 55003, 2012.

[84] B. Verhoff, S. S. Harilal, and a. Hassanein, "Angular emission of ions and mass deposition from femtosecond and nanosecond laser-produced plasmas," *J. Appl. Phys.*, vol. 111, no. 12, p. 123304, 2012.

[85] T. Loewenhoff *et al.*, "Tungsten and CFC degradation under combined high cycle transient and steady state heat loads," *Fusion Eng. Des.*, vol. 87, no. 7–8, pp. 1201–1205, Aug. 2012.

[86] J. H. Yu *et al.*, "The effect of transient temporal pulse shape on surface temperature and tungsten damage," *Nucl. Fusion*, vol. 55, no. 9, p. 93027, Sep. 2015.

[87] G. G. van Eden, "Transient heat load studies on tungsten using a pulsed millisecond laser in a high-flux plasma environment," Utrecht University, 2013.

[88] G. Sinclair *et al.*, "Melt layer erosion during ELM-like heat loading on molybdenum as an alternative plasma-facing material," *Sci. Rep.*, vol. 7, no. 1, p. 12273, Dec. 2017.

[89] A. Huber *et al.*, "Investigation of the Impact on Tungsten of Transient Heat Loads induced by Laser Irradiation," in *4th International Workshop on Plasma Material Interaction Facilities for Fusion*, 2013.

[90] T. Pütterich *et al.*, "Modelling of measured tungsten spectra from ASDEX Upgrade and predictions for ITER," *Plasma Phys. Control. Fusion*, vol. 50, no. 8, p. 85016, Aug. 2008.

[91] A. Kallenbach *et al.*, "Tokamak operation with high-Z plasma facing components," *Plasma Phys. Control. Fusion*, vol. 47, no. 12B, pp. B207–B222, Dec. 2005.

[92] V. M. Mecea, "Is quartz crystal microbalance really a mass sensor?," *Sensors Actuators A Phys.*, vol. 128, no. 2, pp. 270–277, 2006.

[93] N. Lemahieu *et al.*, "Performance of yttrium doped tungsten under 'edge localized mode'-like loading conditions," *Phys. Scr.*, vol. T159, no. T159, p. 14035, Apr. 2014.

[94] D. Nishijima *et al.*, "Response of fuzzy tungsten surfaces to pulsed plasma bombardment," *J. Nucl. Mater.*, vol. 434, no. 1–3, pp. 230–234, 2013.

[95] G. M. Wright *et al.*, "Characterizing the recovery of a solid surface after tungsten nano-tendril formation," *J. Nucl. Mater.*, vol. 463, pp. 294–298, 2015.

[96] S. A. Barengolts, G. A. Mesyats, and M. M. Tsventoukh, "Explosive electron emission ignition at the W-fuzz surface under plasma power load," *IEEE Trans. Plasma Sci.*, vol. 39, no. 9, pp. 1900–1904, Sep. 2011.

[97] F. Sefta *et al.*, "Tungsten surface evolution by helium bubble nucleation, growth and rupture," *Nucl. Fusion*, vol. 53, no. 7, p. 73015, Jul. 2013.

[98] M. J. Baldwin and R. P. Doerner, "Formation of helium induced nanostructure 'fuzz' on various tungsten grades," *J. Nucl. Mater.*, vol. 404, no. 3, pp. 165–173, 2010.

[99] O. El-Atwani *et al.*, "Ultrafine tungsten as a plasma-facing component in fusion devices: effect of high flux, high fluence low energy helium irradiation," *Nucl. Fusion*, vol. 54, no. 8, p. 83013, Aug. 2014.

[100] O. El-Atwani *et al.*, "Early stage damage of ultrafine-grained tungsten materials exposed to low energy helium ion irradiation," *Fusion Eng. Des.*, vol. 93, pp. 9–14, Apr. 2015.

[101] M. J. Baldwin *et al.*, "The effects of high fluence mixed-species (deuterium, helium, beryllium) plasma interactions with tungsten," *J. Nucl. Mater.*, vol. 390–391, pp. 886–890, Jun. 2009.

[102] R. P. Doerner, M. J. Baldwin, and P. C. Stangeby, "An equilibrium model for tungsten fuzz in an eroding plasma environment," *Nucl. Fusion*, vol. 51, no. 4, p. 43001, Apr. 2011.

[103] M. J. Baldwin and R. P. Doerner, "Helium induced nanoscopic morphology on tungsten under fusion relevant plasma conditions," *Nucl. Fusion*, vol. 48, no. 3, p. 35001, 2008.

[104] K. D. Hammond *et al.*, "Large-scale atomistic simulations of low-energy helium implantation into tungsten single crystals," *Acta Mater.*, vol. 144, pp. 561–578, Feb. 2018.

[105] Y. Noiri, S. Kajita, and N. Ohno, "Nanostructure growth by helium plasma irradiation to tungsten in sputtering regime," *J. Nucl. Mater.*, vol. 463, pp. 285–288, Aug. 2015.

[106] A. Al-Ajlony, J. K. Tripathi, and A. Hassanein, "Low energy helium ion irradiation induced nanostructure formation on tungsten surface," *J. Nucl. Mater.*, vol. 488, pp. 1–8, May 2017.

[107] P. Fiflis, D. Curreli, and D. N. Ruzic, "Direct time-resolved observation of tungsten nanostructured growth due to helium plasma exposure," *Nucl. Fusion*, vol. 55, no. 3, p. 33020, Mar. 2015.

[108] S. Kajita *et al.*, "Helium plasma irradiation on single crystal tungsten and undersized atom doped tungsten alloys," *Phys. Scr.*, vol. 89, no. 2, p. 25602, Feb. 2014.

[109] K. Wang *et al.*, "Effect of starting microstructure on helium plasma-materials interaction in tungsten," *Acta Mater.*, vol. 124, pp. 556–567, 2017.

[110] W. S. Rasband, "ImageJ." U. S. National Institutes of Health, Bethesda, Maryland.

[111] Y. Ueda *et al.*, "Effects of helium ions on hydrogen isotope behavior in tungsten," *Fusion Sci. Technol.*, vol. 56, no. 1, pp. 85–90, Jul. 2009.

[112] M. J. Baldwin *et al.*, "Nanostructure formation on tungsten exposed to low-pressure rf helium plasmas: A study of ion energy threshold and early stage growth," *J. Nucl. Mater.*, vol. 415, no. 1, pp. S104–S107, 2011.

[113] M. Zlobinski, "Laserinduzierte Desorption an plasmaerzeugten Wandbeschichtungen," Diploma thesis, Heinrich-Heine-Universität Düsseldorf, 2009.

[114] J. . Davis *et al.*, "Assessment of tungsten for use in the ITER plasma facing components," *J. Nucl. Mater.*, vol. 258–263, pp. 308–312, Oct. 1998.

[115] B. Lipschultz *et al.*, "Plasma–surface interaction, scrape-off layer and divertor physics: implications for ITER," *Nucl. Fusion*, vol. 47, no. 9, pp. 1189–1205, Sep. 2007.

[116] T. Faney and B. D. Wirth, "Spatially dependent cluster dynamics modeling of microstructure evolution in low energy helium irradiated tungsten," *Model. Simul. Mater. Sci. Eng.*, vol. 22, no. 6, p. 65010, Sep. 2014.

[117] K. Nordlund *et al.*, "Multiscale modelling of plasma–wall interactions in fusion reactor conditions," *J. Phys. D. Appl. Phys.*, vol. 47, no. 22, p. 224018, Jun. 2014.

[118] Y. V. Martynenko and M. Y. Nagel', "Model of fuzz formation on a tungsten surface," *Plasma Phys. Reports*, vol. 38, no. 12, pp. 996–999, Dec. 2012.

[119] S. I. Krasheninnikov, T. Faney, and B. D. Wirth, "On helium cluster dynamics in tungsten plasma facing components of fusion devices," *Nucl. Fusion*, vol. 54, no. 7, p. 73019, Jul. 2014.

[120] T. Faney, "Numerical simulations of tungsten under helium irradiation," University of California, Berkeley, 2013.

[121] A. L. Esquisabel, "Atomistic simulations of divertor-plasma interactions in fusion reactors," University of Helsinki, 2014.

[122] A. V. Barashev, H. Xu, and R. E. Stoller, "The behavior of small helium clusters near free surfaces in tungsten," *J. Nucl. Mater.*, vol. 454, no. 1–3, pp. 421–426, Nov. 2014.

[123] V. S. Voitsenya *et al.*, "Some problems arising due to plasma–surface interaction for operation of the in-vessel mirrors in a fusion reactor," *J. Nucl. Mater.*, vol. 290–293, pp. 336–340, Mar. 2001.

[124] Y. Yamamura and H. Tawara, "Energy dependence of ion-induced sputtering yields from monatomic solids at normal incidence," *At. Data Nucl. Data Tables*, vol. 62, no. 2, pp. 149–253, Mar. 1996.

[125] E. D. Palik, *Handbook of Optical Constants of Solids, Volume 1*. Academic Press, 2012.

[126] B. Eren *et al.*, "Roughening and reflection performance of molybdenum coatings exposed to a high-flux deuterium plasma," *Nucl. Fusion*, vol. 53, no. 11, p. 113013, Nov. 2013.

[127] M. Balden *et al.*, "Surface roughening and grain orientation dependence of the erosion of polycrystalline stainless steel by hydrogen irradiation," *J. Nucl. Mater.*, vol. 329–333, pp. 1515–1519, Aug. 2004.

[128] A. Bardamid *et al.*, "Erosion of steel under bombardment with ions of a deuterium plasma," *Vacuum*, vol. 58, no. 1, pp. 10–15, Jul. 2000.

[129] M. Wisse *et al.*, "Spectroscopic reflectometry of mirror surfaces during plasma exposure.," *Rev. Sci. Instrum.*, vol. 83, no. 1, p. 13509, Jan. 2012.

[130] S. Takamura and Y. Uesugi, "Coupled interactions between tungsten surfaces and transient high-heat-flux deuterium plasmas," *Nucl. Fusion*, vol. 55, no. 3, p. 33003, 2015.

[131] S. Takamura, T. Miyamoto, and N. Ohno, "Outstanding Properties of Tungsten Material with Fiber-form Nanostructured Subsurface for the Wall of Fusion Reactor," in *38th EPS Conference on Plasma Physics*, 2011, p. O1.302.

[132] D. Nishijima *et al.*, "Incident ion energy dependence of bubble formation on tungsten surface with low energy and high flux helium plasma irradiation," *J. Nucl. Mater.*, vol. 313–316, no. SUPPL., pp. 97–101, 2003.

[133] G. Sinclair *et al.*, "Structural response of transient heat loading on molybdenum surface exposed to low-energy helium ion irradiation," *Nucl. Fusion*, vol. 56, no. 3, p. 36005, 2016.

[134] Y. Ueda *et al.*, "Exposure of tungsten nano-structure to TEXTOR edge plasma," *J. Nucl. Mater.*, vol. 415, no. 1, pp. S92–S95, 2011.

[135] A. Hassanein, "Prediction of material erosion and lifetime during major plasma instabilities in tokamak devices," *Fusion Eng. Des.*, vol. 60, no. 4, pp. 527–546, 2002.

[136] D. Nishijima, "Effects of Steady-State Plasma Exposure on Tungsten Surface Cracking due to Elm-Like Pulsed Plasma Bombardment," *Fusion Sci. Technol.*, vol. 60, no. 4, pp. 1447–1450, 2011.

[137] E. Dechaumphai *et al.*, "Near-surface thermal characterization of plasma facing components using the 3-omega method," *J. Nucl. Mater.*, vol. 455, no. 1–3, pp. 56–60, 2014.

[138] S. Kajita *et al.*, "Visualized Blow-off from Helium Irradiated Tungsten in Response to ELM-like Heat Load," *Plasma Fusion Res.*, vol. 4, pp. 004–004, 2009.

[139] J. H. Yu *et al.*, "Transient heating effects on tungsten: Ablation of Be layers and enhanced fuzz growth," *J. Nucl. Mater.*, vol. 463, pp. 7–10, 2014.

[140] C. P. C. Wong *et al.*, "Plasma Surface Interaction (PSI) studies at DIII-D," in *2013 IEEE 25th Symposium on Fusion Engineering, SOFE 2013*, 2013, pp. 1–6.

[141] M. Tokitani *et al.*, "Exfoliation of the tungsten fibreform nanostructure by unipolar arcing in the LHD divertor plasma," *Nucl. Fusion*, vol. 51, no. 10, p. 102001, 2011.

[142] W. Sakaguchi *et al.*, "In situ reflectivity of tungsten mirrors under helium plasma exposure," *J. Nucl. Mater.*, vol. 390–391, no. 1, pp. 1149–1152, 2009.

[143] T. E. Evans, "ELM mitigation techniques," *J. Nucl. Mater.*, vol. 438, pp. S11–S18, Jul. 2013.

[144] R. A. Causey, "Hydrogen isotope retention and recycling in fusion reactor plasma-facing components," *J. Nucl. Mater.*, vol. 300, no. 2–3, pp. 91–117, Feb. 2002.

[145] L. Buzi *et al.*, "Response of tungsten surfaces to helium and hydrogen plasma exposure under ITER relevant steady state and repetitive transient conditions," *Nucl. Fusion*, vol. 57, no. 12, p. 126009, Dec. 2017.

[146] S. Bardin *et al.*, "Evolution of transiently melt damaged tungsten under ITER-relevant divertor plasma heat loading," *J. Nucl. Mater.*, vol. 463, pp. 193–197, Aug. 2015.

[147] Casa Software Ltd, "CasaXPS." Casa Software Ltd, 2016.

[148] J. Linke *et al.*, "Performance of different tungsten grades under transient thermal loads," *Nucl. Fusion*, vol. 51, no. 7, p. 73017, Jul. 2011.

[149] M. Wirtz *et al.*, "Influence of helium induced nanostructures on the thermal shock performance of tungsten," *Nucl. Mater. Energy*, vol. 9, pp. 177–180, Dec. 2016.

[150] V. P. Budaev, "Results of high heat flux tests of tungsten divertor targets under plasma heat loads expected in ITER and tokamaks (review)," *Phys. At. Nucl.*, vol. 79, no. 7, pp. 1137–1162, Dec. 2016.

[151] G. Sinclair, J. K. Tripathi, and A. Hassanein, "Erosion dynamics of tungsten fuzz during ELM-like heat loading," *J. Appl. Phys.*, vol. 123, no. 13, p. 133302, Apr. 2018.

[152] G. Miloshevsky and A. Hassanein, "Stability and erosion of melt layers developed on plasma facing components of tokamaks," *Nucl. Fusion*, vol. 54, no. 4, p. 43016, Apr. 2014.

[153] H. Y. Guo *et al.*, "Developing and validating advanced divertor solutions on DIII-D for next-step fusion devices," *Nucl. Fusion*, vol. 56, no. 12, p. 126010, Dec. 2016.

[154] G. J. van Rooij *et al.*, "Tungsten divertor erosion in all metal devices: Lessons from the ITER like wall of JET," *J. Nucl. Mater.*, vol. 438, pp. S42–S47, Jul. 2013.

[155] J. W. Coenen *et al.*, "Tungsten melt layer motion and splashing on castellated tungsten surfaces at the tokamak TEXTOR," *J. Nucl. Mater.*, vol. 415, no. 1, pp. S78–S82, Aug. 2011.

[156] V. Philipps, "Tungsten as material for plasma-facing components in fusion devices," *J. Nucl. Mater.*, vol. 415, no. 1 SUPPL, pp. S2–S9, 2011.

[157] T. J. Petty *et al.*, "Fuzzy tungsten in a magnetron sputtering device," *J. Nucl. Mater.*, vol. 480, pp. 374–385, 2016.

[158] T. J. Novakowski, J. K. Tripathi, and A. Hassanein, "Effect of high-flux, low-energy He+ ion irradiation on Ta as a plasma-facing material," *Sci. Rep.*, vol. 6, no. 1, p. 39746, Dec. 2016.

[159] Y. Ueda *et al.*, "Helium effects on tungsten surface morphology and deuterium retention," *J. Nucl. Mater.*, vol. 442, no. 1–3, pp. S267–S272, Nov. 2013.

[160] S. Kajita *et al.*, "Helium plasma implantation on metals: Nanostructure formation and visible-light photocatalytic response," *J. Appl. Phys.*, vol. 113, no. 13, p. 134301, Apr. 2013.

[161] D. L. Rudakov *et al.*, "Exposures of tungsten nanostructures to divertor plasmas in DIII-D," *Phys. Scr.*, vol. T167, no. T167, p. 14055, Feb. 2016.

[162] A. Zhitlukhin *et al.*, "Effects of ELMs on ITER divertor armour materials," *J. Nucl. Mater.*, vol. 363–365, pp. 301–307, Jun. 2007.

[163] G. Miloshevsky and A. Hassanein, "Modeling of macroscopic melt layer splashing during plasma instabilities," in *Journal of Nuclear Materials*, 2011, vol. 415, no. 1 SUPPL, pp. S74–S77.

[164] M. Wirtz *et al.*, "Thermal shock tests to qualify different tungsten grades as plasma facing material," *Phys. Scr.*, vol. T167, no. T167, p. 14015, Feb. 2016.

[165] A. Loarte *et al.*, "Progress on the application of ELM control schemes to ITER scenarios from the non-active phase to DT operation," *Nucl. Fusion*, vol. 54, no. 3, p. 33007, Mar. 2014.

[166] J. Linke, "High Heat Flux Performance of Plasma Facing Materials and Components under Service Conditions in Future Fusion Reactors," *Fusion Sci. Technol.*, vol. 61, no. 2T, pp. 246–255, Feb. 2012.

[167] T. Hirai *et al.*, "Use of tungsten material for the ITER divertor," *Nucl. Mater. Energy*, vol. 9, pp. 616–622, Dec. 2016.

[168] T. Loewenhoff *et al.*, "ITER-W monoblocks under high pulse number transient heat loads at high temperature," *J. Nucl. Mater.*, vol. 463, pp. 202–205, Aug. 2015.

[169] C. Linsmeier *et al.*, "Development of advanced high heat flux and plasma-facing materials," *Nucl. Fusion*, vol. 57, no. 9, p. 92007, Sep. 2017.

[170] N. Farid *et al.*, "Experimental simulation of materials degradation of plasma-facing components using lasers," *Nucl. Fusion*, vol. 54, no. 1, p. 12002, 2014.

[171] G. De Temmerman *et al.*, "ELM simulation experiments on Pilot-PSI using simultaneous high flux plasma and transient heat/particle source," *Nucl. Fusion*, vol. 51, no. 7, p. 73008, Jul. 2011.

[172] G. G. van Eden *et al.*, "The effect of high-flux H plasma exposure with simultaneous transient heat loads on tungsten surface damage and power handling," *Nucl. Fusion*, vol. 54, no. 12, p. 123010, Dec. 2014.

[173] O. El-Atwani *et al.*, "Helium bubble formation in ultrafine and nanocrystalline tungsten under different extreme conditions," *J. Nucl. Mater.*, vol. 458, pp. 216–223, Mar. 2015.

[174] S. Wurster *et al.*, "Recent progress in R&D on tungsten alloys for divertor structural and plasma facing materials," *J. Nucl. Mater.*, vol. 442, no. 1–3, pp. S181–S189, Nov. 2013.

[175] M. Wirtz *et al.*, "Material properties and their influence on the behaviour of tungsten as plasma facing material," *Nucl. Fusion*, vol. 57, no. 6, p. 66018, Jun. 2017.

[176] A. Huber *et al.*, "Impact on the deuterium retention of simultaneous exposure of tungsten to a steady state plasma and transient heat cycling loads," *Phys. Scr.*, vol. T167, no. T167, p. 14046, Feb. 2016.

[177] I. Steudel *et al.*, "Sequential and simultaneous thermal and particle exposure of tungsten," *Phys. Scr.*, vol. T167, no. T167, p. 14053, Feb. 2016.

[178] ITER Organization, "ITER Materials Assessment Report (MAR)," 2011.

[179] G. Pintsuk, "Tungsten as a Plasma-Facing Material," in *Comprehensive Nuclear Materials*, Elsevier, 2012, pp. 551–581.

[180] "Tungsten," *Midwest Tungsten Service*, 2018. [Online]. Available: https://www.tungsten.com/materials/tungsten.

[181] "Hardness Conversion Chart," *Carbide Depot*, 2018. [Online]. Available: http://www.carbidedepot.com/formulas-hardness.htm.

[182] L. Hu *et al.*, "Dynamics of small mobile helium clusters near tungsten surfaces," *Surf. Sci.*, vol. 626, pp. L21–L25, 2014.

[183] D. Donovan *et al.*, "Characterization of a compact ECR plasma source and its applications to studies of helium ion damage to tungsten," *Phys. Scr.*, vol. T167, no. T167, p. 14040, Feb. 2016.

[184] T. Suzudo, M. Yamaguchi, and T. Tsuru, "Atomistic modeling of He embrittlement at grain boundaries of α -Fe: a common feature over different grain boundaries," *Model. Simul. Mater. Sci. Eng.*, vol. 21, no. 8, p. 85013, Dec. 2013.

[185] T. Suzudo *et al.*, "An atomistic modeling of He bubble stability at grain boundaries in alpha-Fe," *J. Nucl. Mater.*, vol. 442, no. 1, Supplement 1, pp. S655–S659, 2013.

[186] D. U. B. Aussems *et al.*, "The occurrence and damage of unipolar arcing on fuzzy tungsten," *J. Nucl. Mater.*, vol. 463, pp. 303–307, 2015.

[187] G. Sinclair *et al.*, "Structural evolution of tungsten surface exposed to sequential low-energy helium ion irradiation and transient heat loading," *Nucl. Mater. Energy*, vol. 12, pp. 405–411, Aug. 2017.

[188] M. W. Thompson, "The contribution of collision cascades to sputtering and radiation damage," *Philos. Trans. R. Soc. London A Math. Phys. Eng. Sci.*, vol. 362, no. 1814, pp. 5–28, Jan. 2004.

[189] M. Wirtz *et al.*, "Impact of combined hydrogen plasma and transient heat loads on the performance of tungsten as plasma facing material," *Nucl. Fusion*, vol. 55, no. 12, p. 123017, Nov. 2015.

[190] S. Takamura *et al.*, "Formation of Nanostructured Tungsten with Arborescent Shape due to Helium Plasma Irradiation," *Plasma Fusion Res.*, vol. 1, p. 51, Dec. 2006.

[191] S. Kajita *et al.*, "Formation process of tungsten nanostructure by the exposure to helium plasma under fusion relevant plasma conditions," *Nucl. Fusion*, vol. 49, no. 9, p. 095005, Aug. 2009.

[192] S. I. Krasheninnikov, "Viscoelastic model of tungsten 'fuzz' growth," *Phys. Scr.*, vol. T145, no. T145, p. 14040, Dec. 2011.

[193] Y. Ueda *et al.*, "Research status and issues of tungsten plasma facing materials for ITER and beyond," *Fusion Eng. Des.*, vol. 89, no. 7-8, pp. 901-906, Mar. 2014.

[194] G. De Temmerman *et al.*, "Helium effects on tungsten under fusion-relevant plasma loading conditions," *J. Nucl. Mater.*, vol. 438, pp. S78-S83, Jan. 2013.

[195] V. K. Alimov *et al.*, "Temperature dependence of surface morphology and deuterium retention in polycrystalline ITER-grade tungsten exposed to low-energy, high-flux D plasma," *J. Nucl. Mater.*, vol. 420, no. 1–3, pp. 519–524, Jan. 2012.

[196] W. Wang *et al.*, "Blister formation of tungsten due to ion bombardment," *J. Nucl. Mater.*, vol. 299, no. 2, pp. 124–131, Nov. 2001.

[197] R. D. Kolasinski *et al.*, "A multi-technique analysis of deuterium trapping and near-surface precipitate growth in plasma-exposed tungsten," *J. Appl. Phys.*, vol. 118, no. 7, p. 73301, Aug. 2015.

[198] W. M. Shu, G.-N. Luo, and T. Yamanishi, "Mechanisms of retention and blistering in near-surface region of tungsten exposed to high flux deuterium plasmas of tens of eV," *J. Nucl. Mater.*, vol. 367–370, pp. 1463–1467, Aug. 2007.

[199] M. Zibrov *et al.*, "Deuterium trapping and surface modification of polycrystalline tungsten exposed to a high-flux plasma at high fluences," *Nucl. Fusion*, vol. 57, no. 4, p. 46004, Apr. 2017.

[200] W. M. Shu, K. Isobe, and T. Yamanishi, "Temperature dependence of blistering and deuterium retention in tungsten exposed to high-flux and low-energy deuterium plasma," *Fusion Eng. Des.*, vol. 83, no. 7–9, pp. 1044–1048, Dec. 2008.

[201] V. K. Alimov *et al.*, "Surface morphology and deuterium retention in tungsten exposed to low-energy, high flux pure and helium-seeded deuterium plasmas," *Phys. Scr.*, vol. T138, no. T138, p. 14048, Dec. 2009.

[202] S. Gonderman *et al.*, "Suppression of surface microstructure evolution in W and W–Ta alloys during simultaneous and sequential He and D ion irradiation in fusion relevant conditions," *Nucl. Fusion*, vol. 57, no. 8, p. 86001, Aug. 2017.

[203] Y. Ueda *et al.*, "Effects of helium ions on hydrogen isotope behavior in tungsten," *Fusion Sci. Technol.*, vol. 56, pp. 85-90, Jul. 2009.

[204] A. Huber *et al.*, "Deuterium retention in tungsten under combined high cycle ELM-like heat loads and steady-state plasma exposure," *Nucl. Mater. Energy*, vol. 9, pp. 157-164, May 2016.

[205] J. F. Moulder, J. Chastain, and R. C. King, *Handbook of X-Ray Photoelectron Spectroscopy: a Reference Book of Standard Spectra for Identification and Interpretation of XPS Data*. Eden Prarie: Physical Electronics, Inc., 2000.

[206] M. Wirtz *et al.*, "Influence of helium induced nanostructures on the thermal shock performance of tungsten," *Nucl. Mater. Energy*, vol. 9, pp. 177–180, 2016.

[207] O. V. Ogorodnikova, J. Roth, and M. Mayer, "Ion-driven deuterium retention in tungsten," *J. Appl. Phys.*, vol. 103, no. 3, p. 34902, Feb. 2008.

[208] N. Farid *et al.*, "Cracking and damage behavior of tungsten under ELM's like energy loads using millisecond laser pulses," *J. Nucl. Mater.*, vol. 463, pp. 241–245, Aug. 2015.

[209] M. Wirtz *et al.*, "Transient heat load challenges for plasma-facing materials during long-term operation," *Nucl. Mater. Energy*, vol. 12, pp. 148–155, Dec. 2016.

[210] T. Loewenhoff *et al.*, "Evolution of tungsten degradation under combined high cycle edge-localized mode and steady-state heat loads," *Phys. Scr.*, vol. T145, no. T145, p. 14057, Dec. 2011.

[211] A. Huber *et al.*, "Deuterium retention in tungsten under combined high cycle ELM-like heat loads and steady-state plasma exposure," *Nucl. Mater. Energy*, vol. 9, pp. 157–164, Dec. 2016.

[212] L. Buzi *et al.*, "Surface modifications and deuterium retention in polycrystalline and single crystal tungsten as a function of particle flux and temperature," *J. Nucl. Mater.*, vol. 495, pp. 211–219, Nov. 2017.

PUBLICATIONS

1. G. Sinclair, J.K. Tripathi, and A. Hassanein, "Erosion dynamics of tungsten fuzz during ELM-like heat loading," *J. Appl. Phys.*, vol. 123, no. 13, p. 133302, Apr. 2018.

2. S. Gonderman, J. K. Tripathi, G. Sinclair, T. J. Novakowski, T. Sizyuk, and A. Hassanein, "Effects of in-situ dual ion beam (He^+ and D^+) irradiation with simultaneous pulsed heat loading on surface morphology evolution of tungsten-tantalum alloys," *Nucl. Fusion*, vol. 58, no. 2, p. 26016, Feb. 2018.

3. G. Sinclair, J. K. Tripathi, P. K. Diwakar, and A. Hassanein, "Melt layer erosion during ELM-like heat loading on molybdenum as an alternative plasma-facing material," *Sci. Rep.*, vol. 7, no. 1, p. 12273, Dec. 2017.

4. G. Sinclair, J. K. Tripathi, P. K. Diwakar, M. Wirtz, J. Linke, and A. Hassanein, "Structural evolution of tungsten surface exposed to sequential low-energy helium ion irradiation and transient heat loading," *Nucl. Mater. Energy*, vol. 12, pp. 405–411, Aug. 2017.

5. G. Sinclair, J. K. Tripathi, P. K. Diwakar, and A. Hassanein, "Structural response of transient heat loading on molybdenum surface exposed to low-energy helium ion irradiation," *Nucl. Fusion*, vol. 56, no. 3, p. 36005, Feb. 2016.

6. G. Sinclair, S. Gonderman, J.K. Tripathi, and A. Hassanein, "Effect of ELM pacing on morphology evolution and erosion of tungsten as a plasma-facing material in a fusion environment," *J. Nucl. Mat.* (in review).

7. G. Sinclair, S. Gonderman, J. K. Tripathi, T. Ray, and A. Hassanein, "Influence of dual beam ion irradiation and transient heat loading on tungsten surface morphology and erosion," (in preparation).